On the Prediction of Thermodynamic Properties by Atomistic Simulation. From Vapor-Liquid Equilibrium of Alcohols to Self-Assembly in Mixed Solvents

Von der Fakultät Energie-, Verfahrens- und Biotechnik der Universität Stuttgart und dem Stuttgart Center for Simulation Science (SC SimTech) zur Erlangung der Würde eines Doktors der Ingenieurwissenschaft (Dr.-Ing.) genehmigte Abhandlung

Vorgelegt von

Jörg Baz

aus Bietigheim-Bissingen

Hauptberichter:	Apl. Prof. Dr.-Ing. habil. Niels Hansen
Mitberichter:	Prof. Dr.-Ing. Ulrich Nieken
	Prof. Dr. Lars Schäfer

Tag der mündlichen Prüfung: 2. April 2020

Institut für Technische Thermodynamik und Thermische Verfahrenstechnik der Universität Stuttgart

2020

Eidesstattliche Erklärung

Hiermit versichere ich, dass ich die vorliegende Arbeit mit dem Titel

"On the Prediction of Thermodynamic Properties by Atomistic Simulation. From Vapor-Liquid Equilibrium of Alcohols to Self-Assembly in Mixed Solvents"

selbstständig verfasst und keine anderen als die angegebenen Quellen und Hilfsmittel benutzt habe, dass alle Stellen der Arbeit, die wörtlich oder sinngemäß aus anderen Quellen übernommen wurden, als solche kenntlich gemacht sind.
Ich versichere außerdem, dass die vorliegende Dissertation nur in diesem und keinem anderen Promotionsverfahren eingereicht wurde und dass diesem Promotionsverfahren keine endgültig gescheiterten Promotionsverfahren vorausgegangen sind.

I herewidth duly declare that I have authored the dissertation

"On the Prediction of Thermodynamic Properties by Atomistic Simulation. From Vapor-Liquid Equilibrium of Alcohols to Self-Assembly in Mixed Solvents"

independently and only with use of specified aids. I have mentioned all sources used and cited correctly according to scientific rules.

Stuttgart, October 6th, 2019

Jörg Baz

Contents

List of Symbols

Latin Letters - Part 1 of 2

a	parameter specifying the attractive part of the Mie potential
a^i	Helmholtz energy
a_{W}	water activity
A	parameter of Buckingham potential
b	parameter specifying the repulsive part of the Mie potential
B	parameter of Buckingham potential
c	prefactor of potential function
C	parameter of Buckingham potential or fitting parameter
D	dimer
D_0	prefactor of potential energy function
D_{self}	self-diffusion coefficient
E	ethanol
f	objective function
$g(r)$	radial distribution function
$g(z)$	cylindrical distribution function
k_B	Boltzmann constant
k_{ij}	mixture parameter
k_{max}	maximum number of k-vectors
K	association constant
L	liquid or box length
m	attractive exponent
M	monomer
M	molar mass
M_L	molarity
n	repulsive exponent
N	number of particles/atoms/molecules
N_t	computational complexity
p	pressure
p^0	pressure of an ideal gas at 1 molar concentration
$P_{\alpha,\beta}$	pressure tensor components
q	partial charge
r	interaction site distance or distance in general
$\vec{r}$	atom coordinates in space
$\mathbf{r_i}$	center of mass position of a molecule
$\mathcal{R}$	ideal gas constant

Latin Letters - Part 2 of 2

$s(t)$	time depending standard deviation
S	salt
S	solid
t	time
T	temperature
u	dispersion-energy parameter
U	potential energy
V	volume
V^0	standard state volume
V^{E}	excess volumina
w	mass fraction
W	water
x	mole fraction

Greek Letters

α	fitting parameter
α_{sc}	soft-core scaling parameter
β	fitting parameter
ΔG	free energy
ΔH	enthalpy difference of complex formation
ΔN	window of particle numbers
ΔS	entropy difference of complex formation
ϵ	potential depth
ϵ^i	association parameter
ϵ_0	vacuum permittivity
η	shear viscosity
γ_{W}	water activity coefficient
κ_T	isothermal compressibility
κ^i	association parameter
λ	coupling parameter
μ	chemical potential
Ω	torsional angle
Ω_n	number of observables
ϕ	potential energy
ϕ_{W}	fugacity coefficient of water
ρ	density
σ	atom radius
σsc	soft-core scaling parameter
τ	fitting parameter or time origin
τ_p	coupling constant of barostat
τ_T	coupling constant of thermostat
ξ	dimensionless constant

Subscripts

a, b	indices for interaction sites a and b
alc.	alcohol
angle	bond angle bending
A, B	indices for substances A and B
b	bound
bond	covalent bonded
box	simulation box
c	cut-off
C_i	concentration
CH_2	methylene group
electrostatic	electrostatic interaction
fit	fitted
H	hydrogen
H_2O	water
improper	improper angle bending
i, ii	atom specifier
j, jj	atom specifier
ij	atom pair specifier
m	melting
max	maximum
O	oxygen
PMF	corrected potential of mean force
raw	uncorrected potential of mean force
solv	solvation
torsion	torsional angle bending
u	unbound
W	water
∞	infinity
99	99% limit

Superscripts

assoc	associative
c	critical
disp	dispersive
exp	experimental
inter	nonbonded potential energy
m	molar
res	residual
sat	saturated
seg	segments
sim	simulation
species	mole fraction considering dissociated choline chloride

Abbreviations

AAD	absolute average deviation
ATB	automated topology builder
AUA	anistropic united atom
CBMC	configurational bias monte carlo
ChCl	choline chloride
COM	center of mass
DES	deep eutectic solvent
DNA	deoxyribonucleic acid
EtOH	ethanol
exp.	experimental
GAFF	general AMBER force field
GCMC	grand canonical Monte Carlo
Gly	glycerol
HBA	hydrogen bond acceptor
HBD	hydrogen bond donor
IL	ionic liquid
liq	liquid
LJ	Lennard-Jones
MBAR	multistate Bennett acceptance ratio
MeOH	methanol
MC	Monte Carlo
MD	molecular dynamics
MP2	Møller-Plesset perturbation theory
NADES	natural deep eutectic solvents
NH	primary amino group
NMR	nuclear magnetic resonance
NpT	isobaric-isothermal ensemble
NVT	canonical ensemble
OH	hydroxyl group
OPLS	optimized potential for liquid simulations
OPV	organic photovoltaic
PBI	perylene bismide
PC-SAFT	perturbed-chain statistical associating fluid theory
PME	particle-mesh Ewald
PMF	potential of mean force
QM	quantum-mechanics

SPC	simple point charge
SPCE/E	simple point charge extended
TAMie	Transferable Anistropic Mie
TraPPE	Transferable Potentials for Phase Equilibria
TZVPP	basis set
US	umbrella sampling
UV-vis	ultraviolet-visible
vdW	van der Waals
VLE	vapour liquid equilibrium
W	water

Zusammenfassung

Molekulare Simulationen haben sich als wissenschaftliches Gebiet etabliert, das eine Lücke zwischen Experiment und Theorie schließt. Sie spielen eine wertvolle Rolle, wenn es darum geht exakte Ergebnisse für Probleme der statistischen Mechanik zu liefern, die andernfalls nur mit approximierenden Methoden lösbar oder möglicherweise sogar unlösbar wären. Alle in dieser Arbeit durchgeführten Simulationen basieren auf einer klassischen Beschreibung von Wechselwirkungen innerhalb der Moleküle sowie des Einflusses von umgebenden Molekülen. In der vorliegenden Arbeit wurden zwei Aspekte von Molekularsimulationen untersucht, zum einen die Verbindung zwischen Modell und theoretischer Vorhersage und zum anderen die Verbindung zwischen Modell und experimentellen Daten. Die untersuchten Systeme sind für die Materialwissenschaften, die Biotechnologie sowie für das Chemieingenieurwesen relevant. Die in Kapitel 2 dieser Arbeit vorgestellten Ergebnisse beleuchten das Assoziationsverhalten von supramolekularen Komplexen in unterschiedlichen Lösungsmittelumgebungen. Kapitel 3 befasst sich mit der Vorhersage von Eigenschaften wässriger Lösungen des stark eutektischen Lösungsmittels Glycelin unter Verwendung robuster Methoden und Software. Die Kapitel 4 und 5 befassen sich sowohl mit der Entwicklung von Kraftfeldern als auch mit der Vorhersage von Eigenschaften am Beispiel von n-Alkoholen.

Summary

Molecular simulation is an established scientific field that bridges the gap between experiment and theory. It plays a valuable role in providing essentially exact results for problems in statistical mechanics which could otherwise only be handled by approximate methods, or be even intractable. All simulations performed in this work are based on a framework, called force field, made of equations and parameters describing different interactions within single molecules as well as the influence of other molecules. In the present work the dual role of simulation as a bridge between models and theoretical predictions on the one hand and between models and experimental results on the other was explored for systems of varying complexity with relevance in materials science, biotechnology and chemical engineering. The results presented in chapter 2 of this work aims to explain the association behaviour of supramolecular complexes in mixed solvent environments. Chapter 3 is concerned with property prediction for mixtures of the deep eutectic solvent glyceline with water using robust methods and software. The chapters 4 and 5 are concerned with both, development of force fields as well as property prediction using n-alcohols as example.

Journal Publications

This thesis led to the following publications:

- Chapter 2: J. Baz and N. Hansen: Thermodynamic Characterization of the Dimerization of an Anionic Perylene Bisimide Dye Using Molecular Simulation, *The Journal of Physical Chemistry C*, **123**, 8027-8036, 2019.
- Chapter 3: J. Baz, C. Held, J. Pleiss and N. Hansen: Thermophysical Properties of Glyceline-Water Mixtures Investigated by Molecular Modelling, *Physical Chemistry Chemical Physics*, **21**, 6467-6476, 2019.
- Chapter 4: J. Baz, N. Hansen and J. Gross: On the use of transport properties to discriminate Mie-type molecular models for 1-propanol optimized against VLE data, *The European Physical Journal Special Topics*, **227**, 1529-1545, 2019.
- Chapter 5: J. Baz, N. Hansen and J. Gross: Transferable Anisotropic Mie-Potential Force Field for n-Alcohols: Static and Dynamic Fluid Properties of Pure Substances and Binary Mixtures, *Industrial & Engineering Chemistry Research*, **59**, 919-929, 2020.

The chapters 2 to 5 present literal quotes of the published work. Any addition with respect to the published work is marked. Any deletion is indicated with square brackets as ‚[...]'. Cross-references between chapters of this thesis, which are added to the published version of the text to increase readability, are marked by square brackets. The Supporting Informations to the single chapters are presented in the Appendix of this thesis.

Acknowledgements

Throughout working on this dissertation I have received a lot of support and assistance. I would first and foremost like to thank my supervisor Niels Hansen, whose expertise was invaluable in many cases. I really acknowledge your encouragement and guidance during my work on this thesis. In many informative discussions I learned a lot and you gave me a deeper understanding of the scientific work.
I would also like to thank all my colleagues at the ITT which were creating a helpful and kind atmosphere leading to many fruitful discussions.
Finally, I would like to thank my family and friends, especially my wife Alexandra for their support in deliberating over the problems and findings of this thesis as well as providing happy distractions to rest my mind outside of my research.

Chapter 1

Introduction

1.1 Molecular Simulations for Condensed Phase Systems

Molecular simulations are powerful methods that allow fundamental understanding of molecular processes and structures linked with corresponding macroscopic properties. The first simulations describing the properties of aqueous systems were reported in the 1960s using a Monte Carlo (MC) algorithm [1]. Molecular dynamics (MD) simulations for water [2] were conducted in the 1970s followed by studies of electrolyte solutions [3] and later for soluted dipeptides in aqueous surroundings [4]. These research results lead to the possibility to investigate effects in gas and liquid phases as well as solute-solvent interaction mechanisms on a molecular level of understanding [5]. Phase equilibrium calculations as another method of molecular simulations play an important role in the access to physical properties of fluids with industrial relevance that are difficult or impossible to measure experimentally. Important steps in the development of phase equilibria calculations have been the introduction of the Gibbs ensemble technique [6], the configurational-bias Monte Carlo method [7] as well as grand canonical Monte Carlo (GCMC) simulations [8] together with transition matrix Monte Carlo [9, 10]. A short summary of considerable achievements concerning molecular dynamics simulations over the years between 1957 and 2016 is shown in table 1.1 together with the reachable simulation time scales at that time and the corresponding literature references.

Due to the continuous development and improvement of molecular simulations they are nowadays used in industrial frameworks for example in pharmaceutical [22–24] or chemical applications. Current research fields are still the analysis of Lennard-Jones fluids [25–29] where fundamental theories are drawn and examined while simulating cell environments using complex solutions [30, 31] shows how versatile applicable simulations have become.

Table 1.1: Historical overview over molecular dynamics simulations from 1957 to 2016.

Year	Molecular system	Time scale / s	Ref.
1957	First MD simulation (hard discs, two dimensions)		[11]
1964	atomic liquid (argon)	$1 \cdot 10^{-11}$	[12]
1971	molecular liquid (water)	$5 \cdot 10^{-12}$	[2]
1975	simple small protein	$1 \cdot 10^{-11}$	[13]
1976	protein without solvent	$2 \cdot 10^{-11}$	[14]
1983	protein in water	$2 \cdot 10^{-11}$	[15]
1986	DNA in aqueous solution	$1 \cdot 10^{-10}$	[16]
1989	protein-DNA complex in water	$1 \cdot 10^{-10}$	[17]
1998	polypeptide folding in solvent	$1 \cdot 10^{-8}$	[18]
2001	micelle formation	$1 \cdot 10^{-7}$	[19]
2010	folding of a small protein	$5 \cdot 10^{-6}$	[20]
2016	ubiquitin dynamics	$5 \cdot 10^{-3}$	[21]

The broad range of applications holds also a broad range of accuracy concerning the simulation results. While pure component properties could be, depending on the systems complexity, predicted within a few promille deviation to experimental data, the new insights into effects and processes in a complex cell system on an atomistic-level is in most cases more relevant than the actual numerical result. Nevertheless also in these cases the used models should be in agreement with the fundamental physics and should be free of artifacts that could be included in the method itself [32–35] regardless of the precision of the implemented potential energy function.

The activities in molecular simulations can be divided into two main groups, namely into discovery-driven research areas and data-driven research areas [36]. An overview of this two groups with a categorization of activities, examples and the associated tools and users is shown in table 1.2. The area of discovery driven activities includes the prediction of new phenomena, the investigation of observed phenomena to obtain a deeper understanding or get explanations as well as the development of force fields and new simulation methods. With the aid of molecular simulations the vaporization process of ionic liquids could be described [37], new zeolite materials have been discerned [38], increased transport properties of gases through smooth carbon nanotube pores have been predicted [39] as well as for metal organic framework materials negative thermal expansion coefficients have been discovered [40]. While these studies all try to explain unknown phenomena the following works offer a deeper understanding of known phenomena. Starting from the description of hydrophobicity [41] to explanations about crystallization initiated by shear strains [42], to a detailed depiction of the amyloid formation processes [43] and estimations about ionic systems at critical conditions [44]. Section 3 of the discovery-driven area encompasses the

development and improvement of new force fields as well as new methods including better sampling methods for Monte Carlo simulations [6, 45, 46], molecular dynamic methods using non-equilibrium theories [47] but also transferable force fields for the prediction of different properties [48, 49].

In contrast to the discovery-driven research area where often qualitative results are the outcome of molecular simulation, data-driven projects aim the high accuracy prediction of properties without or with less input from experimental data. Molecular simulations in this field can be used to interpolate between given experiments or extrapolate to conditions where no experimental data are available but also can be used to predict missing properties or compounds. Applications are for example the calculation of viscosities for alkanes [50], prediction of phase diagrams for binary mixtures [51] as well as gas absorption isotherms [52]. In the second section of the data-driven simulations theories and models, like the SAFT equation of state [53], are developed, validated and improved by molecular simulations. Also the development of models describing transport and adsorption in porous media [54] and other local composition models [55] are supported by molecular simulations.
The validation of costly and complex experiments can also be provided by molecular simulations as well as the support in cases where experimental results are hard to interpret. In data-driven works it is recommended to use widely accepted and validated code together with accurate force fields.

With regard to table 1.2 a brief overview of physical properties which can be obtained by molecular simulation and which effort must be made is shown in table 1.3. On the abscissa the properties are listed by their molecular simulation relevance. That means the higher the advantage of using molecular simulations compared to experiments the higher is the relevance. As advantage in this case is not only the accuracy but also the expenditure which is necessary to obtain a certain property either by molecular simulation or by experiments. The ordinate classifies the importance of the specific property for their significance in chemical process design and development.
Calculating a density with molecular simulations is often very easy but the importance for chemical process design is also low. Nevertheless the effort for obtaining a density is much lower using molecular simulations compared to experiments which leads to a high molecular simulation relevance.
The properties shown in the top right of table 1.3 are those where molecular simulations have a big advantage compared to experiments and also those properties are highly relevant for chemical process design. For this reason it is most likely that molecular simulations used in this area have an effect on the development of chemical processes.

Table 1.2: Molecular simulation activities divided into discovery-driven and data-driven activities. Adopted from Maginn [56].

	Type of activity	Examples	Tools and Users
Discovery	1. Search for new phenomena	• Simulations of new materials (nanotubes, metal organic frameworks, ionic liquids) • Nanoscale phenomena	• General or custom software • Standard or tailored force fields • New methods often required • Mainly academic users
	2. Explanation of phenomena	• Nature of hydrophobicity • Phase transition • Anomalous behaviour of water • Protein folding	• General or custom software • Standard or tailored force fields • Academic or industrial users • May be associated with experimental projects
	3. Development and validation of methods and force fields	• New free energy methods • Histogram reweighting • Accelerated dynamics • General force fields that can reproduce pVT and transport properties	• Rapid, flexible prototyping software • Automated force field development tools • Mainly academic users • Several methods required if validating against many properties
Data	1. Prediction of properties	• High pressure, temperature properties of materials • Activity coefficients, Henry's Law constants, isotherms • Enthalpies of mixing • Heat capacities	• Robust methods and software • Accurate and transferable force fields • Validated methods • Easy to use software • Database of force fields, properties • Industrial and some academic users
	2. Test theories and models	• Ideal absorbed solution • Stefan-Maxwell • Regular solutions • SAFT • Critical scaling	• Standard force fields • Mainly academic, some industrial users • Specialized codes (wide range of phenomena)
	3. Validation of difficult experiments	• Crystal structure refinement • STM, AFM studies • Complex mixtures • Extreme conditions	• Accurate force fields • Industrial and academic users • Specialized codes (wide range of phenomena)

Table 1.3: Physical properties which can be calculated by molecular simulations sorted by importance and relevance. Adopted from Maginn [56].

Importance	complementary	direct advantage
high	• Vapour pressure • Boiling Point • Phase equilibria • Critical properties • Heat of vaporization	• Gas solubility • Viscosity • Liquid thermal conductivity • Heat capacity • Henry's constant (dilute aqueous organics)
low		• Density

molecular simulation relevance

1.2 Force Fields

All simulations performed in this work are based on a framework made of equations and parameters describing different interactions within single molecules as well as the influence of other molecules. This framework which describes all interactions in a simulated system is called a force field.
The empirical functional form of classical force fields, using fixed charges, was developed in 1969 by Levitt and Lifson [57] and is used in nearly the same expression in todays molecular force fields.

$$E_{\mathrm{pot}}(\vec{r}) = \underbrace{E_{\mathrm{bond}}(\vec{r}) + E_{\mathrm{angle}}(\vec{r}) + E_{\mathrm{torsion}}(\vec{r}) + E_{\mathrm{improper}}(\vec{r})}_{\text{covalent interactions}} + \underbrace{E_{\mathrm{electrostatic}}(\vec{r}) + E_{\mathrm{vdW}}(\vec{r})}_{\text{non-covalent interactions}} \tag{1.1}$$

In equation 1.1 the potential energy function is shown with its individual contributions. It includes the description of every atom in a molecule as a point in space with mass, partial charge and van der Waals parameters. The interactions between those interaction sites are defined by potential energy functions using the atomic coordinates $\vec{r}$. E_{bond}, E_{angle}, E_{torsion} and E_{improper} are covalent terms or intramolecular interactions considering covalent bonds, bond-angle bending, dihedral-angle torsion and improper dihedral-angle bending. These interactions are occurring within a considered molecule. $E_{\mathrm{electrostatic}}$ and E_{vdW} are so called non-covalent terms describing Coulomb (electrostatic) and van der Waals interactions. Since explicit electrons are not part of this consideration, a system in the electronic ground state is implied [58].

Equation 1.2 shows a more explicit form of equation 1.1 with formulated terms for each interaction contribution [59, 60].

$$
\begin{aligned}
E_{\mathrm{pot}}(\vec{r}) = & \underbrace{\sum_{\text{bonds}} \frac{1}{2} k_{ij}^{b} \left(r_{ij} - r_{ij}^{0}\right)^{2}}_{\text{bonded interaction}} + \underbrace{\sum_{\text{angles}} \frac{1}{2} k_{ijk}^{\Theta} \left(\Theta_{ijk} - \Theta_{ijk}^{0}\right)^{2}}_{\text{angle beding interaction}} \\
& + \underbrace{\sum_{\text{prop. dih.}} k_{ijkl}^{\phi} (1 + \cos(n_{ijkl}\phi_{ijkl} - \phi_{ijkl}^{0}))}_{\text{proper dihedral interaction}} \\
& + \underbrace{\sum_{\text{imp. dih.}} \frac{1}{2} k_{ijkl}^{\xi} \left(\xi_{ijkl} - \xi_{ijkl}^{0}\right)^{2}}_{\text{improper dihedral interaction}} \\
& + \underbrace{\sum_{\text{pairs } i,j} \frac{q_i q_j}{4\pi\epsilon_0}}_{\text{electrostatic interaction}} + \underbrace{\sum_{\text{pairs } i,j} 4\epsilon_{ij} \left[\left(\frac{\sigma_{ij}}{r_{ij}}\right)^{n} - \left(\frac{\sigma_{ij}}{r_{ij}}\right)^{m}\right]}_{\text{van der Waals interaction}}
\end{aligned}
\tag{1.2}
$$

In this equation the bonded interactions are represented as harmonic potential with a force constant k_{ij}^{b}, an equilibrium distance r_{ij}^{0} and the actual distance between atom i and atom j, r_{ij}. The angle bending interactions are also represented by a harmonic potential with a force constant k_{ijk}^{Θ}, an equilibrium angle Θ_{ijk}^{0} and the actual angle included by the atoms i, j and k, Θ_{ijk}. Proper dihedral interactions are represented by a function using a force constant k_{ijkl}^{ϕ}, a phase shift ϕ_{ijkl}^{0}, a multiplicity n_{ijkl} and an actual torsional angle ϕ_{ijkl}. Improper dihedral interactions are instead represented as harmonic potential with a force constant k_{ijkl}^{ξ}, an equilibrium angle ξ_{ijkl}^{0} and the actual torsional angle ξ_{ijkl}^{0}. Electrostatic interactions are represented by two partial charges q_i and q_j divided by the dielectric constant in vacuum ϵ_0 and π. Van der Waals interactions are represented by Lennard-Jones or Mie-potentials with a potential energy parameter ϵ_{ij}, an atom radius parameter σ_{ij} and the actual distance between the atoms i and j, r_{ij}.

In fact quantum mechanical calculations are the most precise method for describing intramolecular interactions but in most cases only few molecules in vacuum or implicit solvents are considered while the computational expenditure is comparable to molecular simulations. Moreover, condensed phase thermodynamic properties are often not very sensitive to the details of the covalent interactions. Equations of state and semi-empirical approaches are popular tools for the prediction of less complex systems because they show high accuracy together with fast calculations and thus very low computational costs. But these methods also fail with increasing complexity of the solute molecules as it is shown exemplary in chapter 3 where the results of the PC-SAFT equation of state are directly compared to those of molecular simulations.

This classical force fields include the assumption of fixed partial charges during the simulation. The response to the electrostatic surrounding of the considered single atom is not taken into account explicitly. This simplification arised in those days the force fields were invented from insufficient computational capabilities accompanied by polarization effects [61].

Since each term in equation 1.2 includes a sum over terms taking one to four atoms and thus several parameters into account it is easily imaginable that a system of 1000 atoms would lead to the definition of a multiple of 1000 parameters. Another simplification included in the force fields to address this problem is the assumption of transferable force field parameters which are fitted to experimental data or higher-level quantum-mechanical (QM) calculations [58].

Despite these assumptions which are reducing the number of parameters drastically the determination of force field parameters is still a strongly under determined problem. This fact is leading to multiple parameter combinations which are all in the same quality concerning the underlying objective function.

Although the developed fixed-charge force fields have been advanced over the past decades and are able to give insights into (bio)-molecular processes which are not accessible by experiments there are still recent research topics to improve and develop classical force fields.

Fixed-charge force fields can be improved by using anistropic approaches which delocate the charge site from the van der Waals site to take charge distributions caused by ionic pairs into account [58, 62–65]. Another option using fixed-charge force fields is the representation of multivalent ions by multi-interaction sites to enhance the ion-water, ion-nucleic acids or ion-protein interactions[66–69].

In most cases current force fields for small molecules in the condensed phase are parameterized against several thermodynamic quantities. However, the investigation of larger biomolecules becomes possible due to the increasing computational power and the focus on macroscopic characteristics and kinetic behaviour of those molecules is drastically increasing in actual research projects. Working on such scientific questions requires a force field which is able to predict kinetics and therefore should be validated against recent experimental data. Todays possibility to perform molecular dynamic simulations in the millisecond range offers the opportunity to calculate kinetics of molecular systems and thus validate or even parameterize them in this working field [70–74].

The problem with fitting force field parameters that multiple sets of parameters are obtained all leading to the same error in the underlying objective function can be accounted by using Bayesian methods [75–78]. Similar to other estimation methods the Bayesian methods also do estimate a parameter set which fits best to the associated training set but further more information about uncertainties or variabilities of all qualified parameter sets are provided and can be used for further selections [79].

In most of the classical fixed-charge force fields specific atom types are used together with a method called indirect perception. With this method atom types are defined including identifiers which provide all information to parameterize a molecular system by looking up the corresponding parameters, e.g. bond-streching, angle-bending, torsion and Lennard-Jones, in parameter tables [80]. The chemical surrounding of the considered atom is accounted by introducing different atom types for the same chemical element. This procedure is often leading to many different atom types with mostly identical parameters which results in confusing parameter tables including multiple identical parameters stored for different atom types. Note that parameterization of new large molecules, such as proteins or biomolecules, is often not possible in a systematic and consistent way and needs human expertise to choose suitable atom types in specific cases.
A possible approach to counteract this challenge is called direct chemical perception developed by Mobley et al. [80] which is reducing the number of identical parameters drastically. In this method the chemical surrounding of the considered atom is taken into account and force field parameters are assigned due the neighbouring atoms. The necessary information about the neighbouring atoms and thus the chemical surrounding are provided by SMARTS patterns [81] written in the SMIRKS chemical query language [82] which is a flexible programming language for the definition of molecular structures. The resulting new force field format is called SMIRKS Native Open Force Field (SMIRNOFF) with a corresponding minimalistic general force field named SMIRNOFF99Frosst [80]. A promising possibility of this method is a flexible, systematic and consistent assignment of force field parameters to large (bio)-molecules under the elimination of human choices.
Another option which may could improve the results of molecular simulations is to use machine learning algorithms and thus change the functional form of the force field. The underlying equations in classical force fields describing different atomistic interactions are physically motivated. The situation is different if machine learning algorithms are used to predict interaction energies or forces where no explicit functional form is specified. The machine learning approach was already successfully used to compute pair interaction energies in the same quality as the QM calculations which were used as training set [83, 84]. Also the application of these potentials to molecular dynamics simulations of relative simple systems led to promising results [79, 84, 85].

1.3 Validation

Molecular simulations whether molecular dynamics or Monte Carlo simulations are based on a framework of mathematical expressions consisting of equations which are trying to represent the physical behaviour of molecules in different conditions. In a case where the physical world is simulated there are always approximations, compromises and uncertainties no matter which methods are utilized [86–88]. With the software packages and the hardware performance available today it is much easier to perform simulations and obtain results compared to those days when molecular simulations were invented. Precisely because it has become easier to produce data using molecular simulations it is of absolute importance to make sure that results are valid and the used models are consistent and implemented correctly [89, 90]. Additionally every simulation result is strongly depending on the validity of the physical model and the corresponding assumptions made [91].
In this section a series of arising challenges setting up molecular simulations is presented together with possible approaches to reduce errors and by that doubtful simulation results. Not only deficiency in physical validity of the underlying model but also the treatment of interactions and simulation parameters can lead to very different results. For example the folding of biomolecules in reaction-field simulations are depending on the handling of non-bonded interaction cut-offs [92] while the ordering of lipid bilayers as well as the area per lipid is strongly affected by truncating the electrostatic interactions [93, 94]. It is assumed that using the charge-group cut-off scheme together with a faulty buffer generating pairlists is leading to simulation results promising a water flow through nanotubes [95]. As it can be seen simulation results are not only depending on the underlying physical model but also on the parameter adjustment which is necessary to set up simulations. In an attempt to reduce such misleading results, different validation approaches and methods at different stages of molecular simulations have been developed over the last years ranging from correct implementation to error estimation of results as well as comparison to experimental data.

Validating the molecular model includes to make sure the basic equations and connections are implemented correctly on a fundamental level. Because molecular simulations are based on large software codes including about 100000 lines they are harbouring great potential for errors. Studies estimate an error expectation rate between 2 and 7 errors in 1000 lines of professional and well maintained software code [96, 97], leading to a number of errors between 200 and 1000 within a molecular simulation code. The estimated error rate is increasing for codes written in small academic groups without good maintenance and not provided to a broad range of users. Note that not every bug in the software has immediately lead to an error in the results of the simulation and are thus hard to find.

But those programming errors which are propagating through to simulation results can be detected by automated tests. Most of those tests are focusing on the correctness of code including the reproduction of reliable results to validate new versions before releasing it [89]. A very extensive testing environment was presented by Merz and Shirts in 2018 which is additionally validating physical assumptions, kinetic and potential energy, mean values and standard deviation, discontinuities in potentials and forces as well as temperature and pressure control algorithms [98].

Even if the used simulation code is validated in a way mentioned above there are several pitfalls which can cause strong influence on simulation results. It is noteworthy that also experienced users of molecular simulation software are often trapped by making mistakes mentioned below [34, 97, 99].

Since molecular simulations are sampling a part of a $3N$- (MC) or $6N$-dimensional (MD) phase space of the given system, the simulation period is one component which can strongly affect the obtained results. Because the convergence is depending on the system composition and size there is no fixed rule how long simulations have to run for a sufficient sampling of the phase space. For this reason determining the required number of simulation steps is not a trivial decision [100, 101].
Directly connected to this issue is the choice of the equilibration period. Before generating samples evaluated to simulation results it is necessary to equilibrate the molecular system to compensate possible artifacts arised from setting up the system. Often observables like potential or kinetic energy as well as restrained properties like temperature or pressure are used to decide whether the system is equilibrated or not. It is important to make sure that a possible non-physical behaviour, as it could occur during the equilibration, is not included in the evaluated production samples.

Another aspect which should be considered setting up molecular simulations is the evaluation of interactions. Due to the infinitely computational costs necessary to evaluate all interactions in a molecular system in entirety it is required to make simplifications in order to reduce the computational effort. The cut-off for van der Waals interactions as well as electrostatic interactions, corrections for interactions beyond this cut-of, the selected cut-off scheme as well as the treatment of covalent bonds are parameters strongly affecting the behaviour of molecular simulations [91, 97]. Note that the cut-off radii are a parameter of the force field and thus are depending on the parameterization. That means changing the value of the cut-off radius to a significant other value compared to that used during the parameterization could lead to artifacts [91]. A classical approximation to represent covalent bonds is the usage of rigid bonds. Due to the fact that

high frequency bond vibrations are primarily in their ground state at ambient conditions fixed bond lengths are an appropriate way for representation [102]. However, assuming constant bond lengths between two atoms instead of classical harmonic oscillators can lead to effects which are not physical because of the quantum nature of the bonds and thus can affect the simulation results [103].
The van der Waals and electrostatic corrections accounting for interactions beyond the cut-off radii are usually analytical expression to correct average values of multiple properties evaluated of from simulation. The configurations used for these evaluations however are generated using truncated interactions schemes and thus using wrong forces. The utilization of such evaluated properties to validate the molecular simulation is very limited for this reason unless long-range corrections are applied in each step during the simulation run [104].

The system size is another parameter which should be chosen with care. It may be obvious to select a small system size in order to reduce computational effort, but the smaller the system the stronger are the finite size effects and the stronger are the influence of the selected boundary conditions [33].
Almost always periodic boundary conditions together with the nearest image conventions are applied to molecular simulations. For this the simulated system is surrounded by identical copies of itself pretending an infinitely large system. However, also this artificial recurrence raises distortion effects [105, 106].
The last issue within the set up of molecular simulations is the choice of the ensemble. Coupling a system to a temperature or pressure bath offers the opportunity to set thermodynamic boundary conditions and thus set a corresponding thermodynamic ensemble [60]. Even though the selected thermodynamic ensemble should not affect the emerging simulation results as a matter of fact it still makes a difference [107, 108]. To impose a temperature or a pressure to a molecular system the four different methods are available, stochastic, first-order weak-coupling, constraints or extended Lagrangian techniques. The advantages and disadvantages of each method have been discussed by van Gunsteren and Berendsen in 1990 [60].

It can easily be seen that apart from errors occurring in the software code there are several settings and parameters which choice is affecting the behaviour of the molecular simulation and thus is influencing the results. Even if the simulation was set up with great care and the used methods were validated meticulously it is still necessary to validate the methods of evaluating the simulation results. Often the underlying trajectories are correct within the framework of the force field assumptions but the evaluation method provides misleading results. Since the trajectories of molecular simulations are correlated

to a certain amount and correlated data do not contain completely new information it is necessary to only use decorelated data to obtain meaningful results [109–111]. The accuracy of the evaluated properties are often stated with the statistical error of the corresponding time series or with an error obtained using the block averaging method [112]. Since there is no best principle to calculate errors the only important thing is to provide a description how properties and errors are calculated from trajectories as exactly as possible.

At the end in most cases simulation results are compared with experimental data and often such comparisons are used to validate the employed simulation method. In such a case it is important that the force field is evaluated against as many observables, properties and different molecules as possible. The validation properties should be distributed over the categories thermodynamic properties such as heat of vaporization, density or free energy of solvation, dielectric properties like dielectric permittivity, structural properties such as radial distribution functions or degree of hydrogen bonding and dynamic properties like diffusion or viscosity.
Note that not only simulation results are afflicted by uncertainties but also experimental data are. Collecting experimental data including error estimations from the literature can be strenuous because often there are no estimations given or it is not clearly stated how the given errors are obtained. Alternatively it is possible to use mean values and deviations for a property of interest from different sources. Thereby high deviations between different sources can occur leading to high standard deviations [113]. For comparing simulation and experimental data it is therefore not only important to validate the simulation part but also take care of the accuracy of the experimental data.

1.4 Purpose of this Work

With regard to table 1.1 the work presented in chapter 2 aims at explaining the association behaviour of supramolecular complexes in mixed solvent environments. Chapter 3 is concerned with property prediction for mixtures of the deep eutectic solvent glyceline with water using robust methods and software. The chapters 4 and 5 are concerned with both, development of force fields as well as property prediction using n-alcohols as example. In the following a brief introduction into the three topics is provided and the main research questions are highlighted.

1.4.1 Supramolecular Complexes

In chapter 2 a system known for constructing supramolecular complexes in aqueous solutions based on perylene bisimide (PBI) dyes is investigated.
Supramolecular complexes formed by amphiphilic macromolecules especially in aqueous solutions provide a broad range of applications and new opportunities in the field of advanced materials and nanotechnology [114–119]. For this reason especially experimentally driven studies using ultraviolet-visible (UV-vis), fluorescence and nuclear magnetic resonance (NMR) spectroscopy were carried out to understand dye-dye interactions and the impact of single molecules on larger aggregates held together by π-stacking [120]. Commonly aromatic π-π interactions [121–123] are the most prominent non-covalent interactions forming supramolecular complexes and thus have a high impact on structure and macroscopic properties of such assemblies. While Syamakumari et al. established the first self-assembled PBI dimer [124], thermodynamics of self-assembly were studies less intensive and mainly with the focus on Gibbs energy of aggregation [125–127] but not on enthalpic or entropic contributions. However experimental results indicate that there is a complex connection between solvent composition and the thermodynamic signature of the monomeric PBI molecule [125]. It is also known that shape and strength of the supramolecular complex and thus the macroscopic behaviour is strongly depending on solvent, solvent composition, temperature and the structure of the single molecule [128]. With this, the variety of possibilities to influence the behaviour of the supramolecular complexes are infinitely. Atomistic molecular simulations in explicit solvent are a promising tool for designing monomeric structures for individual applications with the advantage that simulations offer information on energetic processes on time and length scales which are experimentally not accessible. Moreover it is easy to simulate precise aggregate conditions such as dimers, trimers or higher oligomers which is still challenging in experimental works [120]. Recent studies on complexation provide a theoretical basis which can be used to describe the thermodynamic signature of complex systems [129–131].

The basic PBI dye cores can be substituted at different positions and in different ways to optimize or at least modify the single molecules for different applications. A schematic structure of a PBI molecule with possible positions for substituents are shown in figure 1.1. Substituents placed at the ortho-position can influence the optical and electronic properties while the planarity of the PBI core is not affected [132]. By modifying these substituents applications in organic photovoltaic (OPV) devices [133–139], field-effect transistors [140], light emitting diodes [141–145], nonlinear optical materials [146–150] or light harvesting in general [151, 152] are becoming feasible. In addition to the structure of the single PBI molecules also the organization of assimilated components on the nanometer scale show a significant influence on the optical attributes [153]. The influence

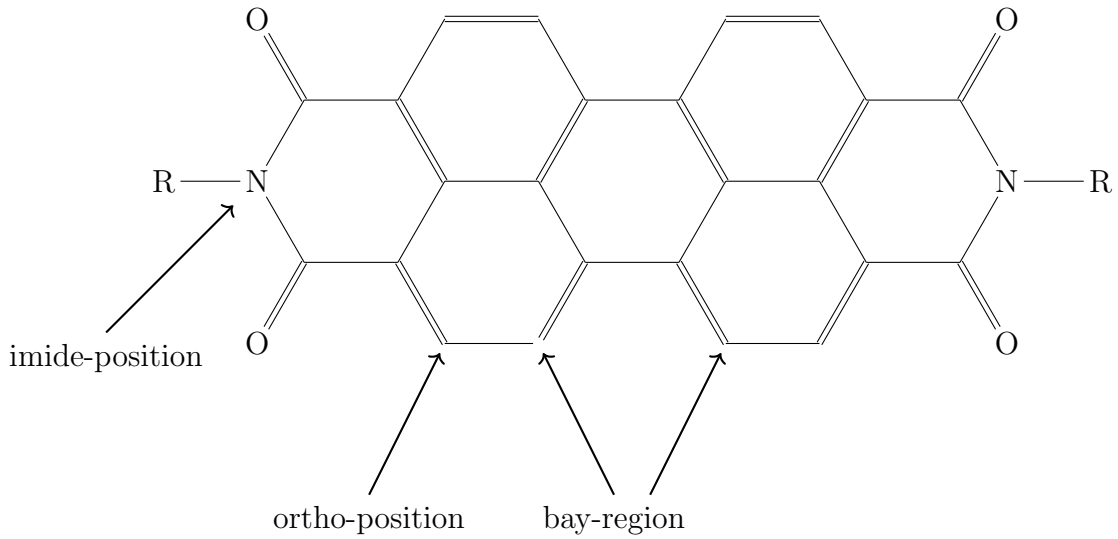

Figure 1.1: Schematic structure of a PBI core with tunable functional sites.

of temperature, solvent and solvent composition on optical attributes of π-stacking PBI molecules is part of recent studies [124, 128, 154–158].
Modifications in the bay-region lead to a twist of the two naphthalene rings and thus to changes in the spectroscopy properties. Substituents at this position can also influence the redshift drastically in the absorption maximum with an increased Stokes shift.
The production of hydrogels based on supramolecular complexes made of PBI molecules for applications in drug delivery [159], tissue engineering [160] or biosensing [161, 162] often takes place in organic solvents while luminescent hydrogels are produced with melamine in aqueous solution [163]. For this reason the solubility of PBI molecules in various solvents is an important aspect which can be tuned by selective rest groups substituted at the imide-position. The fact that optical or electronic properties are hardly affected by substituents at the imide-position is another advantage of supramolecular complexes based on PBI molecules [164].

The solvent plays another important role regarding the formation and behaviour of supramolecular complexes and can be adjusted for specific applications of self-assembled components [165]. Changing the polarity of solvents e.g. leads to various nanostructures of amphiphilic PBI molecules and also to changing surface properties [166].

The work presented in chapter 2 includes functionalized PBI molecules where the rest (shown as R in figure 1.1) is -CH_2COO^-. Until now only model systems of supramolecular complexes in absence of electrostatic interactions have been studied due to their binding affinity and the corresponding thermodynamics. The investigation of a real supramolecular system including a detailed thermodynamic analysis of the monomer molecules as well

as the initial binding process of dimers is discussed in chapter 2. The decomposition of the binding free energy into entropic and enthalpic contributions as well as the discrimination of the potential of mean force into solute-solvent and solvent-solvent interactions offer novel insights into molecular processes on a level which is experimentally not accessible. The experimentally observed behaviour of the supramolecular complex in different solvents was reproduced by the simulations including atomistic information giving a deeper understanding of the procedures.
Using a model, based on a perturbation theory of first order, allows to predict the temperature behaviour of the binding free energy profile requiring only few explicit MD simulation data. This method is reducing the computational costs and provides the opportunity to investigate a coarse-grained potential for aspherical molecules for studying the behaviour of supramolecular complexes at realistic solute concentrations.

1.4.2 Deep Eutectic Solvents

Ionic liquids (IL) haven been extensively investigated in the past 20 years and are applied in fields of catalytic processes [167–169], material science [170, 171], electrochemistry [172, 173], extraction solvents [174, 175] and biomedical applications [176]. First investigation on IL have concentrated on mixing metal salts, especially zinc, aluminium, tin and iron chlorides with quaternary ammonium salts [177]. The great interest on IL is due to their physicochemical properties, like density, viscosity, hydrophilicity which can be modified and optimized for specific uses by different combinations of cations and anions [178, 179]. However, IL have the disadvantage that they are poor biodegradable, environmentally harmful and not sustainable [180]. A promising alternative to ILs are deep eutectic solvents (DES) which produce no waste within the process, do not need to be purified and are cheaper in preparation [181]. DES have been seriously investigated since the beginning of this century.

Only a few manuscripts about eutectic mixtures have been reported in the 1990s. Gill and Vulfson used eutectic mixtures as substrates for enzymatic reactions in 1994 [182, 183]. Four years later Eberdinger et al. worked on enzymatic synthesis under the usage of heterogeneous eutectic mixtures with a mass recovery of up to 80 %. This work strongly affected novel industrial developments especially on large systems [184]. A work published in 1995 in Nature uses eutectic mixtures for emulsion crystallization as a cheaper alternative for separating and purifying molecular mixtures [185]. The first time developing drug delivery devices, especially for transdermal medication was introduced by Stott et al. in 1998 [186].

The expression deep eutectic solvents was first introduced by Andrew Abbott [187, 188] who proposed the concept of combining two solid organic compounds to obtain a fluid mixture possessing a melting temperature far below the melting temperatures of the individual parts [188–191]. DES are made of mixtures of two or more Lewis acids and bases which act as hydrogen bond acceptor (HBA) or Brønsted-Lowry acids and bases which act as hydrogen bond donor (HBD). Both components may include several kinds of anionic and or cationic species [189]. In contrast ILs are commonly made of one discrete anion compound and a discrete cation compound while DES are normally prepared by combining non-ionic ingredients like molecular components or salts [177]. The proportion of the hydrogen bond donor to hydrogen bond acceptor is guessed to define the melting point of the deep eutectic mixture. This assumption is evidenced by the fact that increased hydrogen bond interactions with anionic groups lead to decreased interactions between anionic and cationic groups. This interaction reduction between anionic and cationic groups as well as the charge delocalization arising from the hydrogen bonds between HBA and HBD results in a low lattice energy and thus in a reduced melting point [192–194].

The principal behaviour of DES is shown in figure 1.2. It can be seen that the melting temperatures of the pure components ($T_{m,A}$ and $T_{m,B}$) are much higher than the melting point of the mixture at a certain composition ($T_{m,\mathrm{DES}}(x_B)$). Above the melting temperatures of the pure components the system is a homogenous liquid while below these temperatures a solid system is present. The two miscibility gaps contain solid as well as liquid phases and are marked with S + L.

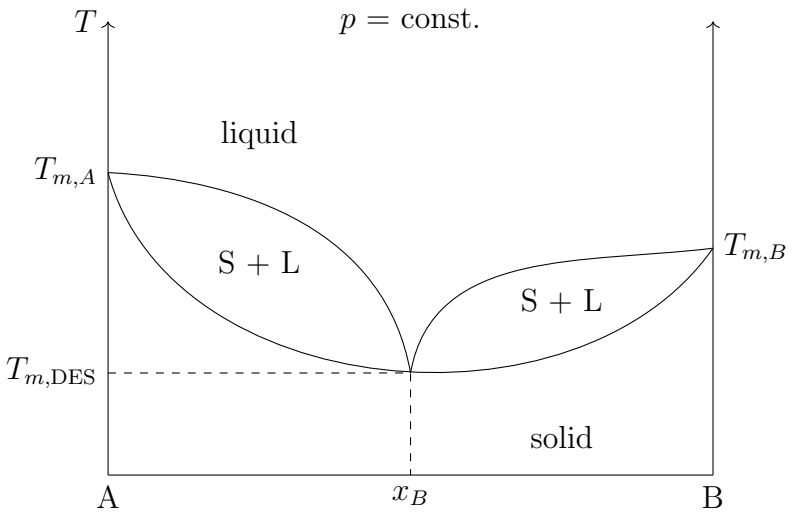

Figure 1.2: Schematic phase diagram of the melting temperature T_m of a DES system.

A subgroup of DES are natural deep eutectic solvents (NADES) which are in contrast to DES exclusively based on natural components, especially metabolites and bio-renewable ingredients like organic acids, sugars, sugar alcohols or amino acids [195, 196]. Although

the physical characteristics of DES and NADES compared to ILs are very similar their chemical properties offer applications in very different fields. DES as well as NADES have been investigated and developed for several fields of applications established mainly in biotechnology [197–200], organic synthesis [189, 201, 202], electrochemistry [203], biodiesel preparation [204] and polymer synthesis [194, 205]. In these applications DES are replacing volatile and hazardous organic solvents [189, 192, 206–208]. DES also have a low saturation vapor pressure, remain as liquid in biocatalytic processes due to their low melting temperature and are slightly or not toxic. Additionally DES shown a good solubility for various materials including drugs, metal oxides and carbon dioxide [187, 188, 209, 210]. Furthermore pharmaceutical ingredients, like phenyl acetic acid, acetyl salicylic acid and benzoic acid are efficiently dissoluted in DES due to the included hydrogen bond acceptor [211]. DNA structures are better soluble and less degraded if solved in DES compared to IL [211–213].

The thermophysical properties of DES like density, self-diffusion coefficient, surface tension, viscosity and thermal conductivity are strongly depending on their structure and thereby on the starting ingredients [188–190, 193, 214, 215]. The work of Andrew Abbot et al. showed that DES including choline chloride as ammonium salt lead to the lowest melting point (between 23 °C and 25 °C) [190].
Compared to IL or other molecular solvents, DES commonly show greater viscosities and lower thermal conductivities [189]. A very strong hydrogen-bonding network between the different components within a DES ensure that the mobility of the molecules is heavily restricted which is leading to such high viscosities. This impact of hydrogen bonds on a specific process is often an aspect of interest [216]. While hydrogen bonds are easy extracted from simulation results in a post processing method, great effort is needed in experiments to obtain less exact results. Alternative theoretical methods are often faster but also have limitations due to the shape of molecules or solvent behaviour. Other interactions like van der Waals or electrostatic interactions are also very distinctive in DES and could contribute to this behaviour [177]. While the high viscosities of pure DES are leading to a strongly reduced mass transfer what is often preventing their use in industrial applications, the addition of water or the change of the start ingredients is a degree of freedom to customize DES for specific uses and surmount this obstacle [208, 217].
The surface tension of DES is also higher compared to other conventional solvents. In most cases the surface tension of DES is in the same order of magnitude with molten salts and imidazolium-based IL [218].

As it can be seen the field of applications of DES is wide and there are numerous degrees of freedom for optimizing solvents to specific uses. Especially the multiple combinations of starting ingredients forming DES is one degree of freedom which is evident for the characteristics of the resulting DES. In this context molecular dynamics simulations are a promising tool for a rational design of DES.

Since the framework for predicting thermophysical properties of DES using molecular dynamics simulations is established and works well it is conceivable that starting ingredients and solvent composition of DES are determined, with respect to the conditions of specific applications, by predictions obtained from molecular dynamics simulations. The most noted and best examined DES contains choline chloride with urea, glycerol or ethylene glycol, mostly in a molar ratio of 1:2.
In chapter 3 various thermophysical properties of a DES based on choline chloride, glycerol and water are predicted with the aim to validate the used force fields on their usability for predictions of such systems. This work is among the first works in this field focusing on the solvent optimization including mixtures of DES and water. Further more it was shown that force fields calibrated to thermodynamic properties excluding water as present component are able to predict the behaviour of mixtures including water. An intensive comparison between molecular simulations, advanced equations of state (PC-SAFT) and experimental data is shown for a broad range of thermodynamic properties like density, diffusion, viscosity and activity coefficients of water.

1.4.3 Transferable Force Fields for n-Alcohols

The Mie potential was first introduced by Gustav Mie in 1903 when he was working on the kinetic theory of single atomic bodies. Today this work is the fundamental basis for many interaction theories [219]. Mie suspected that the attractive as well as the repulsive interactions between two particles are inversely proportional to the distance ρ between those particles. His first sketch of a potential energy was

$$\phi = \frac{b}{\rho^n} - \frac{a}{\rho^m} \tag{1.3}$$

where the term including a constitutes the attractive part and the term including b represents the repulsive part of the interaction potential.
While Mie has only taken single atomic gases into account, Grüneisen [220] extended this first draft of an interaction potential (equation 1.3) in 1912 to solid phases which lead to an equation which is used in the same style until today (equation 1.4).

$$\phi = D_0 \left[-\frac{m}{m-n} \left(\frac{\sigma}{r}\right)^n + \frac{n}{m-n} \left(\frac{\sigma}{r}\right)^m \right] \tag{1.4}$$

It is noteworthy that at this time both authors were not interested in the origin of the forces. The differentiation of the van der Waals interactions into Pauli repulsion [221] and London dispersion forces [222] were first introduced in 1925 and 1930, respectively. Fürth first published experimental results for the coefficients m and n in 1944 [223].

A today more famous form of the Mie potential was introduced by Sir John Edward Lennard-Jones in 1924 [224–226] in which the exponents m and n are set to fixed values of 12 and 6 (equation 1.5).

$$\phi = 4\epsilon \left[\left(\frac{\sigma}{r}\right)^{12} - \left(\frac{\sigma}{r}\right)^6 \right] \tag{1.5}$$

This description of pair interactions from Lennard-Jones was again modified by Richard A. Buckingham in 1938 [227] which is shown in equation 1.6.

$$\phi = A \exp\left(-Br\right) - \frac{C}{r^6} \tag{1.6}$$

which is simultaneously a special case of the Lennard-Jones-(exp, 6) potential shown in equation 1.7 [228].

$$\phi = \frac{\epsilon}{1-\frac{6}{\alpha}} \left\langle \frac{6}{\alpha} \exp\left[\alpha\left(1-\frac{r}{\sigma}\right)\right] - \left(\frac{\sigma}{r}\right)^6 \right\rangle \tag{1.7}$$

Nowadays almost exclusively Lennard-Jones (LJ) potentials are used in molecular simulations, equations of state or statistical mechanics in general to describe the van der Waals interactions within the considered system. Since most properties considered in the specific systems are described in a good manner LJ potentials are used together with force fields based on this potential function. Another point is that force field optimization using the LJ potential is easier because the parameters m and n are not part of the objective function and thus the degrees of freedom are reduced. However in some cases the LJ potential shows weaknesses as it can be seen in chapter 4 and 5 where the force field based on the LJ potential function leads to systematical deviations in liquid density and saturation vapour pressure while the force field based on the Mie potential describes these properties in high agreement to experimental data.
Since 2015 a force field based on the Mie potential partly using anisotropic modifications is developed at the Institute of Thermodynamics and Thermal Process Engineering. First parameters for different components of n-alkanes and n-olefins have been optimized [229], followed by ethers [230], aldehydes, ketones, small cyclic alkanes [231, 232] as well as for mixtures of n-alkanes with nitrogen [233].

Alcohols have not been considered so far, although they are an important group of substances with various applications in scientific, medical and commercial fields. Their attribute of associative liquids leads to the usage as excellent solvents for chemical reactions as well as promising alternative energy sources [234]. For the reasons mentioned above a force field describing properties of the group of alcohols very precisely is necessary.
Therefore a force field for n-alcohols between 1-propanol and 1-octanol is developed and validated in chapter 4 and 5 of this thesis.
The problem of force field parameter degeneracy is a well known challenge when developing force fields. Due to the high correlation between the parameters the evaluation of static thermodynamic properties, like vapour pressure or liquid density, do not offer sufficient information for the determination of one best parameter set. Instead a selection of parameter combinations all leading to the same error in the objective function is obtained. With the inclusion of dynamic properties, such as viscosity or self-diffusion coefficients, into the parameter optimization the problem of parameter degeneracy was hoped to be eliminated. Until now the approach to include dynamic properties in the force field parameterization was less studied and is thus examined in this work. However, it was observed that parameter degeneracy is still present for static as well as for dynamic properties even if several molecules within the homologous series of n-alcohols are included in the optimization process.

Chapter 2

Thermodynamic Characterization of the Dimerization of an Anionic Perylene Bisimide Dye Using Molecular Simulation

The content of this chapter is a literal quote of the publication
J. Baz and N. Hansen, The Journal of Physical Chemistry C, 123, 8027-8036, 2019

Abstract

The thermodynamic signature of dimerization of an anionic di(glycyl) perylene bisimide derivative in aqueous solution is characterized using molecular dynamics simulations in explicit solvent, with the aim to unravel the impact of temperature, pressure, and solvent composition on the free energy of aggregation and its enthalpic and entropic contributions. The change in free energy varies only weakly with temperature independent of whether the solvent consists of pure water, an aqueous ethanol/water mixture or an aqueous solution of sodium chloride, respectively. In agreement with experimental findings, the addition of ethanol weakens the interactions between the solute molecules while the addition of sodium chloride leads to more stable aggregates. The temperature dependence of the potential of mean force can be accurately described using a simple expression derived from thermodynamic perturbation theory of first order. Molecular driving forces are discussed in terms of solute-solute and solute-solvent interactions.

2.1 Introduction

Self-assembly processes involving amphiphilic macromolecules provide unique and new opportunities for designing advanced materials for emerging applications in nanotechnology. The delicate balance of intermolecular interactions between the different hydrophobic and hydrophilic domains causes a spatial organization into ordered morphologies on the nanoscale with the production of interesting features relevant in numerous applications in the area of e.g. separation processes, electronics and drug delivery [235–240]. Bola amphiphiles refer to a class of molecules in which two hydrophilic groups are connected to the ends of a hydrophobic domain. They are found to aggregate into spheres, small and large cylinders, small and large discs and vesicles [241, 242]. Perylene bisimide derivatives (PBIs) emerged as a prototype class of such molecules for the elucidation of the transition from monomeric to bulk materials via the supramolecular state. Their self-assembly into complex structures is determined by size and shape of the monomeric unit, system composition and thermodynamic boundary conditions [243, 244]. Consequently, much attention was given to fundamental studies focussing on NMR, UV/Vis, and fluorescence spectroscopy in order to get insight into the dye-dye interactions and how these interactions impact the properties of larger π-π stacked aggregates [120, 245]. In contrast the thermodynamics of self-assembly of PBIs was studied less extensive and, until recently [125] mainly in terms of the free energy of aggregation [126, 127] but hardly with the focus on the enthalpic and entropic contributions. Recent experimental work in this direction points towards a complex dependence of the thermodynamic signature on the monomeric architecture and solvent composition [125, 246]. The interplay of attraction (e.g. through electrostatic interactions) and repulsion (e.g. between water and hydrophobic groups) of the different parts of the molecule with the surrounding solvent leads to an association that can be either entropy-driven or enthalpy-driven depending on the nature of the molecules and the solvent [165, 247–251]. Given this diversity of factors which influence the self-assembly and their complex interplay, studies on simplified model systems provide an important guidance for the design of monomeric building blocks [252] whereas a molecular-level understanding of the driving forces for the concrete system under study is considered to be an important step to understand the onset of the self-assembly process. To gain such understanding molecular simulations are a promising approach [253]. Such simulations are complementary to experimental studies because they provide information at a level of spatial, temporal and energetic resolution that is experimentally elusive [254]. The theoretical framework needed to unravel the thermodynamic signature of complexation is well developed [129–131] and relies on the calculation of the potential of mean force as function of the intermolecular distance to obtain the free enthalpy of association and on long unbiased molecular dynamics simulations of the associated and dissociated

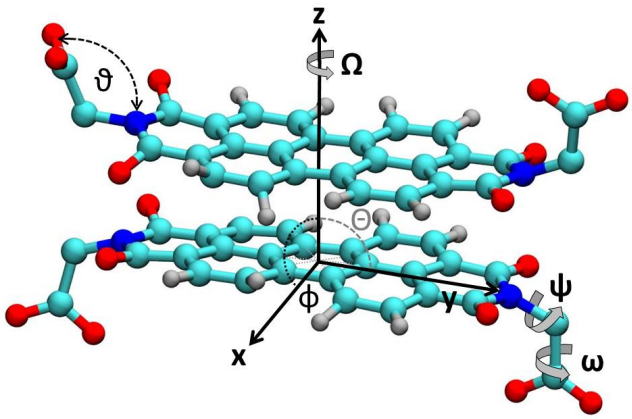

Figure 2.1: A typical dimer configuration of the investigated di(glycyl) derivative of perylene-3,4,9,10-tetracarboxylic acid bisimide (referred to as PBI derivative in the present work) along with intermolecular coordinates used to characterize the configurational variability. Color codes: oxygen (red), nitrogen (blue), carbon (cyan), hydrogen (white).

states to obtain the association enthalpy.

In the present work the core-unsubstituted anionic di(glycyl) PBI derivative shown in figure 2.1 was investigated. Previous experimental work has shown by using UV/Vis absorption and fluorescence spectroscopy that a monomer-dimer equilibrium in alkaline aqueous solution exists with an association constant of $K = 1.0 \cdot 10^7\,\mathrm{M}^{-1}$ at 24.0 °C [255]. The spectroscopic measurements were interpreted in terms of exciton theory for parallel oriented sandwich-type dimer. A considerable salt (NaCl) effect on the aggregation was observed (increase of aggregation strength) which was discussed in terms of counterion shielding of the electrostatic repulsion between the negatively charged PBI molecules. In addition, a considerable effect of ethanol on the aggregation was observed (decrease of aggregation strength) and discussed in terms of preferential binding of ethanol to the hydrophobic parts of the PBI molecules and a depletion of water around them.

Here, we explore the feasibility of describing the thermodynamics of PBI self-assembly using a classical force field representation of the constituents. The influence of temperature, pressure and solvent composition on the dimerization is investigated and issues regarding the comparison to experimental data are discussed.

2.2 Computational Details

2.2.1 Force Field

Lennard-Jones parameters and bonded interaction terms were taken from the GROMOS 54A7 biomolecular force field [256]. The atomic partial charges were obtained from the Automated Topology Builder (ATB) [257] followed by some manual adjustment in order

Table 2.1: Different solvent compositions of all simulated systems in this work.

System	conc.[a]	N_{PBI}	$N_{\mathrm{K^+}}$	$N_{\mathrm{H_2O}}$	$N_{\mathrm{Na^+}}$	$N_{\mathrm{Cl^-}}$	N_{EtOH}	$\langle L_{\mathrm{box}} \rangle$[b]
$\mathrm{W_M}$	-	1	2	4000	0	0	0	4.9777
$\mathrm{W_D}$	-	2	4	8000	0	0	0	6.2674
$\mathrm{W_{US}}$	-	2	4	7475	0	0	0	6.1295
$\mathrm{E1_M}$	25	1	2	1673	0	0	129	3.9896
$\mathrm{E1_D}$	25	2	4	3346	0	0	258	5.0261
$\mathrm{E1_{US}}$	25	2	4	6938	0	0	537	6.4063
$\mathrm{E2_M}$	50	1	2	1561	0	0	242	4.1336
$\mathrm{E2_D}$	50	2	4	3122	0	0	484	5.2078
$\mathrm{E2_{US}}$	50	2	4	6473	0	0	1002	6.6221
$\mathrm{S1_M}$	0.5	1	2	2477	23	23	0	4.2533
$\mathrm{S1_D}$	0.5	2	4	4954	46	46	0	5.3588
$\mathrm{S1_{US}}$	0.5	2	4	7406	69	69	0	6.1241
$\mathrm{S2_M}$[c]	1.0	1	2	2453	47	47	0	4.2510
$\mathrm{S2_D}$[c]	1.0	2	4	4906	94	94	0	5.3556
$\mathrm{S2_{US}}$[c]	1.0	2	4	7334	141	141	0	6.1252

[a] The composition is given in vol% for the ethanol/water system and in molar concentration ($\mathrm{mol\,l^{-1}}$) for the aqueous NaCl solution. [b] The simulation box length is given in nm. [c] For the S2 system additional simulations with twice the amount of solvent and sodium chloride were conducted.

to ensure that the distribution of atomic partial charges reflects the symmetry of the molecule. For a small set of building blocks occurring in the PBI entity (i.e. benzene, pyridine, and 2,5-dimethylpyridine) the force field was validated based on a comparison between calculated and experimental liquid phase properties [258]. A full specification of the force field parameters used to model the PBI molecule is provided in the Supporting Information of this article.

2.2.2 Simulated Systems

MD simulations of a single monomer (M) or a single dimer (D) were performed for 1 μs at constant pressure and temperature, either in pure SPC [259] water (W), in a binary ethanol-water mixture (E) or an aqueous NaCl solution (S). In addition umbrella sampling simulations were performed at all compositions. Table 2.1 specifies the compositions of all systems studied in the present work. The negative net charge of -2e of the PBI molecule was compensated by potassium ions [260]. Simulations at ambient pressure were conducted at temperatures of 273.15, 285.15, 293.15, 298.15, 310.15, 323.15, 335.15, 348.15 and 360.15 K. Simulations at elevated pressures of 10 and 100 bar were only performed at 298.15 K.

2.2.3 Simulation Parameters

All simulations were performed under minimum image periodic boundary conditions based on cubic computational boxes using the GROMACS 5.1.4 program package [261–263] compiled in single precision and patched to the free-energy library PLUMED 2.3.0 [264], which was used to control the umbrella sampling simulations. Equations of motion were integrated using the leap frog scheme [265] with a time step of 2 fs. For all systems an energy minimization, followed by a constant-volume equilibration simulation of 1 ns at 298.15 K and a successive constant-pressure equilibration of 1 ns at the desired target temperature were conducted prior to the actual production simulation. All bond lengths were kept fixed using either SETTLE [266] (for water) or LINCS [267, 268] (for the solute and ethanol) with an order of 4. The number of iterations to correct for rotational lengthening in LINCS was set to 2. The temperature was maintained close to its reference value by application of the velocity-rescale thermostat [269], with a coupling constant of $\tau_T = 0.2\,\mathrm{ps}$. Solute and solvent were separately coupled to the heat bath. The pressure was set close to its reference value using the Parrinello-Rahman barostat [270, 271] by isotropic coupling with a coupling constant of $\tau_p = 2.0\,\mathrm{ps}$ and an isothermal compressibility of $\kappa_T = 4.591 \times 10^{-5}\,\mathrm{bar}^{-1}$. Short-range electrostatic and Lennard-Jones interactions were treated with a Verlet-buffered neighbor list [272] with potentials shifted to zero at the cut-off of 1.4 nm. Analytical dispersion corrections were not included. Long-range electrostatics was treated by the smooth particle-mesh Ewald (PME) summation [273, 274] with a PME-order of 4.

Umbrella sampling [275] (US) simulations were performed using the distance between the centers of mass (COM) of the two monomer molecules as reaction coordinate. A harmonic umbrella potential with a force constant of $500\,\mathrm{kJ\,mol^{-1}\,nm^{-2}}$ that acts on the deviation of the reaction coordinate from the reference position of the respective umbrella window was applied. At each of the 11 equidistant windows, placed in the range from 0.3 nm to 2.0 nm along the reaction coordinate, 10 independent US simulations were performed, each lasting for 10 ns.

2.2.4 Trajectory Analysis

Free energy profiles, $\Delta G_{\mathrm{raw}}(r, T)$, as well as the corresponding error estimations were obtained using the Multistate Bennett Acceptance Ratio (MBAR) method with a bin width of 0.034 nm (50 bins) using a freely available python implementation [276]. Uncertainties equal one standard deviation and are obtained using the weighted asymptotic covariance matrix [277]. The free energy of dimerization was then calculated by [278]

$$\Delta G(T) = -RT \ln \left(\frac{4\pi \left(r_{\mathrm{u}}^3 - r_{\mathrm{b}}^3\right) \int_0^{r_{\mathrm{b}}} \exp\left(\frac{-\Delta G_{\mathrm{raw}}(r,T)}{RT}\right) \mathrm{d}r}{3V^0 \int_{r_{\mathrm{b}}}^{r_{\mathrm{u}}} \exp\left(\frac{-\Delta G_{\mathrm{raw}}(r,T)}{RT}\right) \mathrm{d}r} \right) \tag{2.1}$$

where r_u is the upper integration limit (flat region of the potential of mean force) and r_b is the distance separating the bound complex from two individual monomer molecules. The standard state volume of $1.661\,\mathrm{nm}^3$ is denoted by V^0, R is the ideal gas constant and T the absolute temperature. Uncertainties for free energies equal a confidence intervall of 95 % and are obtained using bootstrapping with a number of bootstrap samples of 500. Note that the choice of r_b involves a certain level of arbitrariness [129] as discussed below. The enthalpy of complex formation was calculated from the difference of the total potential energy of a computational box containing the solvated complex and twice the total potential energy of the computational box containing the solvated monomer in half the amount of solvent molecules [279],

$$\Delta H(T) \approx \Delta U(T) = \langle U_{\mathrm{dimer},\,2N}(T) \rangle - 2 \langle U_{\mathrm{monomer},\,N}(T) \rangle \tag{2.2}$$

Using the Gibbs equation the entropy $-T\Delta S$ was then obtained from

$$-T\Delta S(T) = \Delta G(T) - \Delta H(T) \tag{2.3}$$

2.2.5 Modeling the Temperature Dependence of the Potential of Mean Force

It was shown recently that by using thermodynamic perturbation theory [280, 281] of first order for a Lennard-Jones system, a simple expression for the temperature dependence of the potential of mean force can be obtained that does not require an assumption about the actual decomposition of the target potential into the reference and perturbative part [282]. The potential of mean force $\Delta G_{\mathrm{PMF}}(r,T)$ which is obtained from the raw free energy profile $\Delta G_{\mathrm{raw}}(r,T)$ by adding the Jacobian correction $2RT\ln(r)$ [283] can be expressed as

$$\Delta G_{\mathrm{PMF}}(r,T) = a(r)RT + b(r) \tag{2.4}$$

where $a(r)$ and $b(r)$ can be calculated directly from simulations at two different temperatures

$$a(r) = \frac{\Delta G_{\mathrm{PMF}}(r,T_2) - \Delta G_{\mathrm{PMF}}(r,T_1)}{R(T_2 - T_1)} \tag{2.5}$$

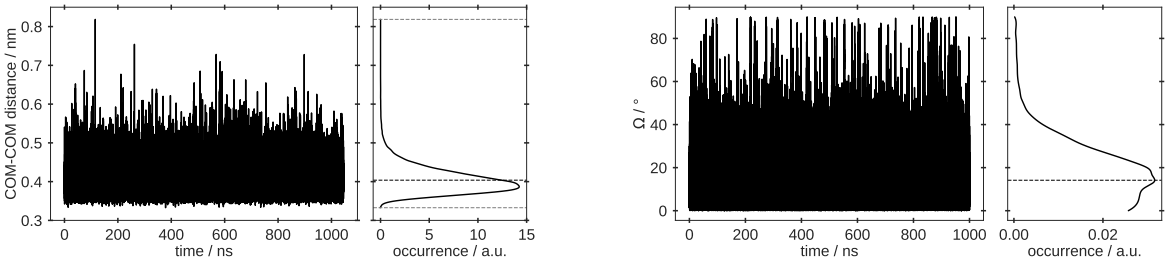

(a) (b)

Figure 2.2: (a) Time series and distribution of the center-of-mass distance for a PBI dimer at 298.15 K in pure water. Maximum and minimum values are 0.82 nm and 0.33 nm, the mean value is 0.44 nm. (b) Time series and distribution of the torsional angle Ω of a dimer system at 298.15 K in pure water.

$$b(r) = \frac{T_1 \Delta G_{\mathrm{PMF}}(r, T_2) - T_2 \Delta G_{\mathrm{PMF}}(r, T_1)}{T_1 - T_2} \tag{2.6}$$

Although developed and tested on a system involving only Lennard-Jones interactions the description should also hold for a system possessing electrostatic interactions since a perturbation expansion in a neutral system is zero in first order because of cancellation of the orientational averages [284].

2.3 Results and Discussion

The dimerization of the PBI derivative was studied at different temperatures, pressures and solvent environments to obtain a molecular interpretation of its thermodynamic driving force. First, the employed analysis is explained in detail for the case of pure water. Second the effect of changing the solvent environment is discussed for ethanol/water mixtures and aqueous NaCl solutions.

2.3.1 Dimerization in Pure Water

The time series of the COM-COM distance in the complexed state at 298.15 K is shown in figure 2.2a for a 1 μs simulation along with the corresponding distribution. Figure 2.2b shows the time series and distribution of the relative orientation of the two plate-like PBI molecules. An Ω-angle of 0° corresponds to a parallel oriented sandwich-type dimer. The most likely configuration is slightly skewed with $\Omega \approx 14°$. While the complex shows high mobility it remains stable in the time frame of the simulation. The largest COM-COM distance sampled amounts to 0.82 nm. Several transitions beyond 90° into the symmetrically equivalent configuration are observed for the Ω-angle.
When being in the complexed state and close to parallel the terminal CH_2COO^- groups

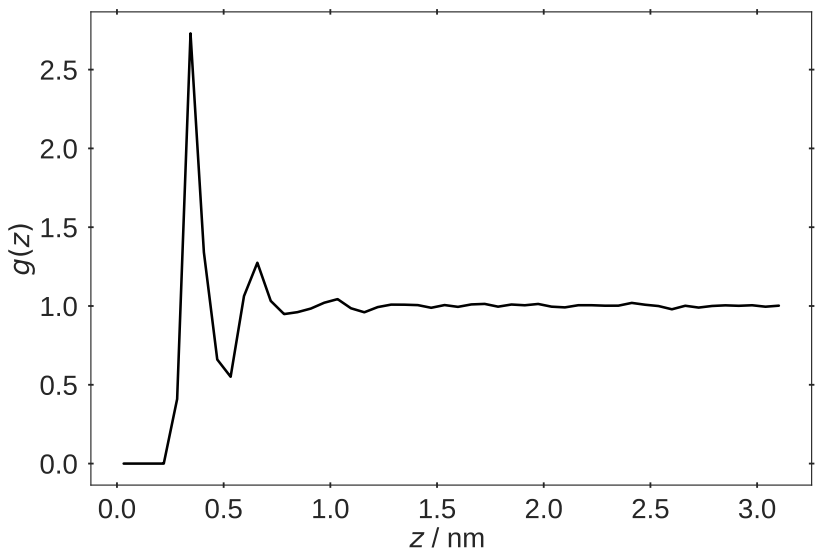

Figure 2.3: Distribution function $g(z)$ of water oxygen atoms. Water molecules that are located in a cylinder with radius 0.1 nm positioned at the center of mass of the PBI molecule and oriented perpendicular to the surface towards the solvent were considered in the calculation of $g(z)$. The two distribution functions obtained for each PBI molecule (see figure S3) in the complexed state were averaged.

point away from each other as indicated in figure 2.1. The other state becomes populated if the configuration becomes more skewed. The rotation around the dihedral angle ω is not affected by the complex formation.

The normalized density profiles $g(z)$ of water perpendicular to the hydrophobic part of the molecular surface is shown in figure 2.3 and displays a typical layer structure with two pronounced maxima and a third one of weaker magnitude which has been observed in several simulation studies on solid-liquid interphases (hydrophobic and hydrophilic ones) before [285–287].

Figure 2.4 shows the potentials of mean force in the temperature range from 273.15 K to 360.15 K.

The well depths slightly change with temperature from $-60\,\mathrm{kJ\,mol^{-1}}$ at 273.15 K to $-55\,\mathrm{kJ\,mol^{-1}}$ at 360.15 K. The position of the minimum at around 0.4 nm is hardly temperature dependent. The free enthalpy of binding or the corresponding equilibrium constant can be obtained from integration according to equation 2.1. However, the numerical result will somewhat depend on the definition of the distance r_b separating the complexed state from the two individual monomer states [129]. This definition of the two states is not uniquely defined and may depend also on the type of experimental data to compare with because spectroscopic signals of different methods may show a different sensitivity to the separation distance.

Figure 2.5 shows that for distances larger than 1 nm the binding free enthalpy becomes

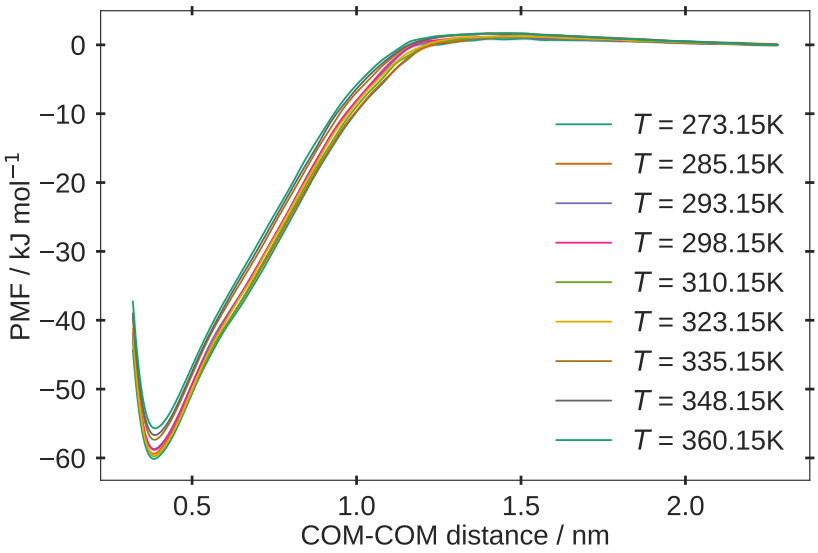

Figure 2.4: Potential of mean force as function of the center-of-mass separation for different temperatures in pure water. Errors are within the line width and correspond to one standard deviation.

essentially distance independent as expected from equation 2.1. However, a reasonable choice of r_b could also be based on the maximum distance sampled in a long unbiased MD simulation.

For the maximum distance of 0.82 nm a binding free enthalpy of $-45\,\mathrm{kJ\,mol^{-1}}$ is obtained compared to the maximum of $-53\,\mathrm{kJ\,mol^{-1}}$ when integrating towards the flat region of the PMF. However, since the focus of the present work is an analysis of the thermodynamic signature of the dimerization process and not to obtain quantitative agreement with experiment an upper bound of 1.4 nm has been used for all cases, corresponding to the cut-off radius of the short range interactions.

Figure 2.6 shows the temperature dependence of the thermodynamic functions ΔG, ΔH and $-T\Delta S$. While the free enthalpy is hardly temperature dependent the enthalpic and entropic components show stronger dependencies, which compensate each other. The slopes of the enthalpic and entropic components computed in the present work have the same sign as in a purely hydrophobic model system consisting of two disc-like plates of 2.1 nm diameter composed of Lennard-Jones spheres [288], i.e. the association enthalpy becomes stronger at elevated temperatures, while being smaller in magnitude. This observation is consistent with the explanation for the sign of the slope of $\Delta H/\Delta T$ proposed previously [288]. With increasing temperature the ability of water molecules at the interface of a hydrophobic solute molecule to maintain their hydrogen bond network decreases. For the amphiphilic PBI molecules studied here this effect is also present but less pronounced. A hydrogen bond analysis carried out at 278.15 K and 360.15 K showed an increase in the total number of hydrogen bonds that are formed during complexation rel-

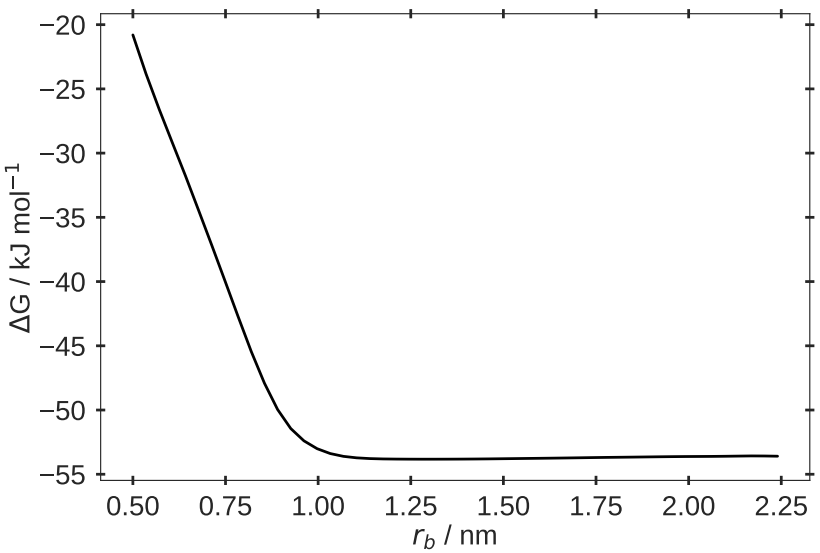

Figure 2.5: Free enthalpy of association as function of the radius of integration r_b (see equation 2.1) at 298.15 K.

ative to the dissociated state of one and two hydrogen bonds for the lower and the higher temperature, respectively, compared to five and nine in the study of Zangi and Berne[288]. These results are in line with other studies of amphiphilic molecules that show a change in driving force when going from pure hydrophobic to amphiphilic monomers [289, 290]. To evaluate the thermodynamic consistency of the obtained results the van't Hoff equation

$$\left(\frac{\partial\left(\ln(K)\right)}{\partial T}\right)_p = \frac{\Delta H}{RT^2} \tag{2.7}$$

was considered, where $K = \exp(-\Delta G/RT)$ is the association constant and ΔH was assumed to be linearly dependent on temperature, i.e. $\Delta H = \alpha + \beta T$,[291, 292] leading to

$$\ln(K(T)) = -\frac{\alpha}{RT} + \frac{\beta}{R}\ln(T) + C \tag{2.8}$$

where C is an integration constant.

Figure 2.7 displays the association constants calculated from simulation as function of the inverse temperature by filled black symbols. When fitting equation 2.8 to the simulated data using all three parameters α, β and C as degrees of freedom the line referred to as *fit1* is obtained corresponding to $\hat{\beta}_\mathrm{fit} = 109.9\,\mathrm{J\,mol^{-1}\,K^{-1}}$ which suggests an increase of ΔH with temperature. By fixing the parameter β to the slope of the linear fit through the simulated ΔH values shown in figure 2.6, i.e. $\hat{\beta}_\mathrm{fix} = -242.35\,\mathrm{J\,mol^{-1}\,K^{-1}}$ while using α and C as degrees of freedom the line referred to as *fit 2* in figure 2.7 is obtained which is also consistent with the association constants obtained from the umbrella sampling

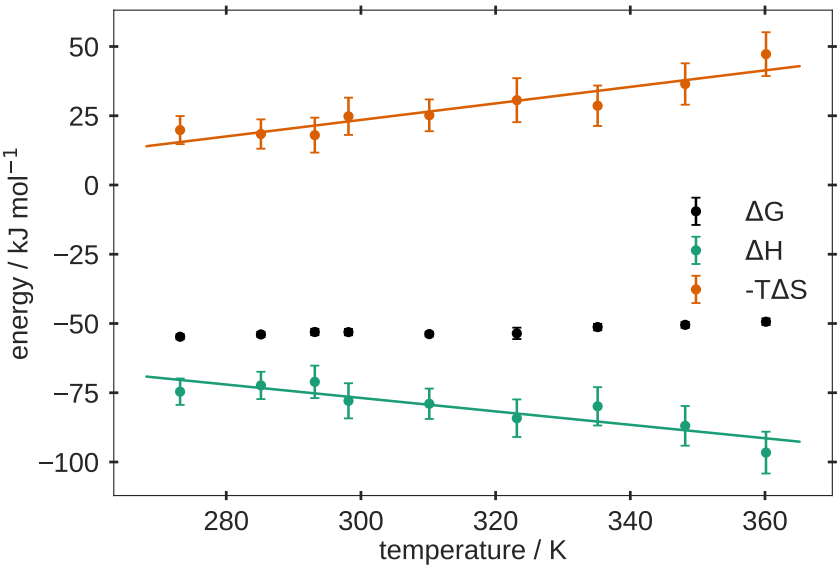

Figure 2.6: Association free enthalpy ΔG, enthalpy ΔH and entropy $-T\Delta S$ as function of temperature in pure water. The error bars correspond to confidence intervals of 95 %. Straight lines represent linear fits $\alpha_i + \beta_i T$ with $\alpha_H = -4.18\,\mathrm{kJ\,mol^{-1}}$, $\beta_H = -0.2424\,\mathrm{kJ\,mol^{-1}\,K^{-1}}$, $\alpha_S = -65.91\,\mathrm{kJ\,mol^{-1}}$, $\beta_S = 0.2980\,\mathrm{kJ\,mol^{-1}\,K^{-1}}$.

simulations. This shows the difficulty of obtaining second derivative properties of the free enthalpy such as the change in heat capacity directly from the temperature dependent free enthalpy values, while first derivative properties such as an enthalpy change might be obtained for smaller systems [293, 294].

We also note that comparatively long simulations are required to obtain reasonably converged enthalpy values, a consequence of the need to subtract two large numbers while the free enthalpy is usually much less affected by statistical noise due to the cancellation of solvent-solvent contributions [295, 296]. Regarding quantitative comparison with experimental data we note that the computed ΔG value of $-53\,\mathrm{kJ\,mol^{-1}}$ at 298.15 K overestimates the magnitude of the experimentally reported value of $-40\,\mathrm{kJ\,mol^{-1}}$ determined from the changes in absorption properties upon dimerization [255]. We note, however, that quantum yield data for the same system did not agree with the absorption results [255], suggesting the possibility that the two methods differ in their underlying relation between spectroscopic signal and molecular configuration. In addition to the uncertainty introduced by the choice of the integration cut-off r_b (see above) inaccuracies in the force field are considered to be the second major source of uncertainty in the present case. However, force field refinement, taking into account a larger sample of representative monomeric building blocks was beyond the scope of the present study.

Finally we investigated whether a simple expression derived from thermodynamic perturbation theory of first order is able to capture the temperature dependence of the potentials of mean force.

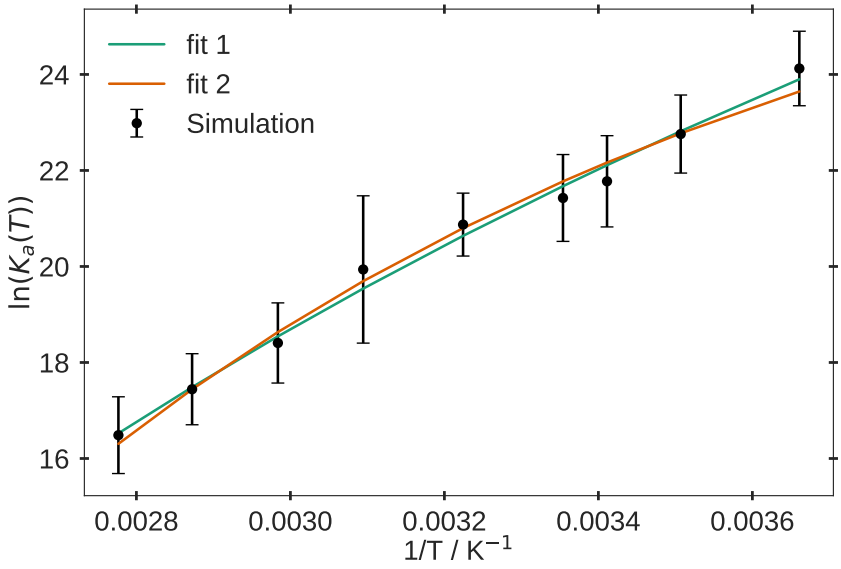

Figure 2.7: van't Hoff plot of the temperature dependence of the equilibrium constant for the dimerization in pure water. The curve labelled *fit1* corresponds to an unconstrained optimization of the three parameters α, β and C (see equation 2.8) leading to $\alpha_1 = -35.566 \times 10^{-5}\,\mathrm{kJ\,mol^{-1}}$, $\beta_1 = 10.985 \times 10^{-2}\,\mathrm{kJ\,mol^{-1}\,K^{-1}}$ and $C_1 = 109.70$. The curve labelled *fit 2* corresponds to an optimization of α_2 and C_2 only while fixing β_2 to $-24.235 \times 10^{-2}\,\mathrm{kJ\,mol^{-1}\,K^{-1}}$, leading to $\alpha_2 = -14.716\,\mathrm{kJ\,mol^{-1}}$ and $C_2 = -91.531$.

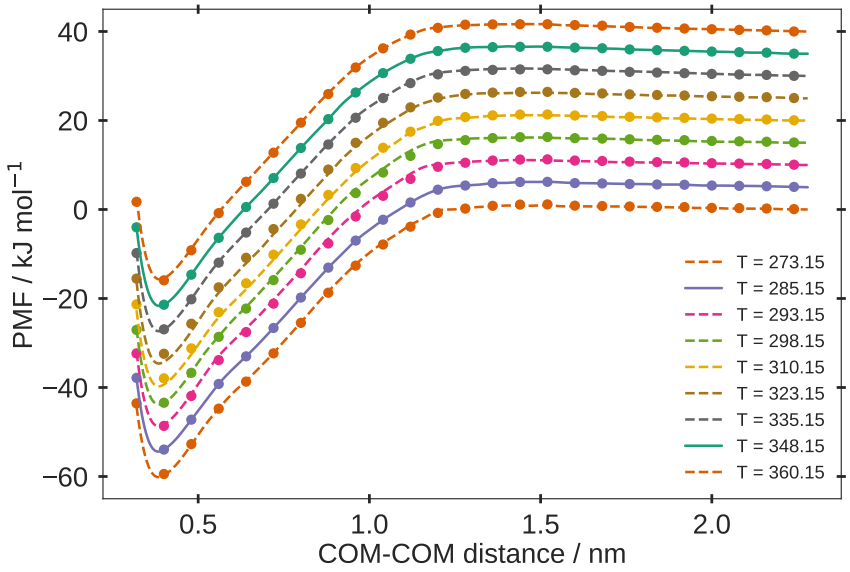

Figure 2.8: Potentials of mean force as function of the center-of-mass separation for different temperatures in pure water. Symbols correspond to MD simulations, solid lines represent the two reference PMFs and dashed lines the predictions according to equation 2.4. For better readability each PMF has been shifted by $5\,\mathrm{kJ\,mol^{-1}}$ relative to the previous PMF at the next lower temperature.

The two functions $a(r)$ and $b(r)$ (see Eqns 2.5 and 2.6) were obtained from the PMFs at 285.15 K and 348.15 K, respectively. Figure 2.8 shows that these functions encode the

entire temperature dependence of the PMFs observed in the MD simulations demonstrating that a decomposition of the PMF into a repulsive and attractive part represented by two temperature-independent functions, initially tested for capped gold nanoparticles in vacuum [282] works also succesfully for the present system. This may have important consequences for developing coarse graining potentials as is discussed below. We note that the two PMFs required for obtaining $a(r)$ and $b(r)$ should correspond to a low and high reference temperature in order to interpolate the remaining PMFs. When extrapolating it has to be ensured that no phase transition occurs within the temperature boundaries [282].

By performing additional simulations at 10 bar and 100 bar the influence of pressure on the dimerization was studied. Figure S4 shows a slight increase of the magnitude of the free enthalpy of association which is however not significant considering the overlapping error bars.

2.3.2 Dimerization in an Ethanol/Water Mixture and in Aqueous NaCl Solution

Figure 2.9 shows the thermodynamic functions ΔG, ΔH and $-T\Delta S$ in the temperature range from 273.15 K to 360.15 K for two ethanol/water mixtures (25 vol% and 50 vol%, respectively) and two aqueous NaCl solutions (0.5 M and 1.0 M, respectively). The corresponding free energy profiles are displayed in the Supporting Information. In all cases the temperature dependence of ΔG remains weak as in the case of pure water. Relative to pure water the addition of ethanol weakens the association strength between the two plate-like molecules. For the 25 vol% mixture the association enthalpy slightly increases while it is nearly temperature independent in the case of the 50 vol% mixture. In contrast to pure water no additional hydrogen bonds are formed at higher temperature.

The addition of NaCl strengthens the binding relative to pure water altough the effect is rather weak for the concentrations investigated. We note however, that the GROMOS ion model underestimates the solubility of NaCl [297], which hampers a quantitative comparison to experimental results. As for pure water the total number of hydrogen bonds that are formed during complexation relative to the dissociated state increases with increasing temperature from one hydrogen bond at 278.15 K to 1.5 hydrogen bonds at 360.15 K leading to a negative slope of $\Delta H/\Delta T$.

The same tests of thermodynamic consistency as for pure water were conducted and are reported in the Supporting Information, showing that sufficient sampling was reached to determine the slope of the temperature dependence of the enthalpy. However, compared to the neat water system convergence in the 50 vol% ethanol system is more difficult to achieve.

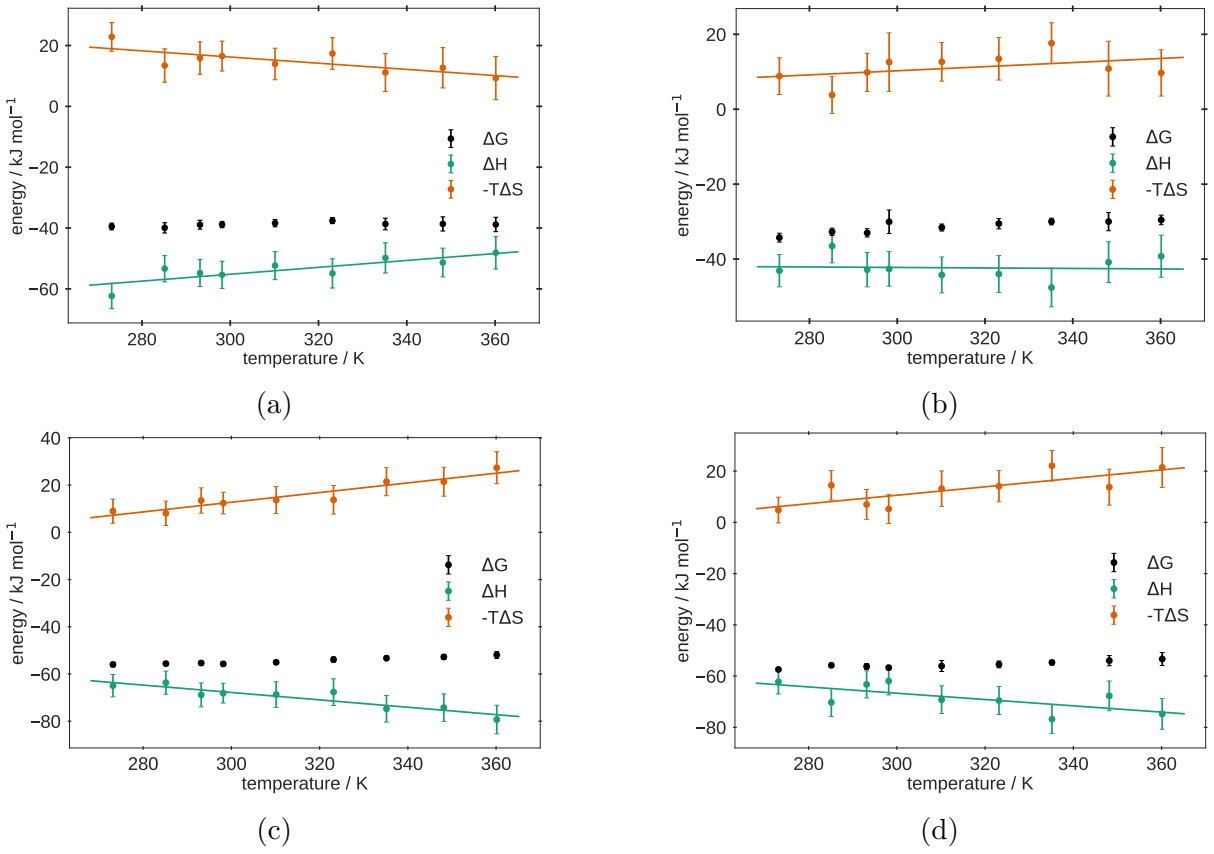

Figure 2.9: Association free enthalpy ΔG, enthalpy ΔH and entropy $-T\Delta S$ as function of temperature in an ethanol/water mixture of 25 vol% (a) and 50 vol% (b), respectively and in an aqueous NaCl solution of 0.5 M (c) and 1.0 M (d), respectively. The error bars correspond to confidence intervals of 95 %. Straight lines represent linear fits $\alpha_i + \beta_i T$ with fitting parameters provided in the Supporting Information.

The observed changes in the association strength in response to changes in the solvent environment are in agreement with experimental data. For NaCl a slightly larger increase in binding strength ($\sim 5\,\mathrm{kJ\,mol^{-1}}$ in 1 M NaCl relative to pure water) was reported [255] compared to the results obtained here while for ethanol no quantitative experimental results were reported. The differences in the local solvent environments around the PBI molecules are analysed in figure 2.10 by means of one-dimensional distribution functions in the direction perpendicular to the molecular surface. The decrease in binding strength due to ethanol can be rationalized due to preferential binding next to the surface and depletion of water, leading to a lower peak compared to the pure water case. It should be emphasized though that the ratio of peak heights between ethanol and water should be interpreted in terms of local number densities, [298] i.e. scaled with the ratio of $N_{\mathrm{H_2O}}/N_{\mathrm{EtOH}}$ leading us to conclude that close to the hydrophobic surface the number density of ethanol is only slightly larger than the one of water. In the aqueous NaCl solution the first layer next to the hydrophobic part of the surface is almost completely void of ions accompanied by a slight increase in water density relative to the simulation

in pure water. The second layer contains more cations than anions. This preferential exclusion picture is in accordance with studies on a hydrophobic model system consisting of two rigid disc-like molecules immersed in aqueous solution of different ionic strength [299]. For complexation in 1 M aqueous NaCl solution the sensitivity of the results with respect to the system size was evaluated. Figure S8 shows that the PMF is insensitive to the system size as is the enthalpy change upon dimerization (data not shown).

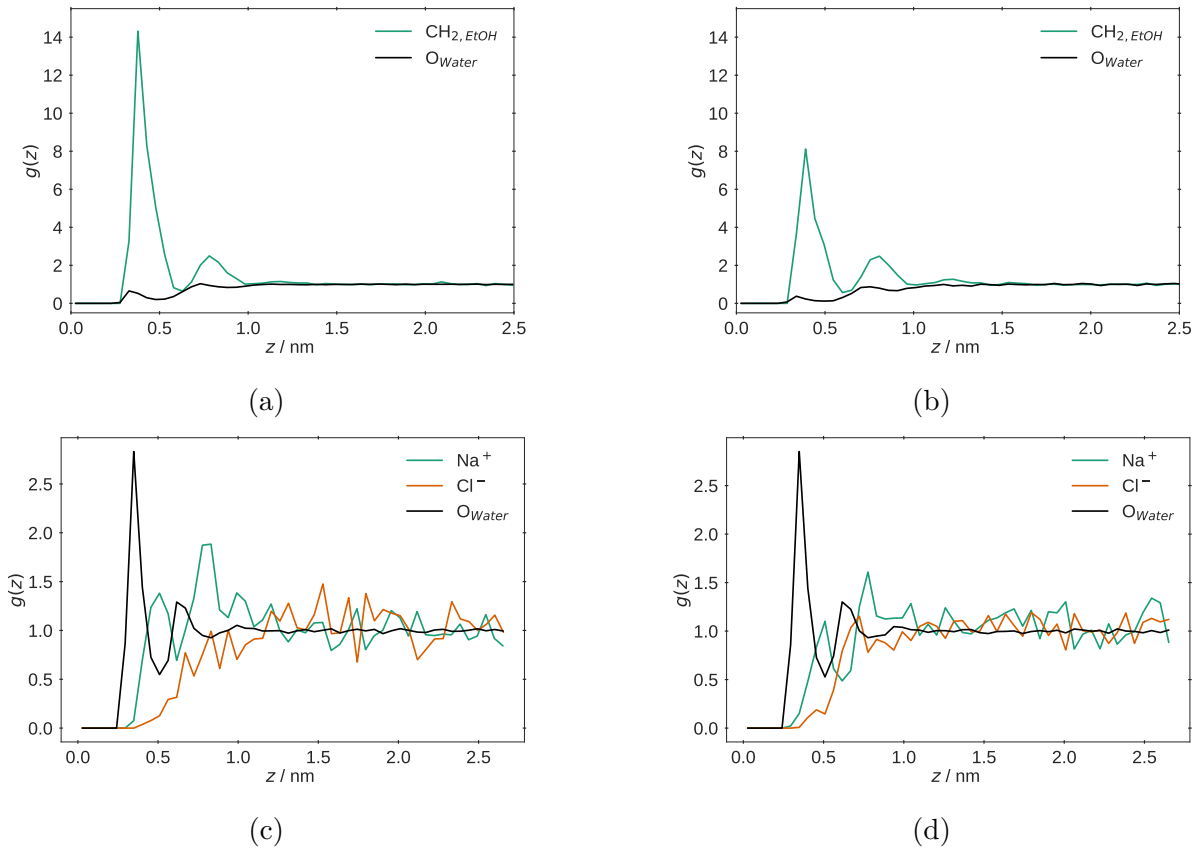

Figure 2.10: Distribution functions $g(z)$ of water and ethanol in 25 vol% (a) and 50 vol% (b) ethanol/water mixture and of water, Na^+ and Cl^- in 0.5 M (c) and 1.0 M (d) aqueous NaCl solution at 298.15 K. Molecules that are located in a cylinder with radius 0.1 nm positioned at the center of mass of one of the two PBI molecules and oriented perpendicular to the surface towards the solvent were considered in the calculation of $g(z)$. The results were averaged over the two plate-like molecules in the complexed state.

Regarding the PBI configurational variability no significant differences between the different solvent environments were found. While in the ethanol/water mixtures larger COM-COM distances were found more frequently than in pure water the opposite was observed in the aqueous NaCl solution (data not shown). Figure S9 of the Supporting Information shows several transitions of the Ω-angle beyond 90° in the S1-system at 298.15 K suggesting that the sampling time was sufficient to cover the conformational fluctuations in the system.

Like for pure water the temperature dependence of the potentials of mean force can be

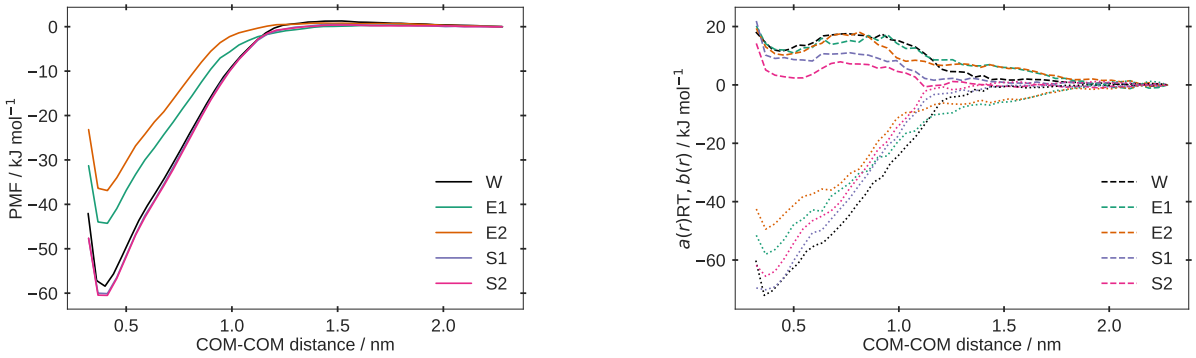

(a) (b)

Figure 2.11: (a) Potentials of mean force at 298.15 K for different solvent environments obtained from equation 2.4. (b) Repulsive ($a(r)RT$, dashed lines) and attractive ($b(r)$, dotted lines) contributions of the PMFs.

accurately described using the simple expression derived from thermodynamic perturbation theory. The corresponding figures are displayed in the Supporting Information. Only in the case of the 50 vol% ethanol/water mixture some deviation between simulations and model are observed which is attributed to the slower convergence in this system. Figure 2.11 shows that compared to the pure water case the presence of ethanol hardly changes the repulsive part of the PMF while the attractive part is stronlgy influenced. In contrast NaCl changes both contributions. While the attractive part is slightly weakened also the repulsion becomes less strong resulting in an overall stronger association compared to the pure water case.

The weaker repulsion might be attributed to counterion shielding of the electrostatic repulsion between the negatively charged dye molecules. Figure S10 shows the increased density of sodium ions in proximity to the carboxylate oxygen atoms of the dimerized PBI.

Finally, we would like to point out the similarity between the approach of modeling the temperature dependence of the PMF according to equation 2.5 and 2.6 and the decomposition of the potential of mean force into an enthalpic, ΔH, and entropic, ΔS, contribution according to [300]

$$\Delta G_{\mathrm{PMF}}(r,T) = \Delta H(r) - T\Delta S(r) \tag{2.9}$$

where the two contributions $\Delta H(r)$ and $\Delta S(r)$ are assumed to be temperature independent. A molecular-scale picture of the underlying driving forces at a fixed temperature can now be obtained, when considering the statistical-mechanical enthalpy-entropy compensation leading to [300]

$$\Delta G_{\mathrm{PMF}}(r) = \Delta H_{\mathrm{UV}}(r) - T\Delta S_{\mathrm{UV}}(r) \tag{2.10}$$

where the solvent-solvent contributions have cancelled out while the remaining terms include both solute-solute and solute-solvent contributions. Although in the present case the particle-mesh Ewald energy cannot be decomposed into interactions between specific parts of the system the analysis of the short-range interactions reveals that the gain in solute-solute interactions upon complexation (e.g. $\sim -90\,\mathrm{kJ\,mol^{-1}}$ for the S2-system) is almost compensated for by a change in solute-solvent interactions that disfavours association (e.g. $\sim 80\,\mathrm{kJ\,mol^{-1}}$ for the S2-system) which can be rationalized by the smaller solvent accessible area of the dimerized complex compared to the separated monomers. As a result the total enthalpy change upon complexation contains significant (e.g. $\sim -58\,\mathrm{kJ\,mol^{-1}}$ for the S2-system) contributions from solvent reorganization that blur the significant contribution of solute-solvent entropy to the stability of the dimer for all systems studied.

2.4 Conclusion

Achieving an atomic-level description and mechanistic understanding of the onset of self-assembly is an important prerequisite in the rational design of both solute and solvent molecules. Atomistic simulations play an important role in these efforts. In the present study the significance of a detailed thermodynamic analysis of the initial phase of self-assembly of a perylene bisimide dye is discussed. A decomposition of the enthalpic and entropic components of the potential of mean force into solute-solvent and solvent-solvent interactions[300] provides a useful molecular-scale picture of the association process and the underlying driving forces that are otherwise difficult to disentangle. Rather than reaching quantitative agreement with experimental data the goal was to achieve converged results for a realistic system that prove to be thermodynamically consistent within a given force field. The experimentally observed dependence of the aggregation strength on the solvent environment was reproduced by the simulations and a molecular-level interpretation was obtained. This opens up the possibility to combine classical MD simulations with quantum chemical calculations in more realistic solvent environments to aid the molecular-level interpretation of absorption spectra that may depend strongly on the relative orientation of the monomers [301, 302]. A further avenue to explore in future work is the development of coarse-grained potentials for such building blocks using the convenient description of the potentials of mean force by a rather generic thermodynamic model based on a perturbation theory of fist order. This model allows to generate a large set of PMFs from relatively few explicit MD simulations of the dimerization and possibly the formation of larger aggregates. These PMFs can in turn be used to parametrize low-dimensional effective interaction potentials for aspherical molecules [303] with the aim to study aggregation behavior at realistic solute concentrations [126, 304].

Chapter 3

Thermophysical Properties of Glyceline-Water Mixtures Investigated by Molecular Modelling

The content of this chapter is a literal quote of the publication

Jörg Baz, Christoph Held, Jürgen Pleiss and Niels Hansen, Physical Chemistry Chemical Physics, 21, 6467-6476, 2019

The manuscript was written by Jörg Baz. All molecular simulations were conducted by Jörg Baz. The PC-SAFT calculations were carried out by Christoph Held (TU Dortmund). Jürgen Pleiss and Niels Hansen supervised the project and manuscript writing.

Abstract

The effect of water content on static and dynamic properties of the deep eutectic solvent glyceline is studied using molecular dynamics (MD) simulations. Static properties are additionally calculated using the PC-SAFT equation of state. Force fields calibrated on water-free glyceline show predictive power for density and water activity over the entire composition range. In contrast, the PC-SAFT approach by pseudo one-component or two-component modelling strategies performed better for the density or the water activity, respectively. The MD simulations show that at low water content the hydrogen-bond network between glycerol molecules as well as between glycerol and the cholinium cation is hardly affected by the water molecules while at higher water content glycerol-glycerol hydrogen bonds are replaced by glycerol-water hydrogen bonds indicating the formation of an aqueous solution accompanied by a strong decrease of the shear viscosity. At the same time the thermodynamic activity of water increases such that the MD simulations are able to guide the optimal composition with respect to requirements in biocatalytic applications such as low viscosity and low water activity. The combined application of PC-SAFT to efficiently predict static properties and molecular dynamics simulations to predict static and dynamic properties offers a powerful framework in solvent design applications.

3.1 Introduction

Deep eutectic solvents (DES) are eutectic mixtures typically formed with a hydrogen bond acceptor, for example choline chloride and a hydrogen bond donor, for example glycerol. Due to their low vapour pressure, they are attractive non-aqueous solvents in chemical or biochemical processes [305]. However, the high viscosity hampers the use as solvent for e.g. biocatalytic applications. The addition of water results in a considerable decrease of viscosity but may lead to undesired side effects such as the occurrence of water-dependent side reactions. On the other hand, many enzymatic reactions require a certain amount of water for the enzyme to function [306] making the thermodynamic activity of water an important process parameter [307]. Thermophysical properties of DES-H2O binary mixtures are difficult to predict as concluded from a recent comprehensive review [308] due to a change of the microscopic structure of the fluid upon the addition of water [309]. Advanced equations of state have been applied to model thermodynamic properties and gas solubility in DES [310–312]. Perturbed-Chain SAFT (PC-SAFT [313]) has been turned out to be a promising equation of state. PC-SAFT characterizes DES as chains of finite volume that exhibit dispersion and hydrogen bonding forces. However, equations of state such as PC-SAFT have not yet been used to predict the water influence on thermophysical properties of DES. Despite of their physical background, advanced equations

of state do not account for the microscopic structure of systems.
To overcome this, atomistic simulations offer the missing link between microscopic structure and macroscopic properties given a suitable molecular model or force field, respectively. Recent studies reported molecular dynamics simulations of common DESs such as reline, ethaline, glyceline [314–316] and their mixtures with water [317–319], with a focus on density, hydrogen bond patterns and pair-correlation functions while other important properties such as water activity or transport coefficients were not considered. Moreover, the recent studies exhibit a considerable force-field dependence of the fluid structure such that additional (thermophysical) properties are required for validating the molecular models.
In the present work, the question is addressed of whether classical molecular dynamics simulations using force fields validated against the pure DES can be used to predict properties of the binary DES-H2O mixture that are of relevance in biocatalytic applications, namely shear viscosity and water activity. Using the example of the mixture of choline chloride and glycerol in the 1:2 molar ratio (glyceline) it is investigated whether the composition of the aqueous mixture can be optimized with the target of low shear viscosity and, at the same time, low thermodynamic activity of water.

3.2 Computational Details

3.2.1 Molecular Dynamics Simulations

3.2.1.1 Force Field

The choline chloride (ChCl) model is based on the GAFF force field [320] as described in Refs [315, 321]. In agreement with previous work [315] the partial charges were scaled by a factor of 0.9 to implicitly account for the effect of electronic polarization [322]. This model was shown to represent successfully the density as function of temperature, the heat capacity, as well as the self-diffusion coefficient of choline chloride in the water-free 1:2 mixture with glycerol (Gly), referred to as glyceline. We note that the choline chloride model has also been used successfully by other authors to study ethaline, a mixture of choline chloride and ethylene glycol [316]. For glycerol a molecular topology was obtained from the FreeSolv database [323]. The atomic partial charges were adapted to the ones reported in table S3 of Ref. [315] which were obtained using the restrained electrostatic potential charge derivation method [324–326]. The molecular topologies were validated by comparing densities and pair correlation functions calculated in the present work for water-free glyceline to those reported by Perkins et al. [315] To represent water the TIP4P/EW model was employed [327]. To assess the influence of the water model on calculated properties selected simulations were also performed with the TIP4P [328] and

System	$x_{\mathrm{W}}^{\mathrm{species}}$ / mol/mol	x_{W} / mol/mol	w_{W} / wt-%	N_{W}	$\langle L_{\mathrm{box}} \rangle$
C0	1.000	1.000	100.00	3000	4.498
C1	0.870	0.900	59.736	8000	7.210
C2	0.692	0.750	33.365	2700	5.990
C3	0.429	0.500	14.303	900	5.447
C4	0.200	0.250	5.270	300	5.247
C5	0.077	0.100	1.821	100	5.185
C6	0.000	0.000	0.000	0	5.413

Table 3.1: System compositions studied in this work. The number of cholinium cations, chloride anions and glycerol molecules was fixed to 300, 300, and 600, respectively, while the number of water molecules N_{W} was adjusted to the desired composition. The system C0 respresents pure water. The average simulation box length according to 50 ns simulation time at 320.15 K is shown in the last column and given in nm.

the SPC/E [329, 330] model. For all molecules used in the present work a detailed description including Lennard-Jones parameters, atomic partial charges and bonded parameters is presented in the Supporting Information along with an analysis of the subsystems glycerol, glycerol-water and choline chloride-water.

3.2.1.2 Simulated Systems

Table 3.1 specifies the compositions of all systems (C0 to C6) studied in the present work together with the corresponding water mass and mole fraction, w_{W} and x_{W}, respectively. The former is unambiguously defined as

$$w_{\mathrm{W}} = \frac{N_{\mathrm{W}} M_{\mathrm{W}}}{N_{\mathrm{Ch^+}} M_{\mathrm{Ch^+}} + N_{\mathrm{Cl^-}} M_{\mathrm{Cl^-}} + N_{\mathrm{Gly}} M_{\mathrm{Gly}} + N_{\mathrm{W}} M_{\mathrm{W}}} \tag{3.1}$$

where M_{i} denotes the molecular weight of species i, and N_{i} the number of molecules of species i in the system. The water mole fraction is usually defined as

$$x_{\mathrm{W}} = \frac{N_{\mathrm{W}}}{N_{\mathrm{ChCl}} + N_{\mathrm{Gly}} + N_{\mathrm{W}}} \tag{3.2}$$

to report experimental data [331, 332], although the DES components are often subsumed into one pseudo component. In the context of molecular dynamics simulations, an alternative definition is appropriate that considers the dissociated choline chloride,

$$x_{\mathrm{W}}^{\mathrm{species}} = \frac{N_{\mathrm{W}}}{N_{\mathrm{Ch^+}} + N_{\mathrm{Cl^-}} + N_{\mathrm{Gly}} + N_{\mathrm{W}}} \tag{3.3}$$

3.2.1.3 Simulation Parameters

All simulations were performed under minimum image periodic boundary conditions based on cubic computational boxes using the GROMACS 2016 program package [108, 261–263, 333–336] compiled in single precision. Equations of motion were integrated using the leap frog scheme [265] with a time step of 2 fs. For all systems an energy minimization, followed by a constant-volume equilibration simulation of 1 ns at 298.15 K and a successive constant pressure equilibration of 1 ns at the desired target temperature were conducted prior to the actual production simulation. All bond lengths were kept fixed using either SETTLE [266] (for water) or LINCS [267, 268] respectively, with an order of 4. The number of iterations to correct for rotational lengthening in LINCS was set to 2. The temperature was maintained close to its reference value by application of the velocity-rescale thermostat [269] with a relaxation of $\tau_T = 0.5\,\mathrm{ps}$. The pressure was set cose to its reference value using the Parrinello-Rahman barostat [270, 271] by isotropic coupling with a coupling constant of $\tau_p = 2.0\,\mathrm{ps}$ and an isothermal compressibility of $\kappa_T = 4.82 \times 10^{-5}\,\mathrm{bar}^{-1}$. Short-range electrostatics and Lennard-Jones interactions were treated with a Verlet-buffered neighbor list [272] with potentials shifted to zero at the cut-off of 1.5 nm. Analytical dispersion corrections were included for energy and pressure. Long-range electrostatics were treated by the smooth particle-mesh Ewald (PME) summation [273, 274] with a PME-order of 4.

3.2.2 Trajectory Analysis

3.2.2.1 Shear Viscosity

The shear viscosity η was determined from the Green-Kubo expression [337, 338]

$$\eta = \frac{V}{k_B T} \int_0^\infty \langle P_{\alpha\beta}(t) \cdot P_{\alpha\beta}(0) \rangle \, \mathrm{d}t \tag{3.4}$$

where V is the simulation box volume, T the temperature, k_B the Boltzmann constant and $P_{\alpha\beta}(\alpha, \beta \in x, y, z)$ are the pressure tensor components. Six independent shear components $1/2\,(P_{xy} + P_{yx})$, $1/2\,(P_{yz} + P_{zy})$, $1/2\,(P_{xz} + P_{zx})$, $1/2\,(P_{xx} - P_{yy})$, $1/2\,(P_{yy} - P_{zz})$ and $1/2\,(P_{xx} - P_{zz})$ are used to improve the statistics of each simulation. The three terms including the diagonal pressure tensor entries (xx, yy and zz) are obtained by a 45° rotation of the pressure tensor around all axis [339]. Correlation integrals $\int_0^\infty \langle ... \rangle \, \mathrm{d}t$ are calculated by a convolution in Fourier-space, according to Wiener-Khintchine theorem [340, 341]. The Fast Fourier Transform algorithm used for this is reducing the computational complexity from $\propto N_t^2$ to $\propto N_t / \ln(N_t)$ compared to the direct calculation [342]. Trajectories for viscosity calculation were obtained from constant-volume simulations with 5 ns production and a 1 ns preceding equilibration time. The predetermined volume was obtained using the average density from a previous constant-pressure simulation at 1 bar

and at the target temperature. The pressure tensor elements were stored in the energy trajectory every 10 fs. To reduce statistical noise in the running integral of equation 3.4, the viscosity calculation was averaged over a set of at least 100 independent simulations. Subsequent a double exponential function $\eta_{\text{fit}}(t)$ was fitted to the average of the time-dependent running integral $\langle\eta(t)\rangle$ with four fitting parameters, namely η_∞, α, τ_1 and τ_2.

$$\frac{\eta_{\text{fit}(t)}}{\eta_\infty} = \frac{\alpha\tau_1\left(1-e^{-t/\tau_1}\right)+(1-\alpha)\,\tau_2\left(1-e^{-t/\tau_2}\right)}{\alpha\tau_1+(1-\alpha)\,\tau_2} \tag{3.5}$$

For larger times the residuals $\langle\eta(t_i)-\eta_{\text{fit}}(t_i)\rangle$ of the objective function are still very noisy and are thus damped by weighting to $1/t_i^b$ as described by Maginn et al [343]. In this case the parameter b results from a previous power law fit to the standard deviation $s(t)$ which is time dependent. The first 2 ps of every individual run are not included in the fitting process. The stationary plateau value of the double-exponential fit is defined as η_∞ and taken as zero shear rate viscosity η. The given errors equal the value of the time dependent standard deviation $s(t_{99})$ at the time t_{99} where the time dependent viscosity $\eta_{\text{fit}}(t)$ equals 99 % of the zero shear rate viscosity.

3.2.2.2 Self-Diffusion Coefficient

The self-diffusion coefficient D_{self}, was calculated from a constant-pressure simulation as the slope of a linear fit to the mean-square displacement of the molecules in the long-time limit using the Einstein relation [344, 345]

$$\lim_{t\to\infty}\left\langle\left(\mathbf{r_i}(\tau+t)-\mathbf{r_i}(\tau)\right)^2\right\rangle_{i,\tau} = 6D_{\text{self}}t + \text{const.} \tag{3.6}$$

where $\mathbf{r_i}$ is the current position of the center of mass of a molecule (following molecules across periodic boundaries) and $\langle\ldots\rangle_{i,\tau}$ denotes averaging over all molecules i and time origins τ. In this work, trajectory fragments of 5 ns were used for a least-square fitting to obtain a series of 10 self-diffusion coefficients from which a mean value as well as the corresponding standard deviation was calculated. The correlation coefficients of the least-square fitting R^2 were at least 0.99 in all cases. Finite size effects were accounted for by extrapolating D_{self} to infinite box size using [346]

$$D_{\text{self}}^{\infty} = \frac{k_B T\xi}{6\pi\eta L} + D_{\text{self}}^{\text{MD}}(L) \tag{3.7}$$

where D_{self}^{∞} is the self-diffusion coefficient in the thermodynamic limit, L is the side length of the cubic simulation box and ξ is a dimensionless constant equal to 2.837297 for cubic simulation boxes with periodic boundary conditions. Assuming a system-size independent shear viscosity η [346] the simulated self-diffusion coefficient $D_{\text{self}}^{\text{MD}}$ evaluated at a particular

box length were corrected based on the simulated η-values. In the results section only corrected self-diffusion coefficients are reported while the uncorrected values are provided in the Supporting Information.

3.2.2.3 Water Activity

The calculation of the solvation free energy ΔG_{solv} (or excess chemical potential) relied on a step-wise decoupling of the molecule from its surrounding using a scaling parameter λ, while retaining the intramolecular interactions. First, the electrostatic interactions were gradually deactivated using 11 equidistant λ-points followed by deactivation of the Lennard-Jones interactions using 14 λ-points distributed as 0.075, 0.150, 0.225, 0.300, 0.375, 0.450, 0.525, 0.600, 0.675, 0.750, 0.825, 0.900, 0.950 and 1.000. Soft-core potentials were used to avoid numerical problems close to the end states employing $\alpha_{sc} = 0.5$, $\sigma_{sc} = 0.3$ and a power for the soft-core scaling function of 1. The multistate Bennett acceptance ratio (MBAR) approach [347] was used as an estimator to obtain the free energy from the differences in the Hamiltonians between all states. Activity coefficients of water based on Rault's law standard state can then be calculated using solvation free energies of water in different compositions and system densities [348, 349]

$$\gamma_{\text{W}}(\text{Ci}) = \exp\left[\frac{\Delta G_{\text{solv}}(\text{Ci}) - \Delta G_{\text{solv}}(\text{C0})}{\mathcal{R}T}\right] \cdot \frac{\rho^m_{\text{Ci}}}{\rho^m_{\text{C0}}} \tag{3.8}$$

where $\gamma_{\text{W}}(\text{Ci})$ is the activity coefficient of water at system composition Ci as described in table 3.1, $\Delta G_{\text{solv}}(\text{Ci})$ is the solvation free energy of one water molecule in the system with composition Ci and $\Delta G_{\text{solv}}(\text{C0})$ its self-solvation free energy (System C0 in table 3.1. The ideal gas constant is denoted with $\mathcal{R}$ and the system temperature with T. The molar density of system Ci is calculated as

$$\rho^m_{\text{Ci}} = \frac{\sum_i N_i}{\langle V_{\text{Ci}} \rangle} \tag{3.9}$$

where the index i runs over all individual species, i.e. cholinium cation and chloride anion are counted as separate species and $\langle V_{\text{Ci}} \rangle$ is the average simulation box volume. The molar density of the pure water system is obtained from the ratio of water molecules and average simulation box volume in the pure water system,

$$\rho^m_{\text{C0}} = \frac{N_{\text{W}}}{\langle V_{\text{C0}} \rangle} \tag{3.10}$$

The activity of water is then obtained from

$$a_{\text{W}}(\text{Ci}) = \gamma_{\text{W}}(\text{Ci}) x^{\text{species}}_{\text{W}} \tag{3.11}$$

3.2.3 PC-SAFT Calculations

3.2.3.1 The Model

In this work classical PC-SAFT [313] was used to predict the influence of water on the thermodynamic properties mixture density and water activity in systems DES + water. Classical PC-SAFT describes the residual Helmholtz energy of a system a^{res} based on perturbation contributions a^{disp} and a^{assoc} to the energy contribution of a hard-chain reference system $a^{\text{hard chain}}$.

$$a^{\text{res}} = a^{\text{hard chain}} + a^{\text{disp}} + a^{\text{assoc}} \tag{3.12}$$

PC-SAFT requires five pure-component parameters for each component, the segment diameter σ, segment number m^{seg}, dispersion-energy parameter u/k_B, and the association parameters $\epsilon^{A_iB_i}$ and $\kappa^{A_iB_i}$. Mixtures are described using Berthelot-Lorenz combining rules for these parameters for the pairs of components i and j

$$\sigma_{ij} = \frac{1}{2}\left(\sigma_i + \sigma_j\right) \tag{3.13}$$

$$u_{ij} = \sqrt{u_i u_j}\left(1 - k_{ij}\right) \tag{3.14}$$

and Wolbach-Sandler mixing rules for the association parameters:

$$\epsilon^{A_iB_j} = \frac{1}{2}\left(\epsilon^{A_iB_i} + \epsilon^{A_jB_j}\right) \tag{3.15}$$

$$\kappa^{A_iB_j} = \sqrt{\kappa^{A_iB_i}\kappa^{A_jB_j}}\left(\frac{\sqrt{\sigma_{ii}\sigma_{jj}}}{\frac{1}{2}\left(\sigma_{ii} + \sigma_{jj}\right)}\right)^3 \tag{3.16}$$

It can be observed from Eqs. 3.13 to 3.16 that one binary parameter between components i and j is introduced.

Thermodynamic properties are derived from equation 3.12 based on differentiation with respect to volume and mole fraction. So-obtained water fugacity coefficients φ_{W} in the mixture and in pure water $\varphi_{0,\text{W}}$ are then used to calculate activity coefficients

$$\gamma_{\text{W}}(T, x_{\text{W}}) = \frac{\varphi_{\text{W}}(T, x_{\text{W}})}{\varphi_{0,\text{W}}(T, x_{\text{W}} = 1)} \tag{3.17}$$

3.2.3.2 PC-SAFT Parameters

For water, the 2B association model from Fuchs et al. [350] was used. Although this model is less realistic than 4C models for water that contain four association sites, the model from Fuchs et al. has turned out to be the best model for biological applications at moderate temperatures and pressures.

For DES, two modeling strategies have been developed, the pseudo-one component strategy and the individual-component strategy. In the former, a DES is considered as a pseudo-pure compound, and its pure-component parameters were adjusted in a previous work [312] using experimental density data of water-free pure DES as function of temperature and pressure. The DES has an average molar mass calculated based on the composition of the DES constituents. In the second strategy, the so-called individual-component strategy, PC-SAFT accounts explicitly for the pure components the DES is part of. The parameters of the pure components were obtained in previous works by fitting to experimental data of aqueous solutions water + choline chloride [311] as choline chloride is a solid until 300 °C at atmospheric pressure. This procedure has been also applied successfully to inorganic salts, amino acids, sugars and proteins [351–354]. For glycerol [355] parameters were obtained by fitting to pure-component data, i.e. liquid-density data and vapor-pressure data of pure glycerol. Hydrogen bonding is a key interaction for modeling DES systems. Independent of the strategy, self-association among DES (or DES constituents) was considered as well as cross-association between the individual DES constituents or DES (or DES constituent) with water. The PC-SAFT parameters are given in table 3.2. Binary parameters were also applied in this work. These k_{ij} parameters are also listed in table 3.2. It is important to mention that they were not adjusted to experimental data containing the DES. Thus, PC-SAFT does not require any calibration and was applied in a fully predictive mode.

Component	M / g mol^{-1}	m^{seg}	σ / Å	u/k_B / K	$\epsilon^{A_iB_i}/k_B$ / K	$\kappa^{A_iB_i}$	k_{ij} to water	Ref.
Water	18.015	1.2047	2.7927	353.95	2425.7	0.045	-	[350]
Choline Chloride	139.62	13.020	2.386	228.07	8000.0	0.200	*	[355]
Glycerol	92.094	2.0070	3.815	430.82	4633.47	0.002	-0.005	[355]
ChCl:Glycerol 1:2	107.95	7.7594	2.5699	275.00	5000.0	0.100	0	[312]

Table 3.2: Pure-component PC-SAFT parameters for water, the DES constituents and the one-component DES. * temperature-dependent function $k_{ij} = 0.001(T - 298.15\,\mathrm{K})$–0.05838.

3.3 Results

3.3.1 Volumetric Properties and Liquid Structure

The liquid density of glyceline:water mixtures was modelled by molecular dynamics simulations at 280.15 K, 320.15 K, and 360.15 K (figure 3.1). At increasing water content, the density decreases gradually from 1187.6 kg/m^3 for pure glyceline (at 320.15 K) to 1166.7 kg/m^3 at $x_W = 0.5$. For higher water content, it steeply drops to the density of pure water (985.99 kg/m^3). While the densities of the pure components ($x_W = 0.0$ and $x_W = 1.0$) are predicted in very good agreement with experimental data (deviation less than 0.9 %), the densities of the mixture are slightly overestimated, with a maximum deviation of 1 % at $x_W = 0.5$. Note that temperature difference of 3 K between simulation target temperature and experimental measured temperature lead to a density change of roughly 0.3 % which is within the error of the statistical uncertainty of the simulations. The pseudo-one component PC-SAFT evaluation slightly underestimates the experimental densities, while the two component PC-SAFT evaluation considerably overestimates the experimental densities at $x_W < 0.5$. The reason behind the latter observation is the fact that PC-SAFT parameters for choline chloride were adjusted to experimental density data of choline chloride:water solutions with $x_W > 0.6$ [311]. As a consequence, at very low x_W values the deviation from experimental data increased to 2.6 %.

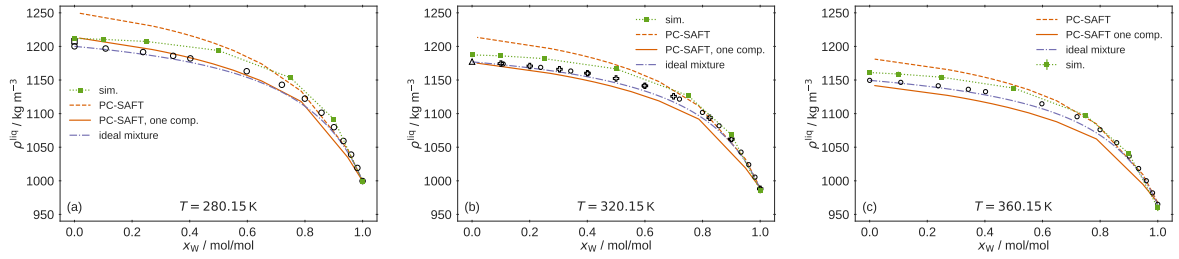

Figure 3.1: Liquid density as function of x_W for three different temperatures at atmospheric pressure. Experimental data at (a) 283.15 K, (b) 323.15 K, and (c) 363.15 K are shown as open symbols (Ref. [315] as squares; Ref [331] as circles, Ref. [356] as crosses and mean of Refs. [331, 356–359] as triangle). Green closed symbols represent simulation results and the two orange lines represent PC-SAFT calculations obtained at (a) 280.15 K, (b) 320.15 K and (c) 360.15 K. Statistical errors in the simulation results equal one standard deviation and are within a maximum absolute value of 5 kg/m^3 which equals error bars within symbol size. The purple line shows the density profile in case of an ideal mixture.

The densities of the real glyceline:water mixtures are higher than expected from ideal mixtures, in agreement with the calculated negative excess molar volumes with a minimum at $x_W = 0.5$ (figure 3.2). Experimental data support the simulation results, though the

simulation overestimates the non-ideality of mixing. Such an overestimation was also observed in a recent MD study employing CHARMM-type molecular models [318] and is indicative of strong interaction between water and glyceline.
Molecular dynamics simulations also slightly overestimate the liquid densities of glycerol-water mixtures and pure glycerol at 280.15 K, but not at 360.15 K (figure S14) and of aqueous ChCl solutions at 298.15 K (figure S16), indicative for a slight overestimation of the interactions between water and glycerol as well as between water and choline chloride by the used force field.

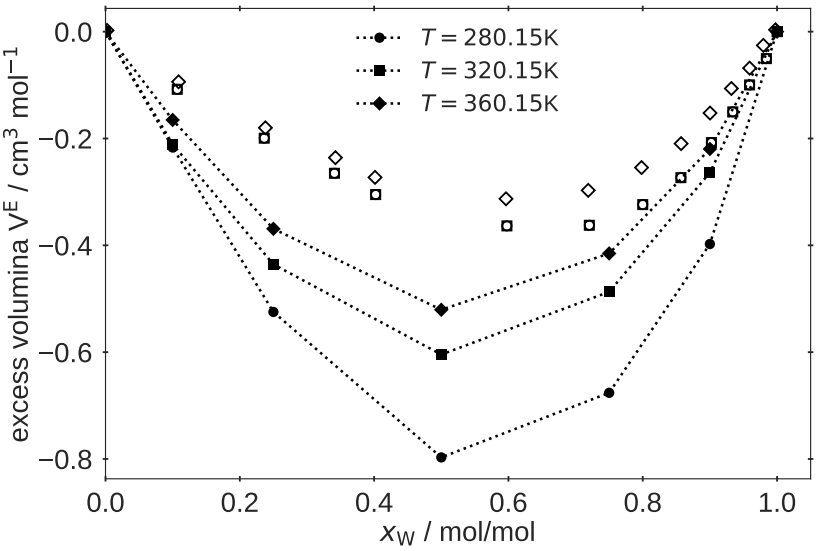

Figure 3.2: Excess molar volume V^{E} as function of x_{W} as predicted by MD simulations (filled symbols) and as obtained from experiment [318] (open symbols: 323.15 K as squares and 363.15 K as diamonds).

Since the temperature dependence of the glycerol density depends considerably on the force field details [360], a refinement of the glycerol model may be attempted in future work.

Radial distribution functions at 320.15 K for seven pairs of atoms (chloride and oxygen atoms of the choline cation, glycerol and water) at $x_{\mathrm{W}} = 0.5$ demonstrate a close contact between chloride and the three oxygen atoms (peak at 0.322 nm). The water-water, water-glycerol and water-cholinium cation radial distribution functions all show a peak at 0.276 nm, while no peak is formed for the choline-choline oxygen atoms (figure 3.3).
The peak positions of all interaction pairs are not significantly affected by water content and temperature (figure S18 to figure S25). These results are in good agreement with recent work by Weng and Toner [318] using a CHARMM force field, except for the lack of the peak at 0.276 nm in the choline-choline radial distribution function. In contrast, Ahmadi et al. [317] observed phase separation.

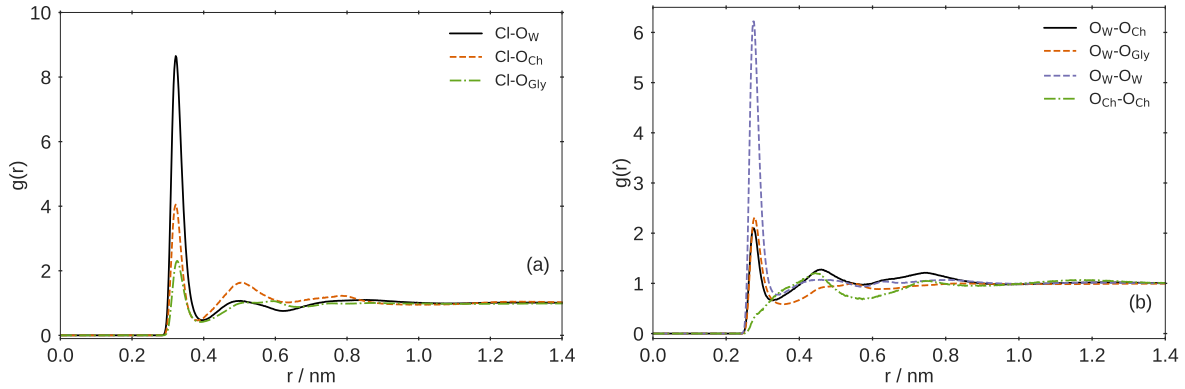

Figure 3.3: Radial distribution function $g(r)$ at 320.15 K for the mixture with $x_W = 0.5$ for different pairs of chloride (a) and oxygen atoms (b). Cl denotes chloride anions, O_W the water oxygens, O_{Ch} the oxygen atom of the cholinium cation and O_{Gly} the oxygen atoms of glycerol.

Hydrogen bonds for different interaction pairs are shown as function of molar water fraction x_W in figure 3.4. Since the amount of choline chloride and glycerol molecules in the different simulated compositions was kept constant (table 3.1), the figure shows how the hydrogen bonds between glycerol molecules disappear in favour of hydrogen bonds between glycerol and water. At high water concentration, glycerol molecules form hydrogen bonds with up to four water molecules.

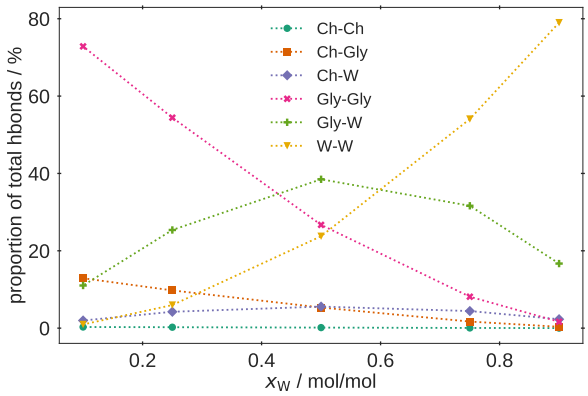

Figure 3.4: Number of hydrogen bonds as function of the water mole fraction x_W at 320.15 K for different molecule pairs. Choline is abbreviated as Ch, glycerol as Gly and water as W, respectively. Hydroxyl (OH) and primary amino groups (NH) are regarded as hydrogen bond donors while oxygen and nitrogen atoms are hydrogen bond acceptors. For identifying hydrogen bonds, a cut off angle of 30° together with a cut off radius of 0.35 nm was chosen. The number of hydrogen bonds between glycerol and water is divided by three.

The figure also shows that hydrogen bonds between choline and glycerol molecules are replaced by hydrogen bonds between choline and water leading to an aqueous solution of the DES components at higher water mole fractions. Signatures of phase separation, such as the insensitivity of the amount of Gly-Gly hydrogen bonds with respect to the water content, as observed recently [317] were not found in the present work. Instead the results obtained in the present work are qualitatively similar to those reported by Zhekenov et al. [319].

3.3.2 Shear Viscosity

The simulated shear viscosity at three different temperatures is in good agreement with experimental value for viscosity values below 30 cP (figure 3.5). At 360.15 K it deviates from experiment by less than 18 % over the entire composition range, but at lower temperatures only the systems with higher water content could be reliably calculated due to convergence problems with the equilibrium MD simulations for high viscosity. While the viscosity of water decreased fourfold upon increasing the temperature by 80 K ($\eta(280.15\,\mathrm{K}) = 1.16\,\mathrm{cP}$, $\eta(320.15\,\mathrm{K}) = 0.51\,\mathrm{cP}$, $\eta(360.15\,\mathrm{K}) = 0.30\,\mathrm{cP}$), the viscosity of pure glyceline was strongly temperature dependent, changing by a factor of 51 ($\eta(283.15\,\mathrm{K}) = 1003.94\,\mathrm{cP}$, $\eta(363.15\,\mathrm{K}) = 19.59\,\mathrm{cp}$). Similarly, glyceline-water mixtures showed a decreasing temperature dependency upon increasing water content.

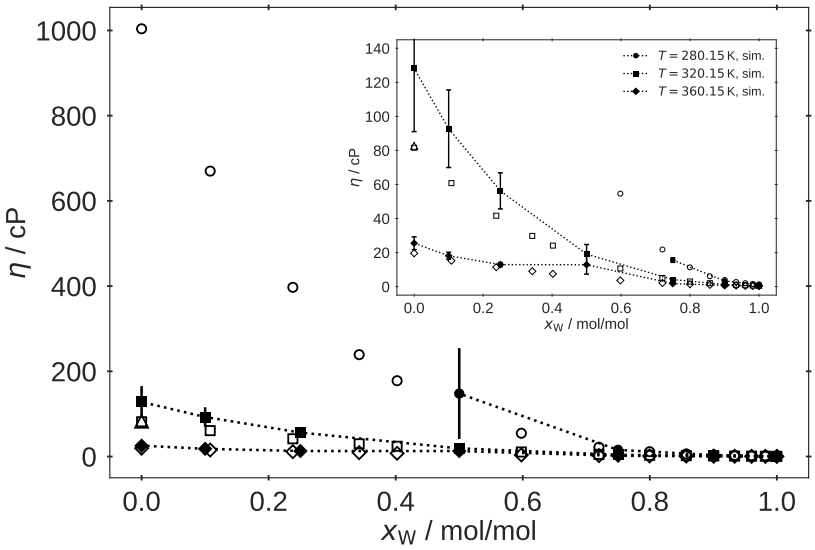

Figure 3.5: Shear viscosity η as function of water fraction x_W for different temperatures. Experimental data are shown as open symbols and correspond to temperatures of 283.15 K (Ref. [331], circles), 323.15 K (Ref. [331], squares; Ref. [361], triangles up) and 363.15 K (Ref. [331], diamonds). Simulation results are shown as closed symbols with dotted lines used as guide to the eye. Error bars equal one standard deviation. Inset shows the same data but with higher resolution on the y-axis.

3.3.3 Self-Diffusion Coefficient

The self-diffusion coefficient of water as a function of temperature for six different water mole fractions x_W was simulated at different box sizes. By accounting for finite size effects [346] and using the simulated shear-viscosity values from figure 3.5, the self-diffusion coefficient was evaluated for infinite size boxes. Figure 3.6 shows the temperature dependence of the self-diffusion coefficient of water at various water mole fractions. At lower water mole fractions the increase of the self-diffusion coefficient with temperature is less pronounced compared to mole fractions larger than $x_W = 0.5$. As expected from previous studies of the TIP4P/EW model [327, 362], the self-diffusion of pure water can be described successfully over the entire temperature range.

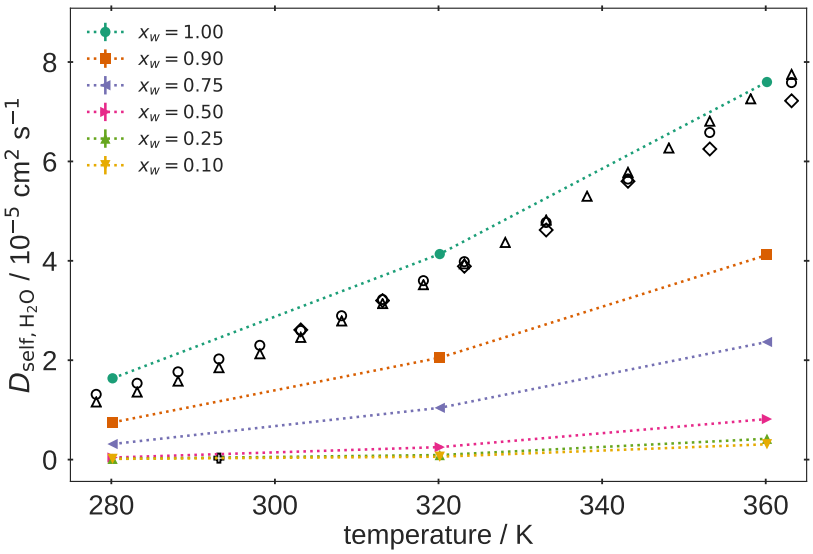

Figure 3.6: Self-diffusion coefficient of water as function of temperature for different water mole fractions x_W. Simulation results are corrected for finite size effects according to ref. [346]. Error bars are within symbol size and equal one standard deviation. Absolute errors are within a maximum value of 8×10^{-7} cm^2/s. Simulation results are shown as closed symbols with dotted lines used as guide to the eye. Different colors describe different solvent compositions while experimental data are shown as open circles from ref. [363], as open triangles from ref. [364], as open diamonds from ref. [365] for $x_W = 1.0$ and as plus symbol from ref. [366] at 293.15 K for $x_W = 0.1$.

Figure 3.7 shows the self-diffusion coefficient as function of the water mole fraction x_W. Compared to pure water, the diffusion coefficient drops significantly upon addition of glyceline. The inset in figure 3.7 demonstrates the good agreement between simulation and experiment at low water content considering that the experimental data were reported at 293.15 K, i.e. 13 K above the simulated temperature of 280.15 K.

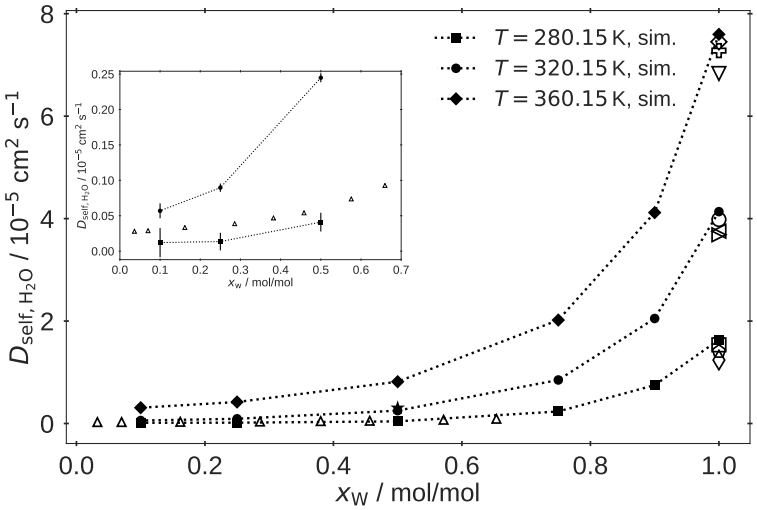

Figure 3.7: Self-diffusion coefficient of water as function of water fraction x_W for different temperatures. Simulation results are corrected for finite size effects according to ref. [346]. Error bars equal one standard deviation and are within symbol size except for the ones shown explicit in the inset. Absolute errors are within a maximum value of 8×10^{-7} cm^2/s. Simulation results are shown as closed symbols with dotted lines used as guide to the eye. Experimental data for pure water are taken from ref. [363] (diamond, circle and square), ref. [365] (triangle down, triangle right) and ref. [364] (plus, triangle left, thin diamond) for 360.15 K, 320.15 K and 280.15 K respectively. Open up triangles are representing experimental data from ref. [366]. Self-diffusion coefficient of TIP4P water model is shown as star symbol at $x_W = 0.5$ for 320.15 K.

3.3.4 Water Activity

The simulated activity coefficient at 320.15 K was less than 1 for all mixtures (figure 3.8), in agreement with experiment. This negative deviation from Raoult's law indicates a stronger interaction of water in the mixture relative to pure water. The simulated water activity at 320.15 K is in good agreement with the experimental data reported by Wu et al. [332] obtained at 323.15 K, while Durand et al. [367] reported lower water activities obtained at 333.15 K, demonstrating a significant deviation between the two experiment datasets. The PC-SAFT results demonstrate that the two components choline chloride and glycerol need to be modelled as separate species to obtain physically correct results which are then in very good agreement with the experimental data from Wu et al. [332]. If the DES is modelled as one pseudo-component PC-SAFT predicts a positive deviation from Raoult's law, i.e. is qualitatively wrong.

At 360.15 K the simulated activities exhibit higher values in accordance with experiment determined at 343.15 K, but deviate more strongly from the PC-SAFT results. Surprisingly the PC-SAFT results predict lower activities although they were also evaluated at 360.15 K.

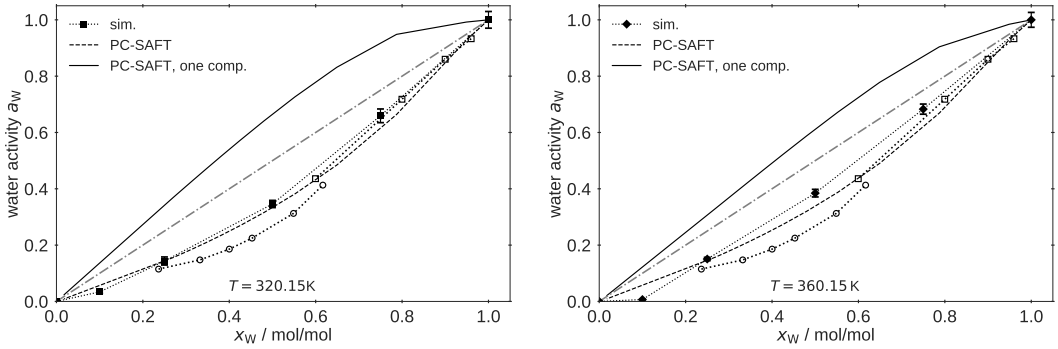

Figure 3.8: Calculated water activity as function of water mole fraction x_{W} at (left) 320.15 K and (right) 360.15 K. Simulation results are shown as closed symbols with dotted lines used as guide to the eye. Error bars equal to a maximum error estimation. For this estimation the sum of the absolute statistical error of ΔG_{C0} and ΔG_{Ci} was added to the value of $\Delta\Delta G$ and evaluated with equation 3.8. PC-SAFT results are present as closed and dashed lines, representing the pseudo-one component strategy (does not account for interactions between choline chloride and glycerol) and the two-component strategy that explicitly accounts for all molecules in the mixture. Experimental data are represented as open symbols. The squares [367] correspond to 323.15 K (a) and 343.15 K (b) while the circles [332] correspond to 333.15 K in both panels. Dash dotted bisecting line is representing an ideal mixture.

It can be concluded that the two-component individual modelling strategy is much more promising than the pseudo-one component modelling strategy. Specific interactions between choline chloride and water and between glycerol and water and between glycerol and choline chloride are explicitly taken into account using the two-component individual modelling strategy, which is essential for the quantitative prediction of water activities. It should be noted that the application of possible binary interaction parameters between DES and water in a pseudo-one component modelling strategy will improve the results, and the failure of such predictions was expected, as binary parameters in binary mixtures with water are generally required using SAFT-based models. However, the use of such binary parameters was not in the focus of this work to keep the results in a predictive mode. To avoid the appearance of multiple models for the same compound a recalibration of model parameters should be based on a larger set of mixture data which was beyond the scope of the present work.

3.4 Discussion

Properties such as the shear viscosity and the water activity are of particular importance in biocatalytic process design. Therefore, the robustness of their calculation is discussed in more detail in the following.

The shear viscosity does not show significant finite size effects [346] and can be reliably obtained by analyzing pressure fluctuations of an NVT simulation according to the Green-Kubo approach. For a glyceline-water mixture at $x_{\mathrm{W}} = 0.5$ and 320.15 K, a shear viscosity $\eta = 19.06\,\mathrm{cP}$ was obtained. Alternatively, it can be obtained by analyzing the self-diffusion coefficient for different box sizes [346]. This route has been recently tested for Lennard-Jones particle systems, water, and an ionic liquid [368], and it is illustrated in figure 3.9, showing the self-diffusion coefficient as function of the inverse box length L_{Box} for the system with $x_{\mathrm{W}} = 0.5$ at 320.15 K. The number of particles as shown in table 3.1 were multiplied by 0.75, 1.25, and 2.0, respectively (see Supporting Information for exact system compositions). A weighted linear fit, where the weights are inverse standard deviations of the self-diffusion coefficients, through the simulation results lead to the self-diffusion coefficient at infinite system size at $1/L_{\mathrm{Box}} = 0$. When comparing this self-diffusion coefficient for infinite system size to a self-diffusion coefficient corrected with the analytical term by Yeh and Hummer [346], shown as black diamond, it can be seen that both methods lead to almost the same system-size independent self-diffusion coefficient. Calculating the shear viscosity from the slope of the linear fit leads to a slightly increased value $\eta = 23.4\,\mathrm{cP}$. Such a deviation between the two methods was also reported by Jamali et al. [368]. For systems with high viscosity this approach might not be beneficious due to high computational costs for obtaining well-converged self-diffusion coefficient. To assess sampling and convergence, the slopes of all components of the mixtures were compared. The plots analogous to figure 3.9 for the cholinium cation, chloride anion and glycerol are shown in the supporting information (figure S26 to S28). For the components cholinium cation and glycerol which show a five times smaller diffusivity than water the corresponding viscosity was larger by 6 cP and 11 cP, respectively. The slope of the chloride component results in a viscosity value of $\eta = 10\,\mathrm{cP}$. Therefore, this indirect approach for viscosity calculation did not show advantages over the direct approach due to different convergence rates of the self-diffusion coefficients of the different mixture components.

In the high viscosity regime, one might resort to non-equilibrium MD simulations. The viscosity can be calculated from the response of the system to an external shear field and extrapolated to zero shear rate by means of the Carreau equation [369] or alternative approaches [370].

The method of choice will therefore depend on the specific system to be studied and of the level of accuracy with which the high viscosity regime needs to be treated [371]. In the low viscosity regime the shear viscosity can be reliably calculated using the Green-Kubo approach as outlined in Section 3.2.2.1.

The activity coefficient is composed by an ideal gas part as ratio of molar densities and a residual part depending exponentially on the difference of two free energies of solvation

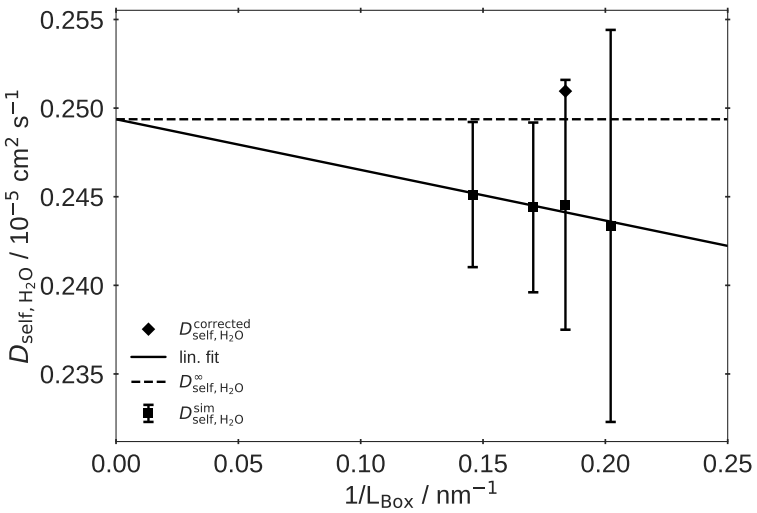

Figure 3.9: Self-diffusion coefficient as function of the inverse box length for system C3. Slope of the weighted linear fit equals $-5.674 \times 10^{-20}\,\mathrm{m^3/s}$. Self-diffusion coefficient for infinite system size equals $2.4934 \times 10^{-5}\,\mathrm{cm^2/s}$ and is shown as dashed line. Error bars equal one standard deviation.

(equation 3.8). For the system studied here, the ratios of molar densities are 1.33 and 3.48 at $x_\mathrm{W} = 0.9$ and 0.1, respectively. The densities are reliably determined by molecular simulation. The exponential term is 0.76 and 0.11 at $x_\mathrm{W} = 0.9$ and 0.1, respectively. The sensitivity of this term with respect to errors in $\Delta\Delta G$ is strong, such that small changes in the free energy difference leads to large deviations in the resulting activity. While the free energy of solvation can be reliably computed with a high degree of convergence, the error in $\Delta\Delta G$ is mainly caused by the quality of the force field. In practice, errors in the force field compensate, resulting in smaller errors of $\Delta\Delta G$ than the individual free energies of solvation indicate (figure 3.10). For three water force fields (TIP4P/EW, TIP4P and SPC/E), the solvation free energies $\Delta G_\mathrm{Solv}(C0)$ and $\Delta G_\mathrm{Solv}(C3)$ differ by $4\,\mathrm{kJ\,mol^{-1}}$. At 320.15 K the calculated numbers are: $\Delta G_\mathrm{Solv}(C0) = -28.32\,\mathrm{kJ\,mol^{-1}}$ and $\Delta G_\mathrm{Solv}(C3) = -26.42\,\mathrm{kJ\,mol^{-1}}$ for TIP4P/EW, $\Delta G_\mathrm{Solv}(C0) = -24.30\,\mathrm{kJ\,mol^{-1}}$ and $\Delta G_\mathrm{Solv}(C3) = -22.17\,\mathrm{kJ\,mol^{-1}}$ for TIP4P and $\Delta G_\mathrm{Solv}(C0) = -28.30\,\mathrm{kJ\,mol^{-1}}$ and $\Delta G_\mathrm{Solv}(C3) = -25.97\,\mathrm{kJ\,mol^{-1}}$ for SPC/E. The self-solvation free energy for the TIP4P is in good agreement with the experimental value of $-25.14\,\mathrm{kJ\,mol^{-1}}$ [372], while the TIP4P/EW and the SPC/E water models deviate by $3\,\mathrm{kJ\,mol^{-1}}$. Despite this deviation, the difference of the solvation free energies $\Delta\Delta G$ are similar for all three water models ($1.90\,\mathrm{kJ\,mol^{-1}}$ for TIP4P/EW, $2.13\,\mathrm{kJ\,mol^{-1}}$ for TIP4P and $2.33\,\mathrm{kJ\,mol^{-1}}$ for SPC/E respectively) due to error compensation. We therefore recommend to investigate the robustness of the activity coefficient for the actual system under study with respect to force field changes. The results presented above suggest that in practice, activity coefficients can be reliably obtained, in agreement with previous work [373].

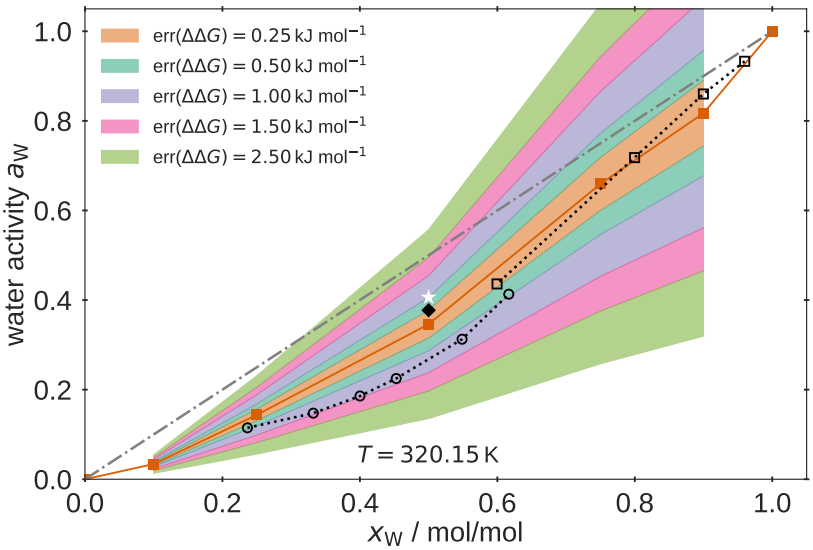

Figure 3.10: Sensitivity analysis of the water activity as function of the water mole fraction at 320.15 K. Experimental data are taken from [367] at 323.15 K shown as open squares and from [332] at 333.15 K shown as open circles. Water activity obtained using TIP4P water model [328, 374, 375] is shown as filled diamond while water activity obtained using SPC/E [329, 330] water model is shown as white star. Filled squares are representing simulation results using TIP4PEW water model at 320.15 K and composition C3. Here, colored areas are shown for different assumed errors in the free energy difference starting from an error of 0.25 kJ mol^{-1} (orange area) up to an error of 2.5 kJ mol^{-1} which equals the thermal energy at room temperature.

3.5 Conclusion

Atomistic simulations provide the link between the microscopic structure of DES-water mixtures and the corresponding thermophysical properties. The latter are experimentally easier to access compared to structural parameters and should therefore be considered when validating molecular models. Here, force fields calibrated to static and dynamic properties of water-free glyceline and the aqueous subsystems showed predictive power regarding properties of glyceline-water mixtures such that the design objective of low viscosity and low water activity can be handled by MD simulations. Equation of state calculations offer a fast evaluation of static properties but showed less predictive capabilities compared to the force field calculations. However, advanced models such as PC-SAFT can be used to pre-screen a large number of mixtures to better target the use of computationally demanding atomistic simulations. Such advanced models should account explicitly for all mixtures constituents in order to achieve quantitative prediction results.

Chapter 4

On the use of transport properties to discriminate Mie-type molecular models for 1-propanol optimized against VLE data

The content of this chapter is a literal quote of the publication
J. Baz, N. Hansen and J. Gross, The European Physical Journal Special Topics, 227, 1529-1545, 2019

Abstract

Parameterization of classical force fields often suffers from highly correlated parameters. In the present work the hypothesis that transport properties such as shear viscosity or self-diffusion coefficient can be used to decouple force field parameters that were fitted to static thermodynamic properties, such as saturation vapor pressure and liquid density is investigated. Here 1-propanol was studied where united-atom sites are described through Mie potentials and point charges. Four models were selected that gave about the same level of agreement with experimental liquid densities and vapor pressures. Shear viscosity and self-diffusion coefficients were evaluated with the aim to discriminate the models. However, the degeneracy of force field parameters observed in the static properties was also observed in the dynamic properties. We conclude that meaningful parameterizations for transferable force fields should simultaneously consider several molecules from a homologous series in order to define a less degenerate optimization problem.

4.1 Introduction

Transferable force fields allow predicting thermodynamic properties and phase equilibria of pure substances and mixtures. A meaningful parameterization of force fields, however, is obscured by degeneracy of force field parameters when regarding typical physical properties. Ketko and Potoff [376] studied dimethyl ether and showed that various combinations of Lennard-Jones parameters gave about equally good results for critical points and phase equilibrium properties. Although for dimethyl ether in earlier work of our group [230] we have seen an optimum in the parameterization for a slightly different objective function, the optimum is shallow with highly correlated parameters. In this work we consider 1-propanol and find even more correlated force field parameters. We here study the hypothesis that transport properties are suitable to discriminate among different parameter sets that reproduce static thermodynamic properties about equally well.

Several force fields were proposed for thermodynamic properties and phase equilibria, such as the Optimized Potential for Liquid Simulations (OPLS) [377–382] or the Transferable Potentials for Phase Equilibria (TraPPE) [48, 383–388]. The OPLS model was parameterized to experimental data of enthalpy of vaporization and liquid densities. The enthalpy of vaporization, due to the Clausius relation, also ensures a reasonable description of vapor pressures. The TraPPE model was parameterized to describe thermodynamic properties and phase equilibria, with emphasis on projections of temperature and density or temperature and composition. The TraPPE force field is based on the Lennard-Jones potential for describing short-range repulsion and van der Waals attraction and uses fixed point charges for modelling the electrostatic field of molecules.

The difficulty in representing both, phase equilibria in temperature projections and vapor pressure led several groups to introduce additional degrees of freedom in the parameterization of transferable force fields. The Buckingham potential with three adjustable parameters has been used instead of the Lennard-Jones model (that only offers 2 parameters per interaction site) with good agreement to experimental data [389]. Toxvaerd [390, 391] suggested to move the interaction site of a CH_3 group, say, away from the position of the carbon atom to account for the presence of hydrogen atoms. The distance of shifting a united-atom group away from the position of the large atom is an additional adjustable parameter in the parameterization of a force field. Ferrando, Boutin, Ungerer and coworkers developed the Anisotropic United Atom (AUA) force field based on this concept [392–396].

Potoff and Brunel used the Mie potential instead of the Lennard-Jones potential. Their work and subsequent studies with coworkers convincingly showed that relaxing the repulsive exponent from the value of $m = 12$ (corresponding to Lennard-Jones model)

allowed parameterizing a force field with very good agreement to static properties of pure substances [397–400].

The Transferable Anisotropic Mie (TAMie) force field was developed in our group. The model represents molecules as Mie interaction sites and partial point charges. The force field parameters were developed based on a well-defined objective function that comprises experimental data on vapor pressure and liquid density of several species simultaneously [229–232].

This work presents a parameterization study for 1-propanol (shown in figure 4.1), where highly correlated force field parameters are found for representing static thermodynamic properties, such as vapor pressure and liquid density. We investigate the hypothesis that transport properties can be used in force field optimization to discriminate various force field parameter sets that otherwise lead to an about equal description of static properties.

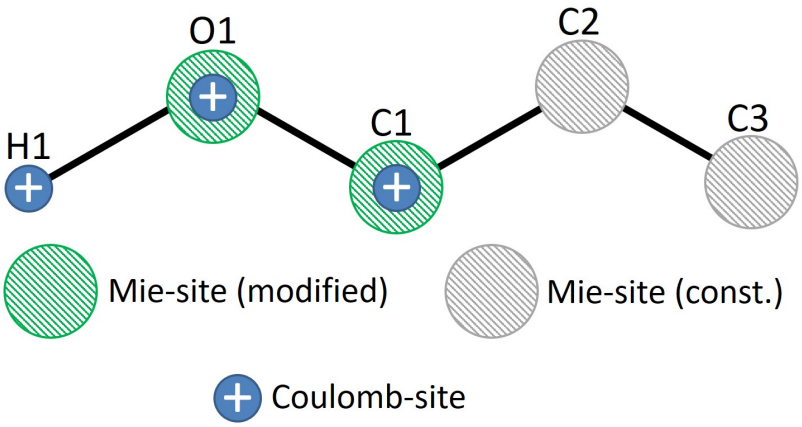

Figure 4.1: Molecular structure of 1-propanol, illustrating site names and schematic positioning of Mie sites and coulombic sites. Sites with optimized force field parameters are colored green, whereas sites with parameters from literature are shown grayshaded. Coulombic sites are included in the force field optimization.

4.2 Force Field

4.2.1 Bonded Energy

Bonded energies are calculated using fixed bond lengths and harmonic potentials for describing angle bending while torsional angles are described through angle expansions, in accordance to earlier work [229, 230]. For determining the appropriate force field parameters for 1-propanol, we performed quantum mechanical calculations using second order Møller-Plesset perturbation theory [401, 402] (MP2) structure optimization using a TZVPP basis set [403]. The calculations were conducted using the quantum chemistry

program package TURBOMOLE [404]. The bond lengths between hydrogen, oxygen, and the three carbon atoms were directly obtained from the structure optimization. Angle potentials and torsional potentials were determined by constraining angles to several values.

4.2.2 Nonbonded Energy

The nonbonded potential energy between two interaction sites i and j located on different molecules or located in the same molecule but separated by more than three bonds is described by the Mie potential plus Coulombic interactions

$$u_{ij}^{\text{inter}} = c_{ij}\varepsilon_{ij}\left[\left(\frac{\sigma_{ij}}{r_{ij}}\right)^{n_{ij}} - \left(\frac{\sigma_{ij}}{r_{ij}}\right)^{m_{ij}}\right] + \frac{q_i q_j}{4\pi\epsilon_0 r_{ij}} \tag{4.1}$$

where r_{ij} denotes the distance between the interaction sites, σ_{ij} and ε_{ij} are the size and energy parameter characterizing the Mie interaction, and q_i and ϵ_0 are the partial atomic charge and the vacuum permittivity, respectively. In the present work an interaction site i can represent a united-atom group such as an aliphatic CH_2 or CH_3 group, respectively, an oxygen atom or a hydrogen atom. The constant c_{ij} is chosen to enforce the minimum of the Mie potential at a value of $-\varepsilon_{ij}$. Depending on the choice of repulsive (n_{ij}) or dispersive m_{ij} exponent the constant is defined as

$$c_{ij} = \frac{n_{ij}}{n_{ij} - m_{ij}}\left(\frac{n_{ij}}{m_{ij}}\right)^{\frac{m_{ij}}{n_{ij}-m_{ij}}} \tag{4.2}$$

Throughout this work the dispersive exponent was set to $m_{ij} = 6$. The repulsive exponent was earlier optimized to $n_{ii} = 14$ for both, aliphatic CH_2 groups and for CH_3 groups [229]. For oxygen, we here set the repulsive exponent to $n_{ii} = 12$. Note that the hydrogen atom interacts exclusively through the Coulombic term as it is schematically shown in figure 4.1. Parameters for unlike interaction sites are determined using the Lorentz-Berthelot combining rules [405, 406] for σ_{ij} and ε_{ij} and using an arithmetic mean for n_{ij} [397],

$$\sigma_{ij} = (\sigma_{ii} + \sigma_{jj})/2 \tag{4.3}$$

$$\varepsilon_{ij} = \sqrt{\varepsilon_{ii}\varepsilon_{jj}} \tag{4.4}$$

$$n_{ij} = (n_{ii} + n_{jj})/2 \tag{4.5}$$

Alternatively equation 4.1 can be expressed as

$$u_{ij}^{\text{inter}} = A(\sigma_{ij}, \varepsilon_{ij}, n_{ij})h(r_{ij}) + C(\sigma_{ij}, \varepsilon_{ij}, m_{ij})g(r_{ij}) + \frac{q_i q_j}{4\pi\epsilon_0} f(r_{ij}) \tag{4.6}$$

where $h(r_{ij}) = r_{ij}^{-n_{ij}}$, $g(r_{ij}) = -r_{ij}^{-m_{ij}}$, and $f(r_{ij}) = r_{ij}^{-1}$. The latter form of the interaction potential energy is particularly convenient if used in the context of tabulated potentials.

4.2.3 Optimization of Force Field Parameters

The two parameters ϵ_{ii} and σ_{ii} defining the Mie potential of equation (4.1) are here defined as effective pair potentials. These parameters should effectively correct for the simplicity of the chosen molecular model (where the functional form of equation (4.1) is prescribed and omitting higher-body interactions as well as static polarizability). The parameters ϵ_{ii} and σ_{ii} are therefore commonly adjusted to experimental data. For 1-propanol, we adopt the parameterization of the TAMie force field [229] for the Mie-sites of the CH_2 group (labeled C2 in figure 4.1) and for the CH_3 group. The remaining force field parameters are ϵ_{ii}, σ_{ii}, and q_i for the hydrogen atom (label H1), the oxygen atom (label O2), and the CH_2 group (label C1) neighboring the alcohol-oxygen. In order to reduce the number of degrees of freedom for optimizing force field parameters, we introduced two definitions: first, the hydrogen atom is represented by a point charge only. The Mie potential of the hydrogen atom is zero, by defining $\epsilon_{\mathrm{H,H}} = 0$. Secondly, the ratio of the point charge on the alcohol-oxygen to the charge on the alcohol-hydrogen is set to $q_{\mathrm{O}}/q_{\mathrm{H}} = -1.609$. The value is adopted from the OPLS force field [377–381]. The force field, as displayed in figure 4.1, has three point charges. Defining the ratio $q_{\mathrm{O}}/q_{\mathrm{H}}$ therefore also implicitly defines the ratio $q_{\mathrm{O}}/q_{\mathrm{CH_2}}$ for a molecule without net charge. Any value of q_{O} then uniquely determines q_{H} and $q_{\mathrm{CH_2}}$ so that the charges only contribute to a single degree of freedom.

Parameters $\sigma_{\mathrm{O,O}}$, $\sigma_{\mathrm{CH_2,CH_2}}$, $\epsilon_{\mathrm{O,O}}$, $\epsilon_{\mathrm{CH_2,CH_2}}$, and q_{O} are degrees of freedom for the optimization of the force field. The charge was varied along a grid of predefined values, $0.625 \leq -q_{\mathrm{O}} \leq 0.75$ in steps of 0.025. Parameters $\epsilon_{\mathrm{O,O}}$ and $\epsilon_{\mathrm{CH_2,CH_2}}$ are strongly correlated and we optimized one of them in an automated algorithm, as detailed below, while varying the other with fixed values of $\epsilon_{\mathrm{O,O}}/\epsilon_{\mathrm{CH_2,CH_2}} = 0.9$, 1.0, 1.1, etc. Similarly parameters $\sigma_{\mathrm{O,O}}$ and $\sigma_{\mathrm{CH_2,CH_2}}$ are highly correlated and we analyzed two fixed ratios between them $\sigma_{\mathrm{O,O}}/\sigma_{\mathrm{CH_2,CH_2}} = 0.79$ and 0.90, where the first value (0.79) was proposed for the OPLS force field [377–381].

The optimization of $\epsilon_{\mathrm{CH_2,CH_2}}$ was automized. We use the analytic PC-SAFT equation of state [313, 407] to approximate the results of molecular simulations, which allows to approximate the objective function for varying force field parameters. Force field parameters are mapped to molecular parameters defining the PC-SAFT model [408]. The force field optimization with PC-SAFT only takes milliseconds of wall-clock time. Because PC-SAFT can only approximate the true objective function, the procedure is iterative requiring molecular simulations for a new evaluation of the actual objective function. Convergence is achieved after few iterations. Hemmen and Gross slightly modified the iterative procedure and showed that the converged result of this method are not altered

by the analytic equation of state, i.e. the method converges to minimum of the actual objective function [229].
The force field optimization minimizes the objective function

$$f(\mathbf{p}) = \frac{1}{N^{\mathrm{exp}}} \sum_{n=1}^{N^{\mathrm{exp}}} \left(\frac{\Omega_n^{\mathrm{sim}}(\mathbf{p}) - \Omega_n^{\mathrm{exp}}}{\Omega_n^{\mathrm{exp}}} \right)^2 \tag{4.7}$$

with Ω_n^{sim} and Ω_n^{exp} as simulated and experimental observables, respectively, and with N^{exp} as the number of considered experimental data. Liquid density and vapor pressure are used as observables, $\Omega \in \left\{\rho^L, p^{\mathrm{sat}}\right\}$, with equal weight between them.

4.3 Computational Details

4.3.1 Monte Carlo Simulations

Monte Carlo simulations were performed in the grand canonical ensemble (GCMC) in order to determine coexisting liquid densities and vapor pressures. The vapor-liquid phase equilibrium properties are determined using histogram reweighting in a post-processing step [409, 410]. In GCMC simulations the temperature T, volume V, and chemical potential μ are defined, whereas the number of molecules fluctuates. We divide the N-space into windows and trivially reject molecule insertions or removals outside the assigned range of N-values in the considered window. The $\{T,\ \mu\}$-conditions for each window is chosen to approximately trace the vapor-liquid phase envelope, i.e. from vapor phase conditions, via a condition close to the expected critical point towards liquid phase conditions. We determine the $\{T,\ \mu\}$-conditions using the analytic PC-SAFT equation of state [230, 313]. A transition matrix sampling scheme [9, 10, 45, 411] is applied to determine a bias potential on the fly, ensuring an approximately equal sampling of N within each window. The simulations of all windows run independent from one another (in parallel) and only require an N-overlap between two neighboring windows. Say, a first window is defined for the N-range from 0 and 10, then the second window samples between $N = 10$ and 20. Using the multiple ensemble technique [412] these windows can be combined to a total histogram with well-sampled conditions close to the vapor-liquid phase envelope. A detailed description of the simulation techniques can be found in previous works [229, 230].
The volume of the simulation box was $40\,000\,\text{Å}^3$, corresponding to about 330 molecules for the highest densities. The probabilities for various Monte Carlo moves were defined as: molecule insertion/deletion 40 %, translation and rotation 50 %, and particle reconfiguration (regrowth) 10 %. The statistics of molecule insertion, deletion and reconfiguration is improved by using a configurational biasing scheme [7, 413] with low number of configura-

tional bias steps, $n^{\mathrm{CBMC}} = 1$, at low densities and $n^{\mathrm{CBMC}} = 8$ at high densities. The cut-off radius is set to $R_c = 14\,\text{Å}$ applying analytic tail corrections. The standard Ewald summation is used for the coulombic point charges, using a damping parameter $\alpha = 0.79/L$ and the maximum number of k-vectors set to $k_{\max} = 9$ in each direction. We conducted GCMC simulations for N-windows of width $\Delta N = 10$ at low densities and $\Delta N = 5$ for high densities. The simulation boxes are initially populated with molecules (with N as the upper bound of the N-window) allowing only trial insertion moves and translation and rotation moves. Subsequently, 6 million trial moves are conducted for equilibrating the system. Sampling thermodynamic properties is done in 30 million production steps.

4.3.2 Molecular Dynamics Simulations

All MD simulations were performed under minimum image periodic boundary conditions based on cubic computational boxes using the GROMACS 5.1.4 program package [108, 261, 263] with tabulated potentials [414] compiled in single precision. The equations of motion were integrated using the leap frog scheme [265] with a time step of 2 fs. Short-range electrostatic and Mie interactions were evaluated up to a cut-off radius r_c. Because GROMACS does not handle analytical tail corrections for interaction potentials with mixed repulsive exponents a relatively large value of $r_c = 2.9\,\text{nm}$ was chosen. This choice was based on a comparison of the liquid density of 1-propanol at 298.15 K calculated with $r_c = 2.9\,\text{nm}$ and no tail correction to the density obtained with $r_c = 1.4\,\text{nm}$ and the appropriate tail correction as implemented in the DL-POLY code [415]. Both density values agreed within 0.05 %. An additional comparison showed that self-diffusion coefficients for $r_c = 2.9\,\text{nm}$ are reaching an r_c-independent value. In the present work the GROMACS program package was selected due to availability of extensive analysis tools. Long-range electrostatics were treated by the smooth particle-mesh Ewald (PME) summation [273, 274] with a PME-order of 4. All bond lengths were kept fixed using LINCS [267, 268] with an order of 4. The number of iterations to correct for rotational lengthening in LINCS was set to 6. The temperature was maintained close to its reference value by application of the velocity-rescale thermostat [269], with a relaxation time of $\tau_T = 2.0\,\text{ps}$. The pressure was kept close to its reference value of 1.0 bar using weak coupling [416] with a relaxation time of $\tau_p = 2.0\,\text{ps}$ and an isothermal compressibility of $\kappa_T = 8.43 \times 10^{-5}\,\text{bar}^{-1}$ [417]. For all systems an energy minimization, followed by a constant-volume simulation of 1 ns at the desired target temperature and a successive constant-pressure equilibration of 1 ns at the desired target temperature were conducted prior to the actual production simulation. The systems simulated in this work contain 1686 1-propanol molecules and were either simulated in the NpT-ensemble or in the NVT-ensemble at 273.15 K, 293.15 K, 323.15 K and 360.15 K using starting configurations and average box volumes from the NpT-ensemble production runs respectively, depending on the properties calculated.

4.3.3 Trajectory Analysis

4.3.3.1 Shear Viscosity

The shear viscosity η was determined from the Green-Kubo expression [337, 338]

$$\eta = \frac{V}{k_B T} \int_0^\infty \langle P_{\alpha\beta}(t) P_{\alpha\beta}(0) \rangle \, \mathrm{d}t \tag{4.8}$$

where $P_{\alpha\beta}(\alpha, \beta \in x, y, z)$ are the pressure tensor components. Six independent shear components $1/2\,(P_{xy} + P_{yx})$, $1/2\,(P_{yz} + P_{zy})$, $1/2\,(P_{xz} + P_{zx})$, $1/2\,(P_{xx} - P_{yy})$, $1/2\,(P_{yy} - P_{zz})$ and $1/2\,(P_{xx} - P_{zz})$ are used to improve the statistics of each simulation. The three terms including the diagonal pressure tensor entries (xx, yy and zz) are obtained by a 45° rotation of the pressure tensor around all axis [339]. Correlation integrals $\int_0^\infty \langle ... \rangle \, \mathrm{d}t$ are calculated by a convolution in Fourier-space, according to Wiener-Khintchine theorem [340, 341]. Trajectories for viscosity calculation were obtained from constant-volume simulations with 5 ns production and a 1 ns preceding equilibration time. The predetermined volume was obtained using the average density from a previous constant-pressure simulation at 1 bar and at the target temperature. The pressure tensor elements were stored in the energy trajectory every 10 fs. To reduce statistical noise in the running integral of equation 4.8, the viscosity calculation was averaged over a set of 100 independent simulations. Subsequently a double-exponential function $\eta_{\mathrm{fit}}(t)$ was fitted to the average of the time-dependent running integral $\langle \eta(t) \rangle$ with four fitting parameters, namely η_∞, α, τ_1 and τ_2

$$\frac{\eta_{\mathrm{fit}(t)}}{\eta_\infty} = \frac{\alpha\tau_1 \left(1 - e^{-t/\tau_1}\right) + (1-\alpha)\,\tau_2 \left(1 - e^{-t/\tau_2}\right)}{\alpha\tau_1 + (1-\alpha)\,\tau_2} \tag{4.9}$$

For larger times the residuals $\langle \eta(t_i) - \eta_{\mathrm{fit}}(t_i) \rangle$ of the objective function are very noisy and are thus damped by weighting to $1/t_i^b$ as described by Maginn et al [343]. In this case the parameter b results from a previous power law fit to the standard deviation $s(t)$ which is time dependent. The first 2 ps of every individual run are not included in the fitting process. The stationary plateau value of the double-exponential fit is defined as η_∞ and taken as zero shear rate viscosity η. The given errors equal the value of the time dependent standard deviation $s(t_{99})$ at the time t_{99} where the time dependent viscosity $\eta_{\mathrm{fit}}(t)$ equals 99% of the zero shear rate viscosity.

4.3.3.2 Self-Diffusion Coefficients

The self-diffusion coefficient D_{self}, was calculated from a constant-pressure simulation as the slope of a linear fit to the mean-square displacement of the molecules in the long-time limit using the Einstein relation [344, 345]

$$\lim_{t\to\infty} \left\langle (\mathbf{r_i}(\tau + t) - \mathbf{r_i}(\tau))^2 \right\rangle_{i,\tau} = 6D_{\text{self}}t + \text{const.} \tag{4.10}$$

where $\mathbf{r_i}$ is the current position of the center of mass of a molecule (following molecules across periodic boundaries) and $\langle ... \rangle_{i,\tau}$ denotes averaging over all molecules i and time origins τ. In this work, trajectory fragments of 5 ns were used for a least-squares fitting to obtain a series of 10 diffusion coefficients from which a mean value as well as the corresponding standard deviation was calculated. The correlation coefficients of the least-square fitting R^2 were at least 0.99 in all cases. Finite size effects were accounted for by extrapolating D_{self} to infinite box size using the linear relation between D_{self} and the inverse box length with the slope calculated from the shear viscosity, as proposed by Yeh and Hummer [346]. In the results section of this work only corrected values are shown while the uncorrected self-diffusion coefficients are listed in the supplementary material.

4.3.3.3 Solvation Free Energy

The calculation of the self-solvation free energy ΔG_{solv} (or excess chemical potential) relied on a step-wise decoupling of one 1-propanol molecule from its surrounding using a scaling parameter λ, while retaining the intramolecular interactions. First, the electrostatic interactions were gradually deactivated uing 8 equispaced λ-points, followed by the deactivation of the Mie potential using 19 equispaced λ-points. The multistate Bennett acceptance ratio (MBAR) approach [277] was used as an estimator to obtain the free energy difference from the differences in the Hamiltonians between all states. The self-solvation free energy can be connected to the saturated vapor pressure using [418]

$$p^{\text{sat}} = p^o M_L \exp\left(\frac{\Delta G_{\text{solv}}}{\mathcal{R}T}\right) \tag{4.11}$$

where p^o is the pressure of an ideal gas at 1 molar concentration (24.788 bar at 298.15 K), M_L is the molarity of the pure liquid, $\mathcal{R}$ is the ideal gas constant and T the temperature. Assuming ideal gas behavior in the vapor phase this equation provides a convenient link between a quantity easily accessible from Monte Carlo simulations (p^{sat}) and a quantity easily accessible from molecular dynamics simulations (ΔG_{solv}). Especially if a direct comparison of the potential energy terms between different codes is ambiguous due to slightly different implementation details, equation 4.11 can be used for validation in addition to simple ensemble averages, such as liquid density in NpT-simulations.

4.4 Results and Discussion

4.4.1 Force Field Optimization

The objective function for the optimization of force field parameters was based on static properties, namely vapor pressure and liquid density according to equation (4.7), for temperatures ranging from $T/T^c = 0.58$ to 0.95, where T^c denotes the experimental critical temperature of 1-propanol. What motivated this study is the degeneracy of force field parameters. Even after eliminating some degrees of freedom, the remaining parameters $\sigma_{O,O}$, σ_{CH_2,CH_2}, $\epsilon_{O,O}$, ϵ_{CH_2,CH_2}, and q_O are correlated to an extent, that rather different parameter combinations can all lead to very good results for the objective function. The shallow optimum can be seen in figure 4.2 by varying $\sigma_{O,O}$ (and thus $\sigma_{CH_2,CH_2} = \sigma_{O,O}/0.79$) and regarding the ratio of two Mie energy parameters as $\epsilon_{O,O}/\epsilon_{CH_2,CH_2}$. Note that $\epsilon_{O,O}$ is optimized for each point shown in figure 4.2. The digram illustrates that almost the same absolute average deviations, with values well below 1%, can be obtained for varying values of $\sigma_{O,O}$. Values of $\epsilon_{O,O}$ and ϵ_{CH_2,CH_2} can thus compensate for varying $\sigma_{O,O}$-values, whereby ratios $\epsilon_{O,O}/\epsilon_{CH_2,CH_2}$ greater than unity are found for one parametrization, whereas values below unity are obtained for another parameterization. The observation in figure 4.2 also implies that variations in $\epsilon_{O,O}/\epsilon_{CH_2,CH_2}$ can in turn be compensated by parameter $\sigma_{O,O}$. For figure 4.3 we constrained the ratio $\epsilon_{O,O}/\epsilon_{CH_2,CH_2}$ to unity and varied q_O. The other parameters, $\sigma_{O,O}$, $\epsilon_{O,O}$ (and thus ϵ_{CH_2,CH_2}) were optimized for each point. We defined the size parameter of the CH_2-group neighboring the hydroxyl oxygen one time as $\sigma_{CH_2,CH_2} = \sigma_{O,O}/0.79$, as proposed in the OPLS force field, and another time as $\sigma_{CH_2,CH_2} = \sigma_{O,O}/0.90$. Figure 4.3 shows that an optimal partial charge can rather clearly be identified, for each of the two ratios $\sigma_{O,O}/\sigma_{CH_2,CH_2}$. Regarding the ratio $\sigma_{O,O}/\sigma_{CH_2,CH_2}$ the objective function, however, is shallow. For both values of this ratio one can find a suitable charge such that the objective function has values well below 1 %. The charge takes on rather different values, depending on the choice of $\sigma_{O,O}/\sigma_{CH_2,CH_2}$.

atom	set 1	set 2	set 3	set 4
H1	0.00000	0.00000	0.00000	0.00000
O1	0.30375	0.30250	0.32000	0.29500
C1	0.38450	0.38290	0.35560	0.37340
C2	0.40400	0.40400	0.40400	0.40400
C3	0.36034	0.36034	0.36034	0.36034

Table 4.1: Mie potential atom radius σ_i/nm for different parameter sets

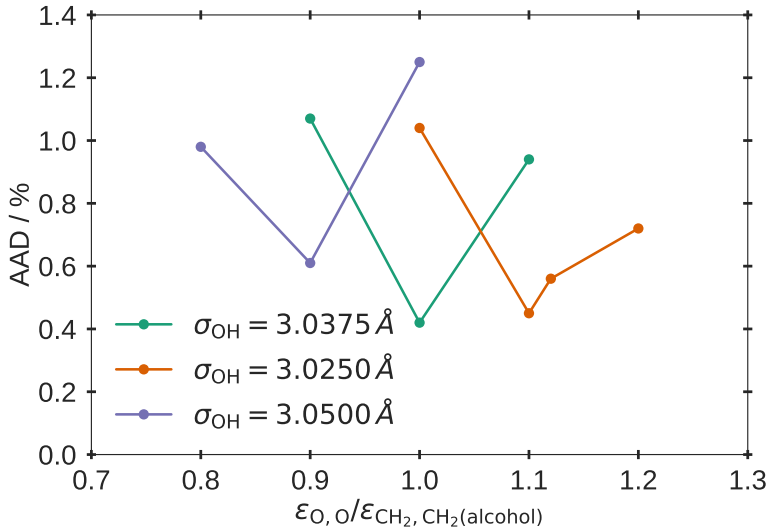

Figure 4.2: Absolute average deviation of molecular simulation results to quasi-experimental data for vapor pressure data and liquid density [419] for three values of $\sigma_{O,O}$ and therewith $\sigma_{CH_2,CH_2} = \sigma_{O,O}/0.79$.

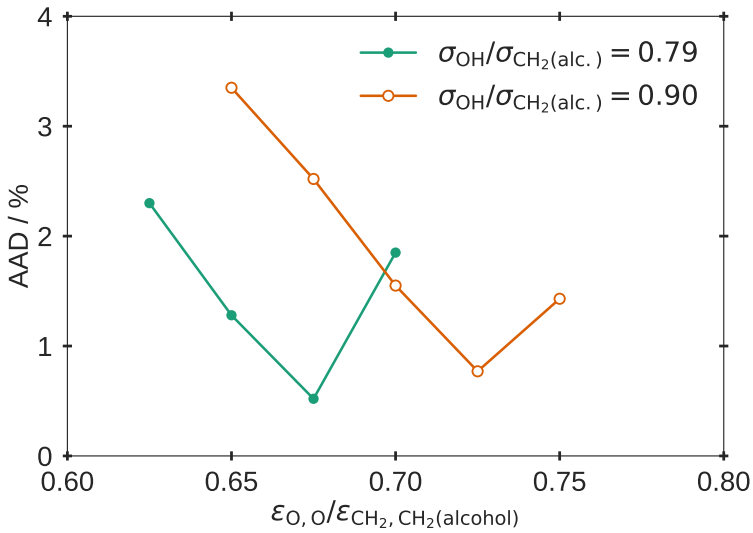

Figure 4.3: Absolute average deviation of molecular simulation results to quasi-experimental data for vapor pressure data and liquid density [419] for a fixed ratio of $\sigma_{O,O}/\sigma_{CH_2,CH_2} = 0.79$ (solid circles) and for $\sigma_{O,O}/\sigma_{CH_2,CH_2} = 0.90$ (open circles).

4.4.2 Force Field Assessment

In view of the shallow minimum of the objective function found in the previous section, we studied four parameter sets for dynamic properties. The underlying hypothesis was that transport properties might better discriminate between various force field parameterizations, that all lead to similar results for static properties. All four investigated parameterizations lead to average errors below 1% AAD in vapor pressure and liquid den-

atom	set 1	set 2	set 3	set 4
H1	0.00 (0.0000)	0.00 (0.0000)	0.00 (0.0000)	0.00 (0.0000)
O1	680.84 (81.8860)	714.38 (85.9200)	654.87 (78.7620)	843.89 (101.4970)
C1	680.84 (81.8860)	649.44 (78.1090)	654.87 (78.7620)	649.15 (78.0750)
C2	439.95 (52.9133)	439.95 (52.9133)	439.95 (52.9133)	439.95 (52.9133)
C3	1133.41(136.3180)	1133.41 (136.3180)	1133.41 (136.3180)	1133.41 (136.3180)

Table 4.2: Mie potential depth $\epsilon_i/\mathrm{J\,mol^{-1}}$ for different parameter sets, values in brackets are in the unit of K.

atom	set 1	set 2	set 3	set 4
H1	0.419	0.419	0.451	0.404
O1	-0.675	-0.675	-0.725	-0.650
C1	0.256	0.256	0.274	0.246
C2	0.000	0.000	0.000	0.000
C3	0.000	0.000	0.000	0.000

Table 4.3: Partial charges q_i (given as factors of unit electron charge) for different parameter sets

sity data in the temperature range covered in the parameter optimization, see figure 4.4(a). The chosen parameter sets are given in tables 4.1, 4.2, and 4.3.

In previous diagrams it was observed that the selected static properties are not sufficiently sensitive to ratio $\epsilon_{\mathrm{O,O}}/\epsilon_{\mathrm{CH_2,CH_2}}$ (figure 4.2) or to ratio $\sigma_{\mathrm{O,O}}/\sigma_{\mathrm{CH_2,CH_2}}$ (figure 4.3). We selected two pairs of parameterizations where these ratios differ. Parameter set 1 and set 2 have different ratios $\epsilon_{\mathrm{O,O}}/\epsilon_{\mathrm{CH_2,CH_2}}$, whereas set 1 and set 3 differ in $\sigma_{\mathrm{O,O}}/\sigma_{\mathrm{CH_2,CH_2}}$. Parameter set 1 and 3 correspond to the two points with lowest AAD-values in figure 4.3. Because parameter sets 1 and 2 were selected with same charge, we chose another pair, namely set 1 and set 4, with more difference in ratio $\epsilon_{\mathrm{O,O}}/\epsilon_{\mathrm{CH_2,CH_2}}$ leading also to different charges.

These parameterizations are in the following analyzed for transport properties and for extrapolations to liquid densities at temperature below the range covered by the training data (in equation (4.7)).

4.4.2.1 Liquid Density

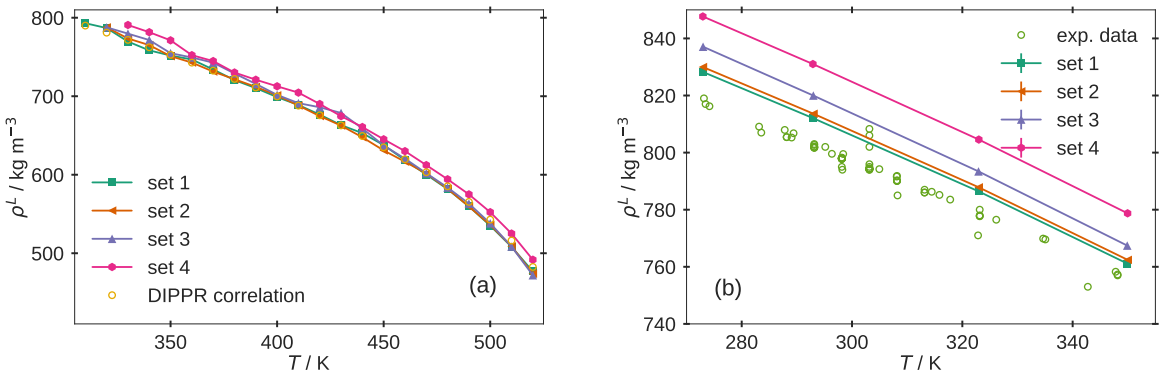

Figure 4.4: Liquid density ρ^{L} as function of temperature T for two different temperature ranges. (a) ρ^{L} at VLE conditions obtained from GCMC simulations. Experimental data are represented by the DIPPR correlation [419]. (b) ρ^{L} obtained from MD simulations at 1 bar. Experimental data are from various sources [420–450]. Error bars are within line-width and equal one standard deviation.

Figure 4.4 shows the liquid density ρ^{L} of all four parameter sets. In subfigure 4.4b, we compare simulated densities to experimental values below 350.15 K, i.e. at temperatures below the temperature range covered during parameter optimization. The results at lower temperature were obtained from MD simulations. We note that GCMC simulations, shown in figure 4.4a, lead to accurate values for vapor pressure, whereas liquid density data is obtained with substantial uncertainty. The low temperatures reveal differences in parameter set 4 from the other three sets, with much weaker agreement to experimental data. Sets 1 and 2 are in equal agreement with experiment while set 3 shows somewhat too large densities.

4.4.2.2 Shear Viscosity

Figure 4.5 shows simulated and experimental [451–490] shear viscosities η in the temperature range from 273.15 K to 350.15 K. All four parameter sets underestimate the shear viscosity while parameter set 1 and 2 are not distinguishable and show the lowest deviation to experiments. Set 3 has the highest deviations to experimental data and underestimates viscosity by about 50 % at lower temperatures. These results show that parameter sets leading to comparable densities can lead to very different behaviors in dynamic properties. Furthermore it is possible that parameter sets with comparable dynamic properties lead to different liquid densities, as shown in figure 4.4(b). Regarding quantitative agreement with experimental data we note that beside non-optimal nonbonded Mie parameters and partial atomic charges also degrees of freedom that are not accounted for in the present model (hydrogen atoms in aliphatic groups and bond vibrations) might have an influence. For water it was shown that fully flexible models cover the temperature dependence of the viscosity better compared to rigid models [491, 492], while for alkanes improvements could be achieved by an explicit description of hydrogen atoms [493].

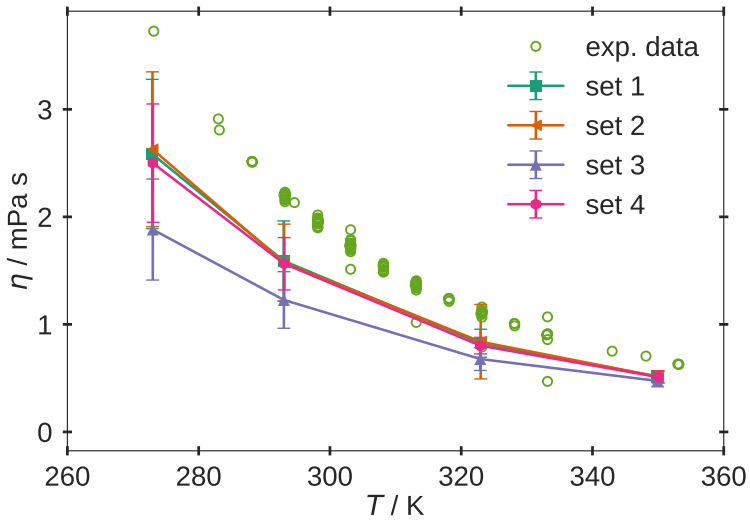

Figure 4.5: Shear viscosity η as function of temperature T. Error bars equal a confidence interval of 99 %.

4.4.2.3 Self-Diffusion Coefficient

Figure 4.6 shows simulated and experimental [363, 451, 494–498] self-diffusion coefficient D_{self} in the temperature range from 273.15 K to 350.15 K. Consistent with the underestimation of the shear viscosity the self diffusion coefficient D_{self} is overestimated by all force fields with set 1 and 2 being closest to the experimental data. The self-diffusion coefficient is known to be rather sensitive to small changes in the distribution of atomic partial charges [499]. It is therefore not surprising that set 3 shows a larger deviation from sets 1 and 2 than set 4 because the partial charges of set 4 are closer to those from set 1 and 2.

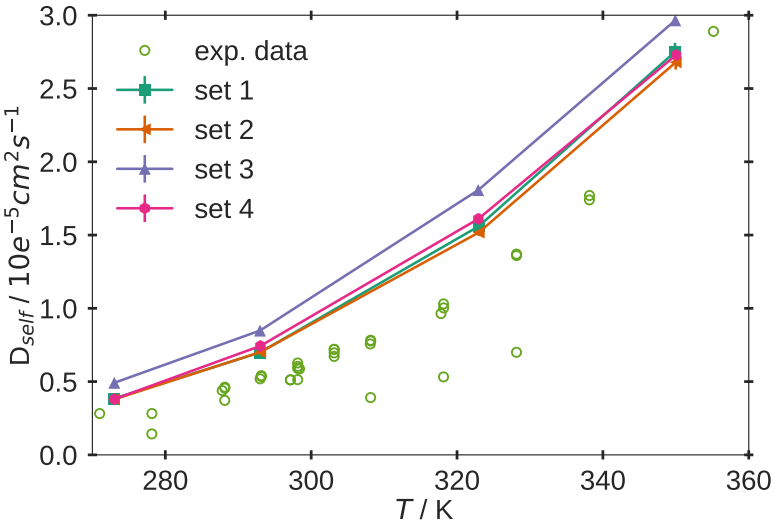

Figure 4.6: Coefficient of self-diffusion D_{self} as function of temperature T. Error bars are within symbol size.

4.4.2.4 Solvation Free Energy

The free energies of self-solvation are reported in table 4.4. The small differences they show are becoming more significant when translated to saturation vapor pressures via equation 4.11. Here set 1 shows the best agreement with experiment while set 4 has the highest deviation. As shown in figure 4.7 the Monte Carlos results for set 1 approach the molecular dynamic results showing compatibility between the two simulation methods. Note that precise values of p^{sat} need a very high accuracy in ΔG_{solv}. For this reason we do not recommend to optimize force fields based on p^{sat} determined from ΔG_{solv} values.

	ΔG_{solv}/kJ mol^{-1}	p^{sat}/mbar
exp. data	-23.22 ± 0.23	28.307 (27.897 $^{+}$)
set 1	-23.38 ± 0.11	26.662
set 2	-23.57 ± 0.11	24.770
set 3	-23.68 ± 0.10	23.869
set 4	-23.97 ± 0.30	21.790

Table 4.4: Solvation free energy of solvation and saturation vapor pressure at 298.15 K for four different parameter set. Vapour pressures are calculated from solvation free energies according to equation 4.11. Experimental data are taken from [372]. Errors of simulation results equal one standard deviation. $^{+}$: Saturation vapor pressure interpolated from DIPPR correlation [419].

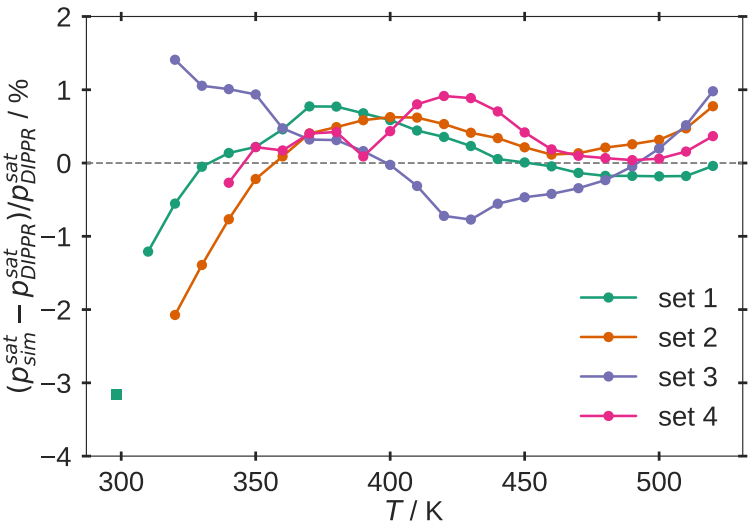

Figure 4.7: Deviation of calculated saturation vapor pressure from quasi-experimental data [419]. Dots represent MC simulation results while square is representing MD simulation results.

4.5 Conclusion

Parameters of classical force fields are known to be highly correlated for the description of static thermodynamic properties, such as vapor pressure and liquid densities. We investigate the hypothesis that transport properties, like shear viscosity or self diffusion coefficient, can be used to better decouple force field parameters. We adjusted force field parameters for 1-propanol, where united-atom sites are described through Mie potentials and point charges. Four models for were selected that gave about the same level of agreement with experimental liquid densities and vapor pressures. Shear viscosity and self-diffusion coefficients were evaluated with the aim to discriminate the models. However, the degeneracy of force field parameters observed in the static properties was also observed in the dynamic properties. We conclude that meaningful parameterizations for transferable force fields should simultaneously consider several molecules from a homologous series in order to define a less degenerate optimization problem. Within this optimization procedure it might be necessary to relax the fixed ratios of partial charges and σ, used in this work, as a degree of freedom.

Chapter 5

Transferable Anisotropic Mie-Potential Force Field for n-Alcohols: Static and Dynamic Fluid Properties of Pure Substances and Binary Mixtures

The content of this chapter is a literal quote of the publication
J. Baz, N. Hansen and J. Gross, Ind. Eng. Chem. Res, submitted September 24, 2019, published in a slightly modified form (vol. 59, pp. 919-929, 2020)

Abstract

This study extends the Transferable Anisotropic Mie potential (TAMie) to 1-alcohols. Force field parameters are adjusted by minimizing squared deviations of calculated vapor pressures and liquid densities from experimental data of 1-propanol, 1-butanol, and 1-pentanol. The force field leads to small average absolute deviations of 1 % in vapor pressures and 0.6 % in liquid densities for temperature ranges of $0.58 \leq T/T^C_{\text{exp}} \leq 0.96$, relative to experimental critical temperatures. The force field is transferable to higher 1-alcohols, as shown for 1-hexanol to 1-octanol. Individual parameter sets are provided for methanol and ethanol, respectively. Dynamic properties, such as shear viscosity and self-diffusion coefficients of pure substances are predicted with fair agreement to experimental data, considering that no dynamic property has entered the parameterization. Further, the phase behavior of binary mixtures of primary alcohols with alkanes is studied and predictions of the TAMie model are found in very good agreement to experimental data.

5.1 Introduction

Classical transferable force fields allow predicting thermodynamic properties of fluids in engineering applications. The challenge in force field parametrization is to find a good compromise between transferability of parameters and accuracy over a broad range of thermodynamic state points.

Structural and thermophysical properties of short chain alcohols have been studied when developing the optimized potential for liquid simulations (OPLS) force field, adjusting parameters to experimental enthalpies of vaporization and liquid density data near ambient conditions [377–382, 500]. With the advent of phase equilibrium calculations, a rich set of experimental data became accessible for force field optimization. Phase equilibria are of particular interest in chemical engineering applications, because they are the basis to separation processes and they determine reaction systems and safety aspects. A prominent force field for correlating and predicting vapor liquid equilibria is the transferable potential for phase equilibria (TraPPE) which is parameterized for many chemical groups including alcohols [48, 383, 385–388]. TraPPE employs the same functional form as OPLS, i.e. Lennard-Jones pair potentials plus fixed point charges as well as fixed bond lengths. Both force fields support all-atom and united-atom variants. A united-atom force field does not assign Lennard-Jones interaction sites for non-polar hydrogen atoms, but considers certain heavy atoms and their neighboring hydrogen atoms as a single Lennard-Jones interaction site. An aliphatic methyl group, CH_3, is a common example. TraPPE was developed with emphasis placed on liquid densities and bubble point temperatures. The model gives excellent results for T-ρ-projections with good results also for the critical temperature, but it has weaknesses in describing vapor pressures [229, 389]. The NERD force field is a united-atom model but includes bond stretching [501]. The homologous series of primary alcohols from ethanol to 1-octanol was described with transferable parameters based on an optimization carried out for 1-pentanol [502]. In contrast to TraPPE a separate set of parameters is used for methanol. The hydrogen atom of the hydroxyl group in the NERD force field carries Lennard-Jones parameters, in contrast to TraPPE, OPLS [380] and alcohol models from the groups of Vrabec and Hasse [503, 504].

With a united-atom model based on Lennard-Jones interactions, it is not possible to obtain both, a good description of phase equilibria in temperature projections as well as the vapor pressure [229, 384]. For good results for both projections, additional degrees of freedom were introduced to increase the number of adjustable parameters. For the Lennard-Jones potential the number of parameters per interaction site is two. The Buckingham potential uses three parameters per interaction site and leads to good agreement to experimental data [389]. Anisotropic models change the position of the interaction site of aliphatic compounds to account for the included hydrogen atoms [390–396]. The

distance, a united-atom interaction site is shifted from the position of the heavy atom is an additional degree of freedom and thus an adjustable parameter.
Mie potentials, where the repulsive exponent ($m = 12$ for Lennard Jones potentials) is treated as an adjustable parameter, were used by Potoff, Brunel and coworkers [397–400]. Their force-field gave excellent agreement to static properties of pure components. A model describing molecules as Mie interaction sites together with partial point charges combined with an anisotropic contribution was developed in our group. This Transferable Anisotropic Mie (TAMie) force field was parameterized using a well-defined objective function which considers vapor pressure and liquid density of different species simultaneously [229–232].
One of the main challenges when optimizing force field parameters is rigorously minimizing a suitably chosen objective function, which is demanding because force field parameters are highly correlated. Earlier studies concerning dimethyl ether [230, 376] have shown that the optimum in the considered objective function is shallow, i.e. the force-field parameters are correlated to an extent where they are almost degenerate. A preceding study to the present work analyses whether transport properties can be used to discriminate different sets of force field parameter that are all approximately equal concerning the objective function (based on static phase equilibrium properties) [505]. For 1-propanol we showed that the degeneracy in force field parameter seen for static properties, also persists for dynamic properties.
This study proposes transferable force field parameters for primary alcohols as an extension to the TAMie force field. The parameter optimization is performed by minimizing an objective function of squared deviations between vapor pressure data and coexisting liquid densities towards experimental values. Three substances are thereby simultaneously considered, namely 1-propanol, 1-butanol and 1-pentanol. The transferability of the force field is then assessed by applying the model to phase equilibrium properties for the homologous series of n-alcohols up to 1-octanol. Individualized force field parameters are proposed for methanol (MeOH) and for ethanol (EtOH). We evaluate dynamic properties for all substances and compare results to experimental data and to results from other force fields. Properties of binary mixtures containing n-alcohols together with alkanes are regarded to assess the predictive power of the proposed force field.

5.2 Force Field

This study is based on a united-atom model, where hydrogen atoms are not individually resolved as Lennard-Jones interaction sites, but are grouped with a neighboring larger atoms as an effective interaction site. For hydrogen atoms with pronounced partial charge, however, such as in a hydroxyl-group (-OH), the hydrogen may very well be considered

as an individual interaction site. Figure 5.1 gives a schematic representation of van der Waals (Mie) interaction sites and of the coulombic (fixed point charge) sites.

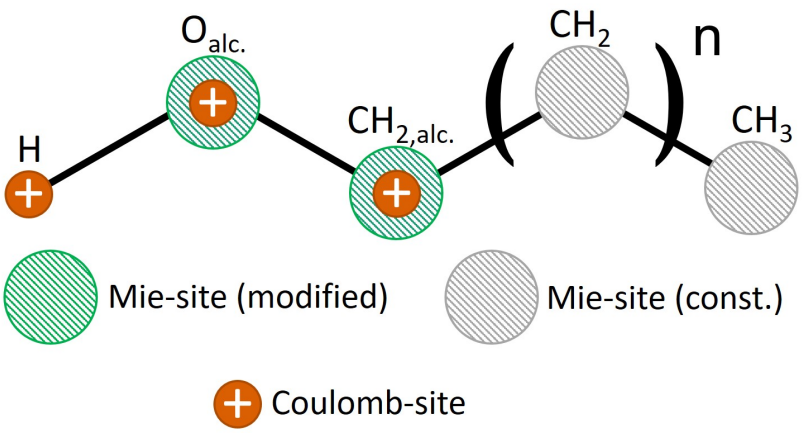

Figure 5.1: Molecular structure of n-alcohols, illustrating site names and schematic positioning of Mie sites and Coulombic sites. $n = 1$ equals the molecular structure of 1-propanol, while $n = 6$ describes 1-octanol. Sites with optimized force field parameters are colored green, whereas sites with parameters from literature are shown gray-shaded. Coulombic sites are included in the force field optimization.

5.2.1 Bonded Energy

The proposed force field uses fixed bond lengths between interaction sites and harmonic potentials for describing bond angle bending as described in tables 5.1 and 5.2. The parameters are based on quantum mechanical structure optimizations on the MP2 [401, 402] level of theory. The torsional potential is described by a cosine series as shown in table 5.3.

5.2.2 Nonbonded Energy

The TAMie force field is based on the Mie potential plus fixed Coulombic interactions to describe the nonbonded potential energy between two interaction sites i and j located on different molecules or located in the same molecule but separated by more than three bonds,

$$u_{ij}^{\text{inter}} = c_{ij}\varepsilon_{ij}\left[\left(\frac{\sigma_{ij}}{r_{ij}}\right)^{n_{ij}} - \left(\frac{\sigma_{ij}}{r_{ij}}\right)^{m_{ij}}\right] + \frac{q_i q_j}{4\pi\epsilon_0 r_{ij}} \tag{5.1}$$

where r_{ij} denotes the distance between the interaction sites, σ_{ij} and ε_{ij} are the size and energy parameter characterizing the Mie interaction, and q_i and ϵ_0 are the partial atomic charge, expressed as a (negative) factor of an electron charge, and the vacuum permittivity,

	i	j	bond length / nm
methanol	H	$O_{alc.}$	0.0970
	$O_{alc.}$	$CH_{3,alc.}$	0.1620
ethanol	H	$O_{alc.}$	0.0970
	$O_{alc.}$	$CH_{2,alc.}$	0.1420
	$CH_{2,alc.}$	CH_3	0.1714
other n-alcohols	H	$O_{alc.}$	0.0945
	$O_{alc.}$	$CH_{2,alc.}$	0.1420
	$CH_{2,alc.}$	CH_2	0.1514
	CH_2	CH_2	0.1540
	CH_2	CH_3	0.1714

Table 5.1: Bond lengths between atoms i and j.

	i	j	k	bond angle θ^0_{ijk} / °	force constant k^θ_{ijk} / kJ/mol/rad^2
methanol	H	$O_{alc.}$	$CH_{3,alc.}$	107.40	382.13268
ethanol	H	$O_{alc.}$	$CH_{2,alc.}$	107.40	382.13268
	$O_{alc.}$	$CH_{2,alc.}$	CH_3	113.50	517.57527
other n-alcohols	H	$O_{alc.}$	$CH_{2,alc.}$	107.40	382.13268
	$O_{alc.}$	$CH_{2,alc.}$	CH_2	113.50	517.57527
	$CH_{2,alc.}$	CH_2	CH_3	114.00	519.65388
	CH_2	CH_2	CH_3	114.00	519.65388

Table 5.2: Equilibrium bending angles θ^0_{ijk} and force constants k^θ_{ijk} between atoms i, j and k used to describe the angle bending potential according to $U_{\text{bend}}(\theta_{ijk}) = \frac{1}{2}k^\theta_{ijk}\left(\theta_{ijk} - \theta^0_{ijk}\right)^2$.

respectively. In the present work an interaction site i can represent a united-atom group such as an aliphatic CH_2 or CH_3 group, respectively, an oxygen atom or a hydrogen atom. By defining the constant c_{ij} as

$$c_{ij} = \frac{n_{ij}}{n_{ij} - m_{ij}} \left(\frac{n_{ij}}{m_{ij}}\right)^{\frac{m_{ij}}{n_{ij}-m_{ij}}} \tag{5.2}$$

the minimum of the Mie potential is enforced at a value of $-\epsilon_{ij}$. In accordance to previous work [505] the attractive exponent was set to $m_{ij} = 6$ for all interaction sites carrying Mie parameters while the repulsive exponent was set to $n_{ii} = 14$ for the aliphatic CH_2, the alcoholic $CH_{2,\,alc.}$ and the CH_3 groups and $n_{ii} = 12$ for oxygen. Parameters for unlike interaction sites were determined using the Lorentz-Berthelot combining rules [405, 406] for σ_{ij} and ϵ_{ij} and using an arithmetic mean for n_{ij} [397] according to

i	j	k	l	ϕ_s / °	force constant $k_{\phi,C(i)}$ / kJ mol^{-1}	n
H	$O_{alc.}$	$CH_{2,alc.}$	CH_x	0.00	-1.53809	0
H	$O_{alc.}$	$CH_{2,alc.}$	CH_x	0.00	0.68179	1
H	$O_{alc.}$	$CH_{2,alc.}$	CH_x	180.00	0.30672	2
H	$O_{alc.}$	$CH_{2,alc.}$	CH_x	0.00	2.52635	3
$O_{alc.}$	$CH_{2,alc.}$	CH_2	CH_x	0.00	0.00000	0
$O_{alc.}$	$CH_{2,alc.}$	CH_2	CH_x	0.00	1.71652	1
$O_{alc.}$	$CH_{2,alc.}$	CH_2	CH_x	180.00	-1.85047	2
$O_{alc.}$	$CH_{2,alc.}$	CH_2	CH_x	0.0	9.02186	3
$CH_{2,alc.}$	CH_2	CH_2	CH_x	0.00	0.00000	0
$CH_{2,alc.}$	CH_2	CH_2	CH_x	0.00	1.71652	1
$CH_{2,alc.}$	CH_2	CH_2	CH_x	180.00	-1.85047	2
$CH_{2,alc.}$	CH_2	CH_2	CH_x	0.0	9.02186	3

Table 5.3: Phase shift ϕ_s, force constant $k_{\phi,C(i)}$ and multiplicities n used to describe the torsional potential energy between atoms i, j, k and l according to $U_{\text{torsion}}(\phi_{ijkl}) = \sum_{C(i)} k_{\phi,C(i)} (1 + \cos(n\phi - \phi_s))$. Index x is a generic symbol which can be 2 for CH_2 or 3 for CH_3-groups.

$$\sigma_{ij} = (\sigma_{ii} + \sigma_{jj})/2 \tag{5.3}$$

$$\varepsilon_{ij} = \sqrt{\varepsilon_{ii}\varepsilon_{jj}} \tag{5.4}$$

$$n_{ij} = (n_{ii} + n_{jj})/2 \tag{5.5}$$

The cut-off radius for the Mie potential is defined as $r_c = 1.4\,\text{nm}$ and we apply analytic tail corrections.

5.2.3 Optimization of Force Field Parameters

The TAMie force field is parameterized by minimizing a well-defined objective function. The objective function is defined as squared deviations in calculated vapor pressure and liquid densities to experimental data, according to

$$f(\mathbf{p}) = \frac{1}{N^{\text{exp}}} \sum_{n=1}^{N^{\text{exp}}} \left(\frac{\Omega_n^{\text{sim}}(\mathbf{p}) - \Omega_n^{\text{exp}}}{\Omega_n^{\text{exp}}} \right)^2 \tag{5.6}$$

with Ω_n^{sim} and Ω_n^{exp} as simulated and experimental properties, respectively, and N^{exp} as the overall number of experimental data points. Liquid densities and vapor pressures are considered as properties in the objective function, $\Omega \in \left\{\rho^{\text{L}}, p^{\text{sat}}\right\}$, with equal weight between them. Several substances are simultaneously considered in the objective function,

namely 1-propanol, 1-butanol, and 1-pentanol, covering a temperature range of $0.58 \leq T/T^c_{\text{exp}} \leq 0.96$ in ΔT-increments of 10 K, where T^c_{exp} denotes the experimental critical temperature. Capturing several substances simultaneously in the optimization procedure, ensures a balanced compromise in the resulting force field parameters.

The united-atom fixed point-charge model using a Mie potential has several degrees of freedom: Mie parameters of the hydroxyl-hydrogen (ϵ_{ii}, σ_{ii}, n_{ii} for i = H(alc.)), of the hydroxyl-oxygen (ϵ_{ii}, σ_{ii}, n_{ii} for i = O(alc.)), and of the CH_2-group neighboring the hydroxyl-group (ϵ_{ii}, σ_{ii}, n_{ii} for $i = CH_2$(alc.)). We assume the hydroxyl-group does not affect the (effective pair-wise) van der Waals potential of the CH_2 or CH_3 groups beyond the first, neighboring CH_2 group. Further, 1-alcohols are here defined through 3 point charges, two of which are degrees of freedom (q_i for i = H(alc.) and for i = O(alc.), whereas the last charge (q_i for $i = CH_2$(alc.)) is obtained from enforcing charge neutrality.

In order to avoid too highly correlated parameters (and too high dimensionality of the optimization problem), we eliminated some of these degrees of freedom through the following definitions: We defined $\epsilon_{ii} = 0$ for the hydroxyl-hydrogen (i = H(alc.)), as earlier proposed for other united-atom force fields [48, 377, 506]. That makes parameters σ_{ii} and n_{ii} of the same Mie group obsolete and leads to the hydrogen atom defined only through a positive fixed point charge. Further, we defined $\epsilon_{\text{O,O}}/\epsilon_{\text{CH}_2\text{CH}_2} = 1$, i.e. the hydroxyl-oxygen and the CH_2-group neighboring the hydroxyl-group are assigned the same Mie energy parameter. The ratio of Mie-size parameters is $\sigma_{\text{OO}}/\sigma_{\text{CH}_2\text{CH}_2} = 0.79$ as suggested for the OPLS-UA force field for ethanol [377–381]. For the hydroxyl-oxygen we define $n_{\text{OO}} = 12$. In an initial study we have used other values than 12 for the repulsive exponent of this group and found no significant advantage. Lastly, the ratio of charges between the hydroxyl-oxygen and the hydroxyl-hydrogen is defined as $q_{\text{O}}/q_{\text{H}} = -1.609$ following OPLS-UA force field for ethanol.

These definitions leave three degrees of freedom for the parameter optimization: ϵ_{ii} and σ_{ii}, q_i of the hydroxyl-oxygen i = O(alc.). The two definitions (described in the preceding paragraph), we felt most uncertain about, were the defined ratio $\epsilon_{\text{OO}}/\epsilon_{\text{CH}_2,\text{CH}_2} = 1$ and the ratio $\sigma_{\text{OO}}/\sigma_{\text{CH}_2,\text{CH}_2} = 0.79$. In our earlier work regarding only 1-propanol [505], we had varied both of these ratios and observed that after optimizing all other degrees of freedom, the results were very close to the obtained results with the original ratios. The similar results were found for the objective function as well as for predictions of transport properties that were not used in the objective function [505].

Parameter ϵ_{ii} of the hydroxyl-oxygen i = O(alc.) was optimized using the analytic PC-SAFT equation of state [313, 407], whereas parameter σ_{ii} and q_i of the hydroxyl-oxygen i = O(alc.) were varied along a grid of predefined values. The PC-SAFT model approximates the objective function analytically and leads to swift convergence along the ϵ_{ii}-parameter [229, 408]. The PC-SAFT model is only approximate, which is why the procedure is

iterative. At converged conditions, however, the approximate nature of the analytic model does not alter the objective function so that the problem converges to the true minimum [229].

Methanol has no CH_2(alc.)-group, like all other 1-alcohols. Methanol is parametrized individually in this work and we adjusted the Mie parameters of the hydroxyl oxygen as well as the negative partial charge on the oxygen, q_O. Mie parameters of the methyl-group were taken from alkanes and the ratio of positive partial charge on the hydroxyl-hydrogen to the charge on the oxygen, q_H/q_O, was taken from the OPLS force field. The methyl-group carries the remaining charge-neutralizing positive partial charge.

	#	atom	σ_{ii},set 1-prop. / nm	σ_{ii},TAMie / nm	ϵ_{ii},set 1-prop. / J mol^{-1}	ϵ_{ii},TAMie / J mol^{-1}	q_i set 1-prop.	q_i TAMie	n_{ii}
MeOH	1	H_{MeOH}	-	0.00000	-	0.00 (0.00)	-	0.413	-
	2	O_{MeOH}	-	0.30850	-	814.89 (98.01)	-	-0.664	12
	3*	$CH_{3,MeOH}$	-	0.36034	-	1133.41(136.318)	-	0.251	14
EtOH	1	H_{EtOH}	-	0.00000	-	0.00 (0.00)	-	0.413	-
	2	O_{EtOH}	-	0.30800	-	631.95 (77.06)	-	-0.664	12
	3	$CH_{2,EtOH}$	-	0.38990	-	631.95 (77.06)	-	0.251	14
	4*	CH_3	-	0.36034	-	1133.41(136.318)	-	0.000	14
alcohols	1	$H_{alc.}$	0.00000	0.00000	0.00 (0.000)	0.00 (0.000)	0.419	0.404	-
	2	$O_{alc.}$	0.30375	0.30350	680.84 (81.886)	700.33 (84.230)	-0.675	-0.650	12
	3	$CH_{2,alc.}$	0.38450	0.38420	680.84 (81.886)	700.33 (84.230)	0.256	0.246	14
	4*	CH_2	0.40400	0.40400	439.95 (52.9133)	439.95 (52.9133)	0.000	0.000	14
	5*	CH_3	0.36034	0.36034	1133.41(136.318)	1133.41 (136.318)	0.000	0.000	14

* The Mie parameters of these united-atom sites are taken from n-alkanes and thus are no degrees of freedom.

Table 5.4: Mie potential parameters σ_{ii}, ϵ_{ii}, n_{ii} as well as partial charges q_i for different parameter sets. Label 'set 1-prop.' indicates a parameter set that was obtained in a preceding study where the parameters were only adjusted to 1-propanol[505]. Label 'TAMie' describes the TAMie force field, optimized for three different 1-alcohols simultaneously. Values given in brackets are energy parameters in the unit Kelvin.

5.3 Simulation Details

5.3.1 Monte Carlo Simulations

Phase equilibrium properties were determined from Monte Carlo simulations in the grand canonical ensemble (GCMC) using the histogram reweighting technique [409, 410]. In GCMC simulations the chemical potential μ, temperature T, and volume V are defined quantities, whereas the system energy and the number of molecules N fluctuate. For pure substances, we use a fixed value of V and define twelve value-pairs $\{\mu,\ T\}$ for conditions that approximately trace the phase envelope, from vapor conditions, via a condition close to the critical point, to liquid-phase conditions [230]. The $\{\mu,\ T\}$-pairs are determined from the analytic PC-SAFT equation of state [313]. For this simulation approach it is sufficient to have good estimates for $\{\mu,\ T\}$-pairs along the actual phase coexisting conditions, because the chemical potential and temperature are varied in histogram reweighting in a post-processing step to find the phase equilibrium points of the considered force-field.

We divide the N-space into windows of $\Delta N = 10$ at low and moderate densities, and use $\Delta N = 5$ at high density conditions. A GCMC-simulation is assigned to any of the N-windows, and they can all run independent of one another in parallel[230]. If we consider a simulation, say the GCMC-simulation assigned to the N-window $200 \leq N \leq 210$, then any MC trial-move for inserting a molecule at $N = 210$ or trial-move for deleting a molecule at $N = 200$ will trivially be rejected [230, 507]. Further, within each window we ensure even sampling of N-space by using transition-matrix sampling [9, 10, 45, 411], building a bias-potential on the fly. All windows can be combined using the multiple ensemble technique [412] for the post-processing histogram reweighting step. A detailed description of the simulation technique is given in previous works [229, 230].
Simulations were conducted with volume $30\,\mathrm{nm}^3$ for methanol, $40\,\mathrm{nm}^3$ for ethanol, propanol, and 1-butanol, $50\,\mathrm{nm}^3$ for 1-pentanol and 1-hexanol, $80\,\mathrm{nm}^3$ for 1-heptanol and 1-octanol. For pure substances we used the following Monte Carlo trial moves: translation and rotation 50 %, molecule insertion/deletion 40 %, and particle reconfiguration (regrowth) 10 %. We apply the configurational biasing technique [7, 413] to increase the probabilities of molecular insertion, deletion, and reconfiguration trial moves. The number of configurational bias steps is defined as $n^{\mathrm{CBMC}} = 1$ for low densities, up to $n^{\mathrm{CBMC}} = 8$ for high densities. The regular Ewald summation is applied for the Coulombic point charges, with a damping parameter $\alpha = 0.79/L$ and with the maximum number of k-vectors set to $k_{\max} = 9$ in all directions. We conducted GCMC simulations for N-windows of width $\Delta N = 10$ at low densities and $\Delta N = 5$ for high densities. The simulation boxes are initially populated with molecules (with N as the upper bound of the N-window) allowing only trial insertion moves and translation and rotation moves. Subsequently, 8 million trial moves are conducted for equilibrating the system. Sampling thermodynamic properties is done in 50 million production steps.
Because the hydrogen-atom is represented as a charge without a 'protecting' Mie potential, one has to take measures to prevent unphysical configurations close to a charge catastrophe. Such configurations can occur (mainly in Monte-Carlo simulations) when a hydroxyl-oxygen is placed in very close vicinity to a hydroxyl-hydrogen. The oxygen-oxygen Mie potential is for a very close approach of the charges not sufficiently repulsive, making artificial (and highly stable) configurations possible. We use a criterion on the Mie potential to avoid such configurations. When the Mie potential is more repulsive than $u_{ij}^{\mathrm{Mie}}/(k_B T) > 200$, we trivially reject the considered configuration. That is equivalent to a hard-sphere interaction between oxygen-sites, with a hard-sphere repulsion at about 0.196 nm for $T = 300\mathrm{K}$.

5.3.2 Molecular Dynamics Simulations

All MD simulations were performed under minimum image periodic boundary conditions based on cubic computational boxes using the GROMACS 2016 program package [108, 261–263, 333–336, 508] with tabulated potentials [414] compiled in single precision. Short-range electrostatic and Mie interactions were evaluated up to a cut-off radius r_c. Because GROMACS does not handle analytical tail corrections for interaction potentials with mixed repulsive exponents a relatively large value of $r_c = 2.9$ nm was chosen for MD simulations, as detailed in previous work [505]. Long-range electrostatic interactions were treated by the smooth particle-mesh Ewald (PME) summation [273, 274] with a PME order of 4. The equations of motion were integrated using the leap frog scheme [265] with a time step of 1 fs. All bond lengths were kept fixed using LINCS [267, 268] with an order of 4. The number of iterations to correct for rotational lengthening in LINCS was set to 6. The temperature was maintained close to its reference value using the velocity-rescale thermostat [269], with a relaxation time of $\tau_T = 2.0$ ps. The pressure was kept close to its reference value of 1 bar using weak coupling [416] with a relaxation time of $\tau_p = 2.0$ ps and an isothermal compressibility of $\kappa_T = 8.43 \times 10^{-5}\,\mathrm{bar}^{-1}$ [417]. For all systems an energy minimization, followed by a constant-volume simulation of 1 ns at the desired target temperature and a successive constant-pressure equilibration of 1 ns at the desired target temperature were conducted prior to the actual production simulation. The systems simulated in this work contain 1500 n-alcohol molecules and were either simulated in the NpT-ensemble or in the NVT-ensemble at different temperatures using starting configurations and average box volumes from the NpT-ensemble production runs at a simulation time of 8 ns, depending on the properties calculated.

5.3.3 Trajectory Analysis

5.3.3.1 Shear Viscosiy

The shear viscosity η was determined from the Green-Kubo expression [337, 338]

$$\eta = \frac{V}{k_B T} \int_0^\infty \langle P_{\alpha\beta}(t) P_{\alpha\beta}(0) \rangle \, \mathrm{d}t \tag{5.7}$$

where t is time and $P_{\alpha\beta}(\alpha, \beta \in x, y, z)$ are elements of the pressure tensor. Six independent shear components $1/2\,(P_{xy} + P_{yx})$, $1/2\,(P_{yz} + P_{zy})$, $1/2\,(P_{xz} + P_{yz})$, $1/2\,(P_{xx} - P_{yy})$, $1/2\,(P_{yy} - P_{zz})$ and $1/2\,(P_{xx} - P_{zz})$ are used to improve the statistics of each simulation. The three terms including the diagonal pressure tensor entries (xx, yy and zz) are obtained by a 45° rotation of the pressure tensor around all axis [339]. Correlation integrals $\int_0^\infty \langle ... \rangle \, \mathrm{d}t$ are calculated by a convolution in Fourier-space, according to Wiener-Khintchine theorem [340, 341]. Trajectories for viscosity calculation were obtained

from constant-volume simulations with 1 ns production and a 1 ns preceding equilibration time. The predetermined volume was obtained using the average density from a previous constant-pressure simulation at 1 bar and at the target temperature. The pressure tensor elements were stored in the energy trajectory every 10 fs. To reduce statistical noise in the running integral of equation 5.7, the viscosity calculation was averaged over a set of 100 independent simulations. Subsequently a double-exponential function $\eta_{\text{fit}}(t)$ was fitted to the average of the time-dependent running integral $\langle\eta(t)\rangle$ [343], as

$$\frac{\eta_{\text{fit}(t)}}{\eta_\infty} = \frac{\alpha\tau_1\left(1-e^{-t/\tau_1}\right)+(1-\alpha)\,\tau_2\left(1-e^{-t/\tau_2}\right)}{\alpha\tau_1+(1-\alpha)\,\tau_2} \tag{5.8}$$

with η_∞, α, τ_1 and τ_2 as adjustable parameters. For larger times the residuals $\langle\eta(t_i)-\eta_{\text{fit}}(t_i)\rangle$ of the target function are noisy and are thus assigned an increasingly low weight $1/t_i^b$ as proposed by Maginn et al [343]. Parameter b of the weighting function is obtained from a previous power-law fit to the standard deviation $s(t)$ which is time dependent. The first 2 ps of every individual run are not included in the fitting process, because the double-exponential function, equation (5.8), is only intended for the long-time correlation. The stationary plateau value of the double-exponential fit is defined as η_∞ and is interpreted as zero shear rate viscosity η. The given errors equal the value of the time dependent standard deviation $s(t_{99})$ at the time t_{99} where the time dependent viscosity $\eta_{\text{fit}}(t)$ equals 99% of the zero shear rate viscosity.

5.3.3.2 Self-Diffusion Coefficient

The self-diffusion coefficient D_{self}, was calculated from a constant-pressure simulation as the slope of a linear fit to the mean-square displacement of the molecules in the long-time limit using the Einstein relation [344, 345]

$$\lim_{t\to\infty}\left\langle(\mathbf{r_i}(\tau+t)-\mathbf{r_i}(\tau))^2\right\rangle_{i,\tau} = 6D_{\text{self}}t + \text{const.} \tag{5.9}$$

where $\mathbf{r_i}$ is the current position of the center of mass of a molecule (following molecules across periodic boundaries) and $\langle\ldots\rangle_{i,\tau}$ denotes averaging over all molecules i and time origins τ. In this work, trajectory fragments of 5 ns were used for a least-squares fitting to obtain a series of 10 diffusion coefficients from which a mean value as well as the corresponding standard deviation was calculated. The correlation coefficients of the least-square fitting R^2 were at least 0.99 in all cases. Finite size effects were accounted for by extrapolating D_{self} to infinite box size using the linear relation between D_{self} and the inverse box length with the slope calculated from the shear viscosity, as proposed by Yeh and Hummer [346]. In the results section of this work only corrected values are shown while the uncorrected self-diffusion coefficients are listed in the supplementary material.

5.4 Results and Discussion

This section presents results for vapor pressures p^{sat} and (coexisting) liquid densities ρ^{L} as static thermodynamic properties as well as shear viscosities η and self-diffusion coefficients D_{self} as dynamic properties of pure 1-alcohols. Results of MC and MD simulations are compared to experimental data. Further, results for binary mixtures of alcohols with alkanes are shown.

5.4.1 Static Pure Component Properties

Force field parameters for methanol and ethanol were individually optimized. The transferability of force field parameters to the lowest constituents of a homologous family is often rather poor. Individualized force fields of course lead to rather good agreement to experimental data of the objective function, which is desirable for methanol and ethanol because of their importance in engineering applications.

The TAMie force field for methanol leads to mean absolute deviations of 0.3 % in vapor pressure and 0.4 % in coexisting liquid density, in the temperature-range $0.66 \leq T/T^C_{\mathrm{exp}} \leq 0.98$.

For ethanol, we adjusted the same type of force field parameters as for the other (higher) alcohols. For ethanol we find mean absolute deviations of 0.9 % in vapor pressure and 0.4 % in coexisting liquid density in the temperature range $0.62 \leq T/T^C_{\mathrm{exp}} \leq 0.97$. Results for coexisting densities of methanol and ethanol are illustrated in figure 5.2, with good agreement of the simulation results to experimental data.

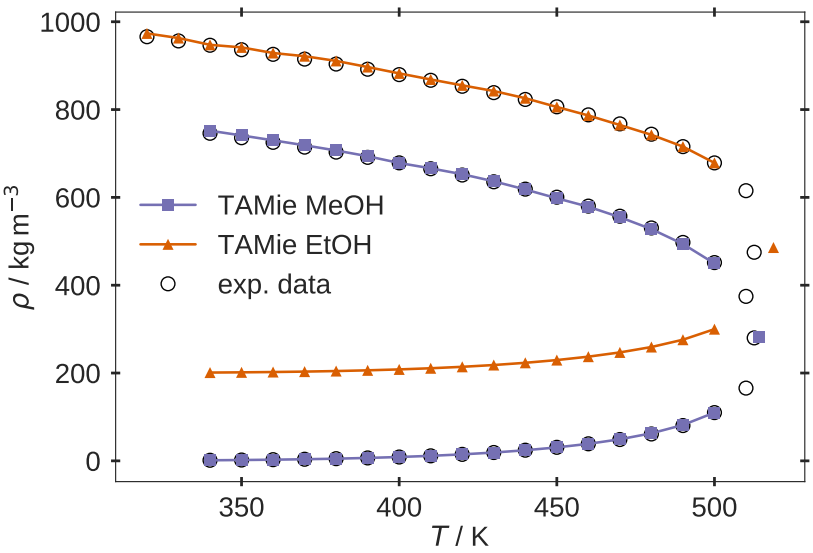

Figure 5.2: Coexisting densities of methanol and ethanol. Ethanol is shifted upward by $200\,\mathrm{kg\,m^{-3}}$ for clarity. Comparison of correlation results from the TAMie force field to quasi-experimental data [419, 509].

Figure 5.3 (a) compares vapor-liquid coexisting densities of 1-pentanol as determined from the developed force field to experimental data. 1-Pentanol was considered in the objective function (within the set of three 1-alcohols) for the force field optimization. The temperature range of the diagram corresponds approximately to the temperature range used for the force field parameterization ($0.58 \leq T/T^{c}_{\mathrm{exp}} \leq 0.96$). The critical point from molecular simulations is not corrected for finite size effects. Results of the TAMie force field are in good agreement with experimental data for the entire temperature range. Experimental data shown in the following figures concerning phase equilibria conditions are quasi-experimental data obtained from empirical correlations provided by DIPPR [419]. For all substances considered in this work, we find deviations of calculated coexisting densities from the TAMie force field compared to experimental data below 1 %. Figure 5.3 (b) shows liquid densities at $p = 1\,\mathrm{bar}$ at temperature-values below the range used for parameter optimization. These results were obtained from MD simulations. One observes somewhat higher average deviations for these lower temperatures. Both diagrams, (a) and (b), show that the force field previously optimized for 1-propanol [505] performs similar to the optimized TAMie force field.

Figure 5.4 is analogous to figure 5.3 but now for 1-heptanol, as a substance that was not part of the objective function for optimizing the TAMie force field. Results from molecular simulations of 1-heptanol are in good agreement to experimental data with average deviations that are comparable to the results earlier obtained for 1-pentanol. The important observation related to figure 5.4 is, that the force field parameters are well transferable to longer-chain 1-alcohols. This conclusion is also supported from other members of the homologous n-alcohols, as reported in the supporting information to this work.

The vapor pressure line $p^{\mathrm{sat}}(T)$ of 1-octanol is shown in figure 5.5 for varying temperature. 1-octanol was not part of the objective function for the force field optimization. Results of the TAMie force field are found in very good agreement to experimental data, suggesting a robust transferability of the TAMie force field also for vapor pressure. The force field parameterized only to 1-propanol is also in rather good agreement with experimental vapor pressures of 1-octanol, supporting a benign transferability of parameters from 1-propanol to 1-octanol. Vapor pressures of other members of the homologous 1-alcohol series are provided in the supporting information to this work. For 1-alcohols ranging from 1-propanol to 1-octanol we find average deviations of calculated vapor pressures to experimental values of below 1 % (considering a temperature range $0.58 \leq T/T^{c}_{\mathrm{exp}} \leq 1.0$). Vapor pressure is a rather sensitive quantity for force fields, as seen in figure 5.5 for the TraPPE model. The TraPPE force field is based on an optimization procedure with less emphasis on vapor pressure and shows average deviations for vapor pressure of 15 % for 1-propanol to 50 % for 1-octanol. An overview of deviations between MC simulation results

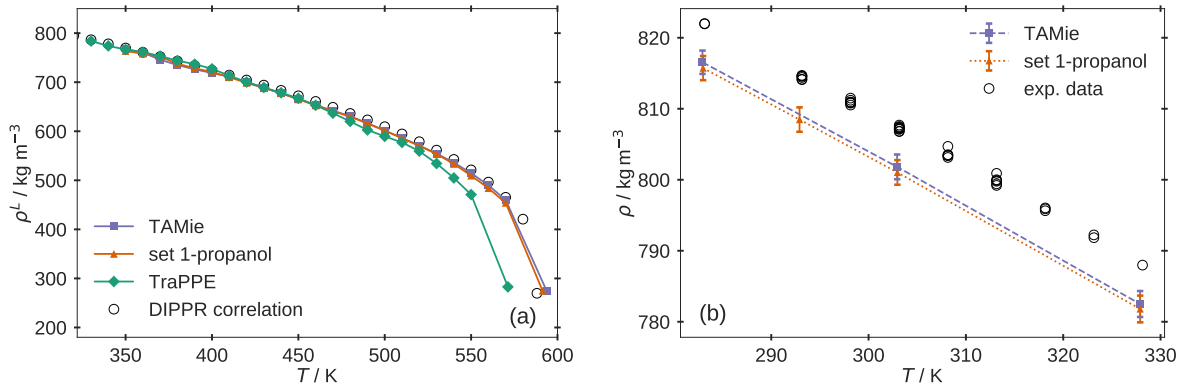

Figure 5.3: Liquid density ρ^{L} of 1-pentanol as function of temperature T for two different temperature ranges. (a) ρ^{L} at VLE conditions obtained from GCMC simulations. Experimental data are represented by the DIPPR correlation [419]. (b) ρ^{L} obtained from MD simulations at 1 bar. Experimental data are from various sources [463, 467, 474, 475, 480, 485, 510–513]. Error bars equal one standard deviation.

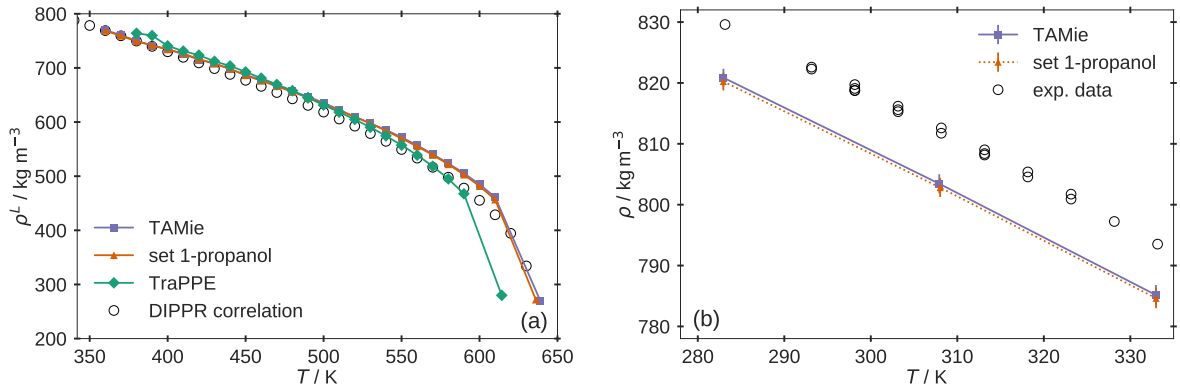

Figure 5.4: Liquid density ρ^{L} of 1-heptanol as function of temperature T for two different temperature ranges. (a) ρ^{L} at VLE conditions obtained from GCMC simulations. Experimental data are represented by the DIPPR correlation [419]. (b) ρ^{L} obtained from MD simulations at 1 bar. Experimental data are from various sources [513–516]. Error bars equal one standard deviation.

and quasi experimental data obtained from DIPPR correlations at phase equilibrium conditions is shown in table 5.5. The table summarizes average absolute deviations in vapor pressure and liquid density for the three different sets of force field parameters: TAMie parameters from this work, set 1-propanol [505], and TraPPE [386].

5.4.2 Shear Viscosities of Pure Substance

Dynamic properties such as shear viscosities η were not considered in the objective function for the optimization of the TAMie force field. Figure 5.6 shows predicted viscosities

Table 5.5: Deviations between MC simulation results and quasi experimental data obtained from DIPPR correlations at phase equilibria conditions for different sets of force field parameters: TAMie parameters from this work, set 1-propanol [505], and TraPPE [386]

n-alcohol	AAD-% vapor pressure			AAD-% liquid density			temperature range
	TAMie	set 1-propanol	TraPPE	TAMie	set 1-propanol	TraPPE	
methanol	0.3 %	-	-	0.4 %	-	-	340 K - 500 K
ethanol	0.9 %	-	-	0.4 %	-	-	320 K - 500 K
1-propanol	1.0 %	0.3 %	15 %	0.3 %	0.5 %	2.3 %	320 K - 530 K
1-butanol	0.6 %	1.2 %	21 %	0.3 %	0.4 %	3.0 %	330 K - 540 K
1-pentanol	1.5 %	2.4 %	26 %	1.0 %	1.1 %	3.0 %	350 K - 570 K
1-hexanol	2.8 %	3.5 %	37 %	1.6 %	1.9 %	4.4 %	370 K - 590 K
1-heptanol	2.5 %	3.5 %	44 %	2.7 %	2.4 %	3.2 %	360 K - 610 K
1-octanol	3.4 %	5.0 %	50 %	0.7 %	0.5 %	2.8 %	380 K - 630 K

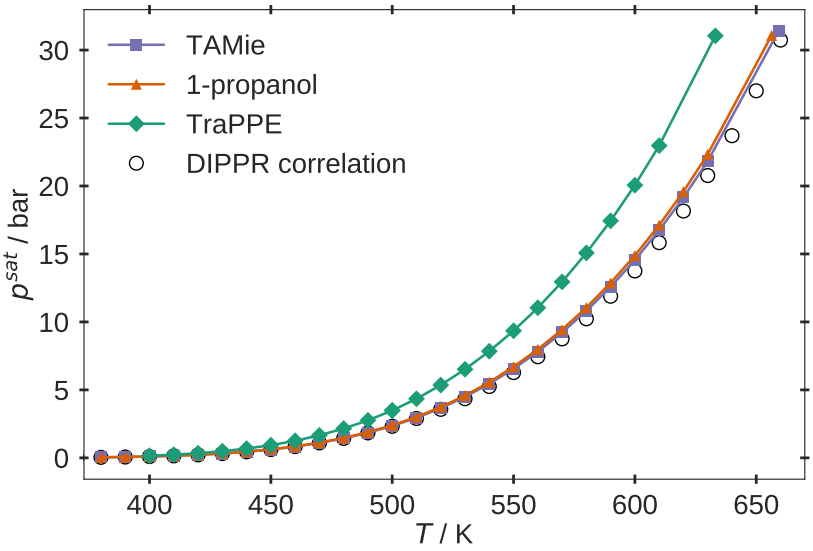

Figure 5.5: Saturation vapor pressure p^{sat} of 1-octanol as function of temperature T. Experimental data are represented by the DIPPR correlation [419].

for 1-pentanol and 1-heptanol for three temperatures, respectively. For all 1-alcohols considered in this work the predicted viscosities underestimate the experimental data. In previous work focusing on 1-propanol, we observed highly correlated force field parameters and a shallow minimum of the objective function, whereby the objective function also captured deviations of the model from experimental vapor pressures and liquid densities (i.e. static properties). Choosing different force field parameter sets, each close to minimum of the objective function, showed that different parameters also lead to very similar predictions for transport properties. It was therefore not a simple exercise to discriminate between these parameter sets. The TAMie force field and the force field optimized for 1-propanol give approximately the same description of viscosities, within the statistical uncertainty. Therefore, we now observe that adjusting the force field parameters to static properties of several pure substances simultaneously, does not improve the prediction

of transport properties significantly. However, the relatively large deviations observed here are not only characteristic of the present parameter set but also apply to other Mie and Lennard-Jones force fields and substances [517]. Viscosities of other 1-alcohols are provided in the supporting information to this work.

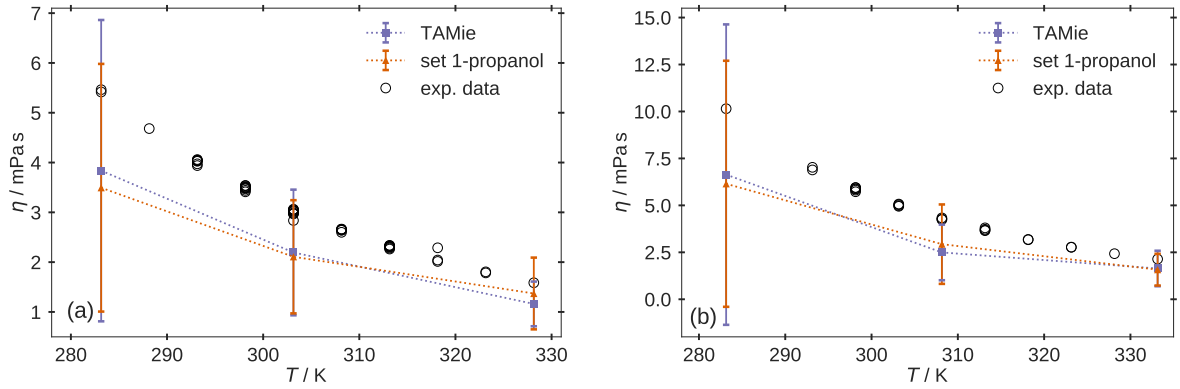

Figure 5.6: Viscosity η of 1-pentanol (a) and 1-heptanol (b) as function of temperature T. Experimental data for subfigure (a) are from various sources [458, 463, 467, 474–476, 480, 485, 510–513, 518] while experimental data for subfigure (b) are taken from [476, 513–516, 518]. Error bars equal one standard deviation.

5.4.3 Self-Diffusion Coefficients of Pure Substance

Figures 5.7 shows the self-diffusion coefficient D_{self} for 1-pentanol and for 1-octanol for various temperatures, respectively. Remaining results of the homologous n-alcohols are shown in the supporting information to this work. Predictions of the TAMie force field overestimate the self-diffusion coefficients as compared to the experimental values. That corresponds with the observation that shear viscosities were underestimated by the TAMie force field, as the Stokes-Einstein relation (applied to molecular fluids) suggests.

5.4.4 Mixture Properties

When adjusting a united-atom force-field with fixed (effective) point charges, one is faced with highly correlated force field parameters. Taking the TAMie force field as a starting point, we may for example factor all charges with a factor of 1.04. If the Mie energy parameters are appropriately reduced one can obtain almost the same result for the objective function. That is how parameter set 1-propanol (see table 5.4), compares to the TAMie force field and that is what we mean by saying the objective function is shallow in parameter-space. The difficulty with shallow minima is that mixtures may strongly discriminate one or the other force field. In particular cross-interactions of a 1-alcohol in mixture with a non-polar solvent are entirely determined by Mie-potentials, where a

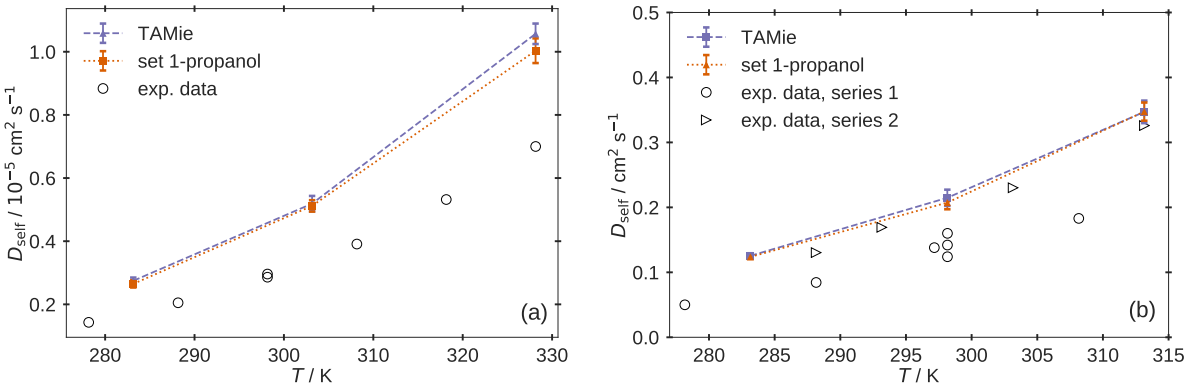

Figure 5.7: Coefficient of self-diffusion D_{self} of 1-pentanol (a) and 1-octanol (b) as function of temperature T. Experimental data for subfigure (a) are from various sources [363, 519] while experimental data for subfigure (b) are taken from [519–522] for series 1 and from [523] for series 2. Corrections for finite size effects have been applied according to Yeh and Hummer [346]. Error bars equal one standard deviation.

too high or too low value of Mie energy parameters can not be compensated by charges scaled too low or too high, respectively. Mixtures with non-polar solvents are therefore a meaningful test for 1-alcohols, and more so than mixtures of, say, 1-alcohol with another 1-alcohol.

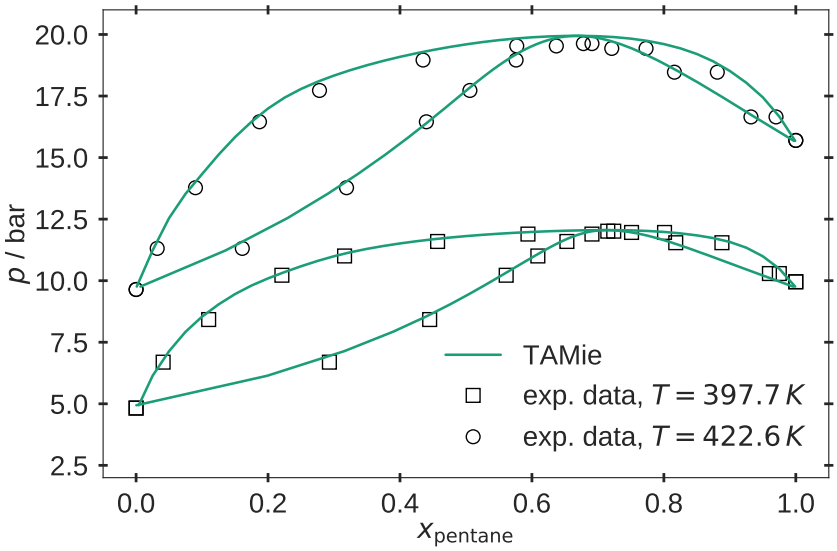

Figure 5.8: Vapor-liquid equilibrium for the mixture ethanol with n-pentane at 397.7 K and 422.6 K. Comparison of predictions from the TAMie force field (lines) with experimental data from Deák et al.[524] (open symbols).

The vapor-liquid phase equilibrium of the binary mixture ethanol and n-pentane is shown in figure 5.8. The mixture has azeotropic phase behavior. All cross-interactions of the Mie potential were obtained from simple Berthelot-Lorentz combining rules and the arithmetic mean for n_{ij}, according to eq. (5.5). Predictions of the TAMie model are in excellent agreement to experimental data.

In figure 5.9 we regard the binary mixture of 1-butanol with n-butane at three temperatures. Predictions of the TAMie model are found in very good agreement to the experimental data for all three temperatures. Robust predictions for varying temperatures suggests that the excess entropy and excess enthalpy are reliable, according to the Gibbs-Helmholtz relation.

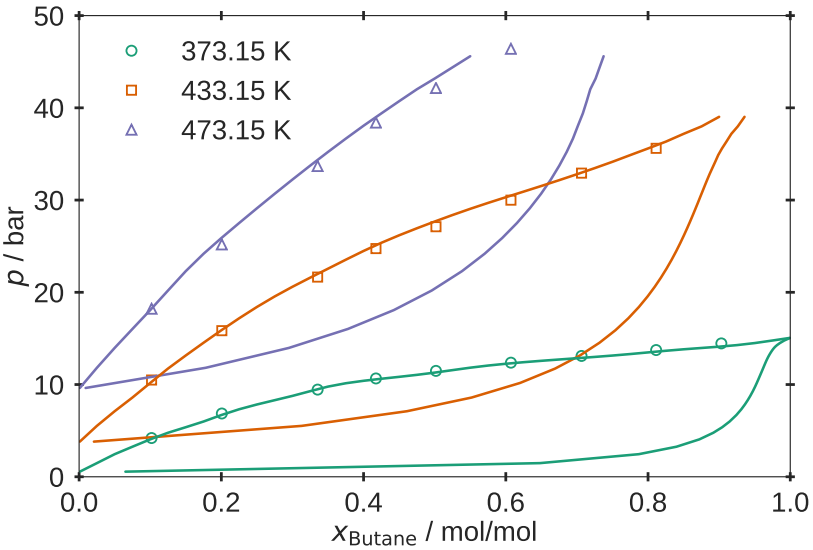

Figure 5.9: Vapor-liquid equilibrium for the mixture 1-butanol with n-butane at three temperatures T. Comparison of results from the TAMie force field (lines) with experimental data from Deák et al.[524] (open symbols).

5.5 Conclusion

As an extension of the TAMie model, a transferable force field is proposed for 1-alcohols with at least 3 carbon atoms. The united-atom model is based on fixed point charges and Mie interaction sites. The force field is parameterized by minimizing an objective function covering squared deviations between vapor pressure data and coexisting liquid densities towards experimental values of (simultaneously) 1-propanol, 1-butanol and 1-pentanol. The model is transferable to other 1-alcohols, as shown for alcohols up to 1-octanol. The force field of methanol and ethanol was individually optimized in order to ensure good agreement to experimental data. Transport properties, such as shear viscosity or self-diffusion coefficients are described in reasonable agreement to experimental data, considering transport properties were not regarded in the objective function for parameterizing the model.

Chapter 6

Conclusion

Molecular simulation is an established scientific field that bridges the gap between experiment and theory. It plays a valuable role in providing essentially exact results for problems in statistical mechanics which could otherwise only be handled by approximate methods, or might be even intractable. The comparison of simulation results with experiment is a test of the underlying model given that sufficient sampling has been achieved. In case of a good model the simulation then offers microscopic details of a system with macroscopic properties of experimental interest. In the present work the dual role of simulation as a bridge between models and theoretical predictions on the one hand and between models and experimental results on the other was explored for systems of varying complexity with relevance in materials science, biotechnology and chemical engineering. In the following the main findings for each of the studied systems are summarized and avenues for future research are identified.

6.1 Supramolecular Complexes

Achieving an atomic-level description and mechanistic understanding of the onset of self-assembly is an important prerequisite in the rational design of both solute and solvent molecules. Atomistic simulations play an important role in these efforts. In this thesis the significance of a detailed thermodynamic analysis of the initial phase of self-assembly of a particular perylene bisimide (PBI) derivative is demonstrated. The results provide a detailed understanding of the influence of the solvent environment on the thermodynamic fingerprint of aggregation. Moreover, technical issues such as computational resources required to achieve converged results as well as the computation of binding free energies from the potential of mean force are provided. This sets the stage for a variety of possible research directions. First, force field refinement should be conducted by comparing simulated binding free energies to experimental data [125, 127] measured in various solvent environments. Second, interesting applications may be considered. For example,

the application of PBI derivatives as sensors is interesting from a computational perspective because various modifications of the perylene core can be conveniently studied in silico. Recent experimental work was directed to the use of an aspartic acid modified perylene bisimide as fluorescence probe for caffeine in aqueous solution [525]. Another study investigated the use of PBI derivatives as sensor for aromatic amines in aqueous solution [526]. For future work it would be also of interest to study optical properties of PBI aggregates by a multiscale approach of time-dependent density functional theory and molecular dynamics simulations [301, 527].

6.2 Deep Eutectic Solvents

The increasing demands for eco-friendly processes within the framework of green and sustainable chemistry has raised deep eutectic solvents (DES) to a prominent position. They show interesting properties similar to those of ionic liquids (IL) including negligible volatility, high conductivity and non-flammability. Compared to ILs they have the advantage of being less expensive, more synthetically accessible, non-toxic, and biodegradable. Despite the enormous interest in DES from the application point of view fundamental questions about DES formation, the nature of its interactions and structure underpinning the liquid phase formation, the solid-liquid phase diagram and its rigorous description using thermodynamic models, the role of water in DES formation and stability as well as the structure and dynamics of DESs at the molecular level have not received the same attention [528]. The present work contributes to the molecular level understanding of the role of water in the DES glyceline. At the same time molecular simulations have shown to be a predictive tool to estimate important process parameters such as viscosity and thermodynamic activity of water. This sets the stage for further investigations of DES as reaction media for biotransformation. An important application is for example the use of DES in enzymatic biodiesel production from waste oils. Here glyceline-water mixtures have recently been successfully tested as a replacement of an ionic liquid [529]. To accelerate progress in this field the combination of molecular simulation, equation of state calculation and systematic experimental measurements is expected to benefit in process design challenges.

6.3 Development of a TAMie Force Field for n-Alcohols

The use of physically based equations of states such as PC-SAFT in force field parametrisation has been demonstrated as an efficient approach for tuning force field parameters.

Allowing for repulsive exponents different from the traditional $n = 12$ choice allows for a very accurate representation of both vapor-liquid equilibria and vapor pressures. However, this improvement in the description of static properties is hardly propagated to the (prediction) of transport properties such as the shear viscosity, not included in the force field optimisation process [517]. Therefore, in future work, it needs to be shown whether the consideration of transport properties in the force field calibration will compromise the VLE and vapor pressure prediction or whether the degrees of freedom available in the model allows for an accurate description of both. The efficient inclusion of transport properties in the optimisation process is an interesting task in itself. Here again the use of an equation of state might be beneficial in the context of the entropy scaling approach [530]. Moreover, by using reweighting techniques [531] the efficiency of probing the large parameter space can be increased which may allow for relaxing some of the parameter constraints used in the suggested TAMie alcohol models. As recent results show, TAMie potentials that are very reliable at normal conditions may fail at extreme temperatures and pressures [532]. Extending the coverage of both chemical space and thermodynamic state points will therefore remain a very active area of force field research [533–535] and force field development will remain one of the cornerstones of computational molecular science.

Bibliography

1. Barker, J. A. & Watts, R. O. Structure of water; A Monte Carlo calculation. *Chem. Phys. Lett.* **3,** 144–145 (1969).
2. Rahman, A. & Stillinger, F. H. Molecular dynamics study of liquid water. *J. Chem. Phys.* **55,** 3336–3359 (1971).
3. Heinzinger, K. & Vogel, P. C. A molecular dynamics study of aqueous solutions I. First results for LiCl in H2O. *Z. Naturforsch. A* **29,** 1164–1171 (1974).
4. Rossky, P. J. & Karplus, M. Solvation. A molecular dynamics study of a dipeptide in water. *J. Am. Chem. Soc.* **101,** 1913–1937 (1979).
5. Jorgensen, W. L. Theoretical studies of medium effects on conformational equilibria. *J. Phys. Chem.* **87,** 5304–5314 (1983).
6. Panagiotopoulos, A. Z. Direct determination of phase coexistence properties of fluids by Monte Carlo simulation in a new ensemble. *Mol. Phys.* **61,** 813–826 (1987).
7. Siepmann, J. I. & Frenkel, D. Configurational bias Monte Carlo: a new sampling scheme for flexible chains. *Mol. Phys.* **75,** 59–70 (1992).
8. Norman, G. & Filinov, V. Investigations of phase transitions by a Monte-Carlo method. *High Temp.* **7,** 216 (1969).
9. Fitzgerald, M., Picard, R. R. & Silver, R. N. Canonical transition probabilities for adaptive Metropolis simulation. *Europhys. Lett.* **46,** 282 (1999).
10. Errington, J. R. Direct calculation of liquid–vapor phase equilibria from transition matrix Monte Carlo simulation. *J. Chem. Phys.* **118,** 9915–9925 (2003).
11. Alder, B. & Wainwright, T. Phase transition for a hard sphere system. *J. Chem. Phys* **27,** 1207 (1957).
12. Rahman, A. Correlations in the motion of atoms in liquid argon. *Phys. Rev.* **136,** A405 (1964).
13. Ryckaert, J.-P. & Bellemans, A. Molecular dynamics of liquid n-butane near its boiling point. *Chem. Phys. Lett.* **30,** 123–125 (1975).

14. McCammon, J. A., Gelin, B. R. & Karplus, M. Dynamics of folded proteins. *Nature* **267,** 585 (1977).

15. Van Gunsteren, W., Berendsen, H., Hermans, J, Hol, W. & Postma, J. Computer simulation of the dynamics of hydrated protein crystals and its comparison with X-ray data. *Proc. Natl. Acad. Sci. USA* **80,** 4315–4319 (1983).

16. Van Gunsteren, W., Berendsen, H., Geurtsen, R. & Zwinderman, H. A Molecular Dynamics Computer Simulation of an Eight-Base-Pair DNA Fragment in Aqueous Solution: Comparison with Experimental Two-Dimensional NMR Data a. *Ann. N.Y. Acad. Sci.* **482,** 287–303 (1986).

17. De Vlieg, J, Berendsen, H. C. & Van Gunsteren, W. An NMR-based molecular dynamics simulation of the interaction of the lac repressor headpiece and its operator in aqueous solution. *Proteins: Struct., Funct., Bioinf.* **6,** 104–127 (1989).

18. Daura, X., Jaun, B., Seebach, D., Van Gunsteren, W. F. & Mark, A. E. Reversible peptide folding in solution by molecular dynamics simulation. *J. Mol. Biol.* **280,** 925–932 (1998).

19. Marrink, S., Tieleman, D. & Mark, A. Molecular dynamics simulation of the kinetics of spontaneous micelle formation. *J. Phys. Chem. B* **104,** 12165–12173 (2000).

20. Shaw, D. E. *et al.* Atomic-level characterization of the structural dynamics of proteins. *Science* **330,** 341–346 (2010).

21. Lindorff-Larsen, K., Maragakis, P., Piana, S. & Shaw, D. E. Picosecond to millisecond structural dynamics in human ubiquitin. *J. Phys. Chem. B* **120,** 8313–8320 (2016).

22. Hillisch, A., Heinrich, N. & Wild, H. Computational chemistry in the pharmaceutical industry: from childhood to adolescence. *ChemMedChem* **10,** 1958–1962 (2015).

23. Muegge, I., Bergner, A. & Kriegl, J. M. Computer-aided drug design at Boehringer Ingelheim. *J. Comput. -Aided Mol. Des.* **31,** 275–285 (2017).

24. Weiss, H., Deglmann, P., in't Veld, P. J., Cetinkaya, M. & Schreiner, E. Multiscale materials modeling in an industrial environment. *Annu. Rev. Chem. Biomol. Eng.* **7,** 65–86 (2016).

25. De Miguel, E. & Jackson, G. The nature of the calculation of the pressure in molecular simulations of continuous models from volume perturbations. *J. Chem. Phys.* **125,** 164109 (2006).

26. Baidakov, V., Protsenko, S. & Kozlova, Z. The self-diffusion coefficient in stable and metastable states of the Lennard–Jones fluid. *Fluid Phase Equilib.* **305,** 106–113 (2011).

27. Valenzuela, G., Saavedra, J., Rozas, R. & Toledo, P. Analysis of energy and friction coefficient fluctuations of a Lennard-Jones liquid coupled to the Nosé–Hoover thermostat. *Mol. Simul.* **41,** 521–530 (2015).

28. Kim, C., Borodin, O. & Karniadakis, G. E. Quantification of sampling uncertainty for molecular dynamics simulation: Time-dependent diffusion coefficient in simple fluids. *J. Comput. Phys.* **302,** 485–508 (2015).

29. Pranami, G. & Lamm, M. H. Estimating error in diffusion coefficients derived from molecular dynamics simulations. *J. Chem. Theory Comput.* **11,** 4586–4592 (2015).

30. Feig, M., Yu, I., Wang, P.-h., Nawrocki, G. & Sugita, Y. Crowding in cellular environments at an atomistic level from computer simulations. *J. Phys. Chem. B* **121,** 8009–8025 (2017).

31. Rivas, G. & Minton, A. P. Toward an understanding of biochemical equilibria within living cells. *Biophys. Rev.* **10,** 241–253 (2018).

32. Mon, K. & Binder, K. Finite size effects for the simulation of phase coexistence in the Gibbs ensemble near the critical point. *J. Chem. Phys.* **96,** 6989–6995 (1992).

33. Frenkel, D. Simulations: The dark side. *Eur. Phys. J. Plus* **128,** 10 (2013).

34. Wong-ekkabut, J. & Karttunen, M. The good, the bad and the user in soft matter simulations. *Biochim. Biophys. Acta - Biomembranes* **1858,** 2529–2538 (2016).

35. Bopp, P. A., Hawlicka, E. & Fritzsche, S. The Hitchhiker's guide to molecular dynamics. *ChemTexts* **4,** 2 (2018).

36. De Pablo, J. J. & Escobedo, F. A. Molecular simulations in chemical engineering: Present and future. *Am. Inst. Chem. Eng. J.* **48,** 2716 (2002).

37. Strasser, D., Goulay, F., Kelkar, M. S., Maginn, E. J. & Leone, S. R. Photoelectron spectrum of isolated ion-pairs in ionic liquid vapor. *J. Phys. Chem. A* **111,** 3191–3195 (2007).

38. Earl, D. J. *et al.* Synthesis and Monte Carlo structure determination of SSZ-77: A new zeolite topology. *J. Phys. Chem. C* **112,** 9099–9105 (2008).

39. Chen, H., Johnson, J. K. & Sholl, D. S. Transport diffusion of gases is rapid in flexible carbon nanotubes. *J. Phys. Chem. B* **110,** 1971–1975 (2006).

40. Dubbeldam, D., Walton, K. S., Ellis, D. E. & Snurr, R. Q. Exceptional negative thermal expansion in isoreticular metal–organic frameworks. *Angew. Chem. Int. Ed.* **46,** 4496–4499 (2007).

41. Giovambattista, N., Lopez, C. F., Rossky, P. J. & Debenedetti, P. G. Hydrophobicity of protein surfaces: Separating geometry from chemistry. *Proc. Natl. Acad. Sci. USA* **105,** 2274–2279 (2008).

42. Duff, N. & Lacks, D. J. Shear-induced crystallization in jammed systems. *Phys. Rev. E* **75,** 031501 (2007).

43. Carol, K. Thermodynamic and kinetic origins of Alzheimer's and related diseases: A chemical engineer's perspective. *AIChE - The 2006 Annual Meeting* (2006).

44. Kim, Y. C., Fisher, M. E. & Panagiotopoulos, A. Z. Universality of ionic criticality: Size-and charge-asymmetric electrolytes. *Phys. Rev. Lett.* **95,** 195703 (2005).

45. Singh, J. K. & Errington, J. R. Calculation of Phase Coexistence Properties and Surface Tensions of n-Alkanes with Grand-Canonical Transition-Matrix Monte Carlo Simulation and Finite-Size Scaling. *J. Phys. Chem. B* **110,** 1369–1376 (2006).

46. Karayiannis, N. C., Giannousaki, A. E., Mavrantzas, V. G. & Theodorou, D. N. Atomistic Monte Carlo simulation of strictly monodisperse long polyethylene melts through a generalized chain bridging algorithm. *J. Chem. Phys.* **117,** 5465–5479 (2002).

47. Hulse, R. J., Rowley, R. L. & Wilding, W. V. Transient nonequilibrium molecular dynamic simulations of thermal conductivity: 1. Simple fluids. *Int. J. Thermophys.* **26,** 1–12 (2005).

48. Martin, M. G. & Siepmann, J. I. Transferable Potentials for Phase Equilibria. 1. United-Atom Description of n-Alkanes. *J. Phys. Chem. B* **102,** 2569–2577 (1998).

49. Gordon, P. A. Development of intermolecular potentials for predicting transport properties of hydrocarbons. *J. Chem. Phys.* **125,** 014504 (2006).

50. Pan, G. & McCabe, C. Prediction of viscosity for molecular fluids at experimentally accessible shear rates using the transient time correlation function formalism. *J. Chem. Phys.* **125,** 194527 (2006).

51. Kamath, G. & Potoff, J. J. Monte Carlo predictions for the phase behavior of H2S+ n-alkane, H2S+ CO2, CO2+ CH4 and H2S+ CO2+ CH4 mixtures. *Fluid Phase Equilib.* **246,** 71–78 (2006).

52. Shi, W. & Maginn, E. J. Atomistic Simulation of the Absorption of Carbon Dioxide and Water in the Ionic Liquid 1-n-Hexyl-3-methylimidazolium Bis (trifluoromethyl-sulfonyl) imide ([hmim][Tf2N]. *J. Phys. Chem. B* **112,** 2045–2055 (2008).

53. Shukla, K. P. & Chapman, W. G. SAFT equation of state for fluid mixtures of hard chain copolymers. *Mol. Phys.* **91,** 1075–1082 (1997).

54. Keskin, S., Liu, J., Johnson, J. K. & Sholl, D. S. Testing the accuracy of correlations for multicomponent mass transport of adsorbed gases in metal- organic frameworks: diffusion of H2/CH4 mixtures in CuBTC. *Langmuir* **24,** 8254–8261 (2008).

55. Hu, Y. & Liu, H. Participation of molecular simulation in the development of molecular-thermodynamic models. *Fluid Phase Equilib.* **241,** 248–256 (2006).

56. Maginn, E. J. From discovery to data: What must happen for molecular simulation to become a mainstream chemical engineering tool. *AIChE J.* **55,** 1304–1310 (2009).

57. Levitt, M. & Lifson, S. Refinement of protein conformations using a macromolecular energy minimization procedure. *J. Mol. Biol.* **46,** 269–279 (1969).

58. Riniker, S. Fixed-charge atomistic force fields for molecular dynamics simulations in the condensed phase: An overview. *J. Chem. Inf. Model* **58,** 565–578 (2018).

59. Van Gunsteren, W. F. & Berendsen, H. J. GROMOS, Groningen molecular simulation package. *GROMOS, University of Groningen, The Netherlands* (1987).

60. Van Gunsteren, W. F. & Berendsen, H. J. Computer simulation of molecular dynamics: Methodology, applications, and perspectives in chemistry. *Angew. Chem. Int. Ed.* **29,** 992–1023 (1990).

61. Berendsen, H. J. Models for protein dynamics. *Report of CECAM Workshop (Orsay)* (1976).

62. Harder, E. *et al.* OPLS3: a force field providing broad coverage of drug-like small molecules and proteins. *J. Chem. Theory Comput.* **12,** 281–296 (2015).

63. Cole, D. J., Vilseck, J. Z., Tirado-Rives, J., Payne, M. C. & Jorgensen, W. L. Biomolecular force field parameterization via atoms-in-molecule electron density partitioning. *J. Chem. Theory Comput.* **12,** 2312–2323 (2016).

64. Dixon, R. W. & Kollman, P. A. Advancing beyond the atom-centered model in additive and nonadditive molecular mechanics. *J. Comput. Chem.* **18,** 1632–1646 (1997).

65. Kramer, C., Spinn, A. & Liedl, K. R. Charge anisotropy: where atomic multipoles matter most. *J. Chem. Theory Comput.* **10,** 4488–4496 (2014).

66. Åqvist, J. & Warshel, A. Free energy relationships in metalloenzyme-catalyzed reactions. Calculations of the effects of metal ion substitutions in staphylococcal nuclease. *J. Am. Chem. Soc.* **112,** 2860–2868 (1990).

67. Åqvist, J. & Warshel, A. Computer simulation of the initial proton transfer step in human carbonic anhydrase I. *J. Mol. Biol.* **224,** 7–14 (1992).

68. Oelschlaeger, P., Klahn, M., Beard, W. A., Wilson, S. H. & Warshel, A. Magnesium-cationic dummy atom molecules enhance representation of DNA polymerase β in molecular dynamics simulations: Improved accuracy in studies of structural features and mutational effects. *J. Mol. Biol.* **366,** 687–701 (2007).

69. Saxena, A. & Sept, D. Multisite ion models that improve coordination and free energy calculations in molecular dynamics simulations. *J. Chem. Theory Comput.* **9,** 3538–3542 (2013).

70. Best, R. B., Buchete, N.-V. & Hummer, G. Are current molecular dynamics force fields too helical? *Biophys. J.* **95,** L07–L09 (2008).

71. Piana, S., Lindorff-Larsen, K. & Shaw, D. E. How robust are protein folding simulations with respect to force field parameterization? *Biophys. J.* **100,** L47–L49 (2011).

72. Beauchamp, K. A., Lin, Y.-S., Das, R. & Pande, V. S. Are protein force fields getting better? A systematic benchmark on 524 diverse NMR measurements. *J. Chem. Theory Comput.* **8,** 1409–1414 (2012).

73. Martín-García, F., Papaleo, E., Gomez-Puertas, P., Boomsma, W. & Lindorff-Larsen, K. Comparing molecular dynamics force fields in the essential subspace. *PLoS One* **10,** e0121114 (2015).

74. Vitalini, F., Mey, A. S., Noé, F. & Keller, B. G. Dynamic properties of force fields. *J. Chem. Phys.* **142,** 02B611_1 (2015).

75. Cailliez, F. & Pernot, P. Statistical approaches to forcefield calibration and prediction uncertainty in molecular simulation. *J. Chem. Phys.* **134,** 054124 (2011).

76. Rizzi, F. *et al.* Uncertainty quantification in MD simulations. Part II: Bayesian inference of force-field parameters. *Multiscale Model. Simul.* **10,** 1460–1492 (2012).

77. Wang, L.-P., Martinez, T. J. & Pande, V. S. Building force fields: An automatic, systematic, and reproducible approach. *J. Phys. Chem. Lett.* **5,** 1885–1891 (2014).

78. Wu, S., Angelikopoulos, P., Papadimitriou, C., Moser, R. & Koumoutsakos, P. A hierarchical Bayesian framework for force field selection in molecular dynamics simulations. *Philos. Trans. Royal Soc. A* **374,** 20150032 (2016).

79. Nerenberg, P. S. & Head-Gordon, T. New developments in force fields for biomolecular simulations. *Curr. Opin. Struct. Biol.* **49,** 129–138 (2018).

80. Mobley, D. L. *et al.* Escaping Atom Types in Force Fields Using Direct Chemical Perception. *J. Chem. Theory Comput.* **14,** 6076–6092 (2018).

81. *DCIS Inc. Daylight Theory: SMARTS - A Language for Describing Molecular Patterns, (accessed June 2019)* 2018. `http://www.daylight.com/dayhtml/doc/theory/theory.smarts.html`.

82. *DCIS Inc. Daylight Theory: SMIRKS - A Reaction Transform Language, (accessed June 2019)* 2018. `http://www.daylight.com/dayhtml/doc/theory/theory.smarts.html`.

83. Smith, J. S., Isayev, O. & Roitberg, A. E. ANI-1: an extensible neural network potential with DFT accuracy at force field computational cost. *Chem. Sci.* **8,** 3192–3203 (2017).

84. Huan, T. D. *et al.* A universal strategy for the creation of machine learning-based atomistic force fields. *npj Comput. Mater.* **3,** 37 (2017).

85. Behler, J. Perspective: Machine learning potentials for atomistic simulations. *J. Chem. Phys.* **145,** 170901 (2016).

86. Berendsen, H. J. *Simulating the physical world: hierarchical modeling from quantum mechanics to fluid dynamics* (Cambridge University Press, 2007).

87. Pohorille, A., Jarzynski, C. & Chipot, C. Good practices in free-energy calculations. *J. Phys. Chem. B* **114,** 10235–10253 (2010).

88. Wan, S., Knapp, B., Wright, D. W., Deane, C. M. & Coveney, P. V. Rapid, precise, and reproducible prediction of peptide–MHC binding affinities from molecular dynamics that correlate well with experiment. *J. Chem. Theory Comput.* **11,** 3346–3356 (2015).

89. Van Gunsteren, W. F. & Mark, A. E. Validation of molecular dynamics simulation. *J. Chem. Phys.* **108,** 6109–6116 (1998).

90. Loeffler, H. H. *et al.* Reproducibility of Free Energy Calculations across Different Molecular Simulation Software Packages. *J. Chem. Theory Comput.* **14,** 5567–5582 (2018).

91. Van Gunsteren, W. F. *et al.* Validation of molecular simulation: an overview of issues. *Angew. Chem. Int. Ed.* **57,** 884–902 (2018).

92. Ni, B. & Baumketner, A. Effect of atom-and group-based truncations on biomolecules simulated with reaction-field electrostatics. *J. Mol. Model.* **17,** 2883–2893 (2011).

93. Patra, M. *et al.* Molecular dynamics simulations of lipid bilayers: major artifacts due to truncating electrostatic interactions. *Biophys. J.* **84,** 3636–3645 (2003).

94. Venable, R. M., Brooks, B. R. & Pastor, R. W. Molecular dynamics simulations of gel (L βI) phase lipid bilayers in constant pressure and constant surface area ensembles. *J. Chem. Phys.* **112,** 4822–4832 (2000).

95. Wong-Ekkabut, J., Miettinen, M. S., Dias, C. & Karttunen, M. Static charges cannot drive a continuous flow of water molecules through a carbon nanotube. *Nat. Nanotechnol.* **5,** 555 (2010).

96. McConnell, S. *Code Complete, Redmond, WA* USA: Microsoft Press. 2004.

97. Schappals, M. *et al.* Round robin study: molecular simulation of thermodynamic properties from models with internal degrees of freedom. *J. Chem. Theory Comput.* **13,** 4270–4280 (2017).

98. Merz, P. T. & Shirts, M. R. Testing for physical validity in molecular simulations. *PLoS One* **13,** e0202764 (2018).

99. Miller, G. *A scientist's nightmare: software problem leads to five retractions* 2006.

100. Seibert, M. M., Patriksson, A., Hess, B. & Van Der Spoel, D. Reproducible polypeptide folding and structure prediction using molecular dynamics simulations. *J. Mol. Biol.* **354,** 173–183 (2005).

101. Day, R., Paschek, D. & Garcia, A. E. Microsecond simulations of the folding/unfolding thermodynamics of the Trp-cage miniprotein. *Proteins: Struct., Funct., Bioinf.* **78,** 1889–1899 (2010).

102. Tironi, I. G., Brunne, R. M. & van Gunsteren, W. F. On the relative merits of flexible versus rigid models for use in computer simulations of molecular liquids. *Chem. Phys. Lett.* **250,** 19–24 (1996).

103. Snow, C. D., Nguyen, H., Pande, V. S. & Gruebele, M. Absolute comparison of simulated and experimental protein-folding dynamics. *Nature* **420,** 102 (2002).

104. Reif, M. M. & Oostenbrink, C. Toward the correction of effective electrostatic forces in explicit-solvent molecular dynamics simulations: restraints on solvent-generated electrostatic potential and solvent polarization. *Theor. Chem. Acc.* **134,** 2 (2015).

105. Luty, B. A. & van Gunsteren, W. F. Calculating electrostatic interactions using the particle- particle particle- mesh method with nonperiodic long-range interactions. *J. Phys. Chem.* **100,** 2581–2587 (1996).

106. Hünenberger, P. H. & McCammon, J. A. Ewald artifacts in computer simulations of ionic solvation and ion–ion interaction: a continuum electrostatics study. *J. Chem. Phys.* **110,** 1856–1872 (1999).

107. Holm, C. & Kremer, K. *Advanced computer simulation approaches for soft matter sciences III* (Springer, 2008).

108. Van Der Spoel, D. *et al.* GROMACS: fast, flexible, and free. *J. Comput. Chem.* **26,** 1701–1718 (2005).

109. Grossfield, A. *et al.* Best Practices for Quantification of Uncertainty and Sampling Quality in Molecular Simulations [Article v1. 0]. *LiveCoMS* **1** (2018).

110. Patrone, P. N. & Dienstfrey, A. Uncertainty Quantification for Molecular Dynamics. *Rev. Comput. Chem.* **31,** 115–169 (2019).

111. Patrone, P. N., Kearsley, A. & Dienstfrey, A. *The role of data analysis in uncertainty quantification: Case studies for materials modeling* in *2018 AIAA Non-Deterministic Approaches Conference* (2018), 927.

112. Petersen, H & Flyvbjerg, H. Error estimates in molecular dynamics simulations. *J. Chem. Phys.* **91,** 461–467 (1989).

113. Van Gunsteren, W. F. *et al.* Biomolecular modeling: goals, problems, perspectives. *Angew. Chem. Int. Ed.* **45,** 4064–4092 (2006).

114. Whitesides, G. M., Mathias, J. P. & Seto, C. T. Molecular self-assembly and nanochemistry: a chemical strategy for the synthesis of nanostructures. *Science* **254,** 1312–1319 (1991).

115. Philp, D. & Stoddart, J. F. Self-assembly in natural and unnatural systems. *Angew. Chem. Int. Ed.* **35,** 1154–1196 (1996).

116. Atwood, J. L., Davies, J. E. D., MacNicol, D. D., Vogtle, F. & Lehn, J. M. *Comprehensive Supramolecular Chemistry* 1996.

117. Ward, M. D. Photo-induced electron and energy transfer in non-covalently bonded supramolecular assemblies. *Chem. Soc. Rev.* **26,** 365–375 (1997).

118. Lehn, J.-M. Toward self-organization and complex matter. *Science* **295,** 2400–2403 (2002).

119. Görl, D., Zhang, X. & Würthner, F. Molecular assemblies of perylene bisimide dyes in water. *Angew. Chem. Int. Ed.* **51,** 6328–6348 (2012).

120. Shao, C., Grüne, M., Stolte, M. & Würthner, F. Perylene Bisimide Dimer Aggregates: Fundamental Insights into Self-Assembly by NMR and UV/Vis Spectroscopy. *Chem. Eur. J.* **18,** 13665–13677 (2012).

121. Hunter, C. A., Lawson, K. R., Perkins, J. & Urch, C. J. Aromatic interactions. *J. Chem. Soc.* **5,** 651–669 (2001).

122. Hunter, C. A. & Sanders, J. K. The nature of. pi.- pi. interactions. *J. Am. Chem. Soc.* **112,** 5525–5534 (1990).

123. Martinez, C. R. & Iverson, B. L. Rethinking the term "pi-stacking". *Chem. Sci.* **3,** 2191–2201 (2012).

124. Syamakumari, A., Schenning, A. P. & Meijer, E. Synthesis, Optical Properties, and Aggregation Behavior of a Triad System Based on Perylene and Oligo (p-phenylene vinylene) Units. *Chem. Eur. J.* **8,** 3353–3361 (2002).

125. Görl, D. & Würthner, F. Entropically Driven Self-Assembly of Bolaamphiphilic Perylene Dyes in Water. *Angew. Chem. Int. Ed.* **55,** 12094–12098 (2016).

126. Chen, Z., Lohr, A., Saha-Möller, C. R. & Würthner, F. Self-assembled π-stacks of functional dyes in solution: structural and thermodynamic features. *Chem. Soc. Rev.* **38,** 564–584 (2009).

127. Chen, Z., Fimmel, B. & Würthner, F. Solvent and substituent effects on aggregation constants of perylene bisimide π-stacks–a linear free energy relationship analysis. *Org. Biomol. Chem.* **10,** 5845–5855 (2012).

128. Chen, Z. *et al.* Photoluminescence and Conductivity of Self-Assembled π–π Stacks of Perylene Bisimide Dyes. *Chem. Eur. J.* **13,** 436–449 (2007).

129. Gilson, M. K., Given, J. A., Bush, B. L. & McCammon, J. A. The statistical-thermodynamic basis for computation of binding affinities: a critical review. *Biophys. J.* **72,** 1047–1069 (1997).

130. Mihailescu, M. & Gilson, M. K. On The Theory of Noncovalent Binding. *Biophys. J.* **87,** 23–36 (2004).

131. Zhou, H.-X. & Gilson, M. K. Theory of free energy and entropy in noncovalent binding. *Chem. Rev.* **109,** 4092–4107 (2009).

132. Sun, M., Muellen, K. & Yin, M. Water-soluble perylenediimides: design concepts and biological applications. *Chem. Soc. Rev.* **45,** 1513–1528 (2016).

133. Mishra, A. & Bäuerle, P. Small molecule organic semiconductors on the move: promises for future solar energy technology. *Angew. Chem. Int. Ed.* **51,** 2020–2067 (2012).

134. Clarke, T. M. & Durrant, J. R. Charge photogeneration in organic solar cells. *Chem. Rev.* **110,** 6736–6767 (2010).

135. Grätzel, M. Photoelectrochemical cells. *Nature* **414,** 338 (2001).

136. O'regan, B. & Grätzel, M. A low-cost, high-efficiency solar cell based on dye-sensitized colloidal TiO2 films. *Nature* **353,** 737 (1991).

137. Hagfeldt, A., Boschloo, G., Sun, L., Kloo, L. & Pettersson, H. Dye-sensitized solar cells. *Chem. Rev.* **110,** 6595–6663 (2010).

138. Ooyama, Y., Ohshita, J. & Harima, Y. Control of Molecular Arrangement and/or Orientation of D–π–A Fluorescent Dyes for Dye-sensitized Solar Cells. *Chem. Lett.* **41,** 1384–1396 (2012).

139. Hagfeldt, A. & Grätzel, M. Molecular photovoltaics. *Acc. Chem. Res.* **33,** 269–277 (2000).

140. Wang, C., Dong, H., Hu, W., Liu, Y. & Zhu, D. Semiconducting π-conjugated systems in field-effect transistors: a material odyssey of organic electronics. *Chem. Rev.* **112,** 2208–2267 (2011).

141. Wu, K.-C. *et al.* The photophysical properties of dipyrenylbenzenes and their application as exceedingly efficient blue emitters for electroluminescent devices. *Adv. Funct. Mater.* **18,** 67–75 (2008).

142. Trattnig, R. *et al.* Deep blue polymer light emitting diodes based on easy to synthesize, non-aggregating polypyrene. *Opt. Express* **19,** A1281–A1293 (2011).

143. Ling, M.-M. *et al.* Air-stable n-channel organic semiconductors based on perylene diimide derivatives without strong electron withdrawing groups. *Adv. Mater.* **19,** 1123–1127 (2007).

144. Brütting, W., Berleb, S. & Mückl, A. G. Device physics of organic light-emitting diodes based on molecular materials. *Org. Electron.* **2,** 1–36 (2001).

145. Facchetti, A. π-Conjugated polymers for organic electronics and photovoltaic cell applications. *Chem. Mater.* **23,** 733–758 (2010).

146. Marder, S. R. *et al.* Large first hyperpolarizabilities in push-pull polyenes by tuning of the bond length alternation and aromaticity. *Science* **263,** 511–514 (1994).

147. Shi, Y. *et al.* Low (sub-1-volt) halfwave voltage polymeric electro-optic modulators achieved by controlling chromophore shape. *Science* **288,** 119–122 (2000).

148. Zyss, J. & Ledoux, I. Nonlinear optics in multipolar media: theory and experiments. *Chem. Rev.* **94,** 77–105 (1994).

149. Kang, H. *et al.* Exceptional Molecular Hyperpolarizabilities in Twisted π-Electron System Chromophores. *Angew. Chem. Int. Ed.* **44,** 7922–7925 (2005).

150. Kang, H. *et al.* Ultralarge hyperpolarizability twisted π-electron system electro-optic chromophores: synthesis, solid-state and solution-phase structural characteristics, electronic structures, linear and nonlinear optical properties, and computational studies. *J. Am. Chem. Soc.* **129,** 3267–3286 (2007).

151. Wasielewski, M. R. Self-assembly strategies for integrating light harvesting and charge separation in artificial photosynthetic systems. *Acc. Chem. Res.* **42,** 1910–1921 (2009).

152. Würthner, F. Perylene bisimide dyes as versatile building blocks for functional supramolecular architectures. *Chem. Commun.* **14,** 1564–1579 (2004).

153. Veldman, D. *et al.* Triplet formation involving a polar transition state in a well-defined intramolecular perylenediimide dimeric aggregate. *J. Phys. Chem. A* **112,** 5846–5857 (2008).

154. Würthner, F. *et al.* Hierarchical Self-Organization of Perylene Bisimide–Melamine Assemblies to Fluorescent Mesoscopic Superstructures. *Chem. Eur. J.* **6,** 3871–3886 (2000).

155. Würthner, F., Thalacker, C., Diele, S. & Tschierske, C. Fluorescent J-type aggregates and thermotropic columnar mesophases of perylene bisimide dyes. *Chem. Eur. J.* **7,** 2245–2253 (2001).

156. Wang, W., Li, L.-S., Helms, G., Zhou, H.-H. & Li, A. D. To fold or to assemble? *J. Am. Chem. Soc.* **125,** 1120–1121 (2003).

157. Wang, W., Wan, W., Zhou, H.-H., Niu, S. & Li, A. D. Alternating DNA and π-conjugated sequences. Thermophilic foldable polymers. *J. Am. Chem. Soc.* **125,** 5248–5249 (2003).

158. Würthner, F., Chen, Z., Dehm, V. & Stepanenko, V. One-dimensional luminescent nanoaggregates of perylene bisimides. *Chem. Commun.* **11,** 1188–1190 (2006).

159. Kiyonaka, S., Sugiyasu, K., Shinkai, S. & Hamachi, I. First thermally responsive supramolecular polymer based on glycosylated amino acid. *J. Am. Chem. Soc.* **124,** 10954–10955 (2002).

160. Silva, G. A. *et al.* Selective differentiation of neural progenitor cells by high-epitope density nanofibers. *Science* **303,** 1352–1355 (2004).

161. Hamachi, I., Nagase, T. & Shinkai, S. A general semisynthetic method for fluorescent saccharide-biosensors based on a lectin. *J. Am. Chem. Soc.* **122,** 12065–12066 (2000).

162. Sugiyasu, K., Fujita, N. & Shinkai, S. Visible-light-harvesting organogel composed of cholesterol-based perylene derivatives. *Angew. Chem. Int. Ed.* **116,** 1249–1253 (2004).

163. Sukul, P. K. *et al.* Assemblies of perylene diimide derivatives with melamine into luminescent hydrogels. *Chem. Commun.* **47,** 11858–11860 (2011).

164. Mishra, R. *et al.* Tuning the Electronic Nature of Mono-Bay Alkynyl–Phenyl-Substituted Perylene Bisimides: Synthesis, Structure, and Photophysical Properties. *Chem. Eur. J.* **20,** 5776–5786 (2014).

165. Jonkheijm, P., van der Schoot, P., Schenning, A. P. & Meijer, E. Probing the solvent-assisted nucleation pathway in chemical self-assembly. *Science* **313,** 80–83 (2006).

166. Bai, S. *et al.* Differential self-assembly and tunable emission of aromatic peptide bola-amphiphiles containing perylene bisimide in polar solvents including water. *Langmuir* **30,** 7576–7584 (2014).

167. Hallett, J. P. & Welton, T. Room-temperature ionic liquids: solvents for synthesis and catalysis. 2. *Chem. Rev.* **111,** 3508–3576 (2011).

168. Wasserscheid, P. & Keim, W. Ionic liquids - new "solutions" for transition metal catalysis. *Angew. Chem. Int. Ed.* **39,** 3772–3789 (2000).

169. Wang, H., Gurau, G. & Rogers, R. D. Ionic liquid processing of cellulose. *Chem. Soc. Rev.* **41,** 1519–1537 (2012).

170. Dupont, J. & Scholten, J. D. On the structural and surface properties of transition-metal nanoparticles in ionic liquids. *Chem. Soc. Rev.* **39,** 1780–1804 (2010).

171. Le Bideau, J., Viau, L. & Vioux, A. Ionogels, ionic liquid based hybrid materials. *Chem. Soc. Rev.* **40,** 907–925 (2011).

172. Walsh, D. A., Lovelock, K. R. & Licence, P. Ultramicroelectrode voltammetry and scanning electrochemical microscopy in room-temperature ionic liquid electrolytes. *Chem. Soc. Rev.* **39,** 4185–4194 (2010).

173. Vidinha, P. *et al.* Ion jelly: a tailor-made conducting material for smart electrochemical devices. *Chem. Commun.,* 5842–5844 (2008).

174. Zaijun, L., Xiulan, S. & Junkang, L. in *Ionic liquids: Applications and perspectives* (IntechOpen, 2011).

175. Tang, B., Bi, W., Tian, M. & Row, K. H. Application of ionic liquid for extraction and separation of bioactive compounds from plants. *J. Chromatogr. B* **904,** 1–21 (2012).

176. Duarte, A. R. C., Silva, S. S., Mano, J. F. & Reis, R. L. Ionic liquids as foaming agents of semi-crystalline natural-based polymers. *Green Chem.* **14,** 1949–1955 (2012).

177. Zhang, Q., Vigier, K. D. O., Royer, S. & Jérôme, F. Deep eutectic solvents: syntheses, properties and applications. *Chem. Soc. Rev.* **41,** 7108–7146 (2012).

178. Rogers, R. D. & Seddon, K. R. Ionic liquids - solvents of the future? *Science* **302,** 792–793 (2003).

179. Seddon, K. Room-temperature ionic liquids: neoteric solvents for clean catalysis. *Kinet. Catal.* **37,** 693–697 (1995).

180. Paiva, A. *et al.* Natural deep eutectic solvents - solvents for the 21st century. *ACS Sustain. Chem. Eng.* **2,** 1063–1071 (2014).

181. Wagle, D. V., Zhao, H. & Baker, G. A. Deep eutectic solvents: sustainable media for nanoscale and functional materials. *Acc. Chem. Res.* **47,** 2299–2308 (2014).

182. Gill, I. & Vulfson, E. Enzymic catalysis in heterogeneous eutectic mixtures of substrates. *Trends Biotechnol.* **12,** 118–122 (1994).

183. López-Fandiño, R., Gill, I. & Vulfson, E. N. Protease-catalyzed synthesis of oligopeptides in heterogenous substrate mixtures. *Biotechnol. Bioeng.* **43,** 1024–1030 (1994).

184. Erbeldinger, M., Ni, X. & Halling, P. J. Enzymatic synthesis with mainly undissolved substrates at very high concentrations. *Enzyme Microb. Technol.* **23,** 141–148 (1998).

185. Davey, R., Garside, J, Hilton, A., McEwan, D & Morrison, J. Purification of molecular mixtures below the eutectic by emulsion crystallization. *Nature* **375,** 664 (1995).

186. Stott, P. W., Williams, A. C. & Barry, B. W. Transdermal delivery from eutectic systems: enhanced permeation of a model drug, ibuprofen. *J Controlled Release* **50,** 297–308 (1998).

187. Abbott, A. P., Boothby, D., Capper, G., Davies, D. L. & Rasheed, R. K. Deep eutectic solvents formed between choline chloride and carboxylic acids: versatile alternatives to ionic liquids. *J. Am. Chem. Soc.* **126,** 9142–9147 (2004).

188. Abbott, A. P., Capper, G., Davies, D. L., Rasheed, R. K. & Tambyrajah, V. Novel solvent properties of choline chloride/urea mixtures. *Chem. Commun.,* 70–71 (2003).

189. Smith, E. L., Abbott, A. P. & Ryder, K. S. Deep eutectic solvents (DESs) and their applications. *Chem. Rev.* **114,** 11060–11082 (2014).

190. Abbott, A. P. *et al.* Preparation of novel, moisture-stable, Lewis-acidic ionic liquids containing quaternary ammonium salts with functional side chains. Electronic supplementary information (ESI) available: plot of conductivity vs. temperature for the ionic liquid formed from zinc chloride and choline chloride (2:1). *Chem. Commun.,* 2010–2011 (2001).

191. Clouthier, C. M. & Pelletier, J. N. Expanding the organic toolbox: a guide to integrating biocatalysis in synthesis. *Chem. Soc. Rev.* **41,** 1585–1605 (2012).

192. Tang, B., Zhang, H. & Row, K. H. Application of deep eutectic solvents in the extraction and separation of target compounds from various samples. *J. Sep. Sci.* **38,** 1053–1064 (2015).

193. Kareem, M. A., Mjalli, F. S., Hashim, M. A. & AlNashef, I. M. Phosphonium-based ionic liquids analogues and their physical properties. *J. Chem. Eng. Data* **55,** 4632–4637 (2010).

194. Carriazo, D., Serrano, M. C., Gutiérrez, M. C., Ferrer, M. L. & del Monte, F. Deep-eutectic solvents playing multiple roles in the synthesis of polymers and related materials. *Chem. Soc. Rev.* **41,** 4996–5014 (2012).

195. Choi, Y. H. *et al.* Are natural deep eutectic solvents the missing link in understanding cellular metabolism and physiology? *Plant Physiol.* **156,** 1701–1705 (2011).

196. Dai, Y., van Spronsen, J., Witkamp, G.-J., Verpoorte, R. & Choi, Y. H. Natural deep eutectic solvents as new potential media for green technology. *Anal. Chim. Acta* **766,** 61–68 (2013).

197. Mbous, Y. P., Hayyan, M., Wong, W. F., Looi, C. Y. & Hashim, M. A. Unraveling the cytotoxicity and metabolic pathways of binary natural deep eutectic solvent systems. *Sci. Rep.* **7,** 41257 (2017).

198. De Maria, P. D. & Maugeri, Z. Ionic liquids in biotransformations: from proof-of-concept to emerging deep-eutectic-solvents. *Curr. Opin. Chem. Biol.* **15,** 220–225 (2011).

199. Francisco Casal, M, van den Bruinhorst, A & Kroon, M. New natural renewable low transition temperature mixtures (LTTMs): screening as solvents for lignocellulosic biomass processing. *Green Chem.* **14,** 2153–2157 (2012).

200. Xia, S., Baker, G. A., Li, H., Ravula, S. & Zhao, H. Aqueous ionic liquids and deep eutectic solvents for cellulosic biomass pretreatment and saccharification. *RSC Adv.* **4,** 10586–10596 (2014).

201. Jhong, H.-R., Wong, D. S.-H., Wan, C.-C., Wang, Y.-Y. & Wei, T.-C. A novel deep eutectic solvent-based ionic liquid used as electrolyte for dye-sensitized solar cells. *Electrochem. Commun.* **11,** 209–211 (2009).

202. Ruß, C. & König, B. Low melting mixtures in organic synthesis–an alternative to ionic liquids? *Green Chem.* **14,** 2969–2982 (2012).

203. Nkuku, C. A. & LeSuer, R. J. Electrochemistry in deep eutectic solvents. *J. Phys. Chem. B* **111,** 13271–13277 (2007).

204. Zhao, H. & Baker, G. A. Ionic liquids and deep eutectic solvents for biodiesel synthesis: a review. *J. Chem. Technol. Biotechnol.* **88,** 3–12 (2013).

205. Sharma, M., Mukesh, C., Mondal, D. & Prasad, K. Dissolution of α-chitin in deep eutectic solvents. *RSC Adv.* **3,** 18149–18155 (2013).

206. Bi, W., Tian, M. & Row, K. H. Evaluation of alcohol-based deep eutectic solvent in extraction and determination of flavonoids with response surface methodology optimization. *J. Chromatogr. A* **1285,** 22–30 (2013).

207. Duan, L., Guo, L., Liu, K., Liu, E.-H. & Li, P. Characterization and classification of seven Citrus herbs by liquid chromatography–quadrupole time-of-flight mass spectrometry and genetic algorithm optimized support vector machines. *J. Chromatogr. A* **1339,** 118–127 (2014).

208. Duan, L., Dou, L.-L., Guo, L., Li, P. & Liu, E.-H. Comprehensive evaluation of deep eutectic solvents in extraction of bioactive natural products. *ACS Sustain. Chem. Eng.* **4,** 2405–2411 (2016).

209. Leron, R. B. & Li, M.-H. Solubility of carbon dioxide in a choline chloride–ethylene glycol based deep eutectic solvent. *Thermochim. Acta* **551,** 14–19 (2013).

210. Li, Z. *Investigation of Deep Eutectic Solvents and Their Derivatives for Pharmaceutical Applications* PhD thesis (Graduate Department of Pharmaceutical Sciences, University of Toronto, 2015).

211. Aroso, I. M. *et al.* Dissolution enhancement of active pharmaceutical ingredients by therapeutic deep eutectic systems. *Eur. J. Pharm. Biopharm.* **98,** 57–66 (2016).

212. Mamajanov, I., Engelhart, A. E., Bean, H. D. & Hud, N. V. DNA and RNA in anhydrous media: Duplex, triplex, and G-quadruplex secondary structures in a deep eutectic solvent. *Angew. Chem. Int. Ed.* **49,** 6310–6314 (2010).

213. Lannan, F. M., Mamajanov, I. & Hud, N. V. Human telomere sequence DNA in water-free and high-viscosity solvents: G-quadruplex folding governed by Kramers rate theory. *J. Am. Chem. Soc.* **134,** 15324–15330 (2012).

214. Abbott, A. P. *et al.* Glycerol eutectics as sustainable solvent systems. *Green Chem.* **13,** 82–90 (2011).

215. Shahbaz, K., Mjalli, F., Hashim, M. & AlNashef, I. Prediction of deep eutectic solvents densities at different temperatures. *Thermochim. Acta* **515,** 67 –72. ISSN: 0040-6031. `http://www.sciencedirect.com/science/article/pii/S0040603111000050` (2011).

216. Liu, Y. *et al.* Self-Assembly and Characterization of Hydrogen-Bond-Induced Nanostructure Aggregation. *Chem. Phys. Chem.* **5,** 1210–1215 (2004).

217. Mbous, Y. P. *et al.* Applications of deep eutectic solvents in biotechnology and bioengineering—Promises and challenges. *Biotechnol. Adv.* **35,** 105 –134. ISSN: 0734-9750. `http://www.sciencedirect.com/science/article/pii/S0734975016301525` (2017).

218. Abbott, A. P., Harris, R. C. & Ryder, K. S. Application of Hole Theory to Define Ionic Liquids by their Transport Properties. *J. Phys. Chem. B* **111.** PMID: 17388488, 4910–4913. eprint: `https://doi.org/10.1021/jp0671998`. `https://doi.org/10.1021/jp0671998` (2007).

219. Mie, G. Zur kinetischen Theorie der einatomigen Körper. *Ann. Phys.* **316,** 657–697 (1903).

220. Grüneisen, E. Theorie des festen Zustandes einatomiger Elemente. *Ann. Phys.* **344,** 257–306 (1912).

221. Pauli, W. On the connexion between the completion of electron groups in an atom with the complex structure of spectra. *Z. Phys.* **31,** 765 (1925).

222. London, F. The general theory of molecular forces. *Trans. Faraday Soc.* **33,** 8b–26 (1937).

223. Fürth, R. On the equation of state for solids. *Proc. Roy. Soc. London* **183,** 87–110 (1944).

224. Jones, J. E. On the determination of molecular fields. I. - From the variation of the viscosity of a gas with temperature. *Proc. Roy. Soc. London* **106,** 441–462 (1924).

225. Jones, J. E. On the determination of molecular fields. II. - From the equation of state of a gas. *Proc. Roy. Soc. London* **106,** 463–477 (1924).

226. Jones, J. On the determination of molecular fields. III. - From crystal measurements and kinetic theory data. *Proc. Roy. Soc. London* **106,** 709–718 (1924).

227. Buckingham, R. A. The classical equation of state of gaseous helium, neon and argon. *Proc. Roy. Soc. London* **168,** 264–283 (1938).

228. Mason, E. A. Transport Properties of Gases Obeying a Modified Buckingham (Exp-Six) Potential. *J. Chem. Phys.* **22,** 169–186 (1954).

229. Hemmen, A. & Gross, J. Transferable anisotropic united-atom force field based on the Mie potential for phase equilibrium calculations: n-alkanes and n-olefins. *J. Phys. Chem. B* **119,** 11695–11707 (2015).

230. Hemmen, A., Panagiotopoulos, A. Z. & Gross, J. Grand Canonical Monte Carlo Simulations Guided by an Analytic Equation of State Transferable Anisotropic Mie Potentials for Ethers. *J. Phys. Chem. B* **119,** 7087–7099 (2015).

231. Weidler, D. & Gross, J. Transferable Anisotropic United-Atom Force Field Based on the Mie Potential for Phase Equilibria: Aldehydes, Ketones, and Small Cyclic Alkanes. *Ind. Eng. Chem. Res.* **55,** 12123–12132 (2016).

232. Weidler, D. & Gross, J. Individualized force fields for alkanes, olefins, ethers and ketones based on the transferable anisotropic Mie potential. *Fluid Phase Equilib.* **470,** 101–108 (2018).

233. Waibel, C., Stierle, R. & Gross, J. Transferability of cross-interaction pair potentials: Vapor-liquid phase equilibria of n-alkane/nitrogen mixtures using the TAMie force field. *Fluid Phase Equilib.* **456,** 124–130 (2018).

234. Scheller, W. Grain alcohol as renewable energy and automotive fuel. *Starch-Staerke* **33,** 1–4 (1981).

235. Lombardo, D., Kiselev, M. A., Magazù, S. & Calandra, P. Amphiphiles Self-Assembly: Basic Concepts and Future Perspectives of Supramolecular Approaches. *Adv. Condens. Matter Phys.* **2015** (2015).

236. Turchanin, A. *et al.* One Nanometer Thin Carbon Nanosheets With Tunable Conductivity and Stiffness. *Adv. Mater.* **21,** 1233–1237 (2009).

237. Choucair, A., Lim Soo, P. & Eisenberg, A. Active Loading and Tunable Release of Doxorubicin From Block Copolymer Vesicles. *Langmuir* **21,** 9308–9313 (2005).

238. Ballesteros-Gómez, A., Sicilia, M. D. & Rubio, S. Supramolecular Solvents in the Extraction of Organic Compounds. A Review. *Anal. Chim. Acta* **677,** 108–130 (2010).

239. Krieg, E., Albeck, S., Weissman, H., Shimoni, E. & Rybtchinski, B. Separation, Immobilization, and Biocatalytic Utilization of Proteins by a Supramolecular Membrane. *PLoS One* **8,** e63188 (2013).

240. Yin, J.-J., Zhou, Z.-W. & Zhou, S.-F. Cyclodextrin-Based Targeting Strategies for Tumor Treatment. *Drug Deliv. and Transl. Res.* **3,** 364–374 (2013).

241. Nagarajan, R. Self-Assembly of Bola Amphiphiles. *Chem. Eng. Commun.* **55,** 251–273 (1987).

242. Dhasaiyan, P. & Prasad, B. L. Self-Assembly of Bolaamphiphilic Molecules. *Chem. Rev.* **17,** 597–610 (2017).

243. Krieg, E., Bastings, M. M. C., Besenius, P. & Rybtchinski, B. Supramolecular Polymers in Aqueous Media. *Chem. Rev* **116,** 2414–2477 (2016).

244. Würthner, F. *et al.* Perylene Bisimide Dye Assemblies as Archetype Functional Supramolecular Materials. *Chem. Rev.* **116,** 962–1052 (2016).

245. Sung, J., Kim, P., Fimmel, B., Würthner, F. & Kim, D. Direct Observation of Ultrafast Coherent Exciton Dynamics in Helical π-Stacks of Self-Assembled Perylene Bisimides. *Nat. Commun.* **6,** 8646 (2015).

246. Ogasawara, M. *et al.* Water-Induced Self-Assembly of an Amphiphilic Perylene Bisimide Dyad Into Vesicles, Fibers, Coils, and Rings. *Mater. Chem. Front.* **2,** 171–179 (2018).

247. Hua, L., Zangi, R. & Berne, B. J. Hydrophobic Interactions and Dewetting Between Plates With Hydrophobic and Hydrophilic Domains. *J. Phys. Chem. C* **113,** 5244–5253 (2009).

248. Hillyer, M. B. & Gibb, B. C. Molecular Shape and the Hydrophobic Effect. *Annu. Rev. Phys. Chem.* **67,** 307–329 (2016).

249. Jeong, K.-J. & Yethiraj, A. The Driving Force for the Association of Gemini Surfactants. *J. Phys. Chem. B* **122,** 3259–3265 (2018).

250. Engstler, J. & Giovambattista, N. Temperature Effects on Water-Mediated Interactions at the Nanoscale. *J. Phys. Chem. B* **122,** 8908–8920 (2018).

251. van der Vegt, N. F. A. & Nayar, D. The Hydrophobic Effect and the Role of Cosolvents. *J. Phys. Chem. B* **121,** 9986–9998 (2017).

252. Xu, X., Kanduč, M., Wu, J. & Dzubiella, J. Potential of Mean Force and Transient States in Polyelectrolyte Pair Complexation. *J. Chem. Phys.* **145,** 034901 (2016).

253. Frederix, P. W., Patmanidis, I. & Marrink, S. J. Molecular Simulations of Self-Assembling Bio-Inspired Supramolecular Systems and Their Connection to Experiments. *Chem. Soc. Rev.* **47,** 3470–3489 (2018).

254. Bottaro, S. & Lindorff-Larsen, K. Biophysical Experiments and Biomolecular Simulations: A Perfect Match? *Science* **361,** 355–360 (2018).

255. Ford, W. E. Photochemistry of 3,4,9,10-Perylenetetracarboxylic Dianhydride Dyes: Visible Absorption and Fluorescence of the Di(glycyl) Imide Derivative Monomer and Dimer in Basic Aqueous Solutions. *J. Photochem.* **37,** 189–204 (1987).

256. Schmid, N. *et al.* Definition and Testing of The GROMOS Force-Field Versions 54A7 and 54B7. *Eur. Biophys. J.* **40,** 843–856 (2011).

257. Malde, A. K. *et al.* An Automated Force Field Topology Builder (ATB) and Repository: Version 1.0. *J. Chem. Theory Comput.* **7,** 4026–4037 (2011).

258. Baz, J., Gebhardt, J., Kraus, H., Markthaler, D. & Hansen, N. Insights into Noncovalent Binding Obtained from Molecular Dynamics Simulations. *Chem. Ing. Tech.* **in press.** doi:10.1002/cite.201800050 (2018).

259. Berendsen, H. J. C., Postma, J. P. M., van Gunsteren, W. F. & Hermans, J. in *Intermolecular Forces* (ed Pullmann, B.) 331–342 (Reidel, Dordrecht, the Netherlands, 1981).

260. Reif, M. M. & Hünenberger, P. H. Computation of Methodology-Independent Single-Ion Solvation Properties From Molecular Simulations. IV. Optimized Lennard-Jones Interaction Parameter Sets for The Alkali and Halide Ions in Water. *J. Chem. Phys.* **134,** 144104 (2011).

261. Berendsen, H. J. C., van der Spoel, D. & van Drunen, R. GROMACS: A Message-Passing Parallel Molecular Dynamics Implementation. *Comput. Phys. Commun.* **91,** 43–56 (1995).

262. Hess, B., Kutzner, C., Van Der Spoel, D. & Lindahl, E. GROMACS 4: Algorithms for Highly Efficient, Load-Balanced, and Scalable Molecular Simulation. *J. Chem. Theory Comput.* **4,** 435–447 (2008).

263. Abraham, M. J. *et al.* GROMACS: High Performance Molecular Simulations Through Multi-Level Parallelism From Laptops to Supercomputers. *SoftwareX* **1,** 19–25 (2015).

264. Tribello, G. A., Bonomi, M., Branduardi, D., Camilloni, C. & Bussi, G. PLUMED 2: New Feathers for an Old Bird. *Comput. Phys. Commun.* **185,** 604–613 (2014).

265. Hockney, R. W. The Potential Calculation and Some Applications. *Methods Comput. Phys.* **9,** 136–211 (1970).

266. Miyamoto, S. & Kollman, P. A. SETTLE: An Analytical Version of The SHAKE and RATTLE Algorithm for Rigid Water Models. *J. Comput. Chem.* **13,** 952–962 (1992).

267. Hess, B. P-LINCS: A Parallel Linear Constraint Solver for Molecular Simulation. *J. Chem. Theory Comput.* **4,** 116–122 (2008).

268. Hess, B., Bekker, H., Berendsen, H. J. C. & Fraaije, J. G. E. M. LINCS: A Linear Constraint Solver for Molecular Simulations. *J. Comput. Chem.* **18,** 1463–1472 (1997).

269. Bussi, G., Donadio, D. & Parrinello, M. Canonical Sampling Through Velocity Rescaling. *J. Chem. Phys.* **126,** 014101 (2007).

270. Parrinello, M. & Rahman, A. Polymorphic Transitions in Single Crystals: A New Molecular Dynamics Method. *J. Appl. Phys.* **52,** 7182–7190 (1981).

271. Nosé, S. & Klein, M. L. Constant Pressure Molecular Dynamics for Molecular Systems. *Mol. Phys.* **50,** 1055–1076 (1983).

272. Páll, S. & Hess, B. A Flexible Algorithm for Calculating Pair Interactions on SIMD Architectures. *Comput. Phys. Commun.* **184,** 2641–2650 (2013).

273. Nymand, T. M. & Linse, P. Ewald Summation and Reaction Field Methods for Potentials With Atomic Charges, Dipoles, and Polarizabilities. *J. Chem. Phys.* **112,** 6152–6160 (2000).

274. Darden, T., York, D. & Pedersen, L. Particle Mesh Ewald: An N · log (N) Method for Ewald Sums in Large Systems. *J. Chem. Phys.* **98,** 10089–10092 (1993).

275. Torrie, G. M. & Valleau, J. P. Nonphysical Sampling Distributions in Monte Carlo Free-Energy Estimation: Umbrella Sampling. *J. Comput. Phys.* **23,** 187–199 (1977).

276. Chodera, J. D. *https://github.com/choderalab/pymbar* Accessed on November 28, 2017.

277. Shirts, M. R. & Chodera, J. D. Statistically Optimal Analysis of Samples From Multiple Equilibrium States. *J. Chem. Phys.* **129,** 124105 (2008).

278. De Jong, D. H. *et al.* Determining Equilibrium Constants for Dimerization Reactions From Molecular Dynamics Simulations. *J. Comput. Chem.* **32,** 1919–1928 (2011).

279. Fenley, A. T., Henriksen, N. M., Muddana, H. S. & Gilson, M. K. Bridging Calorimetry and Simulation Through Precise Calculations of Cucurbituril–Guest Binding Enthalpies. *J. Chem. Theory Comput.* **10,** 4069–4078 (2014).

280. Zwanzig, R. W. High-Temperature Equation of State by a Perturbation Method. I. Nonpolar Gases. *J. Chem. Phys.* **22,** 1420–1426 (1954).

281. Barker, J. A. & Henderson, D. Perturbation theory and equation of state for fluids: the square-well potential. *J. Chem. Phys.* **47,** 2856–2861 (1967).

282. Bauer, G., Lange, A., Gribova, N., Holm, C. & Gross, J. Effective Potentials Between Gold Nano Crystals–Functional Dependence on Temperature. *Mol. Simul.* **41,** 1153–1158 (2015).

283. Trzesniak, D., Kunz, A.-P. E. & van Gunsteren, W. F. A Comparison of Methods to Compute The Potential of Mean Force. *Chem. Phys. Chem.* **8,** 162–169 (2007).

284. Henderson, D., Blum, L. & Tani, A. Equation of State of Ionic Fluids. *ACS Symp. Ser.* **300,** 281–296 (1986).

285. Sedlmeier, F. *et al.* Water at Polar and Nonpolar Solid Walls. *Biointerphases* **3,** FC23 (2008).

286. Jamadagni, S. N., Godawat, R. & Garde, S. Hydrophobicity of Proteins and Interphases: Insights from Density Fluctuations. *Annu. Rev. Chem. Biomol. Eng.* **2,** 147–171 (2011).

287. Ardham, V. R. & Leroy, F. Thermodynamics of Atomistic and Coarse-Grained Models of Water on Nonpolar Surfaces. *J. Chem. Phys.* **147,** 074702 (2017).

288. Zangi, R. & Berne, B. J. Temperature Dependence of Dimerization and Dewetting of Large-Scale Hydrophobes: A Molecular Dynamics Study. *J. Phys. Chem. B* **112,** 8634–8644 (2008).

289. Mondal, J. & Yethiraj, A. Driving Forces for The Association of Amphiphilic Molecules. *J. Phys. Chem. Lett.* **2,** 2391–2395 (2011).

290. Yu, T., Lee, O.-S. & Schatz, G. C. Steered Molecular Dynamics Studies of The Potential of Mean Force for Peptide Amphiphile Self-Assembly Into Cylindrical Nanofibers. *J. Phys. Chem. A* **117,** 7453–7460 (2013).

291. Kawaguchi, S. & Kuramitsu, S. Thermodynamics and Molecular Simulation Analysis of Hydrophobic Substrate Recognition by Aminotransferases. *J. Biol. Chem.* **273,** 18353–18364 (1998).

292. LiCata, V. J. & Liu, C.-C. Analysis of Free Energy Versus Temperature Curves in Protein Folding and Macromolecular Interactions. *Methods Enzymol.* **488,** 219–238 (2011).

293. Henriksen, N. M., Fenley, A. T. & Gilson, M. K. Computational Calorimetry: High-Precision Calculation of Host-Guest Binding Thermodynamics. *J. Chem. Theory Comput.* **11,** 4377–4394 (2015).

294. Dahlgren, B., Reif, M. M., Hünenberger, P. H. & Hansen, N. Calculation of Derivative Thermodynamic Hydration and Aqueous Partial Molar Properties of Ions Based on Atomistic Simulations. *J. Chem. Theory Comput.* **8,** 3542–3564 (2012).

295. Roseman, M. & Jencks, W. P. Interactions of Urea and Other Polar Compounds in Water. *J. Am. Chem. Soc.* **97,** 631–640 (1975).

296. Yu, H.-A. & Karplus, M. A Thermodynamic Analysis of Solvation. *J. Chem. Phys.* **89,** 2366–2379 (1988).

297. Moučka, F., Nezbeda, I. & Smith, W. R. Molecular Force Fields for Aqueous Electrolytes: SPC/E-Compatible Charged LJ Sphere Models and Their Limitations. *J. Chem. Phys.* **138,** 154102 (2013).

298. Vaisman, I. I. & Berkowitz, M. L. Local Structural Order and Molecular Associations in Water-DMSO Mixtures. Molecular Dynamics Study. *J. Am. Chem. Soc.* **114,** 7889–7896 (1992).

299. Zangi, R., Hagen, M. & Berne, B. J. Effect of Ions on The Hydrophobic Interaction Between Two Plates. *J. Am. Chem. Soc.* **129,** 4678–4686 (2007).

300. van der Vegt, N. F. A., Lee, M.-E., Trzesniak, D. & van Gunsteren, W. F. Enthalpy-Entropy Compensation in the Effects of Urea on Hydrophobic Interactions. *J. Phys. Chem. B* **110,** 12852–12855 (2006).

301. Haverkort, F., Stradomska, A. & Knoester, J. First-Principles Simulations of the Initial Phase of Self-Aggregation of a Cyanine Dye: Structure and Optical Spectra. *J. Phys. Chem. B* **118,** 8877–8890 (2014).

302. Engels, B. & Engel, V. The dimer-approach to characterize opto-electronic properties of and exciton trapping and diffusion in organic semiconductor aggregates and crystals. *Phys. Chem. Chem. Phys.* **19,** 12604–12619 (2017).

303. Gay, J. G. & Berne, B. J. Modification of The Overlap Potential to Mimic a Linear Site-Site Potential. *J. Chem. Phys.* **74,** 3316–3319 (1981).

304. Martin, R. B. Comparisons of Indefinite Self-Association Models. *Chem. Rev.* **96,** 3043–3064 (1996).

305. Kim, S. H. *et al.* Effect of deep eutectic solvent mixtures on lipase activity and stability. *J. Mol. Catal. B: Enzym.* **128,** 65–72 (2016).

306. Stepankova, V *et al. Strategies for stabilization of enzymes in organic solvents. ACS Catal 3: 2823–2836* 2013.

307. Blandamer, M. J., Engberts, J. B., Gleeson, P. T. & Reis, J. C. R. Activity of water in aqueous systems; a frequently neglected property. *Chem. Soc. Rev.* **34,** 440–458 (2005).

308. Ma, C., Laaksonen, A., Liu, C., Lu, X. & Ji, X. The peculiar effect of water on ionic liquids and deep eutectic solvents. *Chem. Soc. Rev.* **47,** 8685–8720 (2018).

309. Hammond, O. S., Bowron, D. T. & Edler, K. J. The effect of water upon deep eutectic solvent nanostructure: An unusual transition from ionic mixture to aqueous solution. *Angew. Chem. Int. Ed.* **56,** 9782–9785 (2017).

310. Dietz, C. H. *et al.* PC-SAFT modeling of CO2 solubilities in hydrophobic deep eutectic solvents. *Fluid Phase Equilib.* **448,** 94–98 (2017).

311. Zubeir, L. F., Held, C., Sadowski, G. & Kroon, M. C. PC-SAFT modeling of CO2 solubilities in deep eutectic solvents. *J. Phys. Chem. B* **120,** 2300–2310 (2016).

312. Verevkin, S. P. *et al.* Separation performance of BioRenewable deep eutectic solvents. *Ind. Eng. Chem. Res.* **54,** 3498–3504 (2015).

313. Gross, J. & Sadowski, G. Perturbed-chain SAFT: An equation of state based on a perturbation theory for chain molecules. *Ind. Eng. Chem. Res.* **40,** 1244–1260 (2001).

314. Mainberger, S. *et al.* Deep eutectic solvent formation: a structural view using molecular dynamics simulations with classical force fields. *Mol. Phys.* **115,** 1309–1321 (2017).

315. Perkins, S. L., Painter, P. & Colina, C. M. Experimental and computational studies of choline chloride-based deep eutectic solvents. *J. Chem. Eng. Data* **59,** 3652–3662 (2014).

316. Ferreira, E. S., Voroshylova, I. V., Pereira, C. M. & DS Cordeiro, M. N. Improved Force Field Model for the Deep Eutectic Solvent Ethaline: Reliable Physicochemical Properties. *J. Phys. Chem. B* **120,** 10124–10137 (2016).

317. Ahmadi, R. *et al.* Deep Eutectic-Water Binary Solvent Associations Investigated by Vibrational Spectroscopy and Chemometrics. *Phys. Chem. Chem. Phys.* (2018).

318. Weng, L. & Toner, M. Janus-faced role of water in defining nanostructure of choline chloride/glycerol deep eutectic solvent. *Phys. Chem. Chem. Phys.* **20,** 22455–22462 (2018).

319. Zhekenov, T., Toksanbayev, N., Kazakbayeva, Z., Shah, D. & Mjalli, F. S. Formation of type III Deep Eutectic Solvents and effect of water on their intermolecular interactions. *Fluid Phase Equilib.* **441,** 43–48 (2017).

320. Wang, J., Wolf, R. M., Caldwell, J. W., Kollman, P. A. & Case, D. A. Development and testing of a general amber force field. *J. Comput. Chem.* **25,** 1157–1174 (2004).

321. Perkins, S. L., Painter, P. & Colina, C. M. Molecular dynamic simulations and vibrational analysis of an ionic liquid analogue. *J. Phys. Chem. B* **117,** 10250–10260 (2013).

322. Leontyev, I. & Stuchebrukhov, A. Accounting for electronic polarization in non-polarizable force fields. *Phys. Chem. Chem. Phys.* **13,** 2613–2626 (2011).

323. Mobley, D. L. & Guthrie, J. P. FreeSolv: a database of experimental and calculated hydration free energies, with input files. *J. Comput. -Aided Mol. Des.* **28,** 711–720 (2014).

324. Case, D. A. *et al.* AMBER 10 Manual. *University of California, San Francisco* **10** (2008).

325. Wang, J., Wang, W., Kollman, P. A. & Case, D. A. Automatic atom type and bond type perception in molecular mechanical calculations. *J. Mol. Graphics Modell* **25,** 247–260 (2006).

326. Bayly, C. I., Cieplak, P., Cornell, W. & Kollman, P. A. A well-behaved electrostatic potential based method using charge restraints for deriving atomic charges: the RESP model. *J. Phys. Chem.* **97,** 10269–10280 (1993).

327. Horn, H. W. *et al.* Development of an improved four-site water model for biomolecular simulations: TIP4P-Ew. *J. Chem. Phys.* **120,** 9665–9678 (2004).

328. Jorgensen, W. L., Chandrasekhar, J., Madura, J. D., Impey, R. W. & Klein, M. L. Comparison of simple potential functions for simulating liquid water. *J. Chem. Phys.* **79,** 926–935 (1983).

329. Berendsen, H. J. C., Grigera, J. R., Straatsma, T. P., *et al.* The missing term in effective pair potentials. *J. Phys. Chem.* **91,** 6269–6271 (1987).

330. Kusalik, P. G. & Svishchev, I. M. The spatial structure in liquid water. *Science* **265,** 1219–1221 (1994).

331. Yadav, A., Trivedi, S., Rai, R. & Pandey, S. Densities and dynamic viscosities of (choline chloride+ glycerol) deep eutectic solvent and its aqueous mixtures in the temperature range (283.15–363.15) K. *Fluid Phase Equilib.* **367,** 135–142 (2014).

332. Wu, S.-H., Caparanga, A. R., Leron, R. B. & Li, M.-H. Vapor pressure of aqueous choline chloride-based deep eutectic solvents (ethaline, glyceline, maline and reline) at 30–70 C. *Thermochim. Acta* **544,** 1–5 (2012).

333. Bekker, H *et al. GROMACS: A parallel computer for molecular dynamics simulations* in *Physics computing* **92** (1993), 252–256.

334. Lindahl, E., Hess, B. & Van Der Spoel, D. GROMACS 3.0: a package for molecular simulation and trajectory analysis. *Mol. mod. ann.* **7,** 306–317 (2001).

335. Pall, S., Abraham, M. J., Kutzner, C., Hess, B. & Lindahl, E. *Tackling exascale software challenges in molecular dynamics simulations with GROMACS* in *International Conference on Exascale Applications and Software* (2014), 3–27.

336. Pronk, S. *et al.* GROMACS 4.5: a high-throughput and highly parallel open source molecular simulation toolkit. *Bioinformatics* **29,** 845–854 (2013).

337. Hess, B. Determining the shear viscosity of model liquids from molecular dynamics simulations. *J. Chem. Phys.* **116,** 209–217 (2002).

338. Smith, P. E. & van Gunsteren, W. F. The viscosity of SPC and SPC/E water at 277 and 300 K. *Chem. Phys. Lett.* **215,** 315–318 (1993).

339. Holian, B. L. & Evans, D. J. Shear viscosities away from the melting line: A comparison of equilibrium and nonequilibrium molecular dynamics. *J. Chem. Phys.* **78,** 5147–5150 (1983).

340. Wiener, N. Generalized harmonic analysis. *Acta Math.* **55,** 117–258 (1930).

341. Khintchine, A. Korrelationstheorie der stationären stochastischen Prozesse. *Math. Ann.* **109,** 604–615 (1934).

342. Calandrini, V., Pellegrini, E., Calligari, P., Hinsen, K. & Kneller, G. R. nMoldyn-Interfacing spectroscopic experiments, molecular dynamics simulations and models for time correlation functions. *École thématique de la Société Française de la Neutronique* **12,** 201–232 (2011).

343. Zhang, Y., Otani, A. & Maginn, E. J. Reliable viscosity calculation from equilibrium molecular dynamics simulations: a time decomposition method. *J. Chem. Theory Comput.* **11,** 3537–3546 (2015).

344. Einstein, A. Über die von der molekularkinetischen Theorie der Wärme geforderte Bewegung von in ruhenden Flüssigkeiten suspendierten Teilchen. *Ann. Phys.* **322,** 549–560 (1905).

345. Allen, M. P. & Tildesley, D. J. *Computer simulation of liquids* (Oxford university press, 1987).

346. Yeh, I.-C. & Hummer, G. System-size dependence of diffusion coefficients and viscosities from molecular dynamics simulations with periodic boundary conditions. *J. Phys. Chem. B* **108,** 15873–15879 (2004).

347. Klimovich, P. V., Shirts, M. R. & Mobley, D. L. Guidelines for the analysis of free energy calculations. *J. Comput. -Aided Mol. Des.* **29,** 397–411 (2015).

348. Hempel, S. & Sadowski, G. Water activity coefficients in aqueous amino acid solutions by molecular dynamics simulation: 1. Force field development. *Mol. Simul.* **38,** 132–138 (2012).

349. Raabe, G. *Molecular Simulation Studies on Thermophysical Properties* (Springer, 2017).

350. Fuchs, D., Fischer, J., Tumakaka, F. & Sadowski, G. Solubility of amino acids: influence of the pH value and the addition of alcoholic cosolvents on aqueous solubility. *Ind. Eng. Chem. Res.* **45,** 6578–6584 (2006).

351. Hübner, M., Lodziak, C., Do, H. T. J. & Held, C. Measuring and modeling thermodynamic properties of aqueous lysozyme and BSA solutions. *Fluid Phase Equilib.* **472,** 62–74 (2018).

352. Held, C., Reschke, T., Mohammad, S., Luza, A. & Sadowski, G. ePC-SAFT revised. *Chem. Eng. Res. Des.* **92,** 2884–2897 (2014).

353. Chua, Y. Z., Do, H. T., Schick, C., Zaitsau, D. & Held, C. New experimental melting properties as access for predicting amino-acid solubility. *RSC Adv.* **8,** 6365–6372 (2018).

354. Held, C., Sadowski, G., Carneiro, A., Rodríguez, O. & Macedo, E. A. Modeling thermodynamic properties of aqueous single-solute and multi-solute sugar solutions with PC-SAFT. *AIChE J.* **59,** 4794–4805 (2013).

355. Held, C. & Sadowski, G. Compatible solutes: Thermodynamic properties relevant for effective protection against osmotic stress. *Fluid Phase Equilib.* **407,** 224–235 (2016).

356. Leron, R. B., Soriano, A. N. & Li, M.-H. Densities and refractive indices of the deep eutectic solvents (choline chloride+ ethylene glycol or glycerol) and their aqueous mixtures at the temperature ranging from 298.15 to 333.15 K. *J. Taiwan Inst. Chem. Eng.* **43,** 551–557 (2012).

357. Leal-Duaso, A., Pérez, P., Mayoral, J. A., Pires, E. & García, J. I. Glycerol as a source of designer solvents: physicochemical properties of low melting mixtures containing glycerol ethers and ammonium salts. *Phys. Chem. Chem. Phys.* **19,** 28302–28312 (2017).

358. Doherty, B. & Acevedo, O. OPLS force field for choline chloride-based deep eutectic solvents. *J. Phys. Chem. B* **122,** 9982–9993 (2018).

359. Mjalli, F. S. & Jabbar, N. M. A. Acoustic investigation of choline chloride based ionic liquids analogs. *Fluid Phase Equilib.* **381,** 71–76 (2014).

360. Jahn, D. A., Akinkunmi, F. O. & Giovambattista, N. Effects of Temperature on the Properties of Glycerol: A Computer Simulation Study of Five Different Force Fields. *J. Phys. Chem. B* **118,** 11284–11294 (2014).

361. Stefanovic, R., Ludwig, M., Webber, G. B., Atkin, R. & Page, A. J. Nanostructure, hydrogen bonding and rheology in choline chloride deep eutectic solvents as a function of the hydrogen bond donor. *Phys. Chem. Chem. Phys.* **19,** 3297–3306 (2017).

362. Horn, H. W., Swope, W. C. & Pitera, J. W. Characterization of the TIP4P-Ew water model: Vapor pressure and boiling point. *J. Chem. Phys.* **123,** 194504 (2005).

363. Holz, M., Heil, S. R. & Sacco, A. Temperature-dependent self-diffusion coefficients of water and six selected molecular liquids for calibration in accurate 1H NMR PFG measurements. *Phys. Chem. Chem. Phys.* **2,** 4740–4742. `https://doi.org/10.1039/b005319h` (2000).

364. Simpson, J. & Carr, H. Diffusion and nuclear spin relaxation in water. *Phys. Rev.* **111,** 1201 (1958).

365. Yoshida, K., Matubayasi, N. & Nakahara, M. Self-diffusion coefficients for water and organic solvents at high temperatures along the coexistence curve. *J. Chem. Phys.* **129,** 214501 (2008).

366. D'Agostino, C. *et al.* Molecular and ionic diffusion in aqueous–deep eutectic solvent mixtures: probing inter-molecular interactions using PFG NMR. *Phys. Chem. Chem. Phys.* **17,** 15297–15304 (2015).

367. Durand, E. *et al.* Evaluation of deep eutectic solvent–water binary mixtures for lipase-catalyzed lipophilization of phenolic acids. *Green Chem.* **15,** 2275–2282 (2013).

368. Jamali, S. H. *et al.* Shear Viscosity Computed from the Finite-Size Effects of Self-Diffusivity in Equilibrium Molecular Dynamics. *J. Chem. Theory Comput.* **14,** 5959–5968 (2018).

369. Borodin, O., Smith, G. D. & Kim, H. Viscosity of a room temperature ionic liquid: predictions from nonequilibrium and equilibrium molecular dynamics simulations. *J. Phys. Chem. B* **113,** 4771–4774 (2009).

370. Heyes, D., Dini, D & Smith, E. Incremental viscosity by non-equilibrium molecular dynamics and the Eyring model. *J. Chem. Phys.* **148,** 194506 (2018).

371. Maginn, E. J., Messerly, R. A., Carlson, D. J., Roe, D. R. & Elliott, J. R. Best Practices for Computing Transport Properties 1. Self-Diffusivity and Viscosity from Equilibrium Molecular Dynamics [Article v1. 0]. *LiveCoMS* **1,** 6324 (2018).

372. Moine, E., Privat, R., Sirjean, B. & Jaubert, J.-N. Estimation of Solvation Quantities from Experimental Thermodynamic Data: Development of the Comprehensive CompSol Databank for Pure and Mixed Solutes. *J. Phys. Chem. Ref. Data* **46,** 033102 (2017).

373. Ferrario, V., Hansen, N. & Pleiss, J. Interpretation of cytochrome P450 monooxygenase kinetics by modeling of thermodynamic activity. *J. Inorg. Biochem.* **183,** 172–178 (2018).

374. Jorgensen, W. L. & Madura, J. D. Temperature and size dependence for Monte Carlo simulations of TIP4P water. *Mol. Phys.* **56,** 1381–1392 (1985).

375. Mahoney, M. W. & Jorgensen, W. L. A five-site model for liquid water and the reproduction of the density anomaly by rigid, nonpolarizable potential functions. *J. Chem. Phys.* **112,** 8910–8922 (2000).

376. Ketko, M. B. H. & Potoff, J. J. Effect of partial charge parameterization on the phase equilibria of dimethyl ether. *Mol. Simul.* **33,** 769–776 (2007).

377. Jorgensen, W. L., Madura, J. D. & Swenson, C. J. Optimized intermolecular potential functions for liquid hydrocarbons. *J. Am. Chem. Soc.* **106,** 6638–6646 (1984).

378. Jorgensen, W. L. & Swenson, C. J. Optimized Intermolelcular Potential Functions for Amides and Peptides. Structure and Properties of Liquid Amides. *J. Am. Chem. Soc.* **107,** 569–578 (1985).

379. Jorgensen, W. L. & Swenson, C. J. Optimized Intermolelcular Potential Functions for Amides and Peptides. Hydration of Amides. *J. Am. Chem. Soc.* **107,** 1489–1496 (1985).

380. Jorgensen, W. L. Optimized Intermolecular Potential Functions for Liquid Alcohols. *J. Phys. Chem.* **90,** 1276–1284 (1986).

381. Jorgensen, W. L. & Tirado-Rives, J. The OPLS Force Field for Proteins. Energy Minimization for Crystals of Cyclic Peptides and Crambin. *J. Am. Chem. Soc.* **110,** 1657–1666 (1988).

382. Briggs, J. M., Matsui, T. & Jorgensen, W. L. Monte Carlo Simulations of Liquid Alkyl Ethers with the OPLS Potential Functions. *J. Comput. Chem.* **11,** 958–971 (1990).

383. Martin, M. G. & Siepmann, J. I. Novel Configurational-Bias Monte Carlo Method for Branched Molecules. Transferable Potentials for Phase Equilibria. 2. United-Atom Description of Branched Alkanes. *J. Phys. Chem. B* **103,** 4508–4517 (1999).

384. Chen, B. & Siepmann, J. I. Transferable Potentials for Phase Equilibria. 3. Explicit-Hydrogen Description of Normal Alkanes. *J. Phys. Chem. B* **103,** 5370–5379 (1999).

385. Wick, C. D., Martin, M. G. & Siepmann, J. I. Transferable Potentials for Phase Equilibria. 4. United-Atom Description of Linear and Branched Alkenes and Alkylbenzenes. *J. Phys. Chem. B* **104,** 8008–8016 (2000).

386. Chen, B., Potoff, J. J. & Siepmann, J. I. Monte Carlo Calculations for Alcohols and Their Mixtures with Alkanes. Transferable Potentials for Phase Equilibria. 5. United-Atom Description of Primary, Secondary, and Tertiary Alcohols. *J. Phys. Chem. B* **105,** 3093–3104 (2001).

387. Stubbs, J. M., Potoff, J. J. & Siepmann, J. I. Transferable Potentials for Phase Equilibria. 6. United-Atom Description for Ethers, Glycols, Ketones, and Aldehydes. *J. Phys. Chem. B* **108,** 17596–17605 (2004).

388. Wick, C. D., Stubbs, J. M., Rai, N. & Siepmann, J. I. Transferable Potentials for Phase Equilibria. 7. Primary, Secondary, and Tertiary Amines, Nitroalkanes and Nitrobenzene, Nitriles, Amides, Pyridine, and Pyrimidine. *J. Phys. Chem. B* **109,** 18974–18982 (2005).

389. Errington, J. R. & Panagiotopoulos, A. Z. New intermolecular potential models for benzene and cyclohexane. *J. Chem. Phys.* **111,** 9731–9738 (1999).

390. Toxvaerd, S. Molecular dynamics calculation of the equation of state of alkanes. *J. Chem. Phys.* **93,** 4290–4295. `http://scitation.aip.org/content/aip/journal/jcp/93/6/10.1063/1.458709` (1990).

391. Toxvaerd, S. Equation of state of alkanes II. *J. Chem. Phys.* **107,** 5197–5204 (1997).

392. Nieto-Draghi, C., Bonnaud, P. & Ungerer, P. Anisotropic United Atom Model Including the Electrostatic Interactions of Methylbenzenes. I. Thermodynamic and Structural Properties. *J. Phys. Chem. C* **111,** 15686–15699. eprint: `http://dx.doi.org/10.1021/jp0737146`. `http://dx.doi.org/10.1021/jp0737146` (2007).

393. Ferrando, N., Lachet, V, Teuler, J.-M. & Boutin, A. Transferable Force Field for Alcohols and Polyalcohols. *J. Phys. Chem. B* **113.** PMID: 19344171, 5985–5995. eprint: `http://dx.doi.org/10.1021/jp810915z`. `http://dx.doi.org/10.1021/jp810915z` (2009).

394. Ferrando, N., Lachet, V & Boutin, A. Monte Carlo Simulations of Mixtures Involving Ketones and Aldehydes by a Direct Bubble Pressure Calculation. *J. Phys. Chem. B* **114.** PMID: 20540589, 8680–8688. eprint: http://dx.doi.org/10.1021/jp1031724. http://dx.doi.org/10.1021/jp1031724 (2010).

395. Ferrando, N., Lachet, V & Boutin, A. Transferable Force Field for Carboxylate Esters: Application to Fatty Acid Methylic Ester Phase Equilibria Prediction. *J. Phys. Chem. B* **116.** PMID: 22369235, 3239–3248. eprint: http://dx.doi.org/10.1021/jp212060u. http://dx.doi.org/10.1021/jp212060u (2012).

396. Pérez-Pellitero, J. *et al.* Anisotropic United-Atoms (AUA) Potential for Alcohols. *J. Phys. Chem. B* **112,** 9853–9863. eprint: http://dx.doi.org/10.1021/jp802282p. http://dx.doi.org/10.1021/jp802282p (2008).

397. Potoff, J. J. & Bernard-Brunel, D. A. Mie Potentials for Phase Equilibria Calculations: Application to Alkanes and Perfluoralkanes. *J. Phys. Chem. B* **113,** 14725–14731 (2009).

398. Potoff, J. J. & Kamath, G. Mie Potentials for Phase Equilibria: Application to Alkenes. *J. Chem. Eng. Data* **59,** 3144–3150. eprint: http://dx.doi.org/10.1021/je500202q. http://dx.doi.org/10.1021/je500202q (2014).

399. Mick, J. R. *et al.* Optimized Mie potentials for phase equilibria: Application to noble gases and their mixtures with n-alkanes. *J. Chem. Phys.* **143,** 114504 (2015).

400. Barhaghi, M. S., Mick, J. R. & Potoff, J. J. Optimised Mie potentials for phase equilibria: application to alkynes. *Mol. Phys.* **115,** 1378–1388 (2017).

401. Møller, C. & Plesset, M. S. Note on an Approximation Treatment for Many-Electron Systems. *Phys. Rev.* **46,** 618–622 (7 1934).

402. Haase, F. & Ahlrichs, R. Semidirect MP2 gradient evaluation on workstation computers: The MPGRAD program. *J. Comput. Chem.* **14,** 907–912 (1993).

403. Schäfer, A., Huber, C. & Ahlrichs, R. Fully optimized contracted Gaussian basis sets of triple zeta valence quality for atoms Li to Kr. *J. Chem. Phys.* **100,** 5829–5835 (1994).

404. Of Karlsruhe, U. *TURBOMOLE V6.6 2014, a development of University of Karlsruhe and Forschungszentrum Karlsruhe GmbH, 1989-2007, TURBOMOLE GmbH, since 2007; available from* http://www.turbomole.com. (2018).

405. Lorentz, H. A. Über die Anwendung des Satzes vom Virial in der kinetischen Theorie der Gase. *Ann. Phys.* **248,** 127–136 (1881).

406. Berthelot, D. Sur le mélange des gaz. *Compt. Rendus* **126,** 1703–1706 (1898).

407. Gross, J. & Sadowski, G. Application of perturbation theory to a hard-chain reference fluid: an equation of state for square-well chains. *Fluid Phase Equilib.* **168,** 183–199 (2000).

408. Van Westen, T., Vlugt, T. J. H. & Gross, J. Determining Force Field Parameters Using a Physically Based Equation of State. *J. Phys. Chem. B* **115.** PMID: 21568280, 7872–7880 (2011).

409. Panagiotopoulos, A. Z., Wong, V. & Floriano, M. A. Phase Equilibria of Lattice Polymers from Histogram Reweighting Monte Carlo Simulations. *Macromolec.* **31,** 912–918 (1998).

410. Panagiotopoulos, A. Z. Monte Carlo methods for phase equilibria of fluids. *J. Phys. Condens. Matter* **12,** R25 –R52 (2000).

411. Wang, J.-S., Tay, T. K. & Swendsen, R. H. Transition Matrix Monte Carlo Reweighting and Dynamics. *Phys. Rev. Lett.* **82,** 476–479. `http://link.aps.org/doi/10.1103/PhysRevLett.82.476` (3 1999).

412. Lyubartsev, A. P., Martsinovski, A. A., Shevkunov, S. V. & Vorontsov-Velyaminov, P. N. New approach to Monte Carlo calculation of the free energy: Method of expanded ensembles. *J. Chem. Phys.* **96,** 1776–1783. `http://scitation.aip.org/content/aip/journal/jcp/96/3/10.1063/1.462133` (1992).

413. Frenkel, D., Mooij, G. & Smit, B. Novel scheme to study structural and thermal properties of continuously deformable molecules. *J. Phys. Condens. Matter* **4,** 3053 (1992).

414. Abraham, M. J. *User Specified non-bonded potentials in Gromacs* English. 2014. `http://www.gromacs.org/Documentation/How-tos/Tabulated_Potentials`.

415. Todorov, I. T., Smith, W., Trachenko, K. & Dove, M. T. DL_POLY_3: new dimensions in molecular dynamics simulations via massive parallelism. *J. Mater. Chem.* **16,** 1911–1918 (2006).

416. Berendsen, H. J. C., Postma, J. P. l. M., van Gunsteren, W. F., DiNola, A. R. H. J. & Haak, J. R. Molecular dynamics with coupling to an external bath. *J. Chem. Phys.* **81,** 3684–3690 (1984).

417. Haynes, W. M. *CRC handbook of chemistry and physics* (CRC Press, Mortimer House, 37-41 Mortimer Street, London, 2012).

418. Winget, P., Hawkins, G. D., Cramer, C. J. & Truhlar, D. G. Prediction of vapor pressures from self-solvation free energies calculated by the SM5 series of universal solvation models. *J. Phys. Chem. B* **104,** 4726–4734 (2000).

419. Thomson, G. H. The DIPPR® databases. *Int. J. Thermophys.* **17,** 223–232 (1996).

420. Mathews, J. H. The accurate measurement of heats of vaporization of liquids. *J. Am. Chem. Soc.* **48,** 562–576 (1926).

421. Polák, J., Murakami, S., Lam, V. T., Pflug, H. D. & Benson, G. C. Molar excess enthalpies, volumes, and Gibbs free energies of methanol–isomeric butanol systems at 25 C. *Can. J. Chem.* **48,** 2457–2465 (1970).

422. Brown, I., Fock, W. & Smith, F. The thermodynamic properties of solutions of normal and branched alcohols in benzene and n-hexane. *J. Chem. Thermodyn.* **1,** 273–291 (1969).

423. Riggio, R., Martinez, H. E., de Salas, N. Z. & Ramos, J. F. Densities, viscosities, and refractive indexes of tert-butyl methyl ether+ butyl alcohols at 298.15 K. *Can. J. Chem.* **73,** 431–434 (1995).

424. Riggio, R., Martinez, H. E., Salas, N. Z. D., Toigo, M. D. D. & Ramos, J. F. Excess properties for cyclohexanone+ butanols at 298.15 K. *Can. J. Chem.* **73,** 1274–1277 (1995).

425. Riggio R.and Ramos, J. F., Ubeda, M. H. & Espindola, J. A. Mixtures of methyl isobutyl ketone with three butanols at various temperatures. *Can. J. Chem.* **59,** 3305–3308 (1981).

426. Armourdam, M. J. & Laddha, G. S. Diffusivities of some binary liquid systems using a diaphragm cell. *J. Chem. Eng. Data* **12,** 389–391 (1967).

427. Riggio, R., Martinez, H. E., Espindola, J. A. & Ramos, J. F. Viscosities, densities and refractive indexes of mixtures of methyl isobutyl ketone-isobutyl alcohol. *J. Chem. Eng. Data* **29,** 11–13 (1984).

428. Lafuente, C., Pardo, J., Rodriguez, V., Royo, F. M. & Urieta, J. S. Excess volumes of Binary Mixtures of 1, 3-Dichloropropane with Isomeric Butanols at 298.15 and 313.15 K. *J. Chem. Eng. Data* **38,** 554–555 (1993).

429. Sreenivasulu, B. & Naidu, P. R. Excess Volumes and Isentropic Compressibilities of Mixtures of p-Xylene with 2-Propanol, 2-Methyl-1-propanol, and 3-Methyl-1-butanol at 303.15 K. *J. Chem. Eng. Data* **38,** 619–621 (1993).

430. Mallu, B. V. & Rao, Y. C. V. Excess volumes of isobutanol with toluene or o-xylene at 303.15 and 308.15 K. *J. Chem. Eng. Data* **35,** 444–445 (1990).

431. Karunakar, J., Reddy, K. D. & Rao, M. P. V. Isentropic compressibilities of mixtures of aliphatic alcohols with benzonitrile. *J. Chem. Eng. Data* **27,** 348–350 (1982).

432. Mouli, J. C., Naidu, P. R. & Choudary, N. V. Excess volumes, ultrasonic sound velocities, and isentropic compressibilities of 1-chlorobutane with isopropyl, isobutyl, and isopentyl alcohols. *J. Chem. Eng. Data* **31,** 493–496 (1986).

433. Sacco, A. & Rakshit, A. K. Thermodynamic and physical properties of binary mixtures involving sulfolane III. Excess volumes of sulfolane with each of nine alcohols. *J. Chem. Thermodyn.* **7,** 257–261 (1975).

434. Aminabhavi, T. M., Aralaguppi, M. I., Harogoppad, S. B. & Balundgi, R. H. Densities, viscosities, refractive indices, and speeds of sound for methyl acetoacetate+ aliphatic alcohols (C1-C8). *J. Chem. Eng. Data* **38,** 31–39 (1993).

435. Narayanaswamy, G., Dharmaraju, G. & Raman, G. K. Excess volumes and isentropic compressibilities of acetonitrile+ n-propanol,+ i-propanol,+ n-butanol,+ i-butanol, and+ cyclohexanol at 303.15 K. *J. Chem. Thermodyn.* **13,** 327–331 (1981).

436. Smith, G. W. & Sorg, L. V. The Measurement of Boundary Tension by the Pendant-drop Method. I. The Aliphatic Alcohols. *J. Phys. Chem.* **45,** 671–681 (1941).

437. Okano, T., Ogawa, H. & Murakami, S. Molar excess volumes, isentropic compressions, and isobaric heat capacities of methanol–isomeric butanol systems at 298.15 K. *Can. J. Chem.* **66,** 713–717 (1988).

438. Friedman, M. E. & Scheraga, H. A. Volume Changes in Hydrocarbon-Water Systems. Partial Molal Volumes of Alcohol-Water Solutions 1. *J. Phys. Chem.* **69,** 3795–3800 (1965).

439. Radecki, A. & Kaczmarek, B. Liquid-vapor equilibriums in binary systems of hexamethyldisiloxane- 1-butanol, -2-butanol, and-2-methyl-1-propanol. *J. Chem. Eng. Data* **25,** 230–232 (1980).

440. Berro, C., Rogalski, M. & Peneloux, A. Excess Gibbs energies and excess volumes of 1-butanol-n-hexane and 2-methyl-1-propanol-n-hexane binary systems. *J. Chem. Eng. Data* **27,** 352–355 (1982).

441. Berro, C. & Peneloux, A. Excess Gibbs energies and excess volumes of 1-butanol-n-heptane and 2-methyl-1-propanol-n-heptane binary systems. *J. Chem. Eng. Data* **29,** 206–210 (1984).

442. Reddy, K. V. R., Rambabu, K., Devarajulu, T. & Krishnaiah, A. Volumetric behaviour of mixtures of butoxy ethanol with aliphatic alcohols. *Phys. Chem. Liq.* **28,** 161–164 (1994).

443. Jaeger, F. M. Über die Temperaturabhängigkeit der molekularen freien Oberflächenenergie von Flüssigkeiten im Temperaturbereich von -80 bis +1650° C. *Z. anorg. allg. Chem.* **101,** 1–214 (1917).

444. Rao, K. P. & Reddy, K. S. Excess volumes and excess isentropic compressibilities of binary mixtures of N, N-dimethylformamide with branched alcohols at 303.15 K. *Thermochim. Acta* **91,** 321–327 (1985).

445. Riggio, R., Ramos, J. F., Martinez, H. E., Espindola, J. A. & Solimo, H. N. Magnetic behavior of binary liquid mixtures of methyl isobutyl ketone with butanols. *J. Chem. Eng. Data* **28,** 352–354 (1983).

446. Nakanishi, K. Partial molal volumes of butyl alcohols and of related compounds in aqueous solution. *Bull. Chem. Soc. Jpn.* **33,** 793–797 (1960).

447. Kubota, H., Tanaka, Y. & Makita, T. Volumetric behavior of pure alcohols and their water mixtures under high pressure. *Int. J. Thermophys.* **8,** 47–70 (1987).

448. Nain, A. K., Sharma, R. & Ali A. Gopal, S. Densities and volumetric properties of ethyl acrylate+ 1-butanol, or 2-butanol, or 2-methyl-1-propanol, or 2-methyl-2-propanol binary mixtures at temperatures from 288.15 to 318.15 K. *J. Mol. Liq.* **144,** 138–144 (2009).

449. Peralta, R. D., Infante, R., Cortez, G., Cisneros, A. & Wisniak, J. Density, excess volumes, and partial volumes of the binary systems of ethenyl ethanoate+ butanol, 2-butanol, 2-methyl-1-propanol, and 2-methyl-2-propanol at 298.15 K. *Chem. Eng. Commun.* **192,** 1684–1694 (2005).

450. Nain, A. K. Densities and volumetric properties of butyl acrylate+ 1-butanol, or+ 2-butanol, or+ 2-methyl-1-propanol, or+ 2-methyl-2-propanol binary mixtures at temperatures from 288.15 to 318.15 K. *J. Solution Chem.* **42,** 1404–1422 (2013).

451. Tofts, P. *et al.* Test Liquids for Quantitative MRI Measurements of Self-Diffusion Coefficient In Vivo. *Magn. Reson. Med.* **43,** 368–374 (2000).

452. Assael, M. J. & Polimatidou, S. K. Measurements of the viscosity of alcohols in the temperature range 290-340 K at pressures up to 30 MPa. *Int. J. Thermophys.* **15,** 95–107 (1994).

453. Papaioannou, D. & Panayiotou, C. Viscosity of alkanol+ alkane mixtures at moderately high pressures. *J. Chem. Eng. Data* **39,** 463–466 (1994).

454. Papaioannou, D. & Panayiotou, C. Viscosity of binary mixtures of propylamine with alkanols at moderately high pressures. *J. Chem. Eng. Data* **40,** 202–209 (1995).

455. Aminabhavi, T. M. & Gopalakrishna, B. Densities, viscosities, and refractive indices of bis (2-methoxyethyl) ether+ cyclohexane or+ 1, 2, 3, 4-tetrahydronaphthalene and of 2-ethoxyethanol+ propan-1-ol,+ propan-2-ol, or+ butan-1-ol. *J. Chem. Eng. Data* **40,** 462–467 (1995).

456. Papaioannou, D., Bridakis, M. & Panayiotou, C. G. Excess dynamic viscosity and excess volume of N-butylamine+ 1-alkanol mixtures at moderately high pressures. *J. Chem. Eng. Data* **38,** 370–378 (1993).

457. Tanaka, Y., Matsuda, Y., Fujiwara, H., Kubota, H. & Makita, T. Viscosity of (water+ alcohol) mixtures under high pressure. *Int. J. Thermophys.* **8,** 147–163 (1987).

458. Romano, E. *et al.* Thermophysical properties of four binary dimethyl carbonate+ 1-alcohol systems at 288.15–313.15 K. *Fluid Phase Equilib.* **211,** 219–240 (2003).

459. Agarwal, D. & Singh, M. Densities and viscosities of binary liquid mixtures of trichloroethylene and tetrachloroethylene with some polar and nonpolar solvents. *J. Chem. Eng. Data* **49,** 1218–1224 (2004).

460. González, B., Calvar, N., Domínguez, A. & Tojo, J. Dynamic viscosities of binary mixtures of cycloalkanes with primary alcohols at T=(293.15, 298.15, and 303.15) K: New UNIFAC-VISCO interaction parameters. *J. Chem. Thermodyn.* **39,** 322–334 (2007).

461. Bhuiyan, M. M. H., Ferdaush, J. & Uddin, M. H. Densities and viscosities of binary mixtures of {dimethylsulfoxide+ aliphatic lower alkanols (C 1–C 3)} at temperatures from T= 303.15 K to T= 323.15 K. *J. Chem. Thermodyn.* **39,** 675–683 (2007).

462. Calvar, N., Gómez, E., Gonzalez, B. & Dominguez, A. Experimental determination, correlation, and prediction of physical properties of the ternary mixtures ethanol and 1-propanol+ water+ 1-ethyl-3-methylpyridinium ethylsulfate at 298.15 K. *J. Chem. Eng. Data* **54,** 2229–2234 (2009).

463. Gardas, R. L. & Oswal, S. Volumetric and transport properties of ternary mixtures containing 1-propanol, triethylamine or tri-n-butylamine and cyclohexane at 303.15 K: Experimental data, correlation and prediction by ERAS model. *Thermochim. Acta* **479,** 17–27 (2008).

464. Costa, H. F. *et al.* Liquid-Liquid Equilibria, Density, Viscosity, and Surface and Interfacial Tension of the System Water+ n-Butyl Acetate+ 1-Propanol at 323.15 K and Atmospheric Pressure. *J. Chem. Eng. Data* **54,** 2845–2854 (2009).

465. Baylaucq, A., Watson, G., Zéberg-Mikkelsen, C., Bazile, J.-P. & Boned, C. Dynamic viscosity of the binary system 1-propanol+ toluene as a function of temperature and pressure. *J. Chem. Eng. Data* **54,** 2715–2721 (2009).

466. Weber, W. Über die Druckabhängigkeit der Viskosität von Alkohol-Wasser-Gemischen. *Rheol. Acta* **14,** 1012–1025 (1975).

467. Nikam, P. S., Jagdale, B. S., Sawant, A. B. & Hasan, M. Densities and viscosities for binary mixtures of benzonitrile with methanol, ethanol, propan-1-ol, butan-1-ol, pentan-1-ol, and 2-methylpropan-2-ol at (303.15, 308.15, and 313.15) K. *J. Chem. Eng. Data* **45,** 214–218 (2000).

468. González, E. J., Alonso, L. & Domínguez, A. Physical properties of binary mixtures of the ionic liquid 1-methyl-3-octylimidazolium chloride with methanol, ethanol, and 1-propanol at T=(298.15, 313.15, and 328.15) K and at P= 0.1 MPa. *J. Chem. Eng. Data* **51,** 1446–1452 (2006).

469. Djojoputro, H. & Ismadji, S. Density and viscosity of binary mixtures of ethyl-2-methylbutyrate and ethyl hexanoate with methanol, ethanol, and 1-propanol at (293.15, 303.15, and 313.15) K. *J. Chem. Eng. Data* **50,** 1343–1347 (2005).

470. Belda Maximino, R. Viscosity and density of binary mixtures of alcohols and polyols with three carbon atoms and water: equation for the correlation of viscosities of binary mixtures. *Phys. Chem. Liq.* **47,** 515–529 (2009).

471. Sadeghi, R. & Azizpour, S. Volumetric, compressibility, and viscometric measurements of binary mixtures of poly (vinylpyrrolidone)+ water,+ methanol,+ ethanol,+ acetonitrile,+ 1-propanol,+ 2-propanol, and+ 1-butanol. *J. Chem. Eng. Data* **56,** 240–250 (2011).

472. Segade, L. *et al.* Viscosities of di-n-butyl ether+ 1-propanol+ n-decane mixture at 308.15 K. *Fluid Phase Equilib.* **182,** 353–364 (2001).

473. Kurnia, K. A., Mutalib, M. I. A., Murugesan, T. & Ariwahjoedi, B. Physicochemical properties of binary mixtures of the protic ionic liquid bis (2-hydroxyethyl) methylammonium formate with methanol, ethanol, and 1-propanol. *J. Solution Chem.* **40,** 818–831 (2011).

474. Hasan, M. *et al.* Densities, viscosities, speeds of sound, FT-IR and 1 H-NMR studies of binary mixtures of n-butyl acetate with ethanol, propan-1-ol, butan-1-ol and pentan-1-ol at 298.15, 303.15, 308.15 and 313.15 K. *J. Solution Chem.* **40,** 415–429 (2011).

475. Hoga, H. E. & Torres, R. B. Volumetric and viscometric properties of binary mixtures of {methyl tert-butyl ether (MTBE)+ alcohol} at several temperatures and p= 0.1 MPa: Experimental results and application of the ERAS model. *J. Chem. Thermodyn.* **43,** 1104–1134 (2011).

476. Pal, A., Gaba, R. & Kumar, H. Acoustic, Viscometric, and Spectroscopic Studies of Dipropylene Glycol Monopropyl Ether with n-Alkanols at Temperatures of 288.15, 298.15, and 308.15 K. *J. Solution Chem.* **40,** 786–802 (2011).

477. Bridgman, P. W. *The effect of pressure on the viscosity of forty-three pure liquids* in *Proceedings of the American Academy of Arts and Sciences* **61** (1926), 57–99.

478. Xu, Y., Yao, J., Wang, C. & Li, H. Density, viscosity, and refractive index properties for the binary mixtures of n-butylammonium acetate ionic liquid+ alkanols at several temperatures. *J. Chem. Eng. Data* **57,** 298–308 (2012).

479. Shao, D., Lu, X., Fang, W., Guo, Y. & Xu, L. Densities and viscosities for binary mixtures of the ionic liquid N-ethyl piperazinium propionate with n-alcohols at several temperatures. *J. Chem. Eng. Data* **57,** 937–942 (2012).

480. Cano-Gómez, J. J., Iglesias-Silva, G. A., Ramos-Estrada, M. & Hall, K. R. Densities and viscosities for binary liquid mixtures of ethanol+ 1-propanol, 1-butanol, and 1-pentanol from (293.15 to 328.15) K at 0.1 MPa. *J. Chem. Eng. Data* **57,** 2560–2567 (2012).

481. Sanz, L. F., González, J. A., De La Fuente, I. G. & Cobos, J. C. Thermodynamics of mixtures with strongly negative deviations from Raoult's law. XI. Densities, viscosities and refractives indices at (293.15–303.15) K for cyclohexylamine+ 1-propanol, or+ 1-butanol systems. *J. Mol. Liq.* **172,** 26–33 (2012).

482. Xu, Y., Chen, B., Qian, W. & Li, H. Properties of pure n-butylammonium nitrate ionic liquid and its binary mixtures of with alcohols at T=(293.15 to 313.15) K. *J. Chem. Thermodyn.* **58,** 449–459 (2013).

483. Bajić, D. M., Živković, E. M., Šerbanović, S. P. & Kijevčanin, M. L. Experimental measurements and modelling of volumetric properties, refractive index and viscosity of selected binary systems with butyl lactate at 288.15–323.15 K and atmospheric pressure. New UNIFAC-VISCO interaction parameters. *Thermochim. Acta* **562,** 42–55 (2013).

484. Kermanpour, F., Niakan, H. Z. & Sharifi, T. Density and viscosity measurements of binary alkanol mixtures from (293.15 to 333.15) K at atmospheric pressure. *J. Chem. Eng. Data* **58,** 1086–1091 (2013).

485. Estrada-Baltazar, A., Iglesias-Silva, G. A. & Caballero-Ceró, C. Volumetric and transport properties of binary mixtures of n-octane+ ethanol,+ 1-propanol,+ 1-butanol, and+ 1-pentanol from (293.15 to 323.15) K at atmospheric pressure. *J. Chem. Eng. Data* **58,** 3351–3363 (2013).

486. Dubey, G. P. & Kaur, P. Thermodynamic and spectral investigations of binary liquid mixtures of 2-butoxy ethanol with alcohols at temperature range of 293.15–313.15 K. *Fluid Phase Equilib.* **354,** 114–126 (2013).

487. Zhu, C., Han, S., Liu, J. & Ma, Y. Densities and Viscosities of Diaminotoluene with Water, Ethanol, Propan-1-ol, and Butan-1-ol from (293.15 to 333.15) K. *J. Chem. Eng. Data* **59,** 880–889 (2014).

488. Wan Normazan, W. M. D. *et al.* Composition and Temperature Dependence of Density, Surface Tension, and Viscosity of EMIM DEP/MMIM DMP+ Water+ 1-Propanol/2-Propanol Ternary Mixtures and Their Mathematical Representation Using the Jouyban-Acree Model. *J. Chem. Eng. Data* **59,** 2337–2348 (2014).

489. Hassein-bey Larouci, A., Igoujilen, O., Aitkaci, A., Segovia, J. J. & Villamanan, M. A. Dynamic and kinematic viscosities, excess volumes and excess Gibbs energies of activation for viscous flow in the ternary mixture {1-propanol+ N, N-dimethylformamide+ chloroform} at temperatures between 293.15 K and 323.15 K. *Thermochim. Acta* **589,** 90–99 (2014).

490. Bajić, D. M., Zivković, E. M., Serbanović, S. S. & Kijevcanin, M. L. Volumetric and viscometric study of binary systems of ethyl butyrate with alcohols. *J. Chem. Eng. Data* **59,** 3677–3690 (2014).

491. Raabe, G. & Sadus, R. J. Molecular dynamics simulation of the effect of bond flexibility on the transport properties of water. *J. Chem. Phys.* **137,** 104512 (2012).

492. Medina, J. *et al.* Molecular dynamics simulations of rigid and flexible water models: Temperature dependence of viscosity. *Chem. Phys.* **388,** 9–18 (2011).

493. Allen, W. & Rowley, R. L. Predicting the viscosity of alkanes using nonequilibrium molecular dynamics: Evaluation of intermolecular potential models. *J. Chem. Phys.* **106,** 10273–10281 (1997).

494. Pratt, K. C. & Wakeham, W. A. Self-diffusion in water and monohydric alcohols. *J. Chem. Soc., Faraday Trans. 2: Mol. Chem. Phys.* **73,** 997–1002 (1977).

495. Chen, X., Hu, R., Feng, H., Chen, L. & Lüdemann, H.-D. Intradiffusion, Density, and Viscosity Studies in Binary Liquid Systems of Acetylacetone + Alkanols at 303.15 K. *J. Chem. Eng. Data* **57,** 2401–2408. `https://doi.org/10.1021/je3000553` (2012).

496. Emel'yanov, M. I. & Samigullin, F. M. Investigation of Translational Diffusion of Alcohol and Acetic Acid Molecules in Mixtures with Carbon Tetrachloride. *Zh. Strukt. Khim.* **12.** Translation in Mariiskii Pedagogical Institute, Ioshkar-Ola. Kazan' Pedagogical Institute., 585–590 (1971).

497. Suárez-Iglesias, O., Medina, I., de los Ángeles Sanz, M., Pizarro, C. & Bueno, J. L. Self-Diffusion in Molecular Fluids and Noble Gases: Available Data. *J. Chem. Eng. Data* **60,** 2757–2817. `https://doi.org/10.1021/acs.jced.5b00323` (2015).

498. Meckl, S. & Zeidler, M. D. Self-diffusion measurements of ethanol and propanol. *Mol. Phys.* **63,** 85–95. `https://doi.org/10.1080/00268978800100081` (1988).

499. Kulschewski, T. & Pleiss, J. A molecular dynamics study of liquid aliphatic alcohols: simulation of density and self-diffusion coefficient using a modified OPLS force field. *Mol. Simul.* **39,** 754–767 (2013).

500. Jorgensen, W. L. Quantum and statistical mechanical studies of liquids. 7. Structure and properties of liquid methanol. *J. Am. Chem. Soc.* **102,** 543–549 (1980).

501. Nath, S. K., Escobedo, F. A. & de Pablo, J. J. On the simulation of vapor–liquid equilibria for alkanes. *J. Chem. Phys.* **108,** 9905–9911 (1998).

502. Khare, R., Sum, A. K., Nath, S. K. & de Pablo, J. J. Simulation of vapor- liquid phase equilibria of primary alcohols and alcohol- alkane mixtures. *J. Phys. Chem. B* **108,** 10071–10076 (2004).

503. Schnabel, T., Vrabec, J. & Hasse, H. Henry's law constants of methane, nitrogen, oxygen and carbon dioxide in ethanol from 273 to 498 K: Prediction from molecular simulation. *Fluid Phase Equilib.* **233,** 134–143 (2005).

504. Guevara-Carrion, G., Nieto-Draghi, C., Vrabec, J. & Hasse, H. Prediction of transport properties by molecular simulation: methanol and ethanol and their mixture. *J. Phys. Chem. B* **112,** 16664–16674 (2008).

505. Baz, J., Hansen, N. & Gross, J. On the use of transport properties to discriminate Mie-type molecular models for 1-propanol optimized against VLE data. *Eur. Phys. J. Special Topics* **227,** 1529–1545. ISSN: 1951-6401. `https://doi.org/10.1140/epjst/e2019-800178-4` (2019).

506. Ungerer, P. *et al.* Optimization of the anisotropic united atoms intermolecular potential for n-alkanes. *J. Chem. Phys.* **112,** 5499–5510 (2000).

507. Virnau, P. & Müller, M. Calculation of free energy through successive umbrella sampling. *J. Chem. Phys.* **120,** 10925–10930 (2004).

508. Abraham, M., Van Der Spoel, D, Lindahl, E & Hess, B. *GROMACS Development Team, GROMACS User Manual version 2016* 2018.

509. Linstrom, P. J. & Mallard, W. G. The NIST Chemistry WebBook: A chemical data resource on the internet. *J. Chem. Eng. Data* **46,** 1059–1063 (2001).

510. Wei, H., Guo, Y., Yang, F., Fang, W. & Lin, R. Densities and Viscosities of exo-Tetrahydrodicyclopentadiene+ n-Butanol and exo-Tetrahydrodicyclopentadiene+ n-Pentanol at Temperatures of (293.15 to 313.15) K. *J. Chem. Eng. Data* **55,** 1049–1052 (2009).

511. Almasi, M. & Iloukhani, H. Densities, viscosities, and refractive indices of binary mixtures of methyl ethyl ketone+ pentanol isomers at different temperatures. *J. Chem. Eng. Data* **55,** 3918–3922 (2010).

512. Caro, M. N. *et al.* Densities and viscosities of three binary monoglyme+ 1-alcohol systems from (283.15 to 313.15) K. *J. Chem. Eng. Data* **58,** 909–914 (2013).

513. Faria, M. A., Martins, R. J., Cardoso, M. J. & Barcia, O. E. Density and Viscosity of the Binary Systems Ethanol+ Butan-1-ol,+ Pentan-1-ol,+ Heptan-1-ol,+ Octan-1-ol, Nonan-1-ol,+ Decan-1-ol at 0.1 MPa and Temperatures from 283.15 K to 313.15 K. *J. Chem. Eng. Data* **58,** 3405–3419 (2013).

514. Habibullah, M *et al.* Densities, viscosities, and speeds of sound of binary mixtures of heptan-1-ol with 1, 4-dioxane at temperatures from (298.15 to 323.15) K and atmospheric pressure. *J. Chem. Eng. Data* **58,** 2887–2897 (2013).

515. Mahajan, A., Mirgane, S. & Deshmukh, S. Speed of ultrasound and thermodynamic properties of n-tetradecane in binary liquid mixtures at 298.15 K. *Int. J. Res. Phys. Chem.* **2,** 11–19 (2012).

516. Cao, X. *et al.* Density, viscosity, refractive index, and surface tension for six binary systems of adamantane derivatives with 1-heptanol and cyclohexylmethanol. *J. Chem. Eng. Data* **59,** 2602–2613 (2014).

517. Messerly, R. A., Anderson, M. C., Razavi, S. M. & Elliott, J. R. Improvements and limitations of Mie λ-6 potential for prediction of saturated and compressed liquid viscosity. *Fluid Phase Equilib.* **483,** 101–115 (2019).

518. Mohammad, A. A., Alkhaldi, K. H., AlTuwaim, M. S. & Al-Jimaz, A. S. Viscosity and surface tension of binary systems of N, N-dimethylformamide with alkan-1-ols at different temperatures. *J. Chem. Thermodyn.* **56,** 106–113 (2013).

519. Iwahashi, M. *et al.* The dynamical structure of normal alcohols in their liquids as determined by the viscosity and self-diffusion measurements. *Bull. Chem. Soc. Jpn.* **59,** 3771–3774 (1986).

520. Petrowsky, M. & Frech, R. Application of the compensated Arrhenius formalism to self-diffusion: implications for ionic conductivity and dielectric relaxation. *J. Phys. Chem. B* **114,** 8600–8605 (2010).

521. McCall, D. W., Douglass, D. C. & Anderson, E. W. Self-diffusion studies by means of nuclear magnetic resonance spin-echo techniques. *Ber. Bunsenges. Phys. Chem.* **67,** 336–340 (1963).

522. Viel, S., Ziarelli, F., Pagès, G., Carrara, C. & Caldarelli, S. Pulsed field gradient magic angle spinning NMR self-diffusion measurements in liquids. *J. Magn. Reson.* **190,** 113–123 (2008).

523. Iwahashi, M., Hayashi, Y., Hachiya, N., Matsuzawa, H. & Kobayashi, H. Self-association of octan-1-ol in the pure liquid state and in decane solutions as observed by viscosity, self-diffusion, nuclear magnetic resonance and near-infrared spectroscopy measurements. *J. Chem. Soc., Faraday Trans.* **89,** 707–712 (1993).

524. Deák, A, Victorov, A. & De Loos, T. W. High pressure VLE in alkanol+ alkane mixtures. Experimental results for n-butane+ ethanol,+ 1-propanol,+ 1-butanol systems and calculations with three EOS methods. *Fluid Phase Equilib.* **107,** 277–301 (1995).

525. Karmakar, P. *et al.* A Perylene diimide based fluorescent probe for caffeine in aqueous medium. *Supramol. Chem.* **31,** 28–35 (2019).

526. Bettini, S. *et al.* Perylene Bisimide Aggregates as Probes for Subnanomolar Discrimination of Aromatic Biogenic Amines. *ACS Appl. Mater. Interfaces* **11,** 17079–17089 (2019).

527. Haverkort, F., Stradomska, A., de Vries, A. H. & Knoester, J. First-principles calculation of the optical properties of an amphiphilic cyanine dye aggregate. *J. Phys. Chem. A* **118,** 1012–1023 (2014).

528. Florindo, C., Lima, F., Ribeiro, B. D. & Marrucho, I. M. Deep eutectic solvents: Overcoming XXI century challenges. *Curr. Opin. Green Sust. Chem.* **18,** 31–36 (2018).

529. Merza, F., Fawzy, A., AlNashef, I., Al-Zuhair, S. & Taher, H. Effectiveness of using deep eutectic solvents as an alternative to conventional solvents in enzymatic biodiesel production from waste oils. *Energy Reports* **4,** 77–83 (2018).

530. Rosenfeld, Y. Relation between the transport coefficients and the internal entropy of simple systems. *Phys. Rev. A* **15,** 2545 (1977).

531. Messerly, R. A., Soroush Barhaghi, M., Potoff, J. J. & Shirts, M. R. Histogram-free reweighting with grand canonical Monte Carlo: Post-simulation optimization of non-bonded potentials for phase equilibria. *J. Chem. Eng. Data* (2019).

532. Messerly, R. A., Shirts, M. R. & Kazakov, A. F. Uncertainty quantification confirms unreliable extrapolation toward high pressures for united-atom Mie λ-6 force field. *J. Chem. Phys.* **149,** 114109 (2018).

533. Hagler, A. T. Force field development phase II: Relaxation of physics-based criteria... or inclusion of more rigorous physics into the representation of molecular energetics. *J. Comput. -Aided Mol. Des.* **33,** 205–264 (2019).

534. Borhani, D. W. & Shaw, D. E. The future of molecular dynamics simulations in drug discovery. *J. Comput. -Aided Mol. Des.* **26,** 15–26 (2012).

535. Slochower, D. R. *et al.* Binding Thermodynamics of Host–Guest Systems with SMIRNOFF99Frosst 1.0. 5 from the Open Force Field Initiative. *J. Chem. Theory Comput.* **15,** 6225–6242 (2019).

536. Akinkunmi, F. O., Jahn, D. A. & Giovambattista, N. Effects of Temperature on the Thermodynamic and Dynamical Properties of Glycerol–Water Mixtures: A Computer Simulation Study of Three Different Force Fields. *J. Phys. Chem. B* **119,** 6250–6261 (2015).

537. Wolfe, M & Jonas, J. Reorientational motions in compressed viscous fluids: Selectively deuterated glycerol. *J. Chem. Phys.* **71,** 3252–3262 (1979).

538. Bosart, L. & Snoddy, A. Specific gravity of glycerol1. *Ind. Eng. Chem. Res.* **20,** 1377–1379 (1928).

539. D'Errico, G., Ortona, O., Capuano, F. & Vitagliano, V. Diffusion coefficients for the binary system glycerol+ water at 25 C. A velocity correlation study. *J. Chem. Eng. Data* **49,** 1665–1670 (2004).

540. Chen, C., Li, W. Z., Song, Y. C., Weng, L. D. & Zhang, N. Concentration dependence of water self-diffusion coefficients in dilute glycerol–water binary and glycerol–water–sodium chloride ternary solutions and the insights from hydrogen bonds. *Mol. Phys.* **110,** 283–291 (2012).

541. Fleming, R. 953. Some physical properties of aqueous solutions of choline chloride at 25°. *J. Chem. Soc.,* 4914–4916 (1960).

542. Shaukat, S. & Buchner, R. Densities, viscosities [from (278.15 to 318.15) K], and electrical conductivities (at 298.15 K) of aqueous solutions of choline chloride and chloro-choline chloride. *J. Chem. Eng. Data* **56,** 4944–4949 (2011).

543. Patel, C. *et al.* Partition coefficients of vinyl chloride between PVC/liquid/vapor phases. *Polym. J.* **11,** 43 (1979).

544. Long, D. & Miller, G. Intensities in Raman spectra. Part 7.—Intensities in some chloro-bromo-methanes. *J. Chem. Soc., Faraday Trans.* **54,** 330–337 (1958).

545. Nematulloev, U., Belinskii, B. A. & Nozdrev, V. F. Thermal and Ultraaccoustic Properties of some Aliphatic Alcohols in Temperature Interval 20-230°C at Pressures 1-1000 kg/cm^2. *Teplofiziceskie svojstva zidkostej,* 27–31 (1970).

546. Dubey, G. P. & Kumar, K. Densities, viscosities, and speeds of sound of binary liquid mixtures of ethylenediamine with alcohols at T=(293.15 to 313.15) K. *J. Chem. Eng. Data* **56,** 2995–3003 (2011).

547. Domańska, U., Zawadzki, M. & Lewandrowska, A. Effect of temperature and composition on the density, viscosity, surface tension, and thermodynamic properties of binary mixtures of N-octylisoquinolinium bis {(trifluoromethyl) sulfonyl} imide with alcohols. *J. Chem. Thermodyn.* **48,** 101–111 (2012).

548. Knezevic-Stevanovic, A. B., Serbanovic, S. P., Radovic, I. R., Djordjevic, B. D. & Kijevcanin, M. L. Thermodynamic and spectroscopic study of the ternary system dimethyladipate+ tetrahydrofuran+ 1-butanol at T=(288.15 to 323.15) K. *J. Chem. Eng. Data* **58,** 2932–2951 (2013).

549. Knezevic-Stevanovic, A. B., Radovic, I. R., Serbanovic, S. P. & Kijevcanin, M. L. Densities, Viscosities, and Refractive Indices of the Ternary Mixture Dimethyladipate+ 2-Butanone+ 1-Butanol at T=(288.15 to 323.15) K. *J. Chem. Eng. Data* **59,** 4133–4150 (2014).

550. Spasojevic, V. D., Djordjevic, B. D., Serbanovic, S. P., Radovic, I. R. & Kijevcanin, M. L. Densities, refractive indices, viscosities, and spectroscopic study of 1-amino-2-propanol+ 1-butanol and+ 2-butanol solutions at (288.15 to 333.15) K. *J. Chem. Eng. Data* **59,** 1817–1829 (2014).

551. Dubey, G. P. & Kaur, P. Thermodynamic, transport and excess properties of 2-butoxy ethanol+ 1-alkanol (C6, C8, C10) at different temperatures. *J. Chem. Thermodyn.* **64,** 239–248 (2013).

552. Dubey, G. P. & Kumar, R. Densities, speeds of sound and viscosities of binary mixtures of tetrahydrofuran with 1-hexanol, 1-octanol and 1-decanol at T=(298.15 to 313.15) K. *J. Chem. Thermodyn.* **71,** 27–36 (2014).

553. Ling, T & Van Winkle, M. Properties of Binary Mixtures as a Function of Composition. *Ind. Eng. Chem. Res.* **3,** 88–95 (1958).

554. Franjo, C., Menaut, C. P., Jimenez, E., Legido, J. L. & Paz Andrade, M. I. Viscosities and Densities of Octane+ Butan-1-ol, Hexan-1-ol, and Octan-1-ol at 298.15 K. *J. Chem. Eng. Data* **40,** 992–994 (1995).

555. Zhang, J & Liu, H. Determination of viscosity under pressure for organic substances and its correlation with density under high pressure. *J. Chem. Ind. Eng.* **3,** 269–277 (1991).

556. Pal, A. & Gaba, R. Excess Molar Volumes and Viscosities for Binary Mixtures of 1-Alkoxypropan-2-ols with 1-Butanol, and 2-Butanol at 298.15 K and Atmospheric Pressure. *Chin. J. Chem. Phys.* **25,** 1781–1789 (2007).

557. Anouti, M., Vigeant, A., Jacquemin, J., Brigouleix, C. & Lemordant, D. Volumetric properties, viscosity and refractive index of the protic ionic liquid, pyrrolidinium octanoate, in molecular solvents. *J. Chem. Thermodyn.* **42,** 834–845 (2010).

558. Kumar, H., Singla, M., Khosla, A. & Gaba, R. Viscometric studies of binary liquid mixtures of cyclopentane (1)+ 2-propanol (2),+ 1-butanol (2), and+ 2-butanol (2) at T=(298.15 and 308.15) K. *J. Mol. Liq.* **158,** 182–186 (2011).

559. Torín-Ollarves, G. A., Segovia, J. J., Martín, M. C. & Villamañán, M. A. Thermodynamic characterization of the mixture (1-butanol+ iso-octane): Densities, viscosities, and isobaric heat capacities at high pressures. *J. Chem. Thermodyn.* **44,** 75–83 (2012).

560. Belinskii, B. A., Ikramov, S. K. & Timofeev, V. I. A Study of n-Butyl Alcohol Characteristics Subject to p, rho, T States. *Izv. Akad. Nauk Arm. SSR Fiz.* **6,** 57–60 (1971).

561. Kariznovi, M., Nourozieh, H. & Abedi, J. Solubility of carbon dioxide, methane, and ethane in 1-butanol and saturated liquid densities and viscosities. *J. Chem. Thermodyn.* **67,** 227–233 (2013).

562. Zivkovic, N, Serbanovic, S, Kijevcanin, M & Zivkovic, E. Volumetric properties, viscosities, and refractive indices of the binary systems 1-butanol+ PEG 200,+ PEG 400, and+ TEGDME. *Int. J. Thermophys.* **34,** 1002–1020 (2013).

563. Naziev, Y. M., Shkhverdiev, A. N., Abdullaev, T. S. & Mekhtieva, G. R. Viscosity of n-butanol at low temperatures and various pressures. *J. Appl. Chem. USSR* **64,** 1443–1445 (1991).

564. Wong, C. & Hayduk, W. Correlations for prediction of molecular diffusivities in liquids at infinite dilution. *Can. J. Chem.* **68,** 849–859 (1990).

565. Habibullah, M *et al.* Density and viscosity of the binary mixtures of hexan-1-ol with isomeric xylenes at T=(308.15 and 318.15) K and atmospheric pressure. *J. Chem. Eng. Data* **55,** 5370–5374 (2010).

566. Fedeleş, A., Ciocirlan, O. & Iulian, O. Viscometric Studies of Binary Dimethyl Sulfoxide+ 1-Hexanol System. *Rev. Roum. Chim* **56,** 571–576 (2011).

567. Nath, J. & Pandey, J. G. Viscosities of binary liquid mixtures of Butanol+ Pentane,+ Hexane,+ Heptane, and+ Octane at T= 298.15 K. *J. Chem. Eng. Data* **42,** 1133–1136 (1997).

568. Casas, H., Segade, L., Cabeza, O., Franjo, C. & Jiménez, E. Densities, viscosities, and refractive indexes for propyl propanoate+ 1-hexanol+ benzene at 298.15 K. *J. Chem. Eng. Data* **46,** 651–656 (2001).

569. Matsuo, S & Makita, T. Viscosities of six 1-alkanols at temperatures in the range 298–348 K and pressures up to 200 MPa. *Int. J. Thermophys.* **10,** 833–843 (1989).

570. Mohammad, A. A., Alkhaldi, K. H., AlTuwaim, M. S. & Al-Jimaz, A. S. Effect of temperature and chain length on the viscosity and surface tension of binary systems of N, N-dimethylformamide with 1-octanol, 1-nonanol and 1-decanol. *J. Chem. Thermodyn.* **74,** 7–15 (2014).

571. Callaghan, P., Trotter, C. & Jolley, K. A pulsed field gradient system for a Fourier transform spectrometer. *J. Magn. Reson.* **37,** 247–259 (1980).

572. McCall, D. W. & Douglass, D. C. Self-Diffusion in the Primary Alcohols. *J. Chem. Phys.* **32,** 1876–1877 (1960).

573. Valiev, K., Emel'yanov, M. & Samigullin, F. The separate determination of the coefficients of forward diffusion of the molecules in a two-component mixture by the spin echo method. *Struct. Chem.* **5,** 347–351 (1964).

574. Gibbs, S. J., Carpenter, T. A. & Hall, L. D. Diffusion imaging with unshielded gradients. *J. Magn. Reson.* **98,** 183–191 (1992).

575. Partington, J., Hudson, R. & Bagnall, K. Self-diffusion of aliphatic alcohols. *Nature* **169,** 583 (1952).

Appendices

Appendix A

Supporting Information: Thermodynamic Characterization of the Dimerization of an Anionic Perylene Bisimide Dye Using Molecular Simulation

A.1 GROMOS Force Field Parameters for PBI

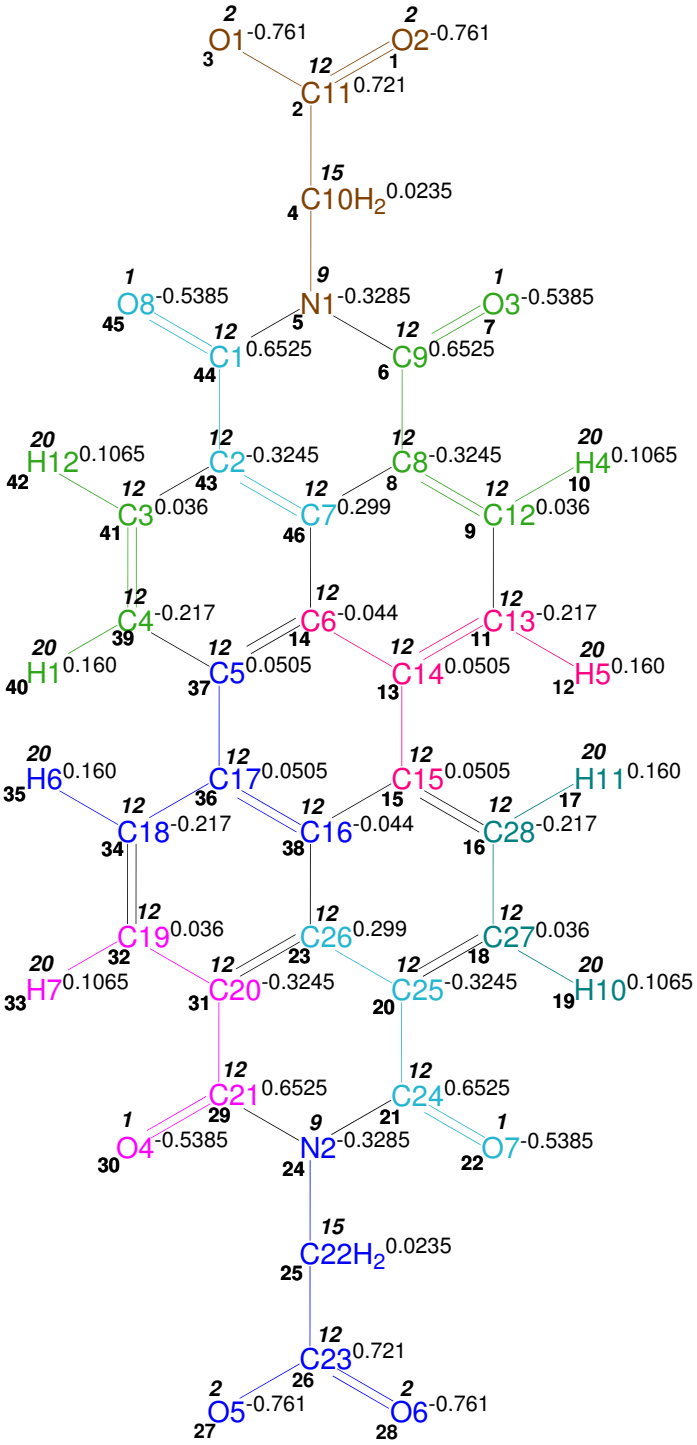

Figure S1: Atom number (plain bold), integer atom code (italic bold), IAC charge (plain). The different colors denote the different charge groups.

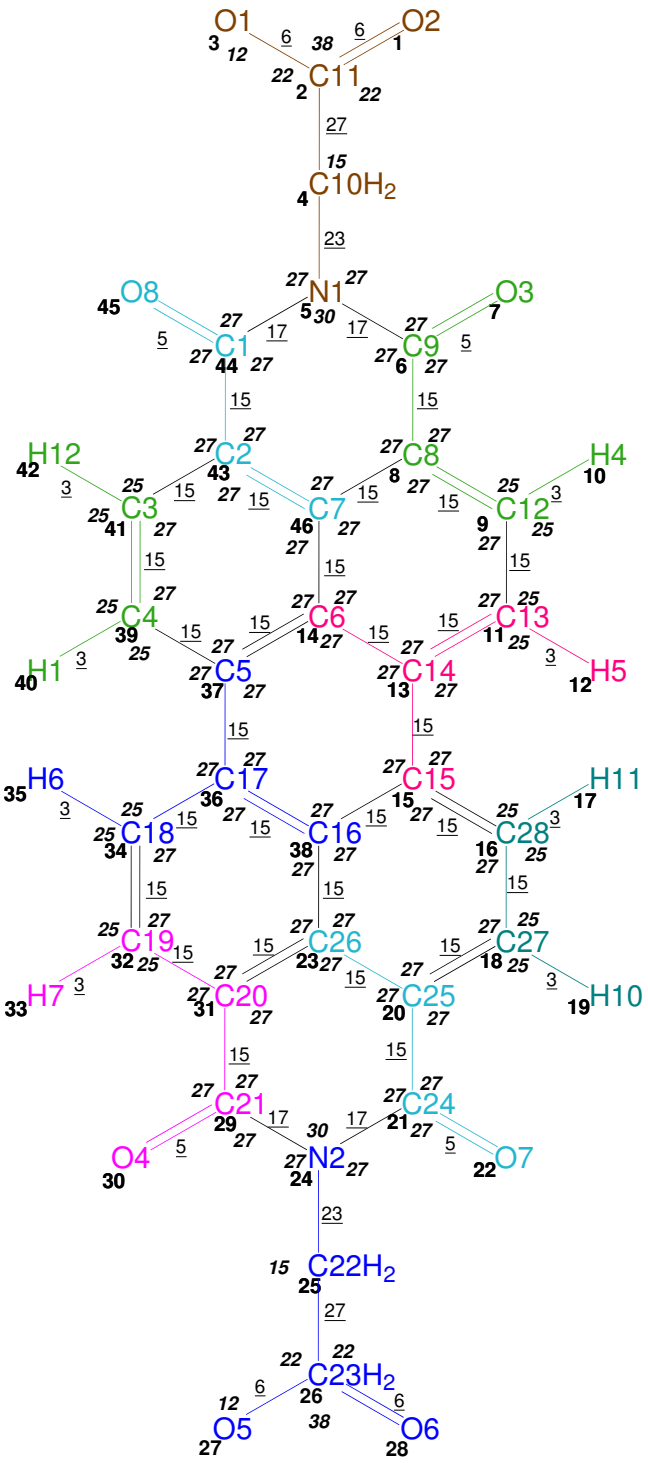

Figure S2: Atom number (plain bold), bond type (plain underlined), bond angle type (italic bold).

Table S1: GROMOS mass atom type codes, masses and names

mass atom type code	mass in a.m.u	mass atom name
1	1.008	H
4	14.022	CH_2
12	12.011	C
14	14.0067	N
16	15.9994	O

Table S2: GROMOS bond-stretching parameters

bond type code	quartic force constant 10^6 kJ mol^{-1} nm^{-4}	harmonic force constant 10^6 kJ mol^{-1} nm^{-2}	ideal bond length nm
3	12.30	0.292273	0.109
5	16.60	0.502283	0.123
6	13.40	0.418750	0.125
15	8.66	0.334640	0.139
17	8.54	0.334768	0.140
23	7.64	0.334693	0.148
27	7.15	0.334749	0.153

Table S3: GROMOS bond-angle bending parameters

bond-angle type code	cosine force constant kJ mol^{-1}	harmonic force constant kJ mol^{-1} deg^{-2}	ideal bond angle deg
15	530.0	0.140487	111.0
22	635.0	0.153360	117.0
25	505.0	0.115184	120.0
27	560.0	0.127749	120.0
30	685.0	0.153127	121.0
38	770.0	0.153365	126.0

Table S4: GROMOS improper-dihedral angle parameters

improper dihedral-angle type code	force constant $kJ\,mol^{-1}\,deg^{-2}$	ideal improper dihedral angle deg
1	0.0510	0.00

Table S5: GROMOS dihedral angle parameters

dihedral-angle type code	force constant $kJ\,mol^{-1}$	phase shift deg	multiplicity
39	1.00	180.00	6
41	3.77	0.00	6

Table S6: GROMOS van der Waals parameters

integer atom code	atom type	$C_6(I,I)^{1/2}$ $(kJ\,mol^{-1}\,nm^6)^{1/2}$	$C_{12}(I,I)^{1/2}$ $10^{-3}\,(kJ\,mol^{-1}\,nm^{12})^{1/2}$		
			1	2	3
1	O	0.04756	1.0000	1.1300	0.0000
2	OM	0.04756	0.8611	1.8410	3.0680
9	NR	0.04936	1.5230	1.8410	0.0000
12	C	0.04838	2.2220	0.0000	0.0000
15	CH_2	0.08642	5.8280	0.0000	0.0000
20	HC	0.00920	0.1230	0.0000	0.0000

Molecular building block of PBI in GROMOS format

```
MTBUILDBLSOLUTE
# RNME
PBI
# number of atoms, number of preceding exclusions
# NMAT, NLIN
46    0
# preceding exclusions
# ATOM            MAE MSAE
# atoms
# ATOM  ANM IACM MASS  CGM   ICGM  MAE  MSAE
1   O1    2   16  -0.761   0    3    2    3    4
2  C11   12   12   0.721   0    3    3    4    5
3   O2    2   16  -0.761   0    1    4
4  C10   15    4   0.0235  0    7    5    6    7    8   43   44   45
5   N1    9   14  -0.3285  1    9    6    7    8    9   41   43   44   45   46
6   C9   12   12   0.6525  0   10    7    8    9   44   46   10   11   14   43   45
7   O3    1   16  -0.5385  0    4    8    9   44   46
8   C8   12   12  -0.3245  0   11    9   46   10   11   14   43   12   13   37   41   44
9  C12   12   12   0.036   0    8   10   11   12   13   46   14   15   43
10   H4   20    1   0.1065  1    4   11   12   13   46
11  C13   12   12  -0.217   0    8   12   13   14   15   16   37   38   46
12   H5   20    1   0.160   0    3   13   14   15
13  C14   12   12   0.0505  0   12   14   15   16   37   38   46   17   18   23   36   39   43
14   C6   12   12  -0.044   0   12   37   46   15   36   39   43   16   34   38   40   41   44
15  C15   12   12   0.0505  1   12   16   38   17   18   23   36   19   20   31   34   37   46
16  C28   12   12  -0.217   0    8   17   18   19   20   38   21   23   36
17  H11   20    1   0.160   0    4   18   19   20   38
18  C27   12   12   0.036   0    8   19   20   21   23   22   24   31   38
19  H10   20    1   0.1065  1    3   20   21   23
20  C25   12   12  -0.3245  0   10   21   23   22   24   31   38   25   29   32   36
21  C24   12   12   0.6525  0    8   22   24   23   25   29   30   31   38
22   O7    1   16  -0.5385  0    4   24   23   25   29
23  C26   12   12   0.299   1   10   31   38   29   32   36   24   30   33   34   37
24   N2    9   14  -0.3285  0    6   25   29   26   30   31   32
25  C22   15    4   0.0235  0    6   26   27   28   29   30   31
26  C23   12   12   0.721   0    2   27   28
27   O5    2   16  -0.761   0    1   28
28   O6    2   16  -0.761   1    0
29  C21   12   12   0.6525  0    6   30   31   32   33   34   38
30   O4    1   16  -0.5385  0    2   31   32
31  C20   12   12  -0.3245  0    6   32   33   34   38   35   36
32  C19   12   12   0.036   0    6   33   34   35   36   37   38
33   H7   20    1   0.1065  1    3   34   35   36
34  C18   12   12  -0.217   0    5   35   36   37   38   39
35   H6   20    1   0.160   0    3   36   37   38
36  C17   12   12   0.0505  0    6   37   38   39   40   41   46
37   C5   12   12   0.0505  0    7   39   38   40   41   46   42   43
38  C16   12   12  -0.044   1    1   39
39   C4   12   12  -0.217   0    6   40   41   42   43   44   46
40   H1   20    1   0.160   0    3   41   42   43
41   C3   12   12   0.036   0    5   42   43   44   45   46
42  H12   20    1   0.1065  1    3   43   44   46
43   C2   12   12  -0.3245  0    3   44   46   45
44   C1   12   12   0.6525  0    2   45   46
45   O8    1   16  -0.5385  0    1   46
46   C7   12   12   0.299   1    0
# total charge of the molecule:  -2.000
# bonds
#  NB
52
#  IB   JB   MCB
1    2    6
2    3    6
2    4   27
4    5   23
5    6   17
5   44   17
6    7    5
6    8   15
8    9   15
8   46   15
9   10    3
9   11   15
11   12    3
```

```
11   13   15
13   14   15
13   15   15
14   37   15
14   46   15
15   16   15
15   38   15
16   17    3
16   18   15
18   19    3
18   20   15
20   21   15
20   23   15
21   22    5
21   24   17
23   31   15
23   38   15
24   25   23
24   29   17
25   26   27
26   27    6
26   28    6
29   30    5
29   31   15
31   32   15
32   33    3
32   34   15
34   35    3
34   36   15
36   37   15
36   38   15
37   39   15
39   40    3
39   41   15
41   42    3
41   43   15
43   44   15
43   46   15
44   45    5
# bond angles
# NBA
86
#  IB   JB   KB   MCB
1    2    3   38
1    2    4   22
3    2    4   22
2    4    5   15
4    5    6   27
4    5   44   27
6    5   44   30
5    6    7   27
5    6    8   27
7    6    8   27
6    8    9   27
6    8   46   27
9    8   46   27
8    9   10   25
8    9   11   27
10    9   11   25
9   11   12   25
9   11   13   27
12   11   13   25
11   13   14   27
11   13   15   27
14   13   15   27
13   14   37   27
13   14   46   27
37   14   46   27
13   15   16   27
13   15   38   27
16   15   38   27
15   16   17   25
15   16   18   27
17   16   18   25
16   18   19   25
16   18   20   27
19   18   20   25
18   20   21   27
```

```
18   20   23   27
21   20   23   27
20   21   22   27
20   21   24   27
22   21   24   27
20   23   31   27
20   23   38   27
31   23   38   27
21   24   25   27
21   24   29   30
25   24   29   27
24   25   26   15
25   26   27   22
25   26   28   22
27   26   28   38
24   29   30   27
24   29   31   27
30   29   31   27
23   31   29   27
23   31   32   27
29   31   32   27
31   32   33   25
31   32   34   27
33   32   34   25
32   34   35   25
32   34   36   27
35   34   36   25
34   36   37   27
34   36   38   27
37   36   38   27
14   37   36   27
14   37   39   27
36   37   39   27
15   38   23   27
15   38   36   27
23   38   36   27
37   39   40   25
37   39   41   27
40   39   41   25
39   41   42   25
39   41   43   27
42   41   43   25
41   43   44   27
41   43   46   27
44   43   46   27
5   44   43   27
5   44   45   27
43   44   45   27
8   46   14   27
8   46   43   27
14   46   43   27
# improper dihedrals
# NIDA
70
#  IB   JB   KB   LB   MCB
43   46   14   37    1
46   14   37   39    1
14   37   39   41    1
37   39   41   43    1
39   41   43   46    1
41   43   46   14    1
46    8    9   11    1
8    9   11   13    1
9   11   13   14    1
11   13   14   46    1
13   14   46    8    1
14   46    8    9    1
14   13   15   38    1
13   15   38   36    1
15   38   36   37    1
38   36   37   14    1
36   37   14   13    1
37   14   13   15    1
36   34   32   31    1
34   32   31   23    1
32   31   23   38    1
31   23   38   36    1
23   38   36   34    1
```

```
38   36   34   32    1
38   15   16   18    1
15   16   18   20    1
16   18   20   23    1
18   20   23   38    1
20   23   38   15    1
23   38   15   16    1
23   31   29   24    1
31   29   24   21    1
29   24   21   20    1
24   21   20   23    1
21   20   23   31    1
20   23   31   29    1
44    5   43   45    1
43   41   44   46    1
41   39   42   43    1
39   37   40   41    1
37   14   36   39    1
14   13   37   46    1
46    8   14   43    1
8    6    9   46    1
6    5    7    8    1
5    4    6   44    1
2    1    3    4    1
9    8   10   11    1
11    9   12   13    1
13   11   14   15    1
15   13   16   38    1
38   15   23   36    1
36   34   37   38    1
34   32   35   36    1
32   31   33   34    1
31   23   29   32    1
29   24   30   31    1
24   21   25   29    1
26   25   27   28    1
21   20   22   24    1
20   18   21   23    1
23   20   31   38    1
18   16   19   20    1
16   15   17   18    1
8   46   43   44    1
8    6    5   44    1
5    6    8   46    1
6    8   46   43    1
6    5   44   43    1
5   44   43   46    1
# dihedrals
# NDA
4
#  IB   JB   KB   LB   MCB
1    2    4    5   39
2    4    5   44   41
29   24   25   26   41
24   25   26   27   39
# LJ Exceptions
# NEX
0
END
```

A.2 Dimerization in Pure Water

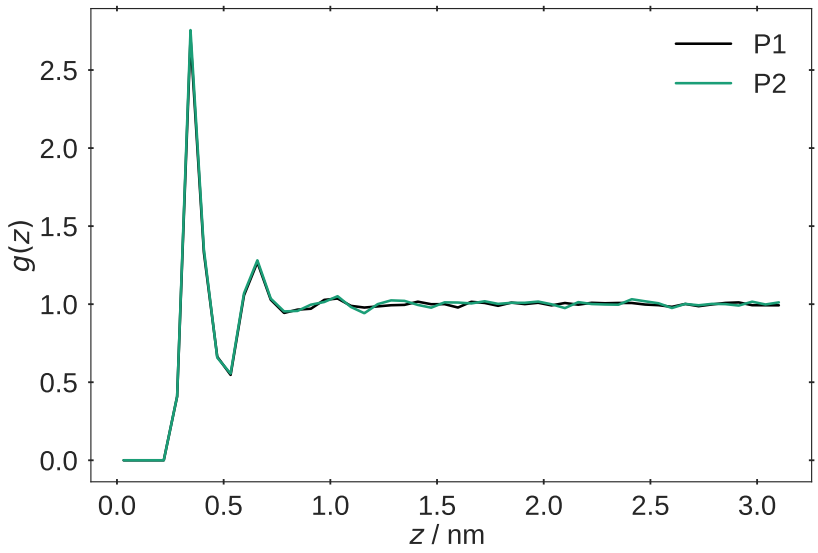

Figure S3: Distribution functions $g(z)$ of water oxygen atoms evaluated separately for each PBI molecule in the complexed state. In Figure 2.3 of the main text the average of the two curves is shown.

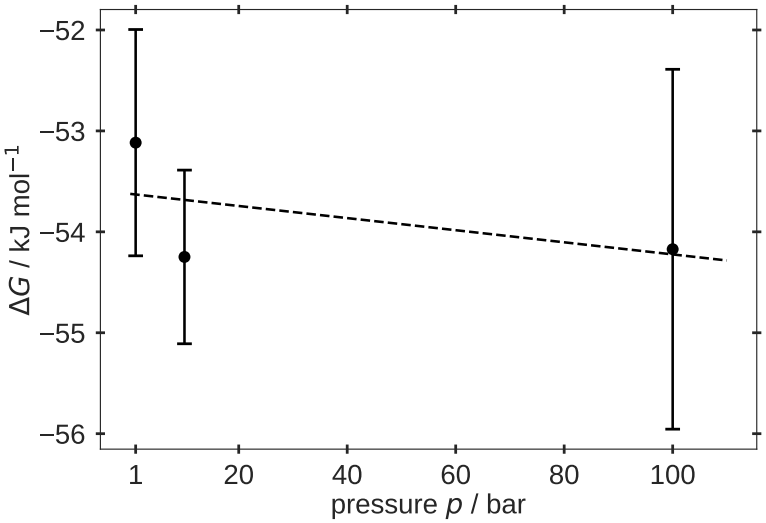

Figure S4: Free energy as function of pressure in pure water. Dots are representing mean values with error bars as confidence interval of 95 %. Linear function $\Delta G(p) = \alpha_p + \beta_p p$ with parameters $\alpha_p = -53.624\,\mathrm{kJ\,mol^{-1}}$ and $\beta_p = -5.9986 \cdot 10^{-3}\,\mathrm{kJ\,mol^{-1}\,bar^{-1}}$ is shown as dashed line.

A.3 Dimerization in Ethanol/Water Mixtures

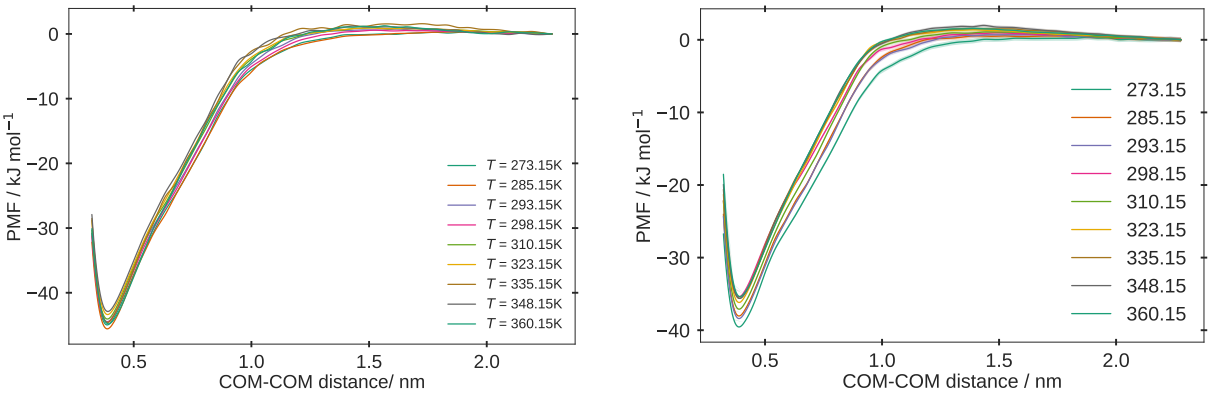

(a) (b)

Figure S5: Potentials of mean force as function of the center-of-mass separation for different temperatures in 25 vol% (a) and 50 vol% (b) ethanol/water mixture, respectively. Errors are within the line width and correspond to one standard deviation.

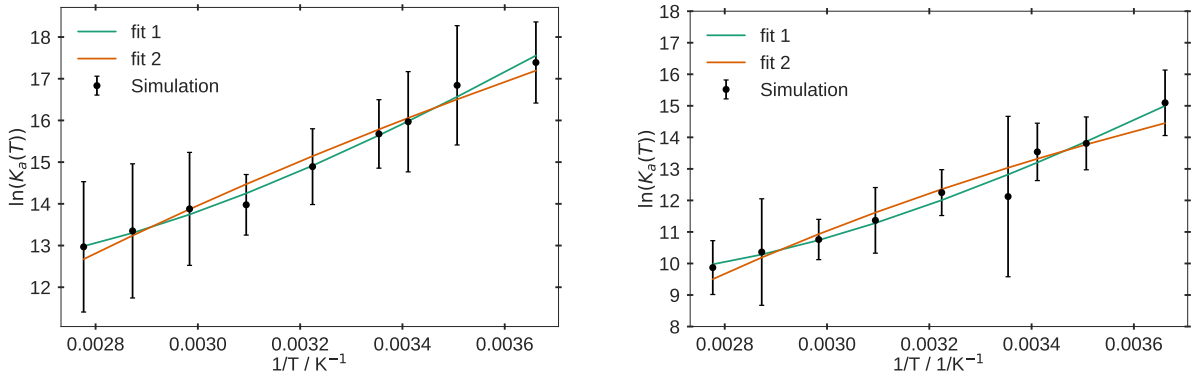

(a) (b)

Figure S6: van't Hoff plots of the temperature dependence of the equilibrium constant for the dimerization in 25 vol% (a) and 50 vol% (b) ethanol/water mixture, respectively. The curves labelled *fit1* correspond to an unconstrained optimization of the three parameters α, β and C (see Eq. 2.8 in the main text). The curves labelled *fit2* correspond to an optimization of α_2 and C_2 only while fixing β_2 to $0.1132\,\mathrm{kJ\,mol^{-1}\,K^{-1}}$ (a) and $-0.0065\,\mathrm{kJ\,mol^{-1}\,K^{-1}}$ (b).

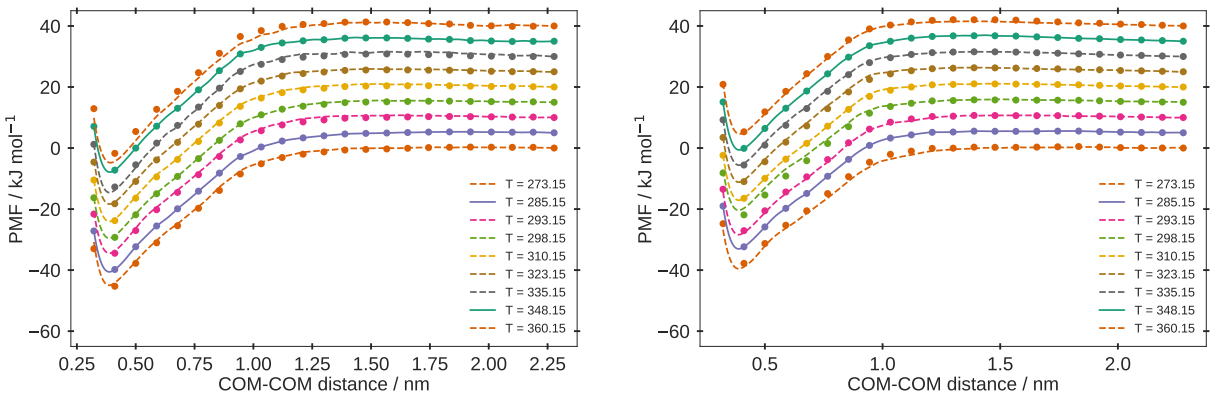

(a) (b)

Figure S7: Potentials of mean force as function of the center-of-mass separation for different temperatures in 25 vol% (a) and 50 vol% (b) ethanol/water mixture, respectively. Symbols corespond to MD simulations, solid lines represent the two reference PMFs and dashed lines the predictions according to Eq. 2.4 of the main text. For better readability each PMF has been shifted by 5 kJ mol^{-1} relative to the previous PMF at the next lower temperature.

A.4 Dimerization in Aqueous NaCl Solution

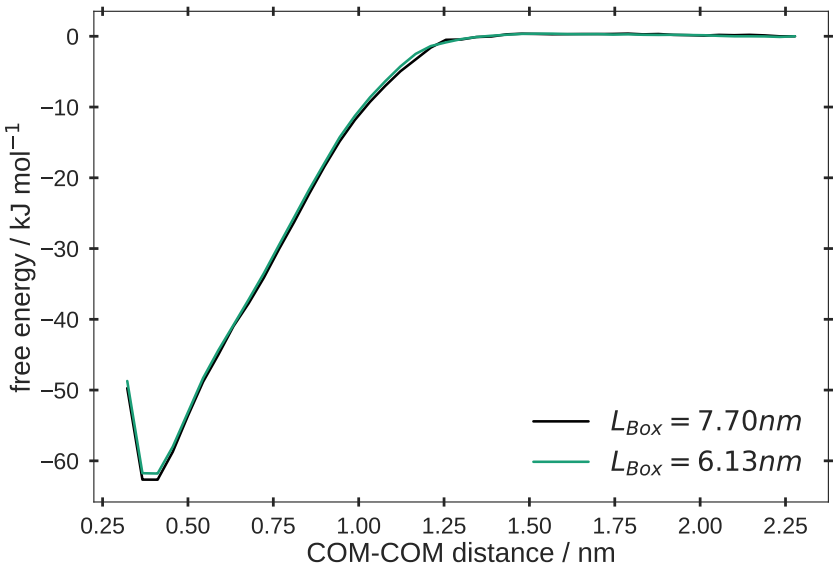

Figure S8: Potentials of mean force at 298.15 K in 1 M aqueous NaCl solution for two different sizes of the computational box. The number of solvent molecules and ions is specified in Table 2.1 of the main text.

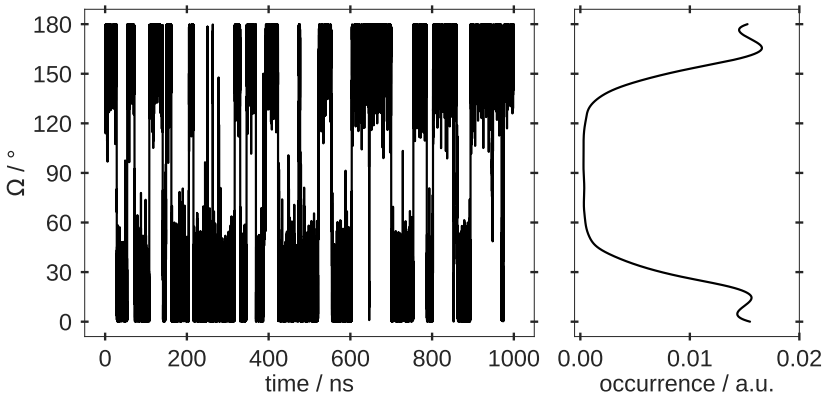

Figure S9: Time series and distribution of the center-of-mass distance for a PBI dimer at 298.15 K in 0.5 M NaCl solution.

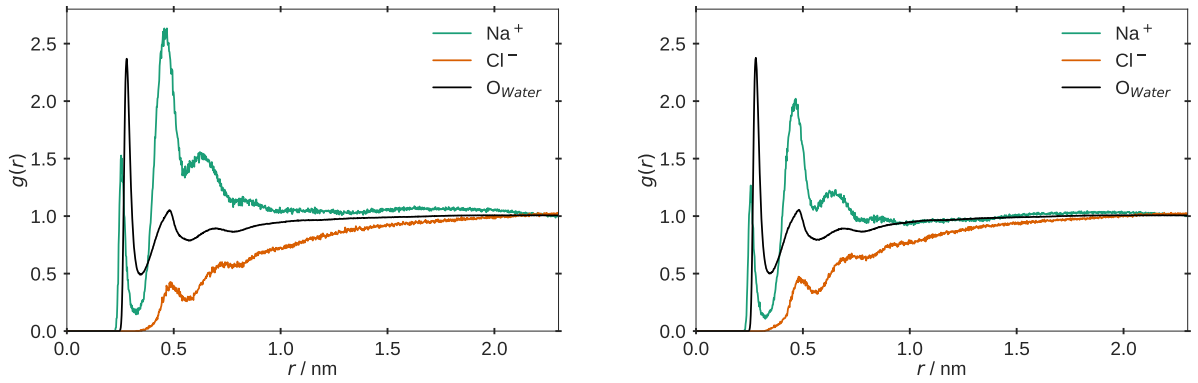

Figure S10: Radial distribution functions of Na^+, Cl^- and water oxygen around the carboxylate oxygens of the dimerized PBI in 0.5 M (a) and 1.0 M (b) aqueous NaCl solution at 298.15 K.

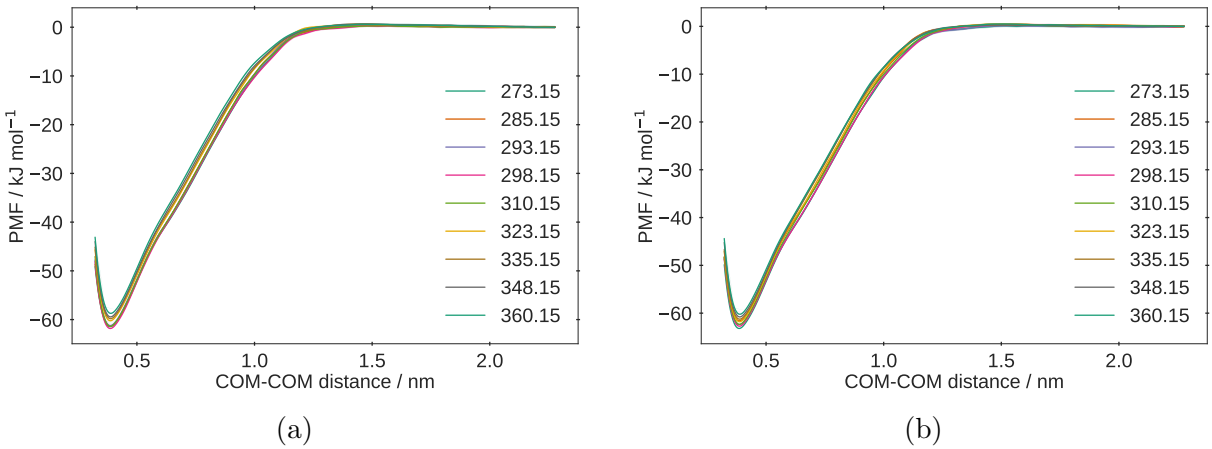

Figure S11: Potentials of mean force as function of the center-of-mass separation for different temperatures in 0.5 M (a) and 1.0 M (b) aqueous NaCl solution, respectively. Errors are within the line width and correspond to one standard deviation.

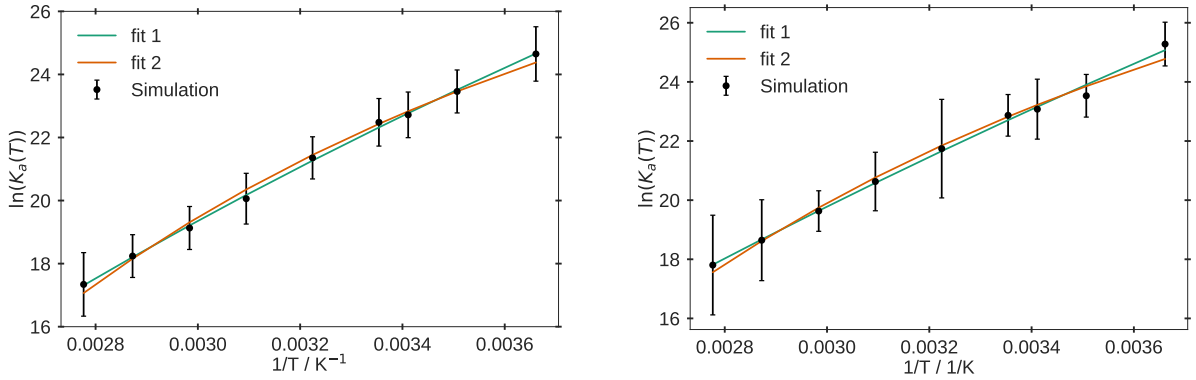

(a) (b)

Figure S12: van't Hoff plots of the temperature dependence of the equilibrium constant for the dimerization in 0.5 M (a) and 1.0 M (b) aqueous NaCl solution, respectively. The curves labelled *fit1* correspond to an unconstrained optimization of the three parameters α, β and C (see Eq. 2.8 in the main text). The curves labelled *fit2* correspond to an optimization of α_2 and C_2 only while fixing β_2 to $-0.1566\,\mathrm{kJ\,mol^{-1}\,K^{-1}}$ (a) and $-0.1230\,\mathrm{kJ\,mol^{-1}\,K^{-1}}$ (b).

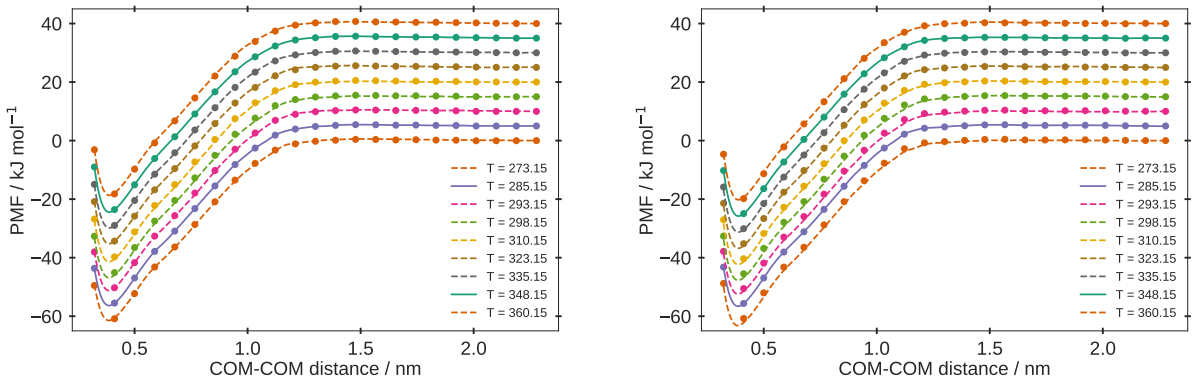

(a) (b)

Figure S13: Potentials of mean force as function of the center-of-mass separation for different temperatures in 0.5 M (a) and 1.0 M (b) aqueous NaCl solution, respectively. Symbols corespond to MD simulations, solid lines represent the two reference PMFs and dashed lines the predictions according to Eq. 2.4 of the main text. For better readability each PMF has been shifted by $5\,\mathrm{kJ\,mol^{-1}}$ relative to the previous PMF at the next lower temperature.

Appendix B

Supporting Information: Thermophysical Properties of Glyceline-Water Mixtures Investigated by Molecular Modelling

B.1 Force Field Parameters for the Cholinium Cation

no.	name	q /e	mass / a.u.
1	CA	-0.12078	12.011
2	HA	0.10737	1.008
3	HA	0.10737	1.008
4	HA	0.10737	1.008
5	NA	0.04518	14.0067
6	CS	-0.02898	12.011
7	CA	-0.12078	12.011
8	CA	-0.12078	12.011
9	HA	0.10737	1.008
10	HA	0.10737	1.008
11	HA	0.10737	1.008
12	HA	0.10737	1.008
13	HA	0.10737	1.008
14	HA	0.10737	1.008
15	HS	0.10044	1.008
16	HS	0.10044	1.008
17	CW	0.13509	12.011
18	OY	-0.55701	15.9994
19	HCW	0.0459	1.008
20	HCW	0.0459	1.008
21	HY	0.40905	1.008

Table S7: Partial charges and atomic masses.

name	σ / nm	ϵ / kJ mol^{-1}
CA	3.39967E-01	4.57730E-01
CS	3.39967E-01	4.57730E-01
CW	3.39967E-01	4.57730E-01
NA	3.25000E-01	7.11280E-01
OY	3.06647E-01	8.80314E-01
HA	1.95998E-01	6.56888E-02
HS	1.95998E-01	6.56888E-02
HCW	2.47135E-01	6.56888E-02
HY	1.99600E-02	4.18000E-03

Table S8: Lennard-Jones parameters.

atom i	atom j	bond length / nm
1	5	0.1499
2	1	0.1091
3	1	0.1091
4	1	0.1091
6	17	0.1535
7	5	0.1499
8	5	0.1499
9	7	0.1091
10	7	0.1091
11	7	0.1091
12	8	0.1091
13	8	0.1091
14	8	0.1091
15	6	0.1091
16	6	0.1091
17	18	0.1426
18	21	0.0974
19	17	0.1093
20	17	0.1093
5	6	0.1499

Table S9: Equilibrium bond lengths.

atom i	atom j	atom k	Θ_{eq} / °	K_0 / kJ/mol/rad^2
1	5	6	110.6400473	525.84512
1	5	7	110.6400473	525.84512
1	5	8	110.6400473	525.84512
2	1	3	110.7400473	326.68672
2	1	4	110.7400473	326.68672
2	1	5	107.9100461	410.19936
3	1	4	110.7400473	326.68672
3	1	5	107.9100461	410.19936
4	1	5	107.9100461	410.19936
5	6	15	107.9100461	410.19936
5	6	16	107.9100461	410.19936
5	6	17	114.3200492	539.31760
6	17	18	109.4300470	566.68096
6	17	19	110.0700471	387.94048
6	17	20	110.0700471	387.94048
7	5	6	110.6400473	525.84512
7	5	8	110.6400473	525.84512
8	5	6	110.6400473	525.84512
9	7	5	107.9100461	410.19936
9	7	10	110.7400473	326.68672
9	7	11	110.7400473	326.68672
10	7	5	107.9100461	410.19936
10	7	11	110.7400473	326.68672
11	7	5	107.9100461	410.19936
12	8	5	107.9100461	410.19936
12	8	13	110.7400473	326.68672
12	8	14	110.7400473	326.68672
13	8	5	107.9100461	410.19936
13	8	14	110.7400473	326.68672
14	8	5	107.9100461	410.19936
15	6	16	109.5500472	327.85824
15	6	17	111.7400478	385.09536
16	6	17	111.7400478	385.09536
17	18	21	108.1600465	394.04912
19	17	18	109.8800469	426.51696
19	17	20	109.5500472	327.85824
20	17	18	109.8800469	426.51696

Table S10: Equilibrium bending angles and force constants.

atom i	atom j	atom k	atom l	ϕ_S / °	K_ϕ / kJ mol^{-1}	n
1	5	7	9	0.0	0.652704	3
1	5	7	10	0.0	0.652704	3
1	5	7	11	0.0	0.652704	3
1	5	8	12	0.0	0.652704	3
1	5	8	13	0.0	0.652704	3
1	5	8	14	0.0	0.652704	3
1	5	6	15	0.0	0.652704	3
1	5	6	16	0.0	0.652704	3
1	5	6	17	0.0	0.652704	3
2	1	5	7	0.0	0.652704	3
2	1	5	6	0.0	0.652704	3
2	1	5	8	0.0	0.652704	3
3	1	5	8	0.0	0.652704	3
3	1	5	6	0.0	0.652704	3
3	1	5	7	0.0	0.652704	3
4	1	5	6	0.0	0.652704	3
4	1	5	8	0.0	0.652704	3
4	1	5	7	0.0	0.652704	3
5	6	17	18	0.0	0.652704	3
5	6	17	19	0.0	0.652704	3
5	6	17	20	0.0	0.652704	3
6	17	18	21	0.0	0.669440	3
6	17	18	21	0.0	1.046000	1
7	5	8	12	0.0	0.652704	3
7	5	8	13	0.0	0.652704	3

Table S11: Dihedral angles - Part 1.

atom i	atom j	atom k	atom l	ϕ_S / °	K_ϕ / kJ mol^{-1}	n
7	5	8	14	0.0	0.652704	3
7	5	6	15	0.0	0.652704	3
7	5	6	16	0.0	0.652704	3
7	5	6	17	0.0	0.652704	3
8	5	6	15	0.0	0.652704	3
8	5	6	16	0.0	0.652704	3
8	5	6	17	0.0	0.652704	3
9	7	5	6	0.0	0.652704	3
9	7	5	8	0.0	0.652704	3
10	7	5	6	0.0	0.652704	3
10	7	5	8	0.0	0.652704	3
11	7	5	6	0.0	0.652704	3
11	7	5	8	0.0	0.652704	3
12	8	5	6	0.0	0.652704	3
13	8	5	6	0.0	0.652704	3
14	8	5	6	0.0	0.652704	3
15	6	17	18	0.0	0.652704	3
15	6	17	19	0.0	0.652704	3
15	6	17	20	0.0	0.652704	3
16	6	17	18	0.0	0.652704	3
16	6	17	19	0.0	0.652704	3
16	6	17	20	0.0	0.652704	3
19	17	18	21	0.0	0.698728	3
20	17	18	21	0.0	0.698728	3

Table S12: Dihedral angles - Part 2.

B.2 Force Field Parameters for Chloride Anion

no.	name	q /e	mass / a.u.
1	Cl	-0.90	35.435

Table S13: Partial charges and atomic masses.

name	σ / nm	ϵ / kJ mol^{-1}
Cl	4.40100E-01	4.18480E-01

Table S14: Lennard-Jones parameters.

B.3 Force Field Parameters for Glycerol

no.	name	q /e	mass / a.u.
1	C3	0.1197	12.010
2	C3	0.1521	12.010
3	C3	0.1197	12.010
4	OH	-0.6270	16.000
5	OH	-0.5848	16.000
6	OH	-0.6270	16.000
7	H1	0.0537	1.008
8	H1	0.0537	1.008
9	H1	0.0221	1.008
10	H1	0.0537	1.008
11	H1	0.0537	1.008
12	HO	0.4096	1.008
13	HO	0.3912	1.008
14	HO	0.4096	1.008

Table S15: Partial charges and atomic masses.

name	σ / nm	ϵ / kJ mol^{-1}
C3	3.40E-01	4.58E-01
H1	2.47E-01	6.57E-02
HO	2.00E-02	4.18E-03
OH	3.07E-01	8.80E-01

Table S16: Lennard-Jones parameters.

atom i	atom j	bond length / nm
1	2	1.54E-01
1	6	1.43E-01
1	7	1.09E-01
1	8	1.09E-01
2	3	1.54E-01
2	5	1.43E-01
2	9	1.09E-01
3	4	1.43E-01
3	10	1.09E-01
3	11	1.09E-01
4	12	9.74E-02
5	13	9.74E-02
6	14	9.74E-02

Table S17: Equilibrium bond lengths.

atom i	atom j	atom k	Θ_{eq} / °	K_0 / kJ/mol/rad^2
1	2	3	1.11E+02	5.29E+02
1	2	5	1.09E+02	5.67E+02
1	2	9	1.10E+02	3.88E+02
1	6	14	1.08E+02	3.94E+02
2	1	6	1.09E+02	5.67E+02
2	1	7	1.10E+02	3.88E+02
2	1	8	1.10E+02	3.88E+02
2	3	4	1.09E+02	5.67E+02
2	3	10	1.10E+02	3.88E+02
2	3	11	1.10E+02	3.88E+02
2	5	13	1.08E+02	3.94E+02
3	2	5	1.09E+02	5.67E+02
3	2	9	1.10E+02	3.88E+02
3	4	12	1.08E+02	3.94E+02
4	3	10	1.10E+02	4.27E+02
4	3	11	1.10E+02	4.27E+02
5	2	9	1.10E+02	4.27E+02
6	1	7	1.10E+02	4.27E+02
6	1	8	1.10E+02	4.27E+02
7	1	8	1.10E+02	3.28E+02
10	3	11	1.10E+02	3.28E+02

Table S18: Equilibrium bending angles and force constants.

atom i	atom j	atom k	atom l	n	K_1 / kJ mol^{-1}	K_2 / kJ mol^{-1}	K_3 / kJ mol^{-1}	K_4 / kJ mol^{-1}
1	2	3	4	3	6.5084E-01	1.95252	0.0000	-2.60336
1	2	3	10	3	6.5084E-01	1.95252	0.0000	-2.60336
1	2	3	11	3	6.5084E-01	1.95252	0.0000	-2.60336
1	2	5	13	3	1.0460E+00	-1.04600	0.0000	-0.00000
1	2	5	13	3	6.6944E-01	2.00832	0.0000	-2.67776
2	1	6	14	3	1.0460E+00	-1.04600	0.0000	-0.00000
2	1	6	14	3	6.6944E-01	2.00832	0.0000	-2.67776
2	3	4	12	3	1.0460E+00	-1.04600	0.0000	-0.00000
2	3	4	12	3	6.6944E-01	2.00832	0.0000	-2.67776
3	2	5	13	3	1.0460E+00	-1.04600	0.0000	-0.00000
3	2	5	13	3	6.6944E-01	2.00832	0.0000	-2.67776
4	3	2	5	3	0.0000E+00	-0.00000	9.8324	-0.00000
4	3	2	5	3	6.0250E-01	1.80750	0.0000	-2.41000
4	3	2	9	3	1.0460E+00	-1.04600	0.0000	-0.00000
4	3	2	9	3	0.0000E+00	-0.00000	0.0000	-0.00000
5	2	3	10	3	1.0460E+00	-1.04600	0.0000	-0.00000
5	2	3	10	3	0.0000E+00	-0.00000	0.0000	-0.00000
5	2	3	11	3	0.0000E+00	-0.00000	0.0000	-0.00000
5	2	3	11	3	1.0460E+00	-1.04600	0.0000	-0.00000
6	1	2	3	3	6.5084E-01	1.95252	0.0000	-2.60336
6	1	2	5	3	0.0000E+00	-0.00000	9.8324	-0.00000
6	1	2	5	3	6.0250E-01	1.80750	0.0000	-2.41000
6	1	2	9	3	0.0000E+00	-0.00000	0.0000	-0.00000
6	1	2	9	3	1.0460E+00	-1.04600	0.0000	-0.00000
7	1	2	3	3	6.5084E-01	1.95252	0.0000	-2.60336
7	1	2	5	3	1.0460E+00	-1.04600	0.0000	-0.00000
7	1	2	5	3	0.0000E+00	-0.00000	0.0000	-0.00000
7	1	2	9	3	6.5084E-01	1.95252	0.0000	-2.60336
7	1	6	14	3	6.9733E-01	2.09199	0.0000	-2.78932
8	1	2	3	3	6.5084E-01	1.95252	0.0000	-2.60336
8	1	2	5	3	1.0460E+00	-1.04600	0.0000	-0.00000
8	1	2	5	3	0.0000E+00	-0.00000	0.0000	-0.00000
8	1	2	9	3	6.5084E-01	1.95252	0.0000	-2.60336
8	1	6	14	3	6.9733E-01	2.09199	0.0000	-2.78932
9	2	3	10	3	6.5084E-01	1.95252	0.0000	-2.60336
9	2	3	11	3	6.5084E-01	1.95252	0.0000	-2.60336
9	2	5	13	3	6.9733E-01	2.09199	0.0000	-2.78932
10	3	4	12	3	6.9733E-01	2.09199	0.0000	-2.78932
11	3	4	12	3	6.9733E-01	2.09199	0.0000	-2.78932

Table S19: Dihedral angles.

B.4 Self-Diffusion Coefficients

System	x_W / $\mathrm{mol\,mol^{-1}}$	$D_{self}(T = 280.15\,K)$ / $10^{-5}\,cm^2/s$	$D_{self}(T = 320.15\,K)$ / $10^{-5}\,cm^2/s$	$D_{self}(T = 360.15\,K)$ / $10^{-5}\,cm^2/s$
C0	1.00	1.5236 ± 0.0282	3.8444 ± 0.0674	7.0428 ± 0.0799
C1	0.90	0.7245 ± 0.0121	1.9774 ± 0.0231	3.9689 ± 0.0297
C2	0.75	0.2287 ± 0.0073	0.8228 ± 0.0147	1.9504 ± 0.0217
C3	0.50	0.0410 ± 0.0133	0.2448 ± 0.0064	0.8053 ± 0.0251
C4	0.25	0.0135 ± 0.0124	0.8962 ± 0.0059	0.4087 ± 0.0242
C5	0.10	0.0121 ± 0.0206	0.0570 ± 0.0106	0.3008 ± 0.0253
TIP4P	1.00	-	0.3038	-

Table S20: Uncorrected self-diffusion coefficients for different compositions and different temperatures. Errors listed equal one standard deviation.

B.5 Finite Size Effects

L_{Box} / nm	N_{Ch} and N_{Cl}	N_{Gly}	N_W
4.94623	225	450	675
5.44400	300	600	900
5.86419	375	750	1125
6.85893	600	1200	1800

Table S21: Composition and box lengths for different system sizes of composition C3.

B.6 Binary Mixture Glycerol and Water

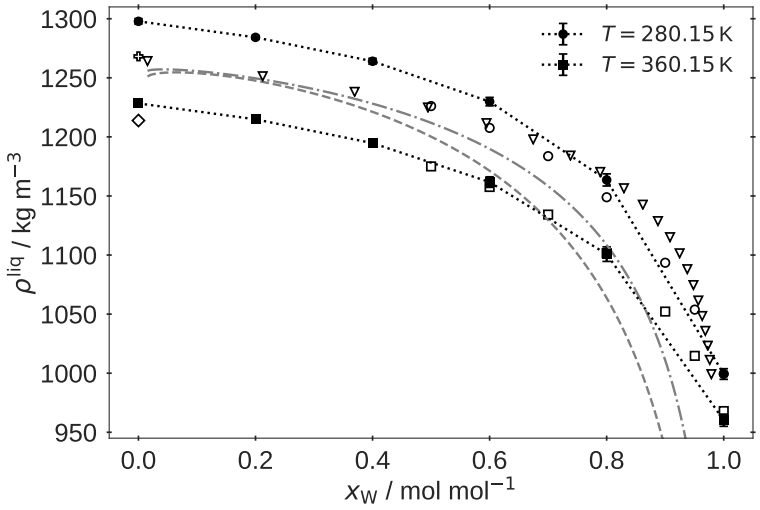

Figure S14: Liquid density of a binary mixture of glycerol and water for different water mole fractions at two different temperatures (280.15 K and 360.15 K). Experimental data are taken from Ref. [536] (open circles at 280.15 K and open squares at 360.15 K), from Ref.[537] (open plus at 283.15 K and open diamond at 368.15 K), from Ref. [538] (open triangles down at 288.15 K).

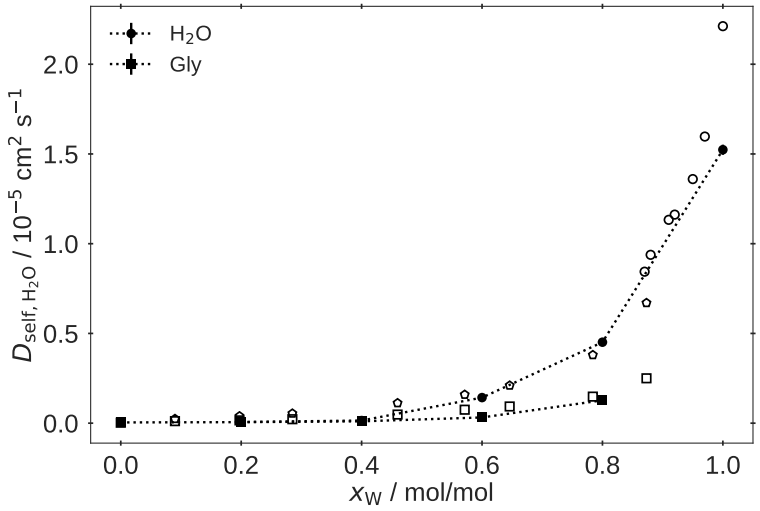

Figure S15: Self-diffusion coefficient of a binary mixture including glycerol and water for different water mole fractions at 280.15 K. Experimental data for water are taken from Ref. [539] (open triangles) and Ref. [540] (open circles) while experimental data for glycerol are taken from Ref. [539] (open squares). Note that all experimental data are measured at 298.15 K.

B.7 Binary Mixture Choline and Water

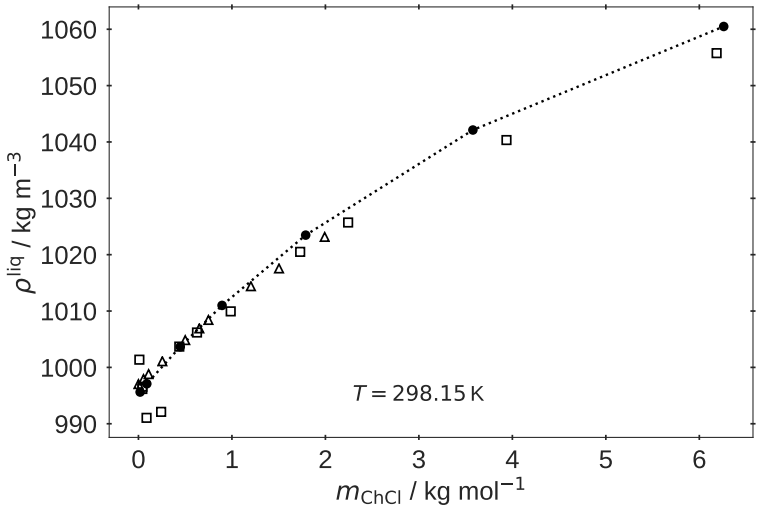

Figure S16: Liquid density of a binary mixture of choline chloride and water as function of ChCl molality at 298.15 K. Experimental data are taken from Refs [541, 542] and are represented by open symbols.

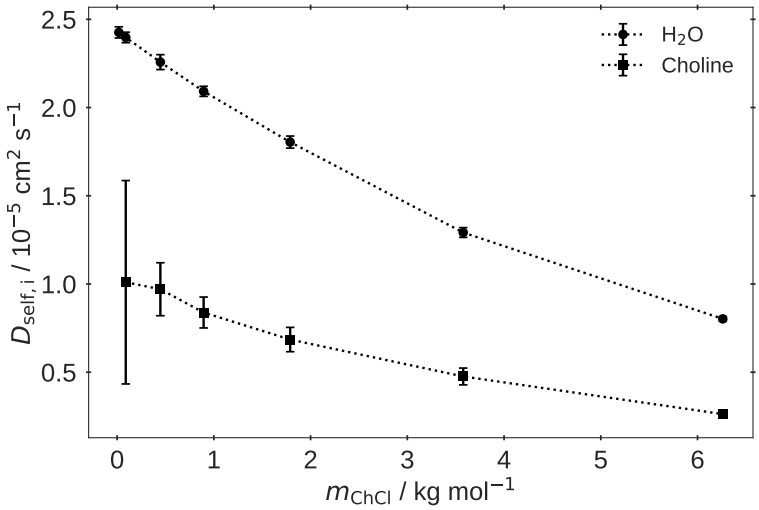

Figure S17: Self-diffusion coefficients in a binary mixture of choline chloride and water as function of ChCl molality at 298.15 K.

B.8 Radial Distribution Functions

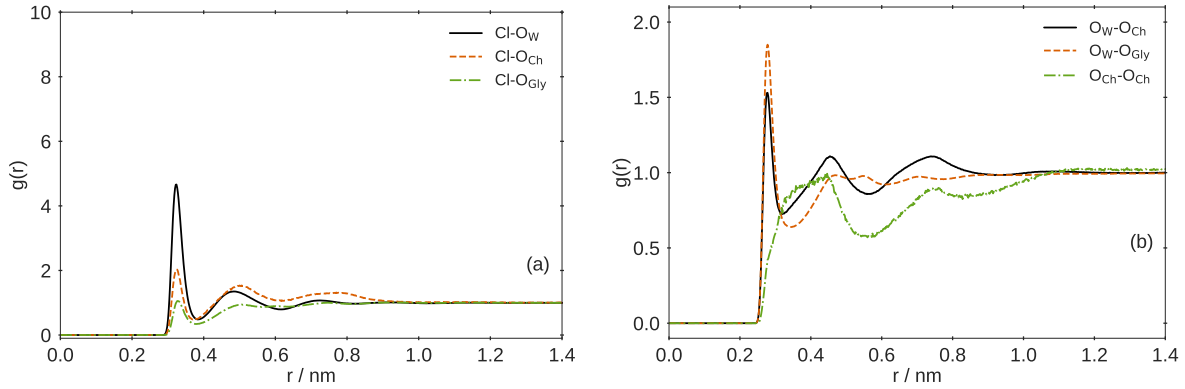

Figure S18: Radial distribution function for composition C1 at 280.15 K.

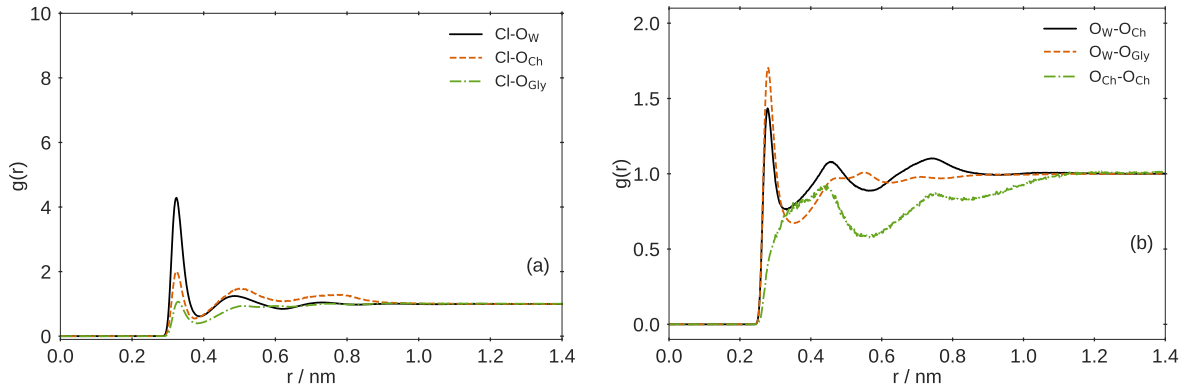

Figure S19: Radial distribution function for composition C1 at 320.15 K.

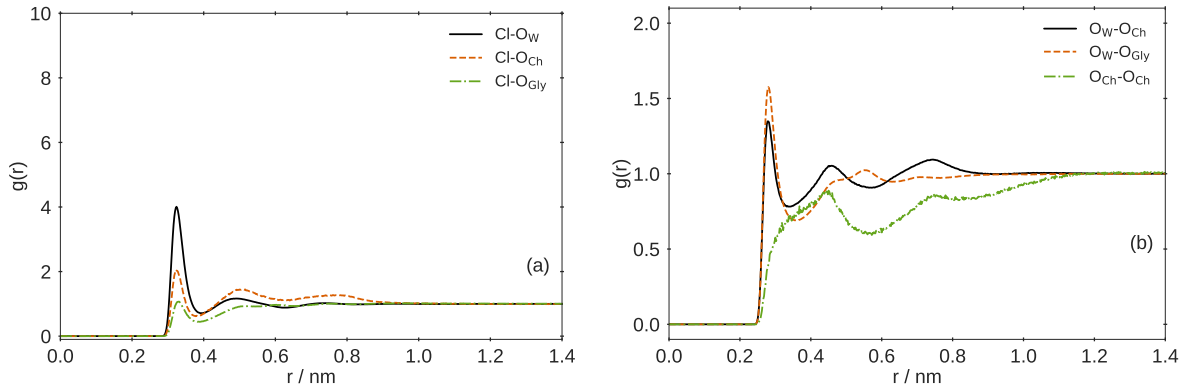

Figure S20: Radial distribution function for composition C1 at 360.15 K.

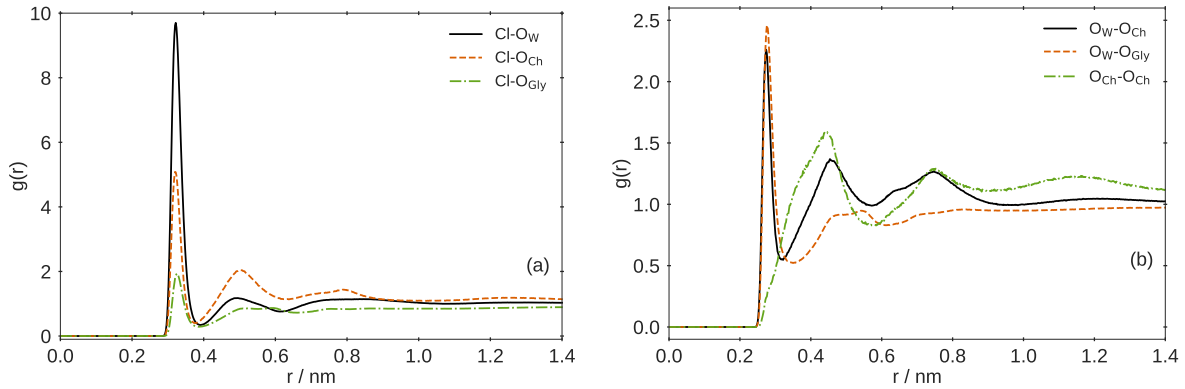

Figure S21: Radial distribution function for composition C3 at 280.15 K.

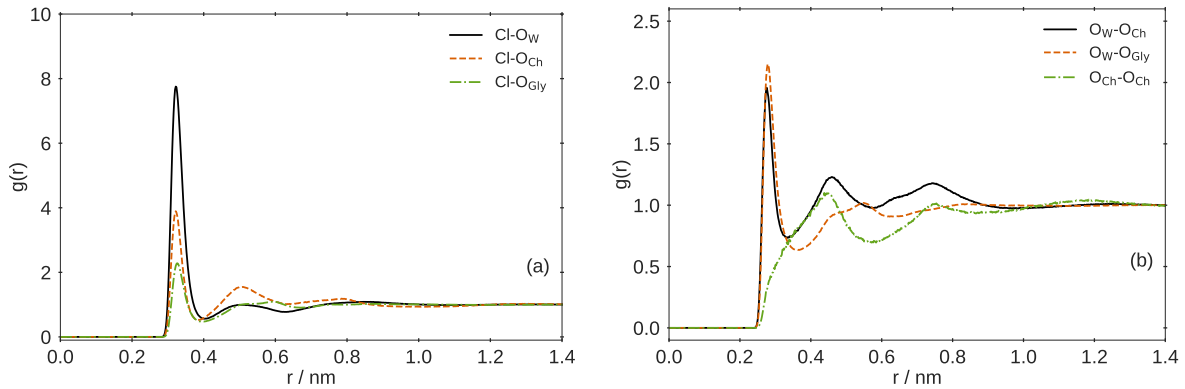

Figure S22: Radial distribution function for composition C3 at 360.15 K.

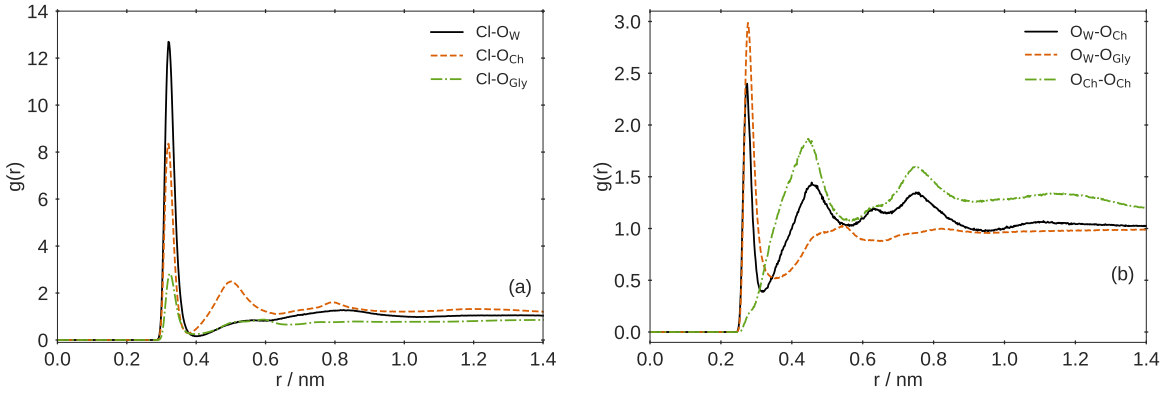

Figure S23: Radial distribution function for composition C5 at 280.15 K.

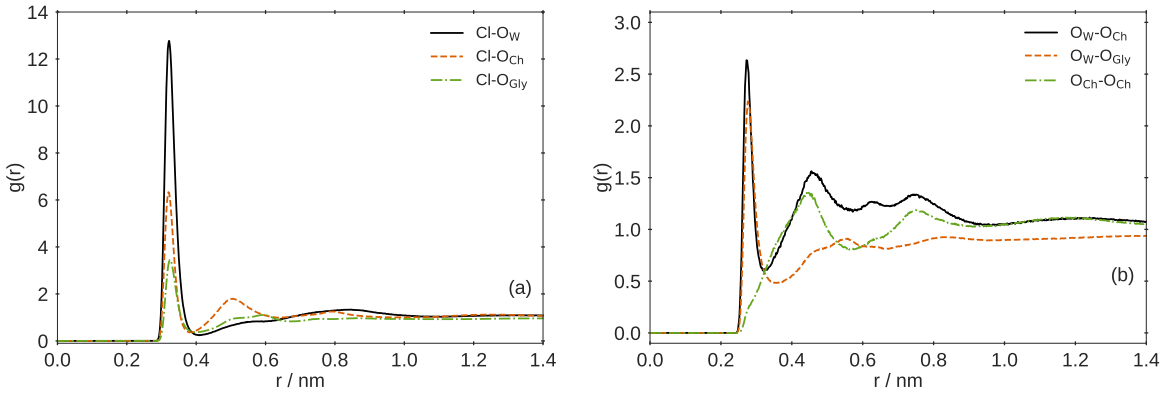

Figure S24: Radial distribution function for composition C5 at 320.15 K.

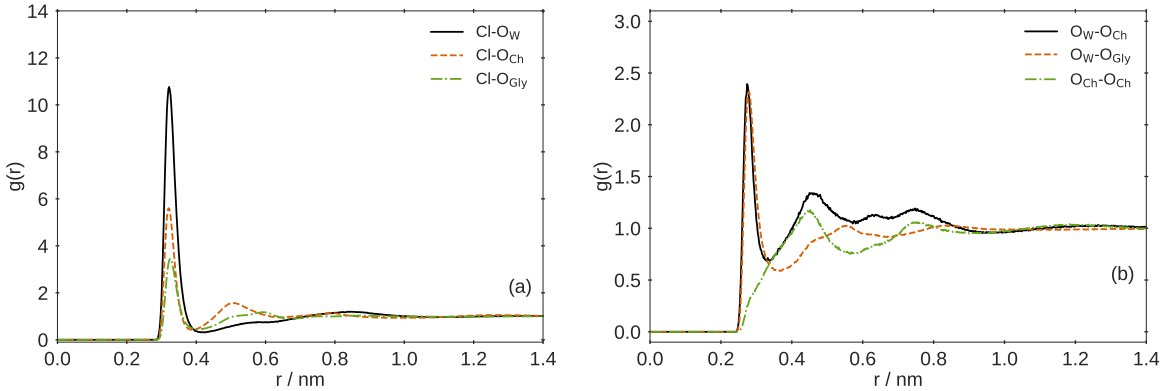

Figure S25: Radial distribution function for composition C5 at 360.15 K.

B.9 Self-Diffusion Coefficients of Choline, Chloride and Glycerol

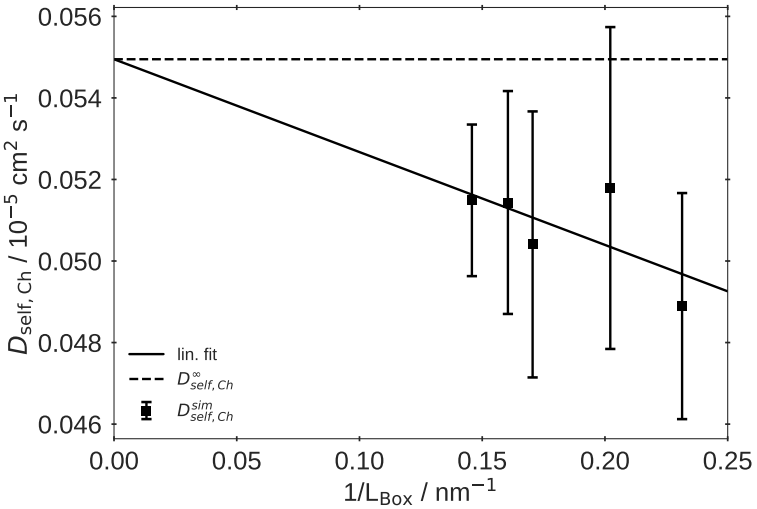

Figure S26: Self-diffusion coefficient of cholinium cation as function of the inverse box length for system C3.

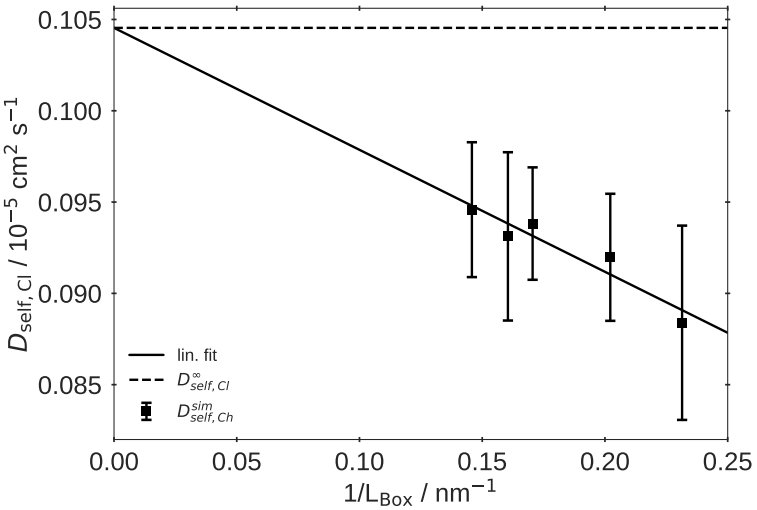

Figure S27: Self-diffusion coefficient of chloride as function of the inverse box length for system C3.

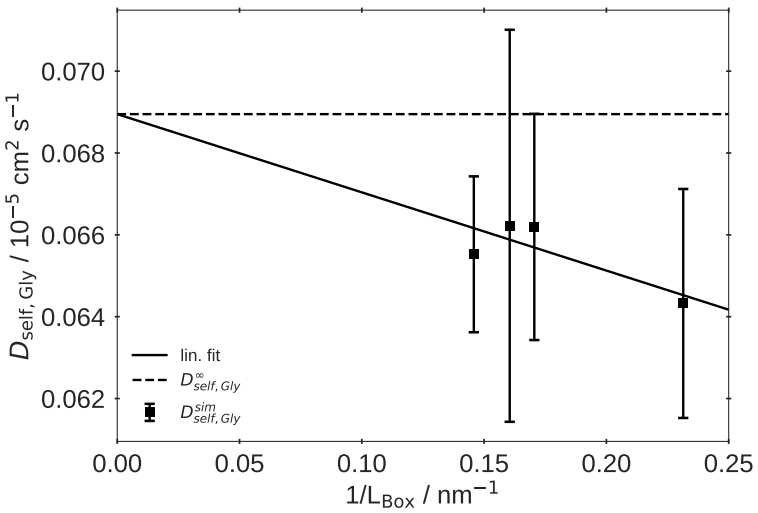

Figure S28: Self-diffusion coefficient of glycerol as function of the inverse box length for system C3.

Appendix C

Supporting Information: On the use of transport properties to discriminate Mie-type molecular models for 1-propanol optimized against VLE data

C.1 Covalent Force Field Parameters

i	j	bond length / nm
H1	O1	0.0945
O1	C1	0.1420
C1	C2	0.1514
C2	C3	0.1714

Table S22: Bond lengths.

i	j	k	bond angle θ^0_{ijk} / °	force constant k^θ_{ijk} / kJ/mol/rad^2
H1	O1	C1	107.40	382.13268
O1	C1	C2	113.50	517.57527
C1	C2	C3	114.00	519.65388

Table S23: Equilibrium bending angles θ^0_{ijk} and force constants k^θ_{ijk} used to describe the angle bending potential according to $U_{\text{bend}}(\theta_{ijk}) = \frac{1}{2} k^\theta_{ijk} \left(\theta_{ijk} - \theta^0_{ijk}\right)^2$.

i	j	k	l	ϕ_s / °	force constant $k_{\phi,C(i)}$ / kJ mol^{-1}	n
H1	O1	C1	C2	0.00	-1.53809	0
H1	O1	C1	C2	0.00	0.68179	1
H1	O1	C1	C2	180.00	0.30672	2
H1	O1	C1	C2	0.00	2.52635	3
O1	C1	C2	C3	0.00	0.00000	0
O1	C1	C2	C3	0.00	1.71652	1
O1	C1	C2	C3	180.00	-1.85047	2
O1	C1	C2	C3	0.00	9.02186	3

Table S24: Phase shift ϕ_s, force constant $k_{\phi,C(i)}$ and multiplicities n used to describe the torsional potential energy according to $U_{\text{torsion}}(\phi_{ijkl}) = \sum_{C(i)} k_{\phi,C(i)} \left(1 + \cos(n\phi - \phi_s)\right)$.

C.2 Self-Diffusion Coefficients - Uncorrected Values

	set 1	set 2	set 3	set 4
T / K	D_{self}	D_{self}	D_{self}	D_{self}
273.15	0.34067	0.3344	0.4404	0.3417
293.15	0.63384	0.6332	0.7640	0.6673
323.15	1.41546	1.3839	1.6409	1.4956
350.15	2.54204	2.5191	2.7109	2.4006

Table S25: Uncorrected self-diffusion coefficients in $10^{-5} cm^2 s^{-1}$.

C.3 Radial Distribution Functions

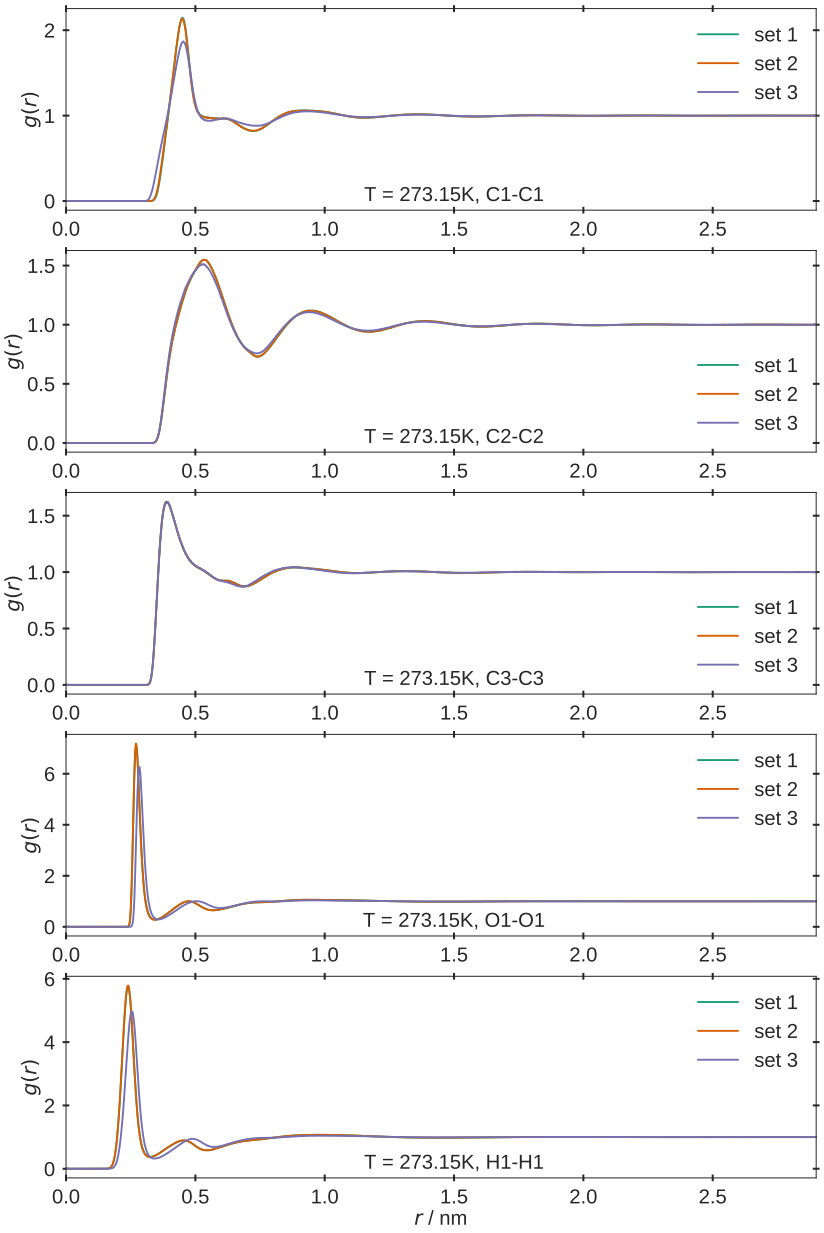

Figure S29: Radial distribution function $g(r)$ at 273.15 K

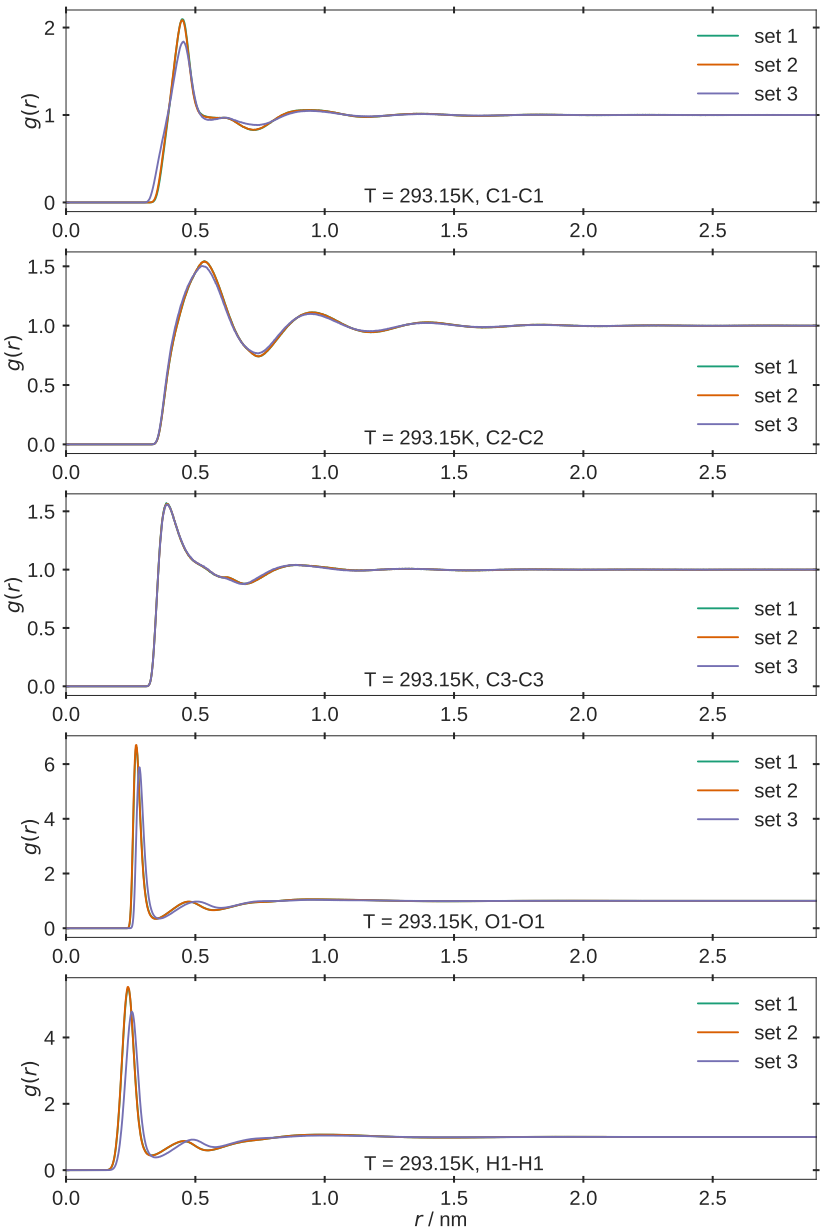

Figure S30: Radial distribution function $g(r)$ at 293.15 K

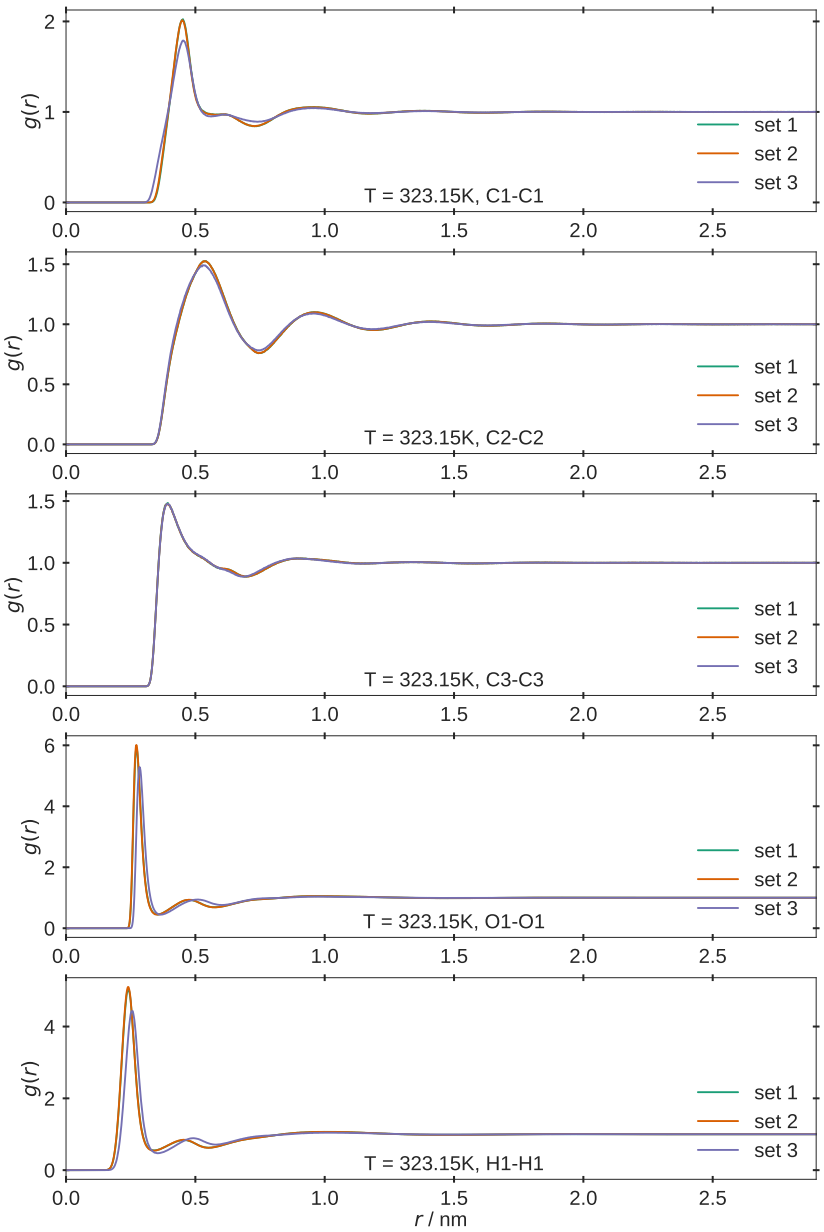

Figure S31: Radial distribution function $g(r)$ at 323.15 K

Appendix D

Supporting Information: Transferable Anisotropic Mie-Potential Force Field for n-Alcohols: Static and Dynamic Fluid Properties of Pure Substances and Binary Mixtures

D.1 Nonbonded Energy Calculation

Alternatively Eq. (5.1) in the main text can be expressed as

$$u_{ij}^{\text{inter}} = A(\sigma_{ij}, \varepsilon_{ij}, n_{ij}, m_{ij})h(r_{ij}) + C(\sigma_{ij}, \varepsilon_{ij}, n_{ij}, m_{ij})g(r_{ij}) + \frac{q_i q_j}{4\pi\epsilon_0} f(r_{ij}) \tag{D.1}$$

with

$$A(\sigma_{ij}, \varepsilon_{ij}, n_{ij}, m_{ij}) = \frac{n_{ij}}{n_{ij} - m_{ij}} \left(\frac{n_{ij}}{m_{ij}}\right)^{\frac{m_{ij}}{n_{ij}-m_{ij}}} \epsilon_{ij}\sigma_{ij}^{n_{ij}} \tag{D.2}$$

and

$$C(\sigma_{ij}, \varepsilon_{ij}, n_{ij}, m_{ij}) = \frac{n_{ij}}{n_{ij} - m_{ij}} \left(\frac{n_{ij}}{m_{ij}}\right)^{\frac{m_{ij}}{n_{ij}-m_{ij}}} \epsilon_{ij}\sigma_{ij}^{m_{ij}} \tag{D.3}$$

where $h(r_{ij}) = r_{ij}^{-n_{ij}}$, $g(r_{ij}) = -r_{ij}^{-m_{ij}}$, and $f(r_{ij}) = r_{ij}^{-1}$. The latter form of the interaction potential energy is particularly convenient if used in the context of tabulated potentials as it is done in this work for carrying out the molecular dynamics simulations.

D.2 Results

D.2.1 Pure Component Properties

D.2.1.1 Liquid Density

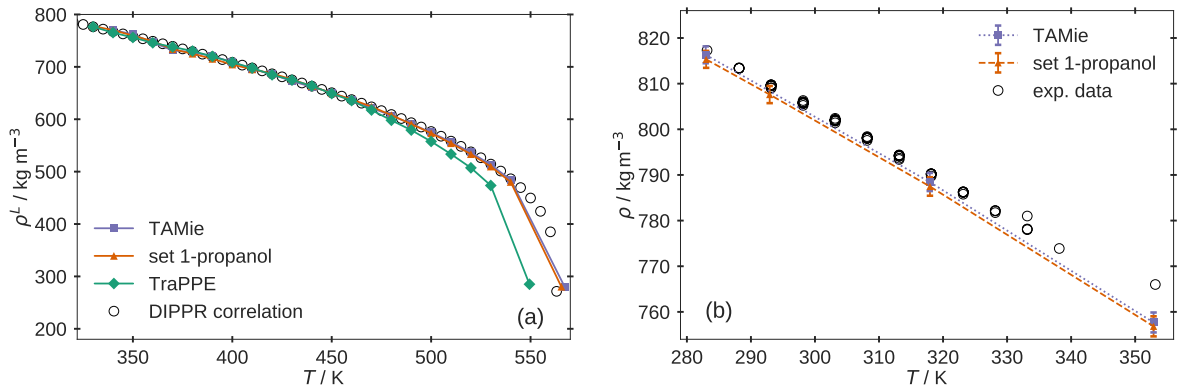

Figure S32: Liquid density ρ^{L} of 1-butanol as function of temperature T for two different temperature ranges. (a) ρ^{L} at VLE conditions obtained from GCMC simulations. Experimental data are represented by the DIPPR correlation [419]. (b) ρ^{L} obtained from MD simulations at 1 bar. Experimental data are from various sources [460, 463, 467, 474, 475, 479–482, 485–487, 490, 510, 513, 543–550] Error bars are within line-width and equal one standard deviation.

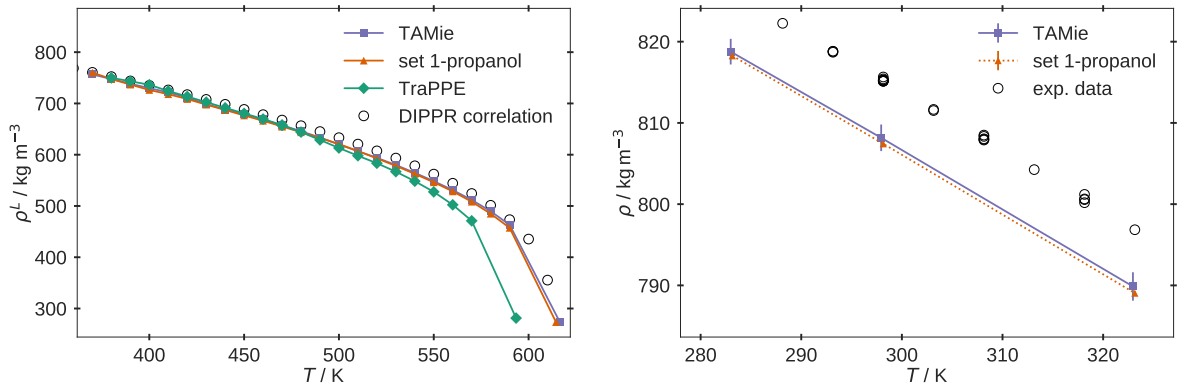

Figure S33: Liquid density ρ^{L} of 1-hexanol as function of temperature T for two different temperature ranges. (a) ρ^{L} at VLE conditions obtained from GCMC simulations. Experimental data are represented by the DIPPR correlation [419]. (b) ρ^{L} obtained from MD simulations at 1 bar. Experimental data are from various sources [519]. Error bars are within line-width and equal one standard deviation.

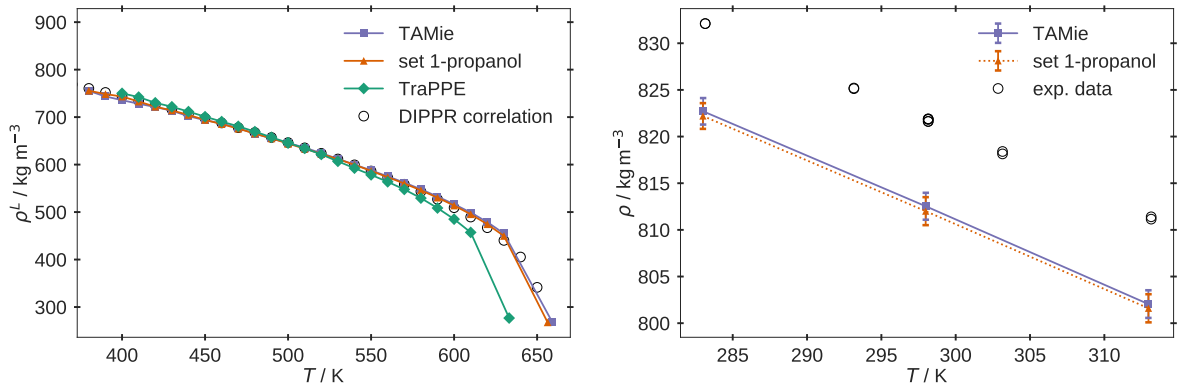

Figure S34: Liquid density ρ^{L} of 1-octanol as function of temperature T for two different temperature ranges. (a) ρ^{L} at VLE conditions obtained from GCMC simulations. Experimental data are represented by the DIPPR correlation [419]. (b) ρ^{L} obtained from MD simulations at 1 bar. Experimental data are from various sources [512, 513, 515, 551, 552]. Error bars are within line-width and equal one standard deviation.

D.2.1.2 Shear Viscosity

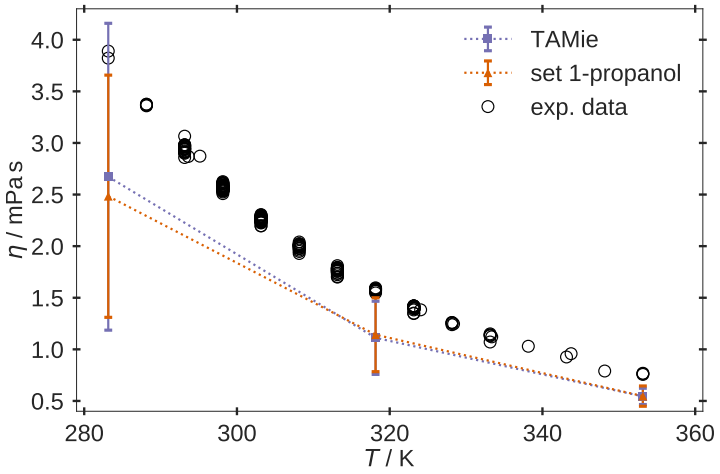

Figure S35: Viscosity η of 1-butanol as function of temperature T. Experimental data are from various sources [423, 424, 452, 454–456, 460, 463, 466, 467, 471, 474, 475, 477–482, 485–487, 490, 510, 545–550, 553–564]. Error bars are within symbol size.

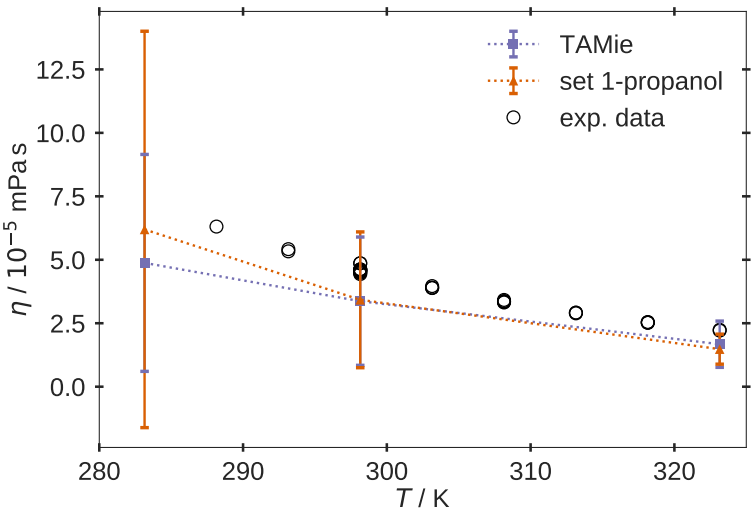

Figure S36: Viscosity η of 1-hexanol as function of temperature T. Experimental data are from various sources [475, 490, 515, 518, 547, 551, 552, 554, 565–569]. Error bars are within symbol size.

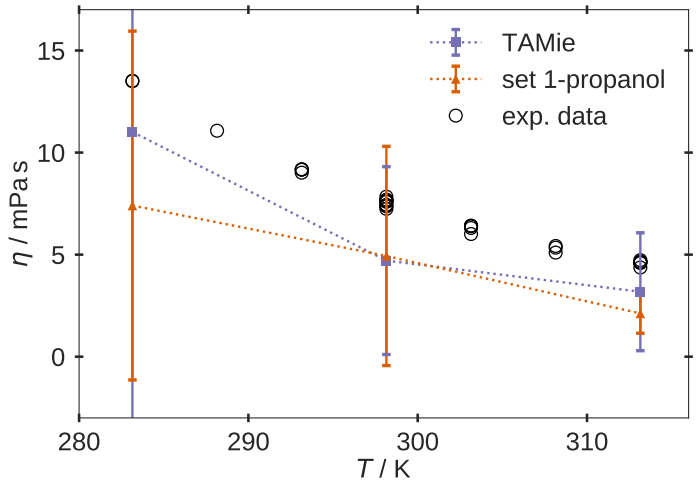

Figure S37: Viscosity η of 1-octanol as function of temperature T. Experimental data are from various sources [458, 513, 515, 516, 551, 552, 554, 557, 569, 570]. Error bars are within symbol size.

D.2.1.3 Self-Diffusion Coefficient

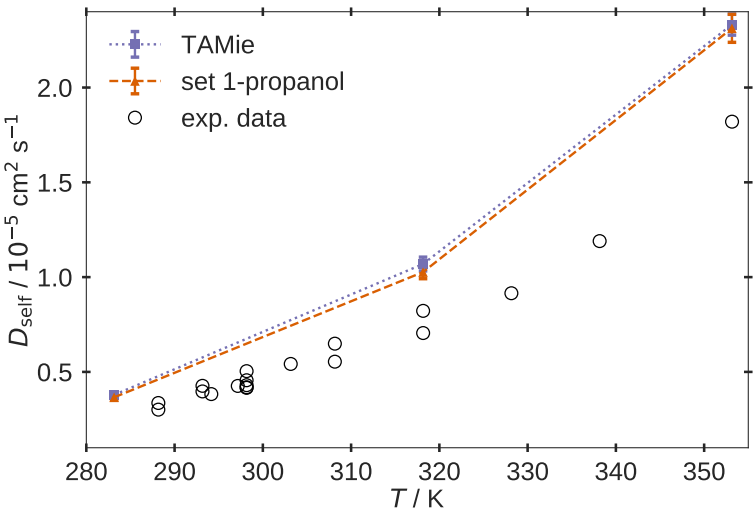

Figure S38: Coefficient of self-diffusion D_{self} of 1-butanol as function of temperature T. Experimental data are from various sources [451, 519–521, 571–575]. Error bars equal one standard deviation. Corrections for finite size effects have been applied according to Yeh and Hummer [346].

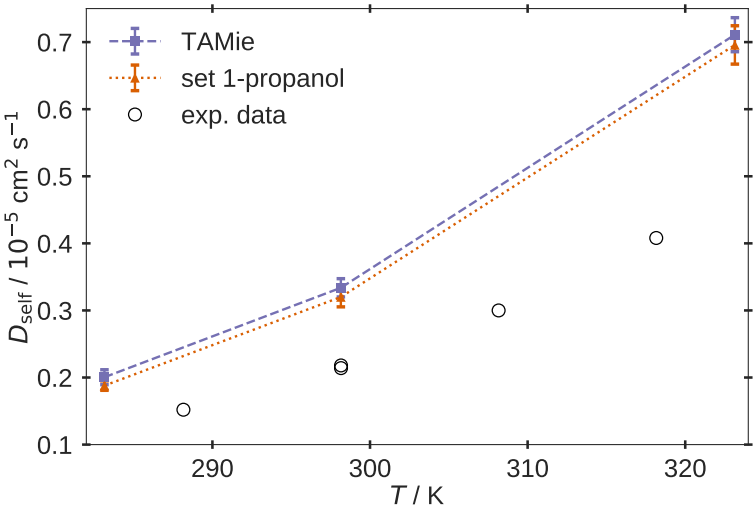

Figure S39: Coefficient of self-diffusion D_{self} of 1-hexanol as function of temperature T. Experimental data are from various sources [519, 520]. Error bars equal one standard deviation. Corrections for finite size effects have been applied according to Yeh and Hummer [346].

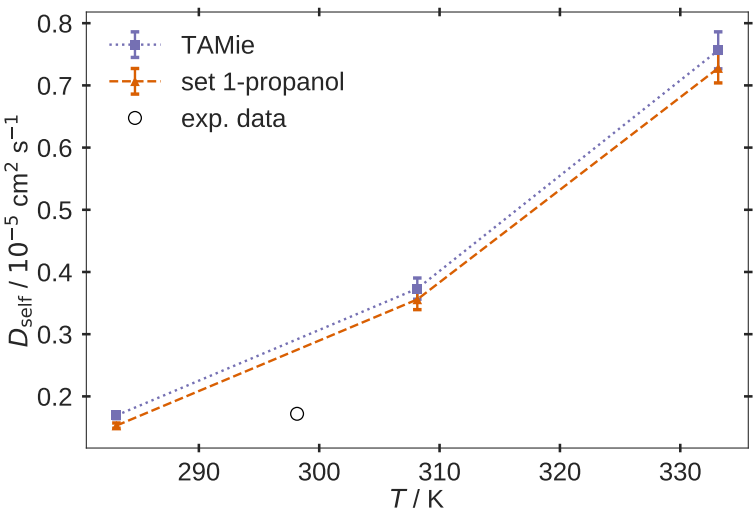

Figure S40: Coefficient of self-diffusion D_{self} of 1-heptanol as function of temperature T. Experimental data are from [519]. Error bars equal one standard deviation. Corrections for finite size effects have been applied according to Yeh and Hummer [346].

D.2.1.4 Saturation Vapor Pressure

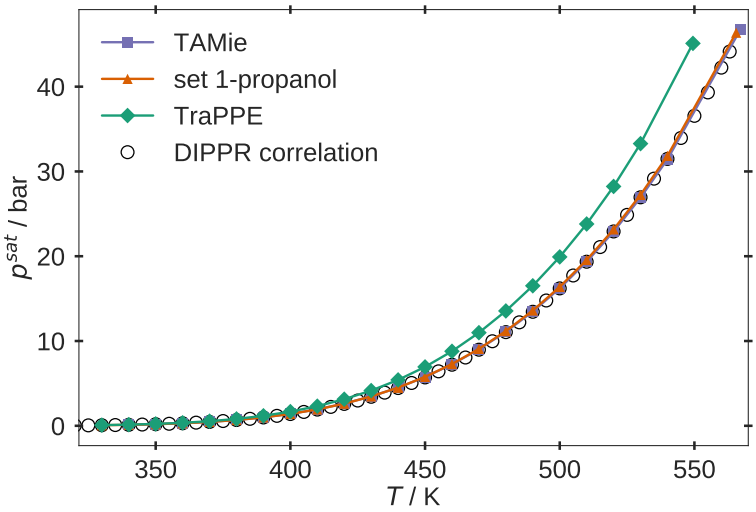

Figure S41: Saturation vapor pressure p^{sat} of 1-butanol as function of temperature T. Experimental data are represented by the DIPPR correlation [419].

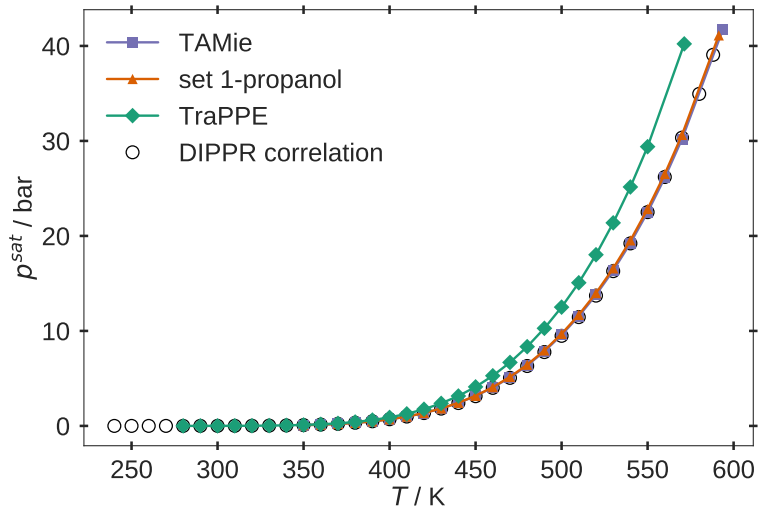

Figure S42: Saturation vapor pressure p^{sat} of 1-pentanol as function of temperature T. Experimental data are represented by the DIPPR correlation [419].

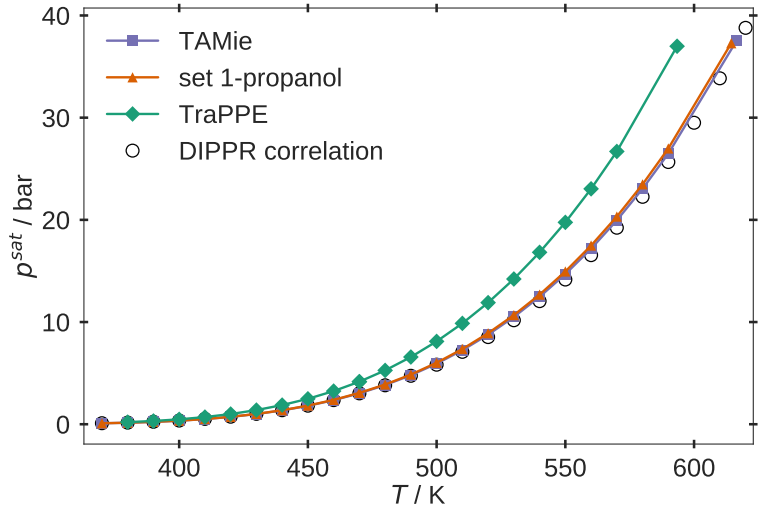

Figure S43: Saturation vapor pressure p^{sat} of 1-hexanol as function of temperature T. Experimental data are represented by the DIPPR correlation [419].

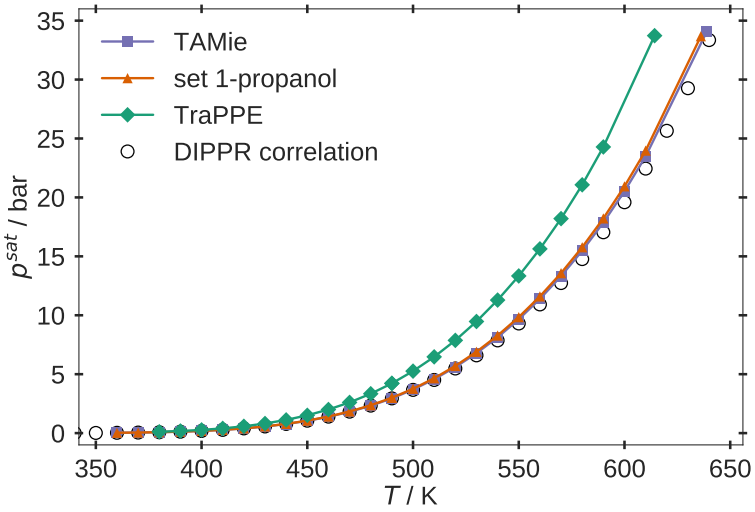

Figure S44: Saturation vapor pressure p^{sat} of 1-heptanol as function of temperature T. Experimental data are represented by the DIPPR correlation [419].